A contribution to the understanding of hydrogen diffusion and embrittlement in metallic materials based on SKPFM measurements and mechanical testing

Elia Tohme

N°d'ordre NNT : 2019LYSEM025

THESE de DOCTORAT DE L'UNIVERSITE DE LYON
opérée au sein de
MINES Saint-Etienne

Ecole Doctorale N° 488
Sciences, Ingénierie, Santé

Spécialité de doctorat : Sciences et Génie des Matériaux

Soutenance prévue publiquement le 17/10/2019, par :

Elia TOHMÉ

A contribution to the understanding of hydrogen diffusion and embrittlement in metallic materials based on SKPFM measurements and mechanical testing.

Devant le jury composé de :

Feaugas, Xavier	Professeur	Univ. de La Rochelle	Président
Briottet, Laurent	Chercheur	CEA Grenoble	Rapporteur
Verbeken, Kim	Professeur	Univ. De Gent	Rapporteur
Bechet, Denis	Ingénieur/Chercheur	Aubert-et-Duval	Examinateur
Wolski, Krzysztof	Directeur de recherche	EMSE	Directeur de thèse
Christien, Frédéric	Professeur	EMSE	Co-directeur de thèse
Bosch, Cédric	Chargé de recherche	EMSE	Co-encadrant
Barnier, Vincent	Ingénieur de recherche	CNRS	Co-encadrant

Spécialités doctorales	Responsables :	Spécialités doctorales	Responsables
SCIENCES ET GENIE DES MATERIAUX	K. Wolski Directeur de recherche	MATHEMATIQUES APPLIQUEES	O. Roustant, Maître-assistant
MECANIQUE ET INGENIERIE	S. Drapier, professeur	INFORMATIQUE	O. Boissier, Professeur
GENIE DES PROCEDES	F. Gruy, Maître de recherche	SCIENCES DES IMAGES ET DES FORMES	JC. Pinoli, Professeur
SCIENCES DE LA TERRE	B. Guy, Directeur de recherche	GENIE INDUSTRIEL	N. Absi, Maitre de recherche
SCIENCES ET GENIE DE L'ENVIRONNEMENT	D. Graillot, Directeur de recherche	MICROELECTRONIQUE	Ph. Lalevée, Professeur

EMSE : Enseignants-chercheurs et chercheurs autorisés à diriger des thèses de doctorat (titulaires d'un doctorat d'Etat ou d'une HDR)

ABSI	Nabil	MR	Génie industriel	CMP
AUGUSTO	Vincent	CR	Image, Vision, Signal	CIS
AVRIL	Stéphane	PR2	Mécanique et ingénierie	CIS
BADEL	Pierre	MA(MDC)	Mécanique et ingénierie	CIS
BALBO	Flavien	PR2	Informatique	FAYOL
BASSEREAU	Jean-François	PR	Sciences et génie des matériaux	SMS
BATTON-HUBERT	Mireille	PR2	Sciences et génie de l'environnement	FAYOL
BEIGBEDER	Michel	MA(MDC)	Informatique	FAYOL
BLAYAC	Sylvain	MA(MDC)	Microélectronique	CMP
BOISSIER	Olivier	PR1	Informatique	FAYOL
BONNEFOY	Olivier	MA(MDC)	Génie des Procédés	SPIN
BORBELY	Andras	MR(DR2)	Sciences et génie des matériaux	SMS
BOUCHER	Xavier	PR2	Génie Industriel	FAYOL
BRODHAG	Christian	DR	Sciences et génie de l'environnement	FAYOL
BRUCHON	Julien	MA(MDC)	Mécanique et ingénierie	SMS
CAMEIRAO	Ana	MA(MDC)	Génie des Procédés	SPIN
CHRISTIEN	Frédéric	PR	Science et génie des matériaux	SMS
DAUZERE-PERES	Stéphane	PR1	Génie Industriel	CMP
DEBAYLE	Johan	MR	Sciences des Images et des Formes	SPIN
DEGEORGE	Jean-Michel	MA(MDC)	Génie industriel	Fayol
DELAFOSSE	David	PR0	Sciences et génie des matériaux	SMS
DELORME	Xavier	MA(MDC)	Génie industriel	FAYOL
DESRAYAUD	Christophe	PR1	Mécanique et ingénierie	SMS
DJENIZIAN	Thierry	PR	Science et génie des matériaux	CMP
DOUCE	Sandrine	PR2	Sciences de gestion	FAYOL
DRAPIER	Sylvain	PR1	Mécanique et ingénierie	SMS
FAUCHEU	Jenny	MA(MDC)	Sciences et génie des matériaux	SMS
FAVERGEON	Loïc	CR	Génie des Procédés	SPIN
FEILLET	Dominique	PR1	Génie Industriel	CMP
FOREST	Valérie	MA(MDC)	Génie des Procédés	CIS
FRACZKIEWICZ	Anna	DR	Sciences et génie des matériaux	SMS
GARCIA	Daniel	MR(DR2)	Sciences de la Terre	SPIN
GAVET	Yann	MA(MDC)	Sciences des Images et des Formes	SPIN
GERINGER	Jean	MA(MDC)	Sciences et génie des matériaux	CIS
GOEURIOT	Dominique	DR	Sciences et génie des matériaux	SMS
GONDRAN	Natacha	MA(MDC)	Sciences et génie de l'environnement	FAYOL
GONZALEZ FELIU	Jesus	MA(MDC)	Sciences économiques	FAYOL
GRAILLOT	Didier	DR	Sciences et génie de l'environnement	SPIN
GROSSEAU	Philippe	DR	Génie des Procédés	SPIN
GRUY	Frédéric	PR1	Génie des Procédés	SPIN
GUY	Bernard	DR	Sciences de la Terre	SPIN
HAN	Woo-Suck	MR	Mécanique et ingénierie	SMS
HERRI	Jean Michel	PR1	Génie des Procédés	SPIN
KERMOUCHE	Guillaume	PR2	Mécanique et Ingénierie	SMS
KLOCKER	Helmut	DR	Sciences et génie des matériaux	SMS
LAFOREST	Valérie	MR(DR2)	Sciences et génie de l'environnement	FAYOL
LERICHE	Rodolphe	CR	Mécanique et ingénierie	FAYOL
MALLIARAS	Georges	PR1	Microélectronique	CMP
MOLIMARD	Jérôme	PR2	Mécanique et ingénierie	CIS
MOUTTE	Jacques	CR	Génie des Procédés	SPIN
NEUBERT	Gilles			FAYOL
NIKOLOVSKI	Jean-Pierre	Ingénieur de recherche	Mécanique et ingénierie	CMP
NORTIER	Patrice	PR1	Génie des Procédés	SPIN
O CONNOR	Rodney Philip	MA(MDC)	Microélectronique	CMP
OWENS	Rosin	MA(MDC)	Microélectronique	CMP
PERES	Véronique	MR	Génie des Procédés	SPIN
PICARD	Gauthier	MA(MDC)	Informatique	FAYOL
PIJOLAT	Christophe	PR0	Génie des Procédés	SPIN
PINOLI	Jean Charles	PR0	Sciences des Images et des Formes	SPIN
POURCHEZ	Jérémy	MR	Génie des Procédés	CIS
ROUSSY	Agnès	MA(MDC)	Microélectronique	CMP
ROUSTANT	Olivier	MA(MDC)	Mathématiques appliquées	FAYOL
SANAUR	Sébastien	MA(MDC)	Microélectronique	CMP
STOLARZ	Jacques	CR	Sciences et génie des matériaux	SMS
TRIA	Assia	Ingénieur de recherche	Microélectronique	CMP
VALDIVIESO	François	PR2	Sciences et génie des matériaux	SMS
VIRICELLE	Jean Paul	DR	Génie des Procédés	SPIN
WOLSKI	Krzystof	DR	Sciences et génie des matériaux	SMS
XIE	Xiaolan	PR0	Génie industriel	CIS
YUGMA	Gallian	CR	Génie industriel	CMP

Mise à jour : 03/02/2017

Contents

Introduction

Hydrogen embrittlement has been the centre of interest of the scientists for many decades. The hydrogen was the main cause of different catastrophic failures during the service, such in bridges, boats and aircrafts… For example, in 2013 six months before the opening of the east span of the Oakland bay bridge, there was a failure during the testing due to catastrophic failures in the shear bolts (30 of the first 96) and it happened due to hydrogen embrittlement after hydrogen was introduced by manufacturing and probably by electroplating [1]. Moreover, in the very known 'Cheesegrater' in the city of London, several steel bolts suffered from hydrogen embrittlement and three of them failed in 2014 and 2015[2].

These effects of hydrogen were not discovered on this decade, but it has been many years since scientists have noticed the catastrophic effects. They shown their interests in studying deeply the hydrogen, its different sources from environmental conditions, at gaseous state or as protons by cathodic discharge in aqueous environment, its adsorption mechanisms in these different states, and its absorption diffusion, trapping and desorption. Then the different mechanisms of hydrogen embrittlement were studied and many theories were proposed. Since then also several technics were developed to better understand the hydrogen behavior. This thesis is divided in two separate parts:

Part 1: Development of a hydrogen detection methodology using Scanning Kelvin Probe Force Microscopy (SKPFM). The objective of that study is to evaluate the potential possibility of mapping the hydrogen in a material. This study was coupled with a finite elements model to approve the experimental observations.

Part 2: A study of the hydrogen embrittlement of an ultra-high strength steel to better understand the role of the different mechanisms involved in the damage and assess their respective contribution. The choice of a maraging steel was mainly guided by the need to be able to separate the effects of hydrogen-dislocation interactions of the decohesion effects at the interfaces in the microstructure. The very high yield strength of these steels offers this possibility. On the other hand, the different conditions of hydrogen charging during mechanical loading or beforehand, as well as the hydrogen entry conditions made it possible to explore the effects of trapping alone and the effects of diffusible hydrogen on the damage. This study was based on conventional mechanical tests on notched specimens at various load rates with and without hydrogen-precharging, and at various pre-strain conditions.

Chapter I: Development of hydrogen detection methodology by Scanning Kelvin Probe Force Microscopy

1. Introduction

Hydrogen embrittlement has been the centre of scientific discussions and studies for several decades, due to its principal role in a lot of steel failures during service. During several years, many theories have been developed. These theories discussed the adsorption, absorption, diffusion mechanism. In addition to that, hydrogen interaction with the material was observed in order to explain some mechanisms of embrittlement. With all that, some cases can still be unexplained, but these theories will be used in our study.

For the past century, many techniques were developed by researchers and many experiments took place in order to prove, modify or make new theories to better understand hydrogen embrittlement. One of these techniques is TDS (Thermo Desorption Spectroscopy)[3], that helps to know the different trap energies and their density, by heating up a hydrogen charged sample and detecting hydrogen degassing, then correlating these energies with the type of the traps (voids, grain boundaries, dislocations…). There is also the permeation test that helps to calculate the diffusion rate, surface concentrations, hydrogen solubility and possibly fugacity of the charging environment, by charging a thin sample cathodically from one side and detecting the hydrogen desorption from the other side[4].

However, those techniques are macroscopic and the relation with the microstructure is only indirect. This is why they should be ideally complemented by techniques allowing to localize the hydrogen in the microstructure. However, the direct analysis of hydrogen at the microstructure scale is exceptionally difficult although progress was made in the recent years using for example SIMS (Secondary Ion Mass Spectroscopy)[5] or APT (Atom Probe Tomography)[6]. Since the year 2010, some studies proposed to use SKPFM (Scanning Kelvin Prob Force Microscopy) as a method to map the hydrogen in the material[7]. This method is an indirect detection technique, based on the variation of the electron work function with the variation of the hydrogen content. SKPFM is a technique applied using an AFM with a special electric mode explained later. This technique can be applied either directly on the studied sample, but it has sometimes its disadvantages, due to the variation of the state of the surface such as oxidation. Or it can be applied on a material coated by what is called a “screen” of palladium which can prevent any variation of the surface state and protect the surface from oxidation[8], [9]. In addition, the work function of the palladium is sensitive to hydrogen content, which will improve the limit of detection.

The coated sample method, where the specimen of interest is covered by a palladium layer, is the most used by scientists, and this is the method we adapted in our work. As said before, many studies suggested that SKPFM can be used as a way to map hydrogen content, even with a palladium layer on the surface. However, this way of using the technique is somehow questionable. Indeed, the technique shows the distribution of hydrogen in the palladium layer, but does it reflect the distribution of hydrogen in the material of interest located under the palladium? And what are the effects of hydrogen diffusivity in the substrate as well as in the palladium layer on the hydrogen measured using that method?

We will try in this study, to address these questions by using mainly an experimental approach, combined with a finite elements model of hydrogen diffusion to explain our observations. The material used in this study is Duplex 2202 stainless steel. It was selected for the following reasons:

1. It is a bi-phased material with equal portions of phases that have very different hydrogen-related parameters (diffusivity, solubility). It is then expected for the two phases to behave very differently with respect to hydrogen.
2. Data are available (diffusivity, solubility) for the two phases which facilitates the modeling of hydrogen diffusion in this system.
3. The microstructure is very anisotropic which can enhance the effect of any potential favorable diffusion paths.

2. Material and experimental methods

2.1. Material composition and microstructure

The material used in this study is the duplex 2202 stainless steel. It was provided as a sheet of 0.6 mm in thickness. In Figure 1, the cross section of the sheet shows the microstructure. It is characterized by very elongated islands of austenite (γ) embedded in a matrix of ferrite (α). The islands can sometimes cover the whole thickness of the sheet. The composition of this steel was determined by x-ray fluorescence (XRF) and is shown in Table 1. Magnetic measurement using a sigmameter showed that the weight fraction of each phase is approximately 50%.

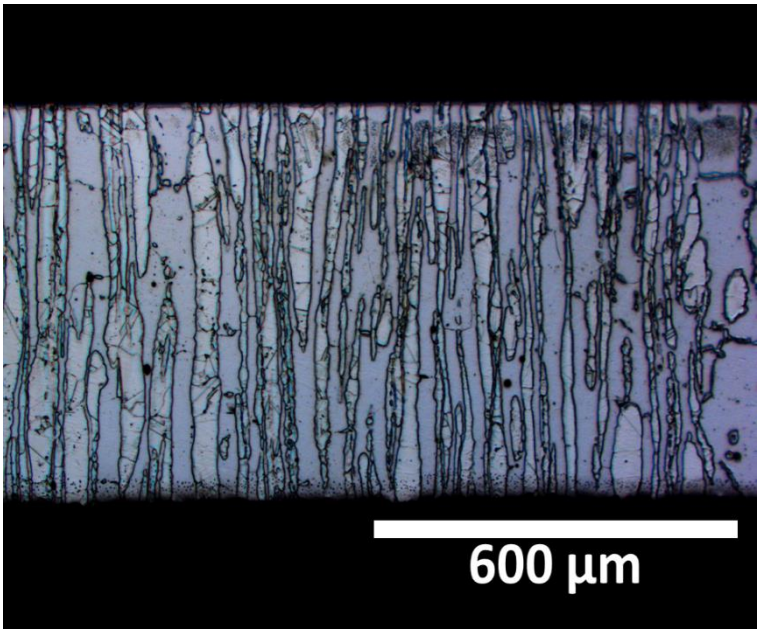

Figure 1 Microstructure observation on a cross-section of the duplex sheet used in this study. The image was obtained using optical microscopy after etching in 60% sulfuric acid.

Table 1 Composition of the duplex 2202 stainless steel used in this study (wt %).

Fe	Cr	Ni	Mn	Mo	Si
Bal.	23.16	2.64	1.29	0.23	0.41

2.2. Sample preparation for SKPFM analysis

The study is based on two different types of procedures: the “Down Charging” procedure, which consists of charging with hydrogen one face and detecting the hydrogen using SKPFM on the second face. The second is the “Top Charging” procedure, which consists of detecting hydrogen using SKPFM on the same surface as that of hydrogen charging. These two procedures are illustrated in Figure 2 and Figure 3. The preparation of the samples is described below.

The sample was cut from the sheet. The size is around 20x20x0.6 mm. Then both faces were polished until 1-micron diamond paste, and finished with silica suspension. One side of the sample (observation side) was then electrochemically etched using 60% sulfuric acid, in order to reveal the topography so phases can be recognized in the AFM as explained later.

For the “Down Charging” experiment, the etched face was then coated with 20 nm of palladium by physical vaporization deposition (PVD) using a PECS machine. The other face was charged electrochemically by hydrogen for 24 hours, and then the sample was transported to the AFM chamber (Figure 2) for SKPFM analysis.

For the “Top Charging” specimen, the etched face was charged electrochemically in 30g/L NaCl with hydrogen for 24 hours. Then it was coated with 5 nm of Palladium, and then transported to the AFM chamber (Figure 3) for SKPFM analysis.

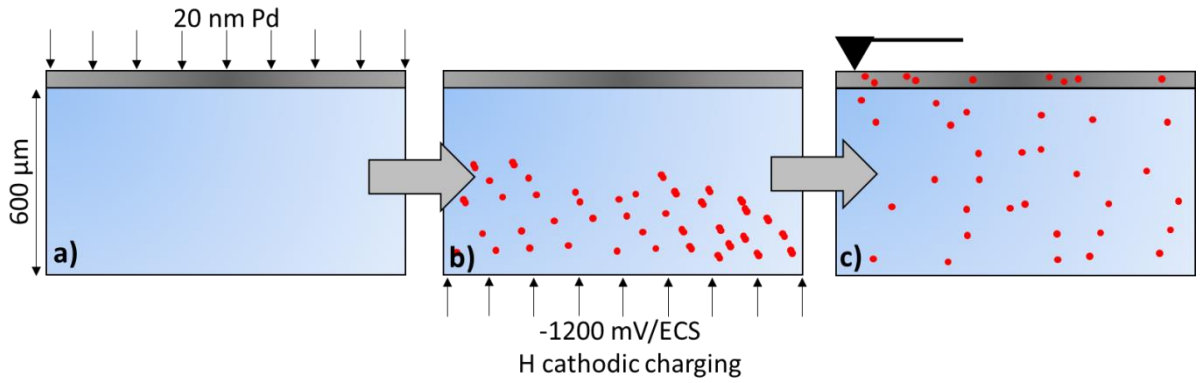

Figure 2 The different steps of the “Down Charging” experiment showing a) coating the sample with palladium, b) charging the sample with hydrogen from the bottom for 24 hours and c) SKPFM observation.

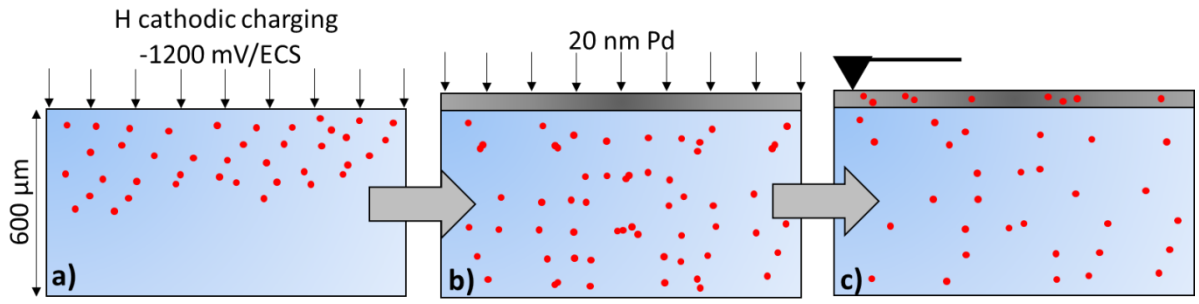

Figure 3 The different steps of the "Top Charging" experiment showing a) charging the sample from the top with hydrogen for 24 hours, b) coating the sample with palladium and c) SKPFM observation.

Palladium here acts as a screen for hydrogen. In other words, the solubility of hydrogen in palladium is much higher than in the steel, so the hydrogen will tend to diffuse from the steel into the palladium. The Pd then does not only act as a screen, but also as a "hydrogen pump".

Also palladium protects the surface from the environment, preventing formation of any oxide layer that would disturb the measurements.

2.3. Electrochemical cell and hydrogen charging procedure

The sample is charged cathodically with hydrogen from one side as shown in Figure 4 using the circuit shown in Figure 5. The solution used is demineralized water with 30 g/L of NaCl, deaerated for more than 24 hours using nitrogen gas. The auxiliary electrode used is a piece of platinum, and the reference electrode used is a saturated calomel electrode (SCE). A potentiostat maintains a potential of -1200 mV/SCE on the working electrode (specimen).

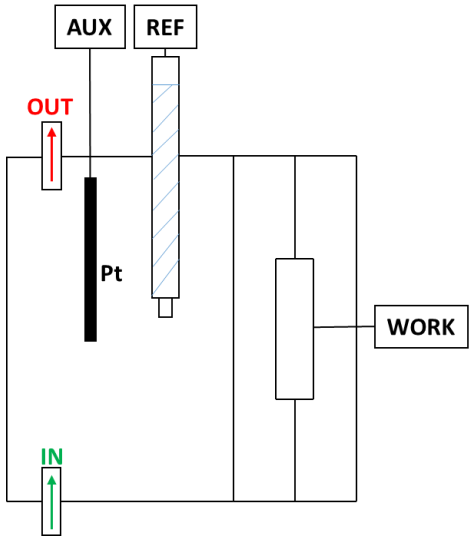

Figure 4 A scheme showing the electrochemical cell used in the hydrogen charging procedure

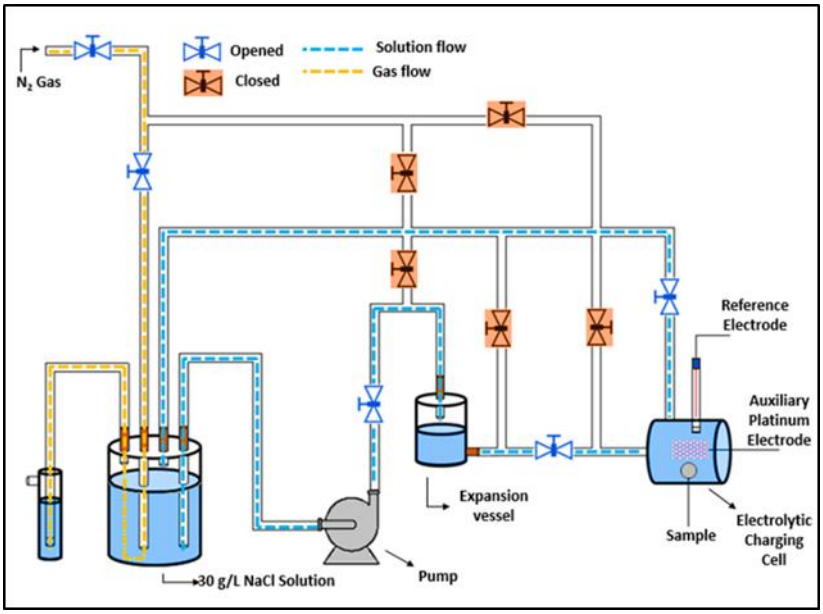

Figure 5 A scheme showing the electrochemical circuit used in the study to perform cathodic hydrogen charging

2.4. SKPFM – procedure of data acquisition

2.4.1. Procedure of measurement

Scanning Kelvin Probe Force Microscopy, is a noncontact electric mode of AFM allowing to map the contact potential difference that varies with the work function of a surface on a nanoscopic scale[10]. The work function is defined as the minimum thermodynamic energy needed to extract an electron from the surface[11]. Many factors can affect it such as catalytic activity, roughness[12], chemical composition, oxidation, temperature, humidity… and in our case the hydrogen content. We mentioned before the importance of using a palladium film covering the specimen of interest, to ensure that there is no evolution of the surface during the measurement. In addition to that, the measurements were conducted in an isolated environment, which reduces any possible impacts of external noises (mechanical vibrations), and of changes in room temperature and humidity over the duration of measurement.

Due to the difference of composition between the α and γ phases, the work function would be already different between the two phases, even without hydrogen. This is also why palladium layer is important. A palladium film will make the chemical composition (palladium) identical on any zone on the surface, and that will leave the hydrogen as the only factor in work function changing.

The SKPFM measurements were conducted using a “JPK Instruments” AFM. The cantilever used is a MIKROMASCH conductive silicon tip, coated with platinum with a tip radius < 30 nm as shown in Figure 6 with a force constant of 42 N/m and a resonance frequency of 350 kHz. The measurements were conducted in air.

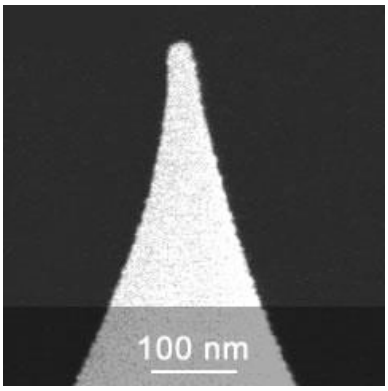

Figure 6 SEM observation of the tip of the cantilever used in the SKPFM measurements

2.4.2. Principle of measurement

Kelvin probe microscopy is usually carried out in hover mode. In a first pass called “trace”, the topography is measured, and then on a return pass called “retrace”, this height information is used to maintain the cantilever at a constant offset height above the surface, see Figure 7 [13]. The cantilever has to be conductive and connected to an external circuit to control the tip potential U_{tip}. U_{tip} is composed of a DC (direct current) component U_{DC} and a small AC (alternating current) component U_{AC}, of frequency ω normally set to be the resonance frequency of the cantilever oscillation. If the surface potential Φ is not equal to U_{tip}, a capacitive force F will act on the cantilever. Since U_{tip} is modulated by U_{AC}, then this capacitive force is also modulated and causes an oscillation of the cantilever with an amplitude A_{tip}. Therefore, when the tip scans the surface while hovering above it, a feedback loop is used to vary the DC potential applied to the cantilever tip in order to minimize the cantilever oscillation A_{tip}. When the oscillation is zero, the applied voltage U_{tip} is equal to the surface potential difference Φ, so the U_{tip} can be saved as the surface or contact potential difference.

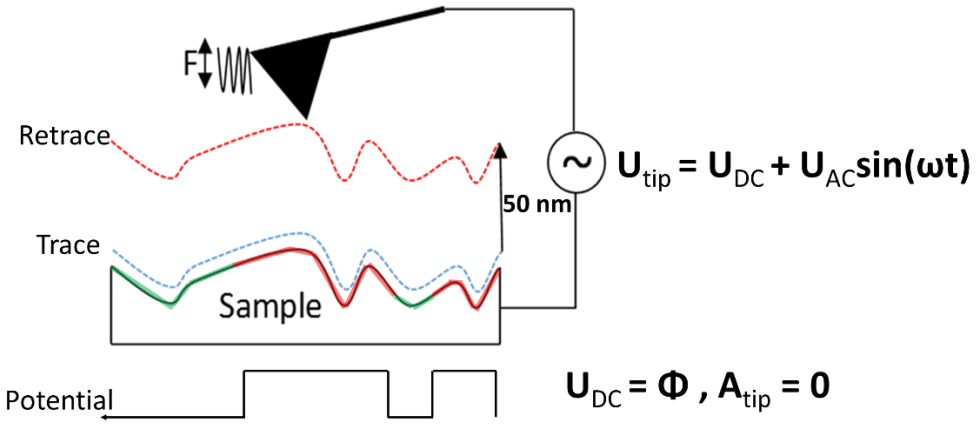

Figure 7 Presentation of the measurements conducted using by SKPFM showing the cantilever scanning the surface on trace, then rescanning it by retrace while keeping a 50 nm distance from the surface

More precisely, the potential mapped is called Contact Potential Difference (CPD) which is the difference of the work function of the tip and the work function of the surface analyzed (see equation (1)) (ideally in a vacuum space)**[14]**.

$$V_{CPD} = \frac{\emptyset_{tip} - \emptyset_{Sample}}{e} \qquad (1)$$

In order to validate the equation (1), and ensure that the higher the measured potential (V_{CPD}) is, the lower the work function (Φ_{sample}) is, we made SKPFM measurement on a reference sample. The reference sample is a silicon sample coated with aluminum and gold. We know from the literature that $\phi_{Au} > \phi_{Si} > \phi_{Al}$,**[15]**.

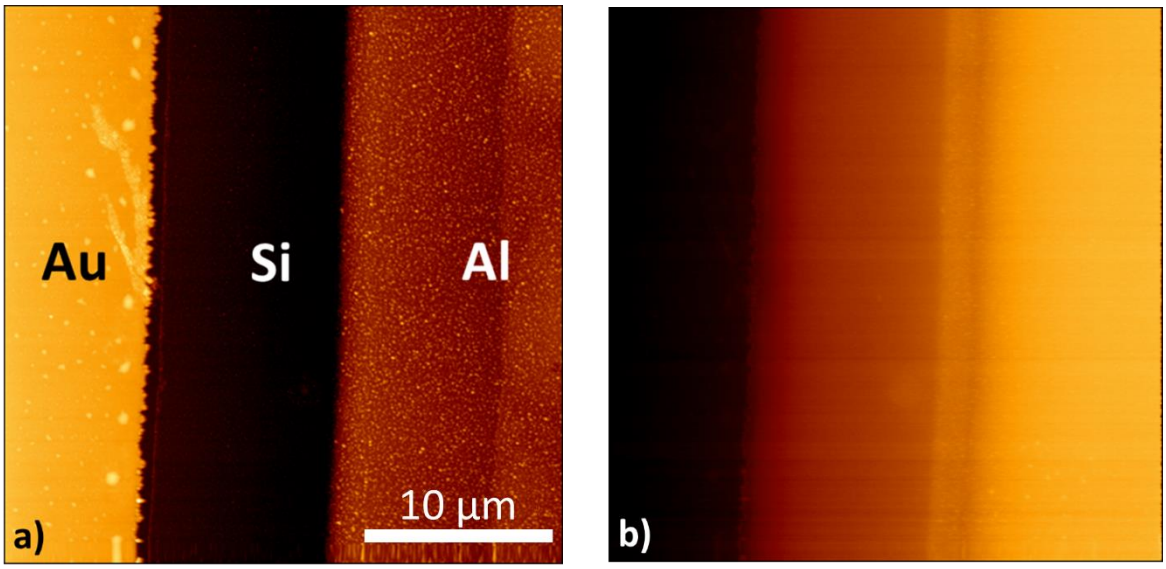

Figure 8 Comparison between gold, silicon and aluminium observed on AFM/SKPFM showing a)the topography map and b) the contact potential difference map

Figure 8 shows the observation done on the reference sample, and it is clear that for the gold that has the highest work function (Φ_{sample}), the potential V_{CPD} is the lowest. Similarly, aluminium has the lowest work function and the highest potential, which is in agreement with equation (1). From literature we know that hydrogen reduces the work function of the surface of palladium[16]. So typically in this study any increase in potential (V_{CPD}) is related to a decrease in work function (Φ), hence an increase in hydrogen content.

We believe that the SKPFM technique is a comparative technique. Even after insulating the measurement chamber from the environment, the values of the potential measured stay qualitative and not quantitative. In other words, we cannot relate the potential measured with a quantity of hydrogen. There is no relation until now that can relate them. However, we can certainly compare the difference of the potential between two zones at one moment, and tell which zone is enriched in hydrogen. Some references in the literature agree on that subject and others believe that it is possible to calibrate the probe and relate the potential measured with the quantity of hydrogen[17]. It is a subject that needs further investigation and it is under development.

2.4.3. Identification of phases using AFM

In order to correlate the SKPFM measurement of hydrogen with the microstructure of the duplex steel, a methodology is proposed here to identify the two phases α and γ from the topography measured using AFM. Figure 9 shows a comparison between a phase map obtained by EBSD and a topography image taken by AFM of a specific zone on the top of the sample (which will be called later the observation face). Figure 10 shows a topographic line-scan along the yellow line shown in Figure 9 b). It shows that sharp steps are present at the phase boundaries. Those steps are always ascending from ferrite to austenite. This is a result of the chemical etching conducted on the specimen. This particular feature allows us to

identify the two phases unambiguously without the need of conducting an EBSD experiment on each analyzed area.

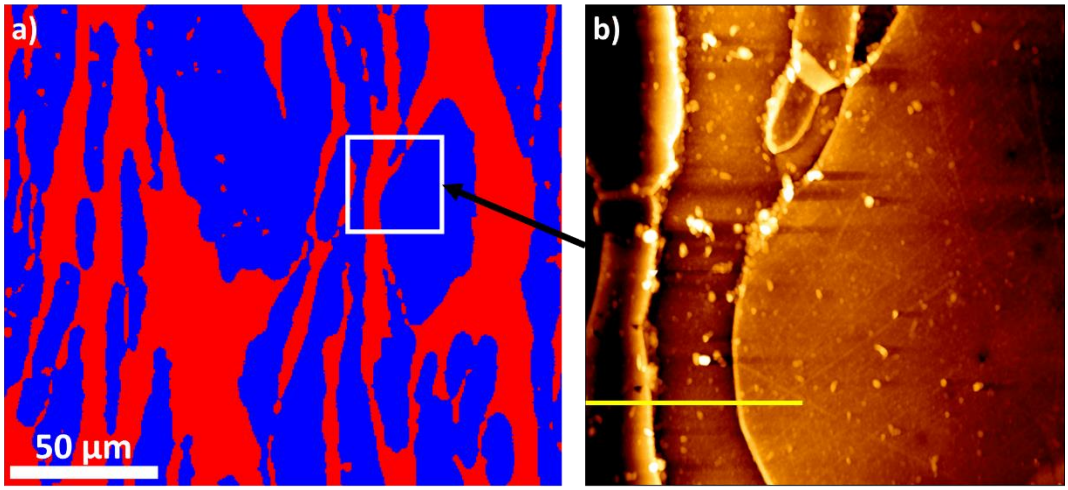

Figure 9 Microscopic observation: a) an EBSD phase map is shown with austenite in blue and ferrite in red, b) is a topography image measured by AFM of a specific zone (white square in EBSD phase map)

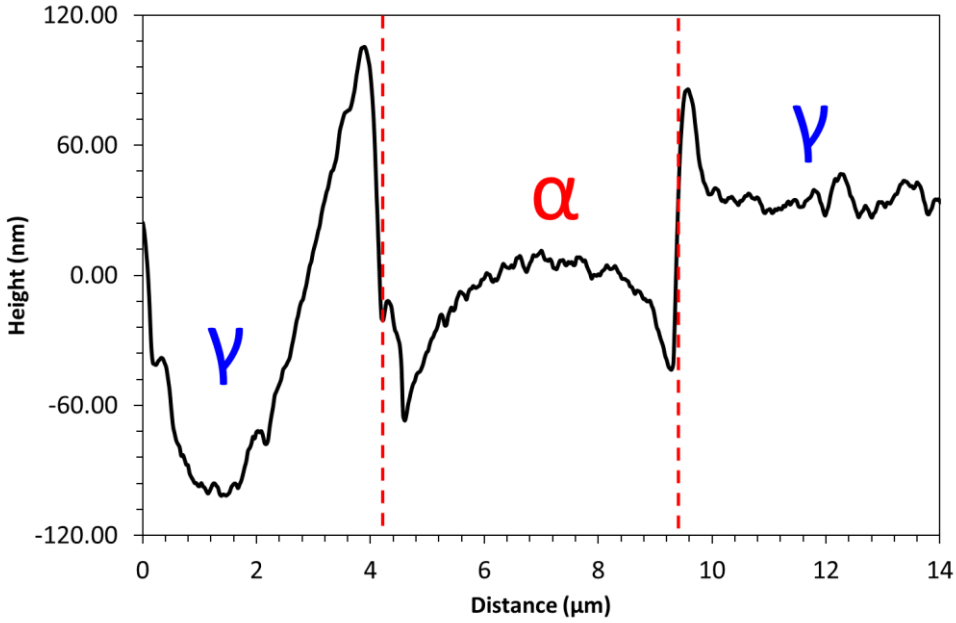

Figure 10 A profile plot of the height variation following the yellow line shown in Figure 9 b). It shows the variation of the topography across phases, especially the steps at the phases boundaries

2.5. Modelling of the hydrogen diffusion during the SKPFM measurement

A 2D finite element modelling of hydrogen diffusion across the specimen was conducted with the objective of simulating the experiments in order to better understand the observations. The modelled specimen consists of a tri-phased system: Duplex stainless steel (ferrite + austenite) and a palladium layer on the top.

2.5.1. Geometry

The geometry of the sample was drawn in a way to represent a rolled steel (similar to the studied one). The geometry is a rectangle of 1000x600 μm^2 of ferrite (in red) containing different shapes of austenite grains (in blue) with a 20 nm thin palladium layer on top (Figure 11).

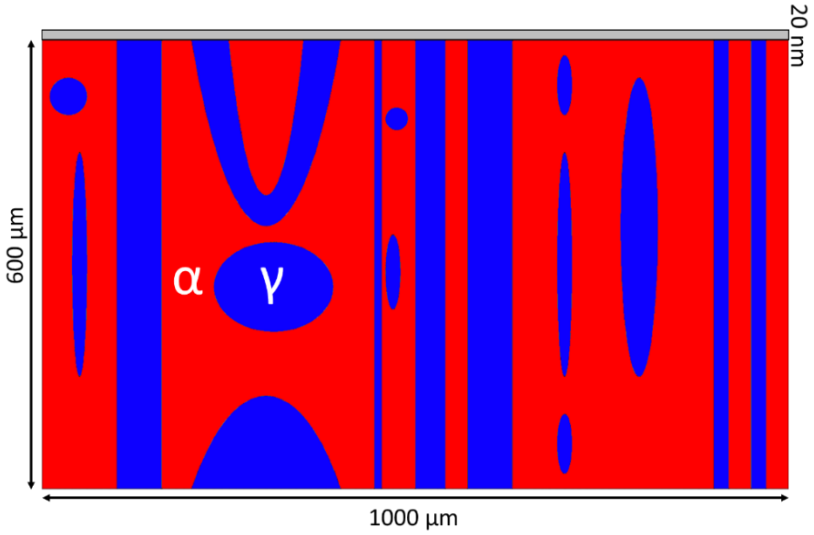

Figure 11 The geometry of the model used in the numerical study with austenite phases in blue, ferrite in red and palladium layer in grey.

2.5.2. Diffusion equation

Due to the fact that the system is composed of three phases, obviously there will be effect of the difference in solubility in different phases on the diffusion of hydrogen. Instead of the usual Fick's law, the following equation (2) was used and was implemented in COMSOL Multiphysics 5.3 using a Heat Transfer like equation.

$$S\frac{\partial\left(\frac{C}{S}\right)}{\partial t} = \nabla\left(DS\nabla\left(\frac{C}{S}\right)\right) \quad \textbf{(2)}$$

where C is the hydrogen concentration in molar fraction, S is the solubility in molar fraction.$Bar^{-0.5}$, t is the time in seconds and D is the diffusion coefficient in $m^2.s^{-1}$.

2.5.3. Boundary conditions

Two kinds of simulations were conducted. Figure 12 illustrates the modelling of the down charging experiment where the sample is already coated with Pd from the top, then charged cathodically for 24 hours from the bottom and then the Pd layer is analysed using SKPFM. Figure 13 illustrates the modelling of the top charging experiment, where the top of the sample is charged with hydrogen for 24 hours, then it was coated with palladium, and finally the Pd layer is analysed using SKPFM.

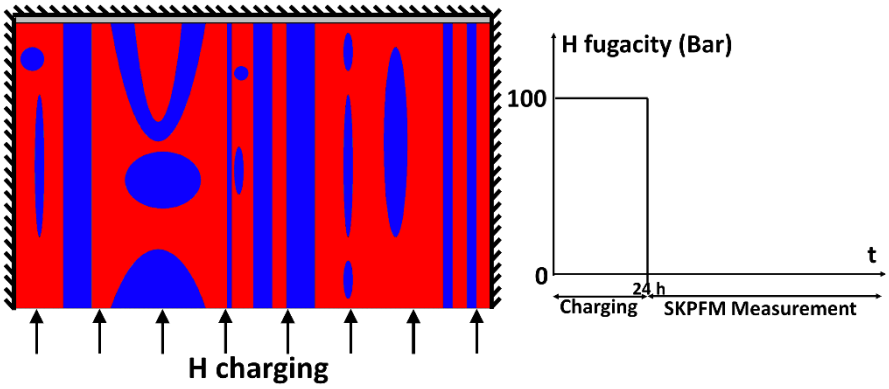

Figure 12 Down charging model: the isolated boundaries are shown on the top, left and right of the geometry, a hydrogen pressure (fugacity) of 100 Bar is fixed at the bottom boundary for 24 hours.

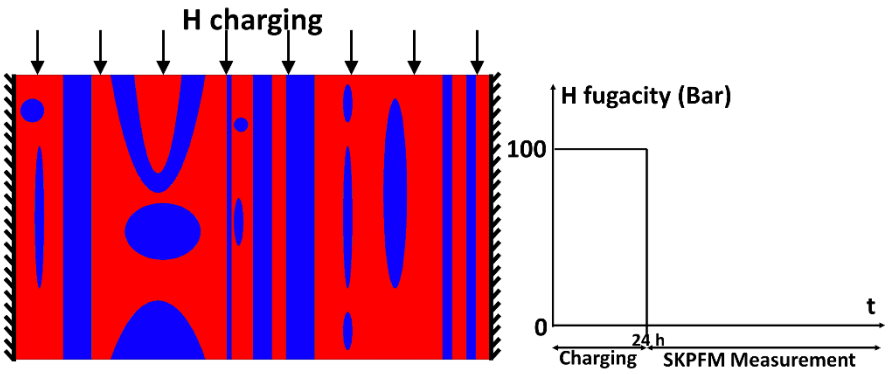

Figure 13 Top charging model: the isolated boundaries are shown on the left and right of the geometry, a fugacity of 100 Bar is fixed at the top boundary for 24 hours.

For symmetry reasons, the left and right sides of the specimen in Figure 12 and Figure 13 are isolated boundaries (i.e. no flux of hydrogen is allowed through those boundaries). A given fugacity f of hydrogen is imposed on the charging surface. This fugacity is a characteristic of the charging conditions. A given fugacity will give two different surface concentrations C_S of hydrogen in the two phases α and γ according to the Sievert law (equation (3)).

$$C_S = S\sqrt{f} \quad \textbf{(3)}$$

The fugacity is time-dependent as shown in Figure 12 and Figure 13. It is set to a positive value (100 Bar) during the 24 hours of hydrogen charging, and then set to zero once the charging is finished. This means that, in the case of the down-charging experiment (Figure 12), for t>24 h, hydrogen desorption is allowed through the bottom surface.

The boundary above the palladium layer is set as isolated. This means that no hydrogen desorption is allowed through that surface. This assumption is debatable but can be justified by the fact that most of the hydrogen in the nanostructured palladium layer is likely deeply trapped in the crystal defects. Experimental evidence of this will be provided later. Note that in the case of the top charging experiment (Figure 13), hydrogen desorption is allowed through the bottom surface at any time.

2.5.4. Input data

Table 2 shows the different parameters used in the finite elements model for down and top charging. The boundary conditions on the charging surface are a fixed fugacity of the charging

medium. A fugacity of 100 Bar was chosen here as a typical value corresponding to our conditions of cathodic charging**[18]**. The time of the simulation is chosen to cover the 24 hours of charging and the time of observation. The diffusion coefficients and the solubilities of the austenite and the ferrite were taken from the literature.

The diffusion coefficient and the solubility of the H in palladium are not available in the literature for nanostructure Pd layers obtained from PVD. It is assumed that the hydrogen is deeply trapped in the Pd layer due to the very high density of crystal defects. This is why the solubility chosen is $S_{(Pd)}$ = 0.1 molar fraction.$Bar^{-0.5}$. This value is chosen high enough to ensure that a driving force exists to transport hydrogen from the ferrite and the austenite into the palladium. It is higher than the solubility in bulk (Pd)[19], after taking in consideration the trap sites.

The hydrogen diffusion coefficient, $D_{(Pd)}$ is chosen to be below D_α and D_γ but high enough to ensure that the concentration of hydrogen is approximately homogeneous across the Pd layer (~20 nm thickness).

Table 2 Parameters used for the simulation of hydrogen diffusion during the SKPFM analysis on the duplex stainless steel using COMSOL for top and down charging experiments

	Down charging	**Top charging**
Parameters	**Numerical values**	
Simulation time	10^6 seconds	302400 seconds
Numbers of meshing elements	1462610	1333436
Number of boundary meshing elements	74550	72661
Diffusion coefficient in ferrite	$D_\alpha = 6x10^{-11}$ $m^2.s^{-1}$[20], [21]	
Diffusion coefficient in austenite	$D_\gamma = 1.4x10^{-16}$ $m^2.s^{-1}$[21], [22]	
Diffusion coefficient in palladium	$D_{Pd} = 10^{-20}$ $m^2.s^{-1}$	
Solubility in ferrite	$S_\alpha = 2.8x10^{-8}$ molar fraction.$Bar^{-0.5}$[23], [24]	
Solubility in austenite	$S_\gamma = 7x10^{-5}$ molar fraction.$Bar^{-0.5}$[24], [25]	
Solubility in palladium	S_{Pd} = 0.1 molar fraction.$Bar^{-0.5}$	
Fixed fugacity of the charging medium	f = 100 Bar	

3. Results

3.1. Down-charging experiment

3.1.1. SKPFM observations

Figure 14 shows the area of a specimen studied in the down charging experiment described before and explained in Figure 2. The ferrite (α) and austenite (γ) phases were identified on the topography map obtained using AFM (Figure 14 a). The method of phase identification is described in section Chapter I:2.4.3. Two types of ferrite grains are observed: "big" grains connected to other ferrite grains called "α" in Figure 14 b) and "small" grains embedded in bigger austenite grains (called "α_e" in Figure 14 b).

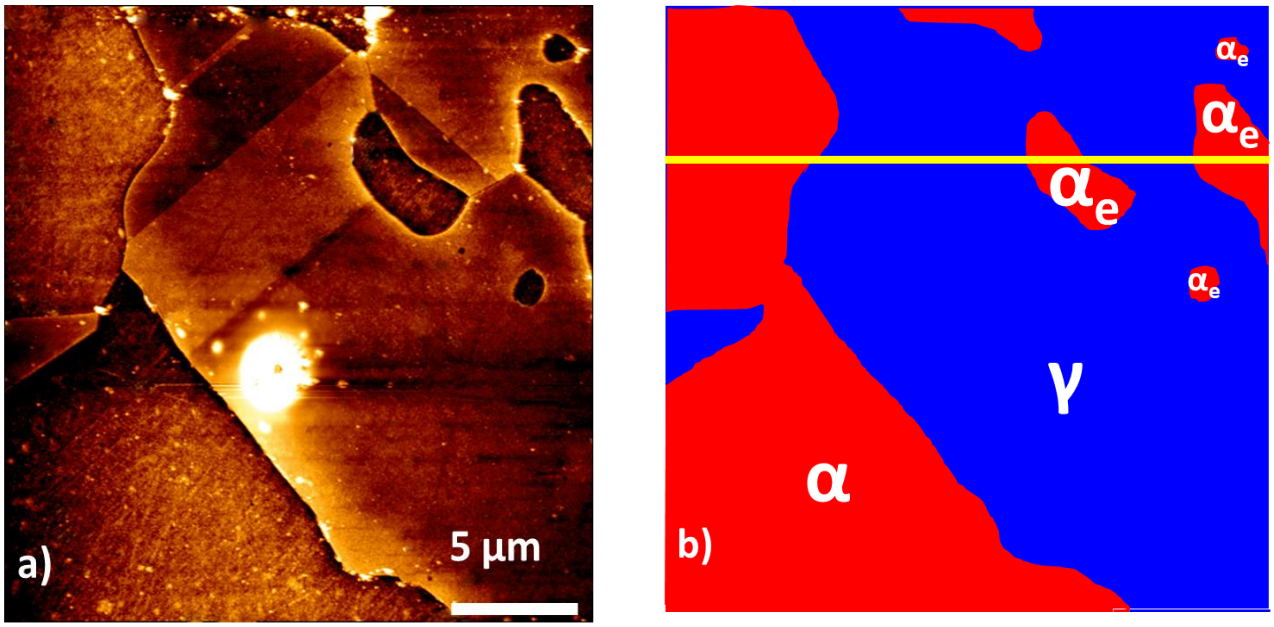

Figure 14 a) Topography of analyzed region as seen by AFM, b) identification of ferrite and austenite phases

Figure 15 shows the time-dependence of a contact potential difference map. The contrast develops over some tens of minutes of observation, where the ferrite grains become brighter than the austenite grains. This contrast develops much slower (or does not develop at all) for the ferrite grains embedded in austenite (α_e) seen in the upper right of the square image. The contrast stabilizes after some hours and is still visible after several tens of hours of observation.

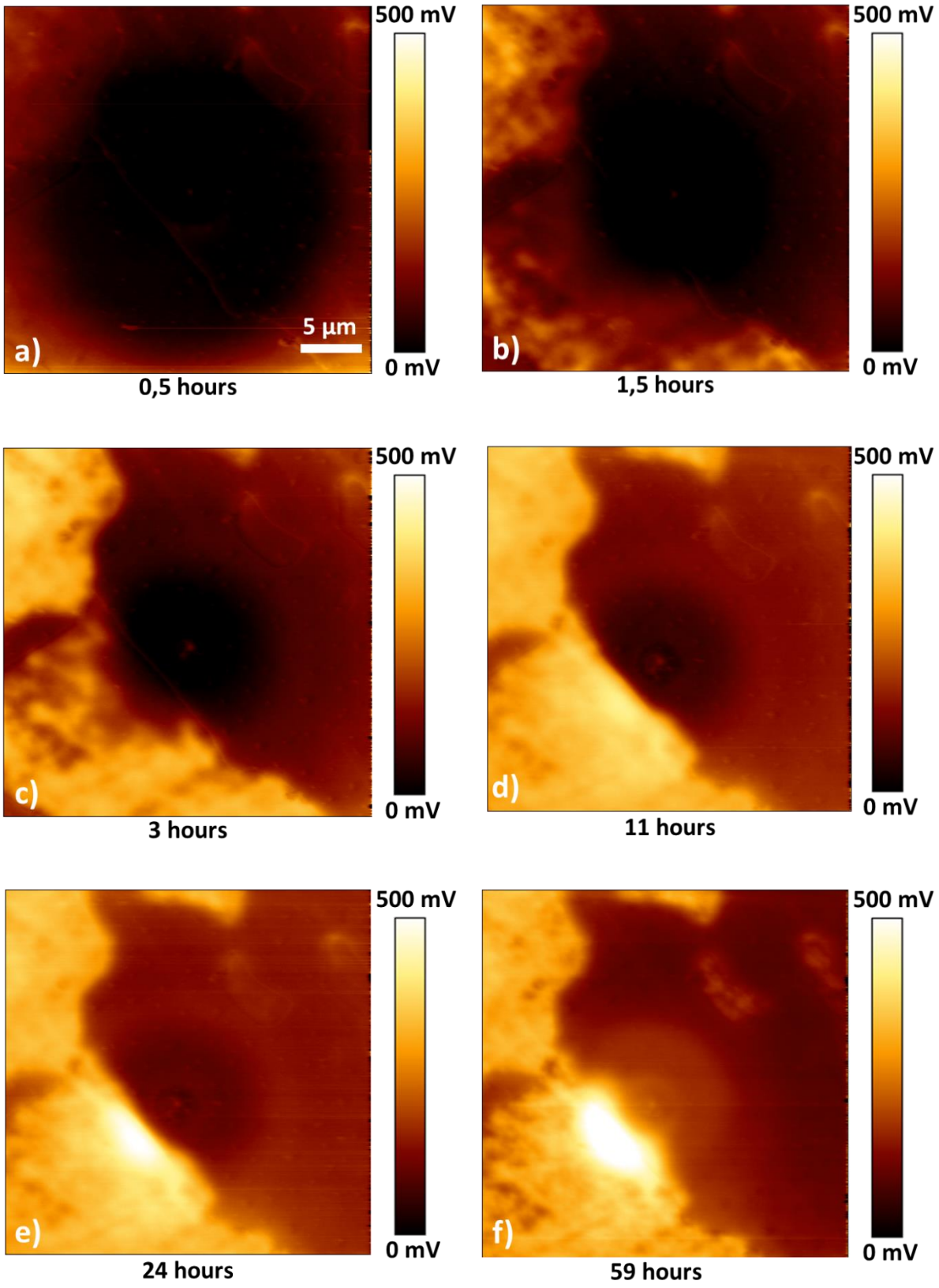

Figure 15 Potential map measured by SKPFM at different times after hydrogen charging was stopped. a) 0,5 hours, b) 1,5 hours, c) 3 hours, d) 11 hours, e) 24 hours and f) after 59 hours

Figure 16 shows the time-dependence of the potential profile along a specific line shown in Figure 14 b). The line has been chosen to cover different grains of austenite (γ) and ferrite (α and α_e). This confirms the observation previously described: the gap of potential between the ferrite and the austenite zones become deeper with time to the benefit of ferrite. However, for the two embedded ferrite grains (α_e) the potential increase with respect to the austenite is much slower and less pronounced than that observed for the big ferrite grains.

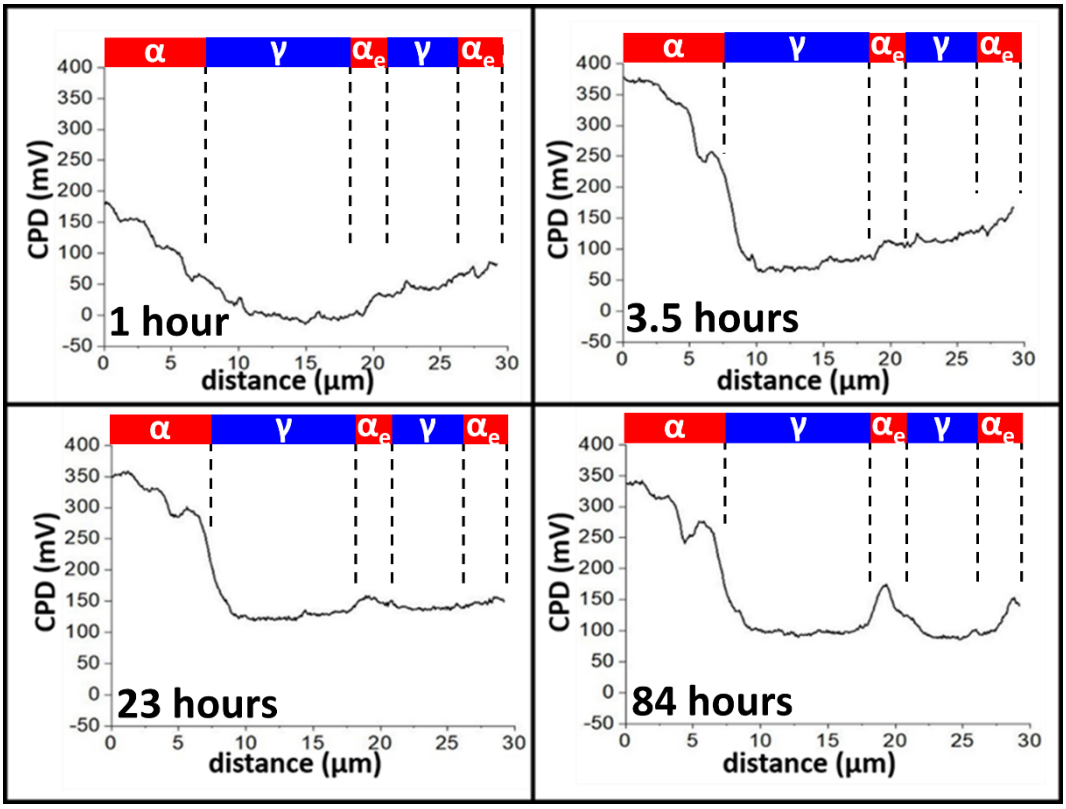

Figure 16 Potential line scan measured by SKPFM along the line indicated in Figure 14 b) at different times after hydrogen charging was stopped: 1 h, 3.5 h, 23 h and 84 h

The same experiment was conducted several times, with similar observations. The potential increases above the ferrite (with respect to the austenite). Figure 17 and Figure 18 shows the results obtained on two different specimens. In Figure 17, a contrast is already observed at t=0, i.e. from the start of the SKPFM measurement. On the other hand, for the specimen illustrated in Figure 18, about fifty hours of SKPFM observation were needed to start to see a contrast in the potential map.

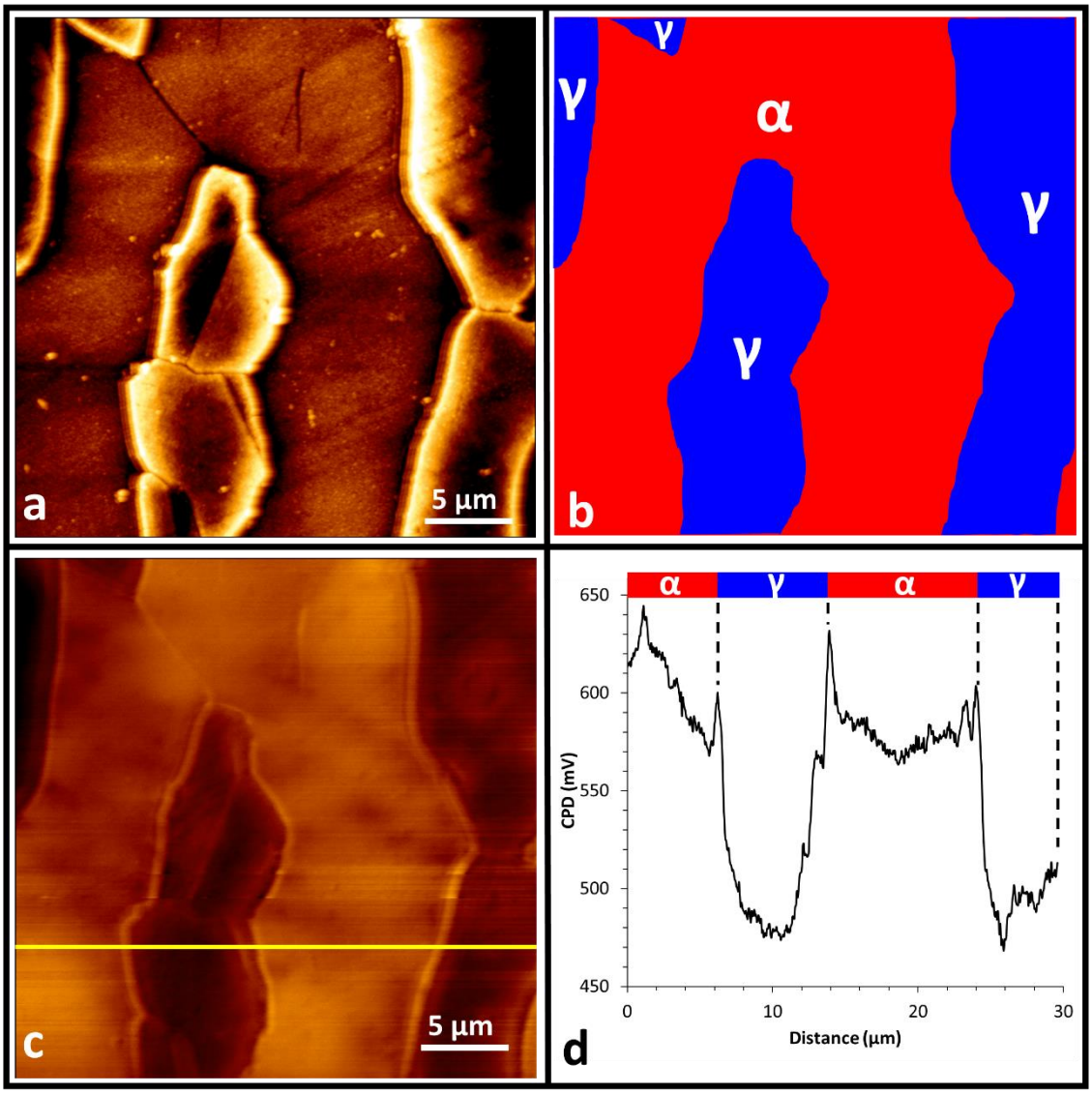

Figure 17 SKPFM observation of a hydrogen down-charged specimen. a) topography from AFM, b) phase identification, c) potential map from SKPFM at t=0, d) potential line scan at t=0 along the line shown in Figure 17 c). In this particular specimen a contrast was observed in the potential map already at t=0.

A comment is due here about the potential scale used in Figure 17 d). It can be seen that the average potential obtained on that particular specimen (~550 mV) is far above that of Figure 16. This can be due to different technical reasons, whereas the ageing of the tip coating. However, in our work we only discuss the difference of potential between different places (i.e. between α and γ) of the studied zone, not the potential itself.

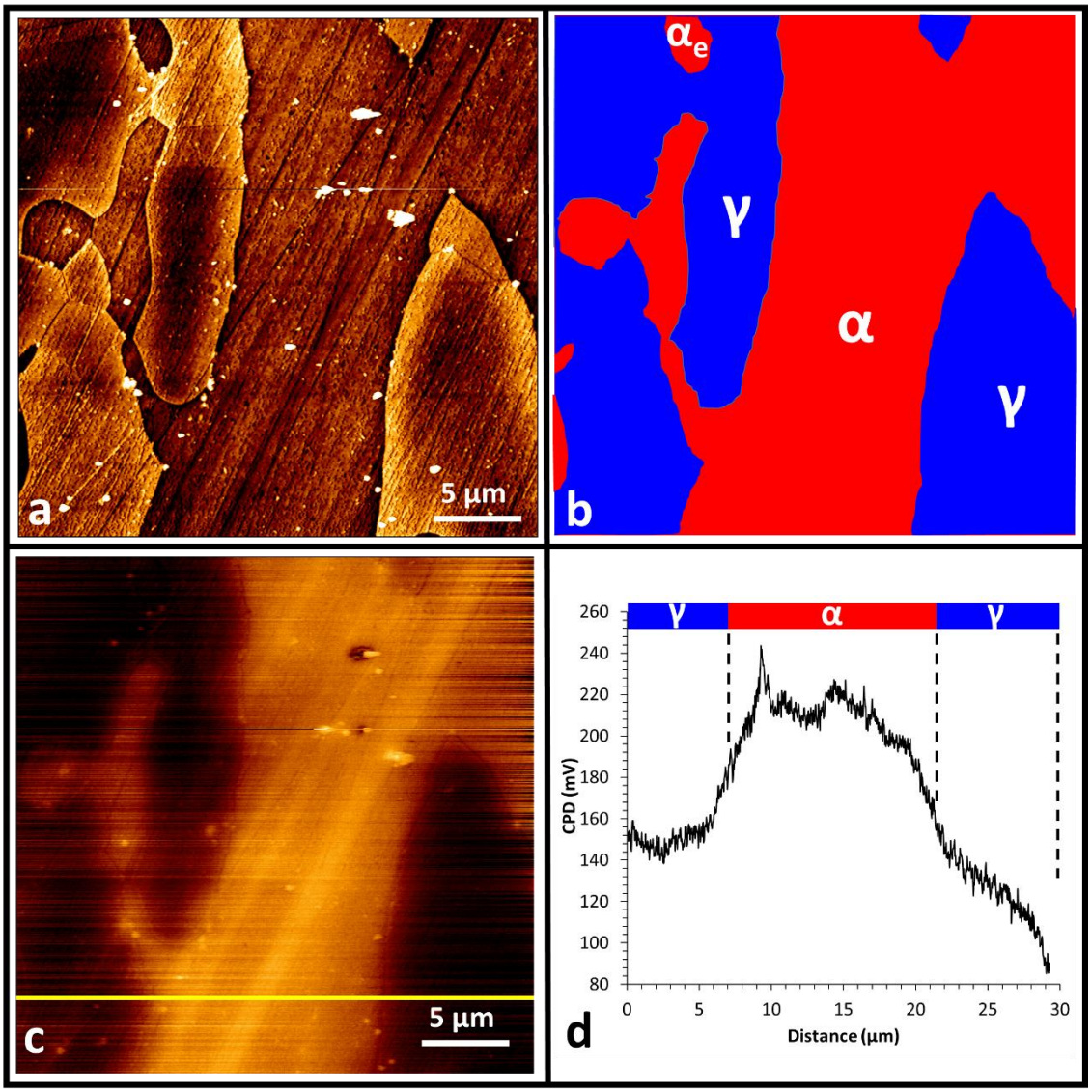

Figure 18 SKPFM observation of a hydrogen down-charged specimen. a) topography from AFM, b) phase identification, c) potential map from SKPFM at t=55 h, d) potential line scan at t=0 along the line shown in Figure 18 c). In this particular specimen, about fifty hours of observation were needed before seeing any contrast in the potential map.

Figure 19 represents the time spent during observation before getting any contrast between phases in the potential map on four different samples. This time is highly variable: it varies from zero to fifty hours although the experimental procedure was exactly the same each time.

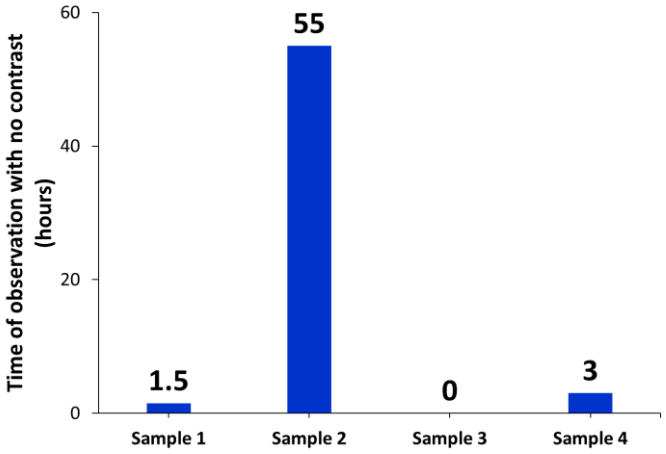

Figure 19 Time spent before observation of any contrast in the potential map measured from SKPFM on four different down charged specimens.

It is reminded that the analyzed area is chosen randomly on the specimen surface. It is possible that the variability illustrated in Figure 19 is not related to the specimen itself, but rather to the area chosen for analysis. In other words, if it were possible to analyze several areas of the same specimen at the same time (which is not technically possible), the same variability may be obtained as well.

3.1.2. Discussion

Assuming that the potential increase is related to the hydrogen enrichment in the Pd film (see Chapter I:2.4.2) we can deduce that:

- First of all, the hydrogen enrichment is faster and more pronounced in the Pd above the ferrite grains than above the austenite.
- Secondly, when analyzing the ferrite grains (α_e) embedded in the austenite, this enrichment is almost inexistent, or at least very slow, and less pronounced. This leads us to say that the hydrogen diffusion properties in the material influence significantly the entry of the hydrogen into the palladium layer. The high diffusivity in the ferrite would make the supply of hydrogen in the Pd film more efficient. On the other hand, the austenite has a low hydrogen diffusivity, which would make the hydrogen supply to the palladium layer less significant.

The high variability in the results between different experiments (the time needed to observe a contrast in the potential map varies from zero to about fifty hours depending on the

specimen, see Figure 19) can be explained by the different hydrogen diffusion paths followed in order to reach the Pd layer. The path can be different for different zones of analysis because of the microstructure beneath the analyzed zone (tortuosity of the path and/or hydrogen diffusion barriers like small austenite grains).

The contrast stays stable for many hours. This can be explained by the facts that:

1. The lateral diffusion of hydrogen in Pd is certainly very limited. Lateral diffusion should result in homogenization of the hydrogen concentration in the Pd film, which should decrease the contrast. However, this is not what we observe here.
2. The hydrogen desorption from the palladium layer is probably very limited as well. Desorption should decrease the hydrogen content in the palladium layer and thus the observed contrast, especially for long observation time. Again this is not what we observe, at least on the timescale investigated here (some tens of hours). This leads us to think, that an important fraction of hydrogen present in the Pd film is trapped deeply enough, which can explain its low diffusivity.

The interpretations provided in this discussion will be confirmed by finite element modeling.

3.1.3. Finite element modelling of hydrogen diffusion

In the following, the results of the finite elements modelling simulating the “down charging” experiment are presented and discussed with respect to the experimental results obtained using SKPFM.

Figure 20 represents the hydrogen distribution in the cross-section of a down-charged specimen at different times. The hydrogen concentration is represented using a logarithmic scale.

The hydrogen concentrations maps obtained are consistent with the solubility and diffusivity input data used for the two phases α and γ:

- The concentration tends to be much more homogeneous in the ferrite due to the high diffusivity of hydrogen in that phase.

- Discontinuities are observed at interface boundaries which are related to the difference of hydrogen solubility in the two phases.

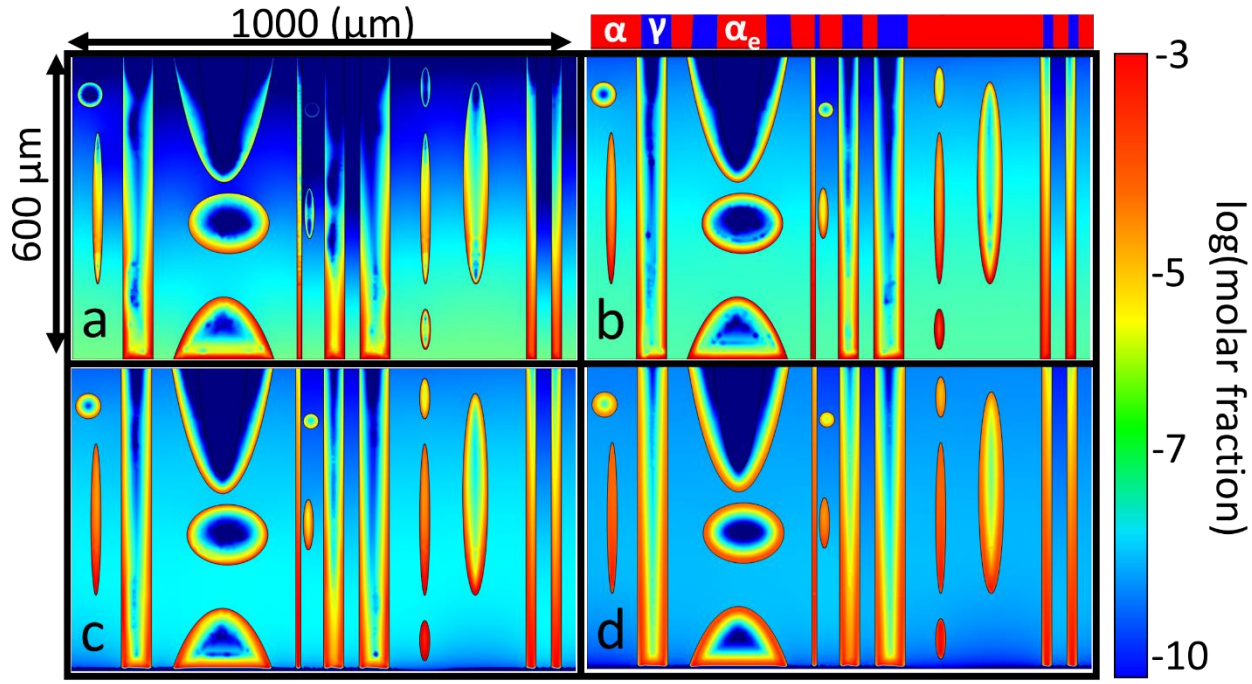

Figure 20 Cross-section hydrogen concentration maps calculated using finite element modelling at different times: a)2.4 hours of hydrogen charging, b) 24 hours (end) of charging, c) 24 h of charging + 6 hours of SKPFM observation and d) 24 h of charging + 36 hours of SKPFM observation. The Pd layer is not represented here. Note that hydrogen desorption occurs through the down side in c) and d).

Figure 21 represents the hydrogen distribution profile on the top of the palladium film at different time during charging and SKPFM observation. It is shown that over the line scale investigated here, the hydrogen concentration in the palladium layer increases significantly above ferrite while remaining close to zero above austenite. This is similar with what was experimentally observed using SKPFM. This is strongly related to the fact that the hydrogen diffuses much faster in ferrite than in austenite. Even though the solubility of hydrogen in the ferrite is low, the ferrite can allow a fast transportation of hydrogen, which can explain the hydrogen enrichment of Pd film above the ferrite. The amount of hydrogen in the palladium film is simply related to the cumulative amount of hydrogen that is able to reach the palladium film through the two phases. Ferrite can provide more hydrogen than austenite to the palladium film.

Considering the ferrite grain α_e embedded in the austenite (zone 250-350 µm see Figure 20 and Figure 21) no hydrogen enrichment above this grain is observed. This can be explained by the fact that this grain is not percolated to the ferrite network. In other words, in order to reach this grain, the hydrogen must go through an austenitic zone, which in this case behaves as a barrier. These results are compatible with the experimental observations concerning the non-percolated ferrite grains (grains α_e in Figure 14, Figure 15 and Figure 16).

Figure 21 shows that the rate at which the hydrogen enrichment occurs in the palladium layer above different ferrite grains is variable from one to another (even excluding disconnected ferrite grains). It is likely due to the morphology of the rolled ferrite grains: the large corridors of ferrite (see for example the one centred in x=750 µm in Figure 21) transfer more hydrogen to the palladium because it is less exposed to lateral "pumping" due to austenite grains than a narrow ferrite corridor (see for example in Figure 21 the one centred in x≈550 µm or x≈940 µm). This can explain the variability of the necessary time we spent on our SKPFM observation in order to have a contrast between the ferrite and the austenite. The time needed to achieve a hydrogen concentration above the ferrite can be very different depending on the analysed zone.

Figure 22 represents the hydrogen distribution profile in the steel (2 µm under the palladium film) at different time during charging and SKPFM observation. Figure 23 represents the logarithmic hydrogen distribution profile in the steel (2 µm under the palladium film) at different time during charging and SKPFM observation. Comparing the Figure 21 with the Figure 22 and Figure 23, it is demonstrated that there is no obvious connection between the hydrogen distribution in the Pd layer (which reflects the measurements done on SKPFM) and the hydrogen distribution in the steel under this layer. The Pd layer enriches with hydrogen above the ferrite, while the concentration of hydrogen is higher in the austenite than in the ferrite. This tends to question the use of the SKPFM technique (with a palladium layer), as a direct hydrogen mapping method in the material.

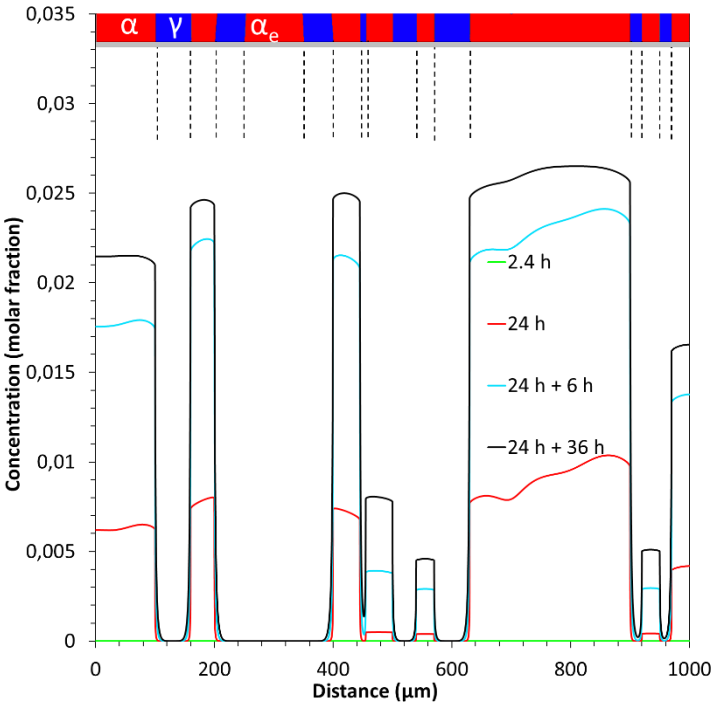

Figure 21 Hydrogen concentration profile at the surface of the palladium film at different time: 2.4 h of charging, and 24 hours (end) of charging, 24 h of charging + 6 and 36 hours of SKPFM observation. FEM modelling.

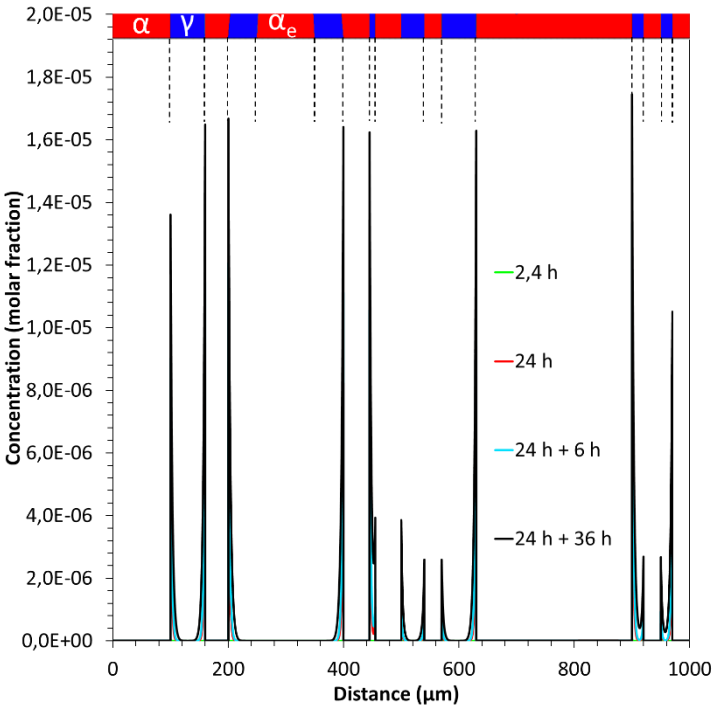

Figure 22 Hydrogen concentration profile in the steel (2 µm under the Pd film) at different time: 2.4 h of charging, and 24 hours (end) of charging, 24 h of charging + 6 and 36 hours of SKPFM observation. FEM modelling.

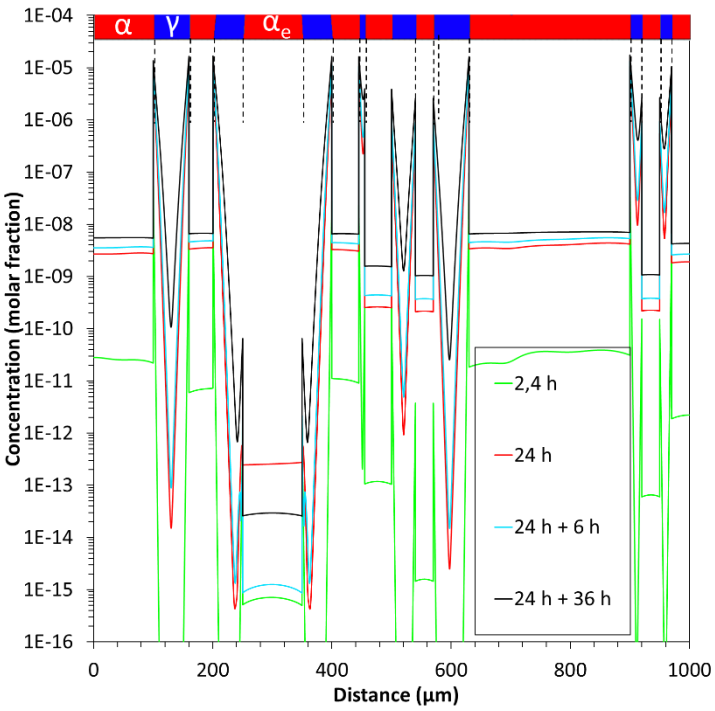

Figure 23 Hydrogen logarithmic concentration profile in the steel (2 µm under the Pd film) at different time: 2.4 h of charging, and 24 hours (end) of charging, 24 h of charging + 6 and 36 hours of SKPFM observation. FEM modelling.

3.2. Top-charging experiment

3.2.1. SKPFM observations

Figure 24 shows the area of a specimen studied in the top-charging experiment described before and explained in Figure 3. The ferrite (α) and austenite (γ) were identified from the topography map obtained using AFM (Figure 9 a).

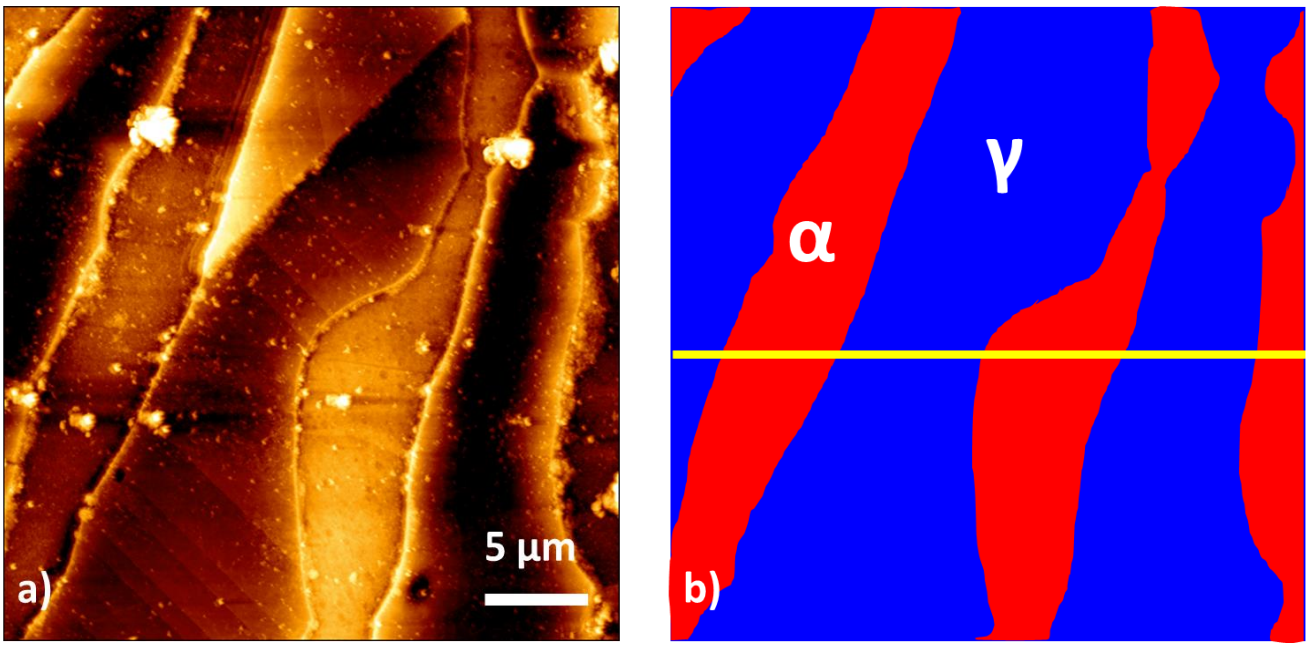

Figure 24 a) Topography of the analyzed region as seen by AFM b) identification of ferrite and austenite phases.

Figure 25 shows the time dependence of a contact potential difference map. A contrast is already visible one hour after the end of hydrogen charging. In contrast to what was observed in the down-charging experiment, it is not so obvious here whether it is the ferrite or the austenite that appears first brighter. For example, regions (1) and (2) in Figure 25 a) (t=1hours) appear respectively bright and dark although they are both located in a ferrite grain. Similar observation is made for austenite regions (3) and (4) appear respectively bright and dark in Figure 25 b) although they are both located in austenite. So it is not so easy here to relate the brighter areas in the potential maps to a particular phase.

One complementary observation is that the potential tends to homogenize in the studied zone over time (Figure 25 e) and f)).

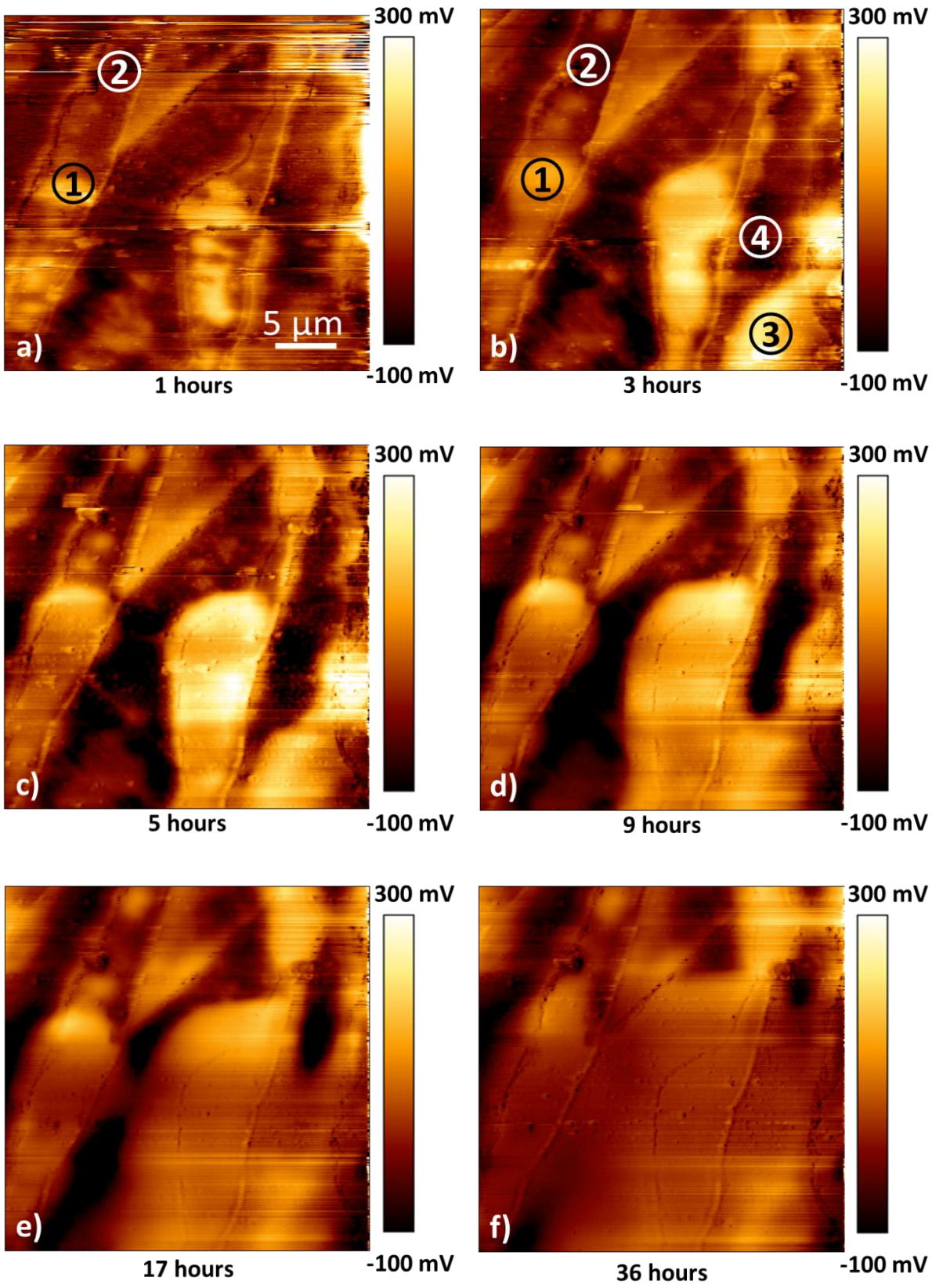

Figure 25 Potential map measured by SKPFM at different time after hydrogen charging was stopped. a) 1 hours, b) 3 hours, c) 5 hours, d) 9 hours, e) 17 hours and f) 36 hours.

Figure 26 shows the time dependence of the potential profile along a specific line shown in Figure 24 b). Along the line chosen, the potential is found higher in the ferrite than in austenite, for short time, although as already mentioned, this observation is not systematic (i.e. the austenite could be found brighter than the ferrite in some other parts of the analyzed zone, compare for example regions (2) and (3) in Figure 25 b)).

Figure 26 also clearly demonstrates that the potential homogenizes over time.

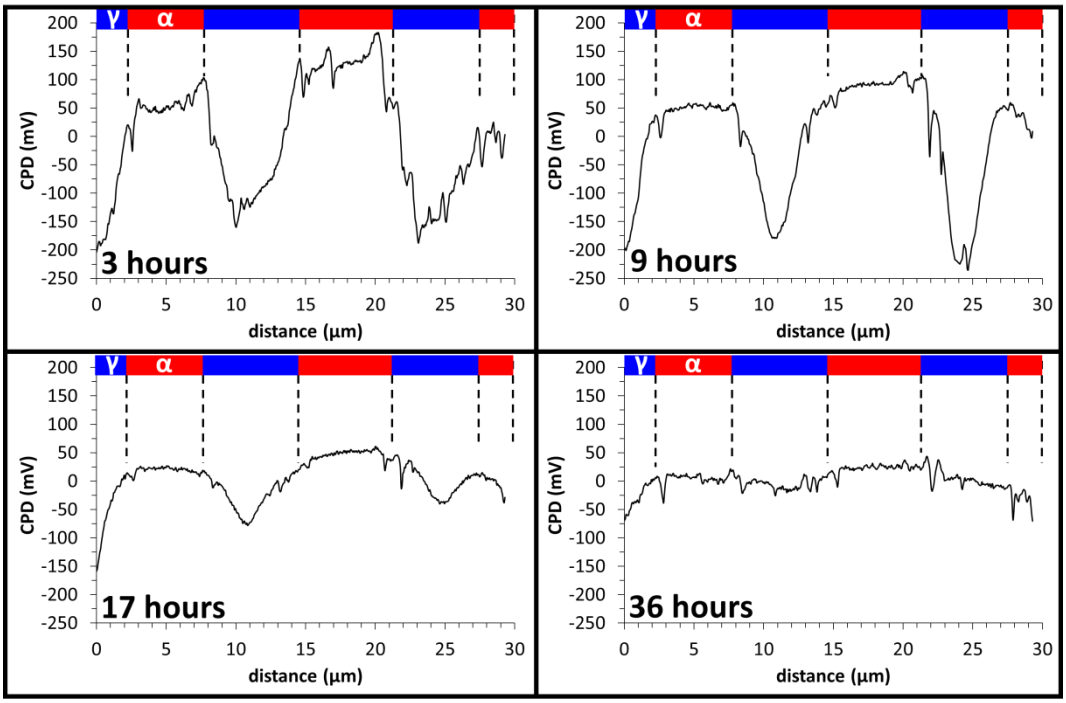

Figure 26 Potential line scan measured by SKPFM along the line indicated in Figure 24 b) at different time after hydrogen charging was stopped: 3h, 9h, 17h and 36h.

3.2.2. Discussion

Again, we assume here that the variations of potential measured using SKPFM are related to the hydrogen concentration in the palladium layer. The down-charging experiment detailed previously has shown that only the ferrite phase was able to provide hydrogen to the palladium layer, because the hydrogen diffusion coefficient in the austenite phase was too low. This allowed us to explain the systematic contrast observed in the down-charging experiment (ferrite always getting brighter than austenite).

On the other hand, in the top-charging experiment, the surface of the specimen in contact with the palladium layer was charged with hydrogen, which means that the two phases α and γ are "filled" with hydrogen over a certain depth ("filled" here means that they were equilibrated with a given hydrogen fugacity related to the charging conditions).

In these conditions it is expectable that austenite also will be able to release hydrogen into the palladium layer, not only ferrite. The low diffusivity of hydrogen in austenite may be counter-balanced by the high hydrogen concentration in that phase.

This could lead to a rather homogeneous hydrogen release into the palladium layer, in contrast to the down-charging experiment in which the hydrogen comes from the ferrite only. This homogeneous hydrogen enrichment of the palladium layer would be aligned with the experimental SKPFM observations showing that:

- The regions getting brighter for "short" observation time do not always correspond to ferrite grains; it can be austenite in some cases (for example region (3) in Figure 25 b)).
- The potential tends to be very homogeneous at least after some hours or tens of hours.

We will now try to confirm that interpretation using finite element modelling of hydrogen diffusion in the case of the top-charging experiment.

3.2.3. Finite element modelling of hydrogen diffusion

In the following the results of the finite element modelling simulating the top-charging experiment are presented and discussed.

Figure 27 represents the hydrogen distribution in the cross-section of a top-charged specimen. The hydrogen concentration is represented using a logarithmic colour scale.

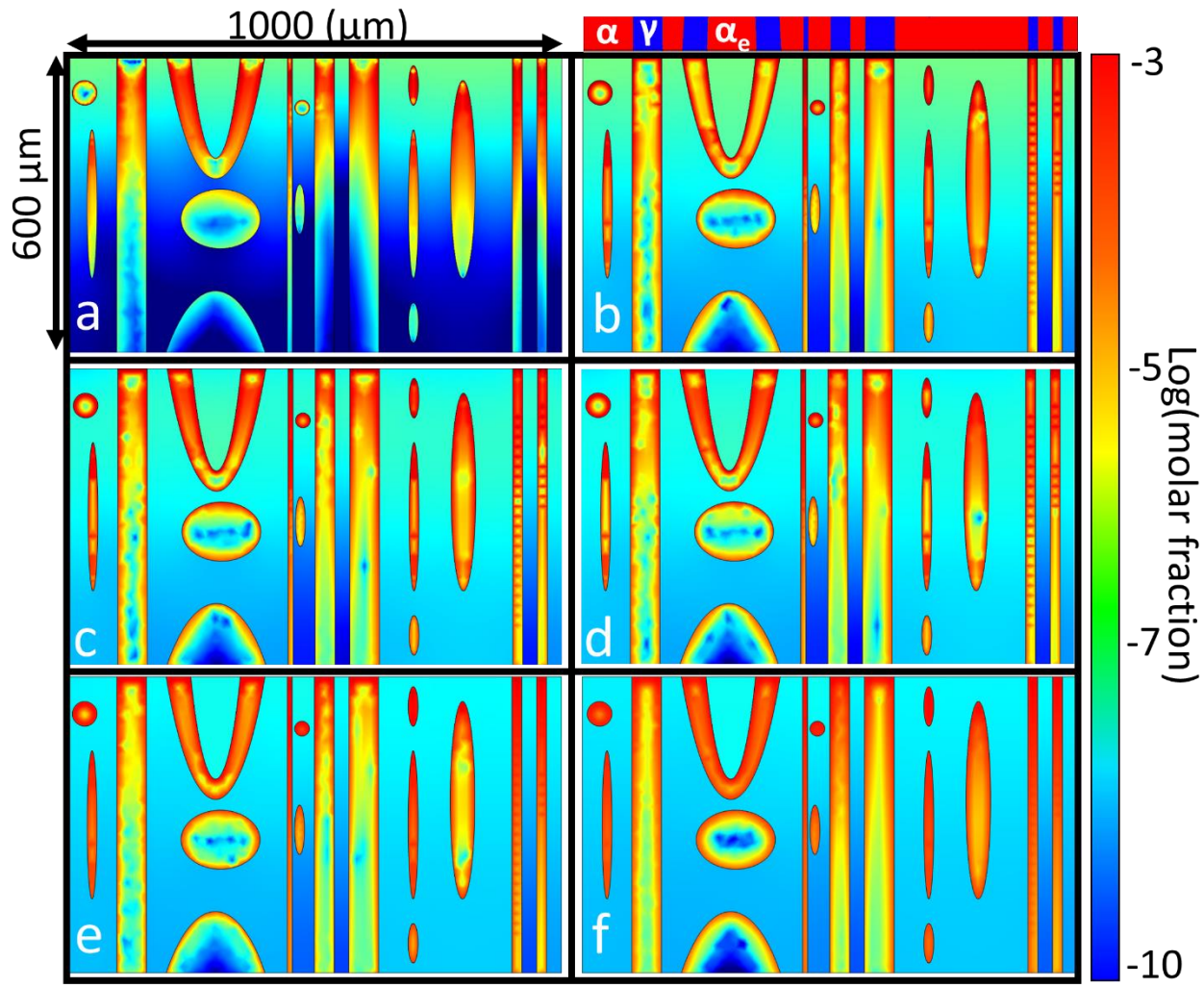

Figure 27 Cross-section hydrogen concentration calculated using finite element modelling at different time: a) 3 hours of charging, b) 24 hours (end) of charging. 24h of charging + c) 3h of SKPFM observation, d) 6h of SKPFM observation, e) 30h of SKPFM observation and f) 60h of SKPFM observation. The palladium layer is not represented here. Note that hydrogen desorption occurs through the down side at any time.

Figure 28, represents the hydrogen concentration profile on the top of the palladium film at different time during SKPFM observation (after 24h of hydrogen charging). It is interesting to

compare those profiles with those of Figure 21 obtained for down-charging experiment. In the case of the down-charging experiment, hydrogen enrichment in the palladium layer was obtained only above the ferrite phase, whereas here the enrichment is much more homogeneous (although slightly more pronounced above the ferrite). This confirms that in the top-charging experiment austenite also not only ferrite, provides hydrogen to the palladium layer.

It can be noted as well that the hydrogen concentration levels obtained in the palladium layer are significantly higher here than in the case of the down-charging experiment (Figure 21).

Figure 29 shows the hydrogen concentration profiles in the steel (under the palladium layer) at different time: 3h, 6h, 30h and 60h after the end of hydrogen charging. As expected the hydrogen concentration is higher at any time by at least 4 orders of magnitude in austenite than in ferrite. On the other hand, the hydrogen concentration in the palladium layer (Figure 28) is homogeneous within a factor of less than 2. So it is demonstrated again that there is no obvious relation between the hydrogen distribution in the palladium layer (which reflects the measurement obtained using SKPFM) and the hydrogen distribution in the steel under this layer.

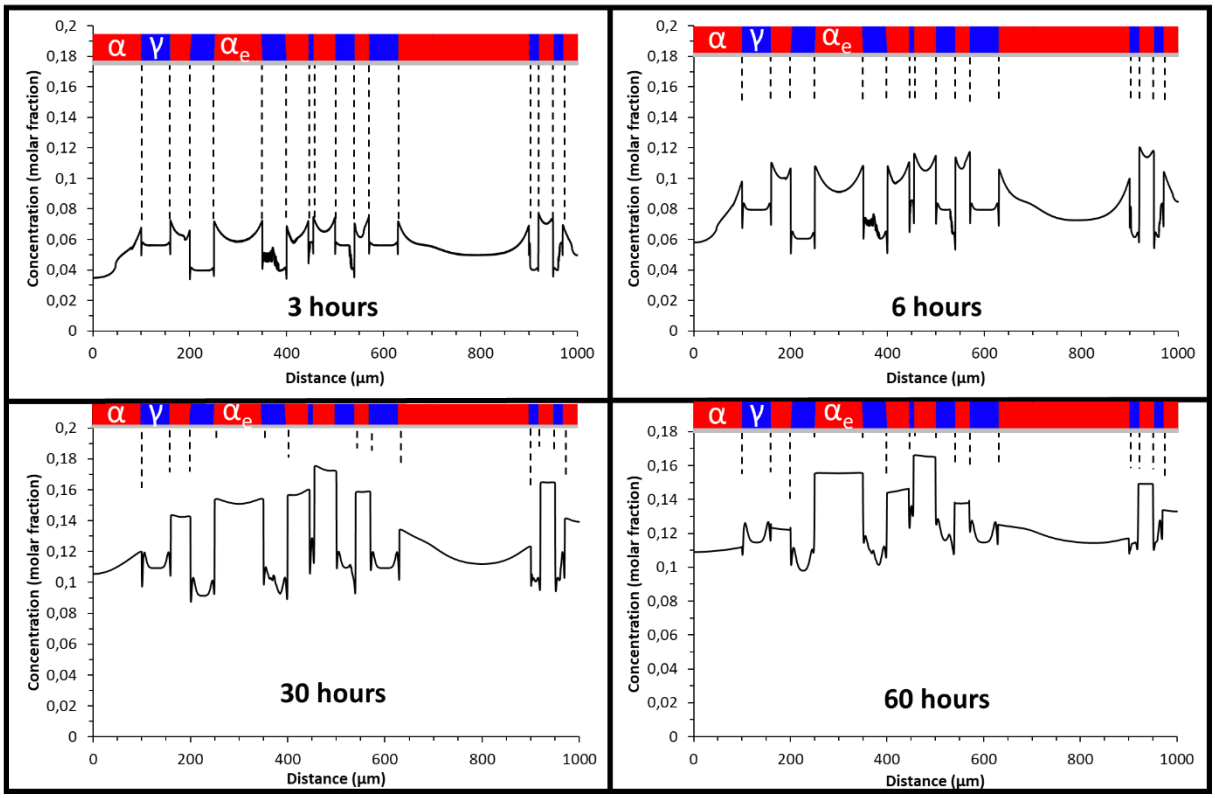

Figure 28 Hydrogen concentration profile at the surface of the palladium film at different time: 24 h of charging + 3h, 6h, 30h and 60h of SKPFM observation.

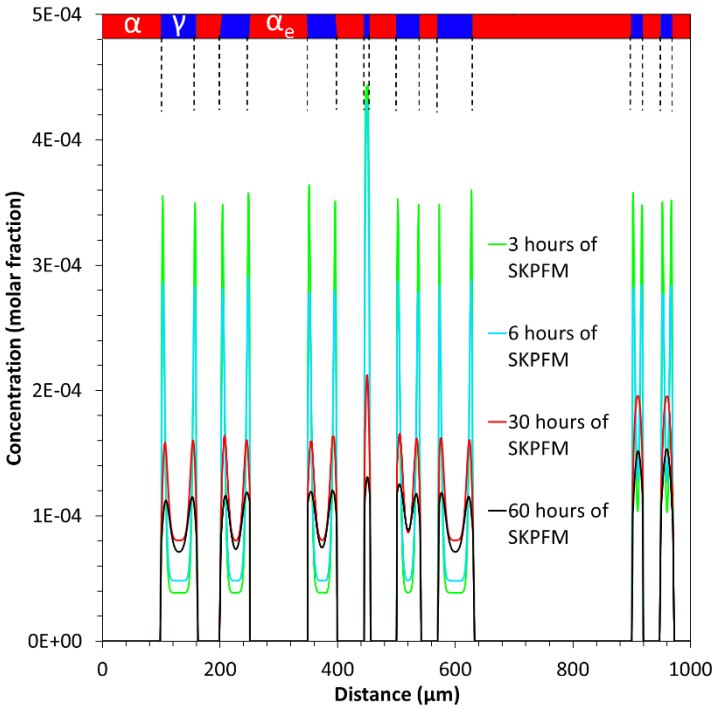

Figure 29 Hydrogen concentration profile in the steel (2 µm under the Pd film) at different time: 24h of charging + 3h, 6h, 30h and 60h hours of SKPFM observation.

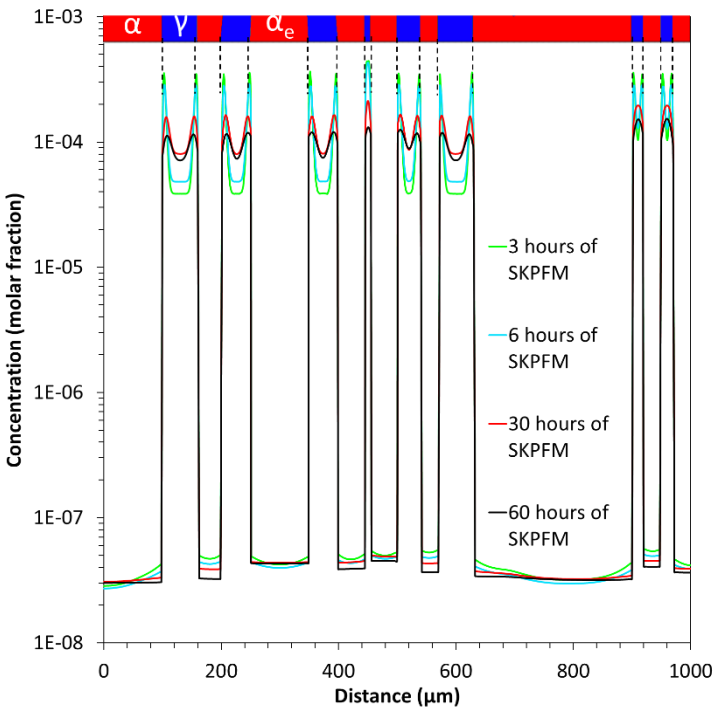

Figure 30 Hydrogen logarithmic concentration profile in the steel (2 µm under the Pd film) at different time: 24h of charging + 3h, 6h, 30h and 60h hours of SKPFM observation.

4. Conclusions

In this study, a method of hydrogen detection was developed using SKPFM. The material used is a dual phase (ferrite + austenite) stainless steel.

With a very anisotropic microstructure (elongated grains), the specimens used were 600 µm in thickness and were covered with a thin layer of palladium (~20nm). The SKPFM measurements were conducted in hydrogen pre-charged specimens. Two approaches were used: down-charging and top-charging.

FEM modelling of the hydrogen diffusion during the experiment was conducted as well. The model developed takes account of the different hydrogen related parameters (diffusion coefficient, solubility) in the three phases present (ferrite, austenite, palladium).

The main conclusions of this work can be summarized as follows:

Down-charging experiment:

1) Only the ferrite phase can provide the palladium layer with a significant amount of hydrogen, thanks to the high hydrogen diffusion coefficient in ferrite compared to austenite. This explains why only the ferrite phase gets brighter in the SKPFM measurement.
2) The contrast obtained in SKPFM is still clearly visible after several tens of hours of observation. This implies that there is no significant lateral hydrogen diffusion in the palladium layer, neither significant desorption from the palladium layer. This can be easily explained by the fact that hydrogen layer is likely deeply trapped on lattice defects of the palladium layer.
3) The time needed to obtain a contrast in the SKPFM observation can be very different from one place to another, and/or one specimen to another. This can be related to the diffusion path that hydrogen has to follow in the ferrite phase across the specimen that can be more or less tortuous and/or narrow depending on where the SKPFM measurement is conducted.
4) It was observed that the embedded (non-percolated) ferrite grains provide much less hydrogen (or even no hydrogen at all in some cases) to the palladium layer. This is

easily understandable considering the surrounding shell of austenite that behaves as a hydrogen diffusion barrier in this case.

Top charging experiment:

1) Both phases (ferrite and austenite) provide the palladium layer with hydrogen in this case. This can be easily understood as the two phases in contact with the palladium layer are “filled” with hydrogen in this case. This explains why the two phases get brighter over time in the SKPFM measurement. The hydrogen release seems to be slightly faster above the ferrite, but this is not a strict rule here, in contrast to what was observed in the down-charging experiment.
2) The potential measured in SKPFM is very homogeneous after some hours/ ten of hours, which confirms that ferrite and austenite release hydrogen into the palladium layer in this case.

Hydrogen diffusion modelling:

1) A 2D model was developed for the diffusion of hydrogen in phase system (ferrite, austenite and palladium) and was used to simulate the down-charging and top-charging experiments. This modelling study allowed us to confirm the interpretations mentioned above:
    a. For the down-charging experiment
        i. Only the ferrite phase releases a significant amount of hydrogen into the palladium layer.
        ii. The rate of release can be very different depending on the place. This is largely due to the lateral “pumping” effect of hydrogen by the austenite from the ferrite. This effect is enhanced for narrow corridors of ferrite.
        iii. Embedded (non-percolated) ferrite grains practically do not release any hydrogen.
    b. For the top-charging experiment:
        i. Both ferrite and austenite release hydrogen into the palladium layer, which gives a much more homogeneous hydrogen concentration in the palladium layer.

2) It was shown that the hydrogen concentration in the palladium layer (which gives the contrast obtained in SKPFM) does not reflect at any time the hydrogen distribution in the underlying material. This is why the SKPFM method used in this study should be considered as a way to monitor locally hydrogen fluxes, rather than a way to map the hydrogen concentration in the material.

Chapter II: Experimental study of the hydrogen embrittlement of a grade 350 maraging steel: effects of hydrogen redistribution on the cracking mode

1. Introduction

Hydrogen embrittlement of high strength steels, and more generally of metallic materials, has received intense study over decades, but is still not completely understood. Like all environmentally-assisted damage phenomena, it may be illustrated by the Figure 31 which explains the damage from the concordance between three factors at once, hydrogen ingress and its different states in the material, critical stress/strain loadings, and susceptible material/microstructure. The combination of these factors producing synergistic effects at the origin of damage. At a macroscopic scale, the effects of hydrogen embrittlement are manifested by many changes in the mechanical parameters that are used to characterize materials, including elongation to fracture, reduction in area, ultimate tensile strength, hardening rate, time to failure and fracture toughness, the extent of the changes depending on the material and the hydrogenating conditions. Moreover, it is currently considered that there are often several mechanisms involved together in the degradation of the mechanical properties of high strength steels, but the difficulty to isolate and study them separately make the processes of hydrogen embrittlement not completely understood.

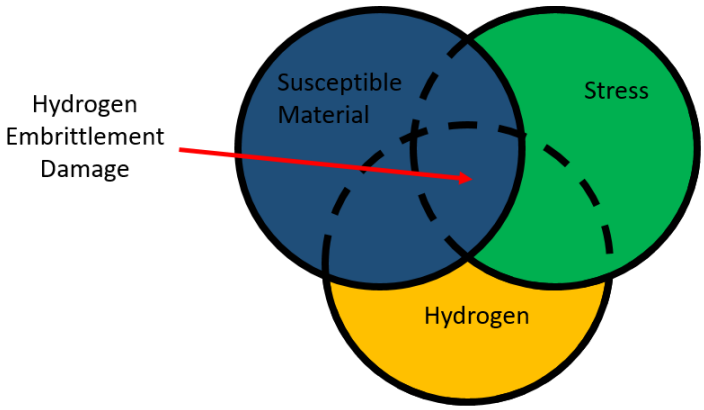

Figure 31 Factors involved in hydrogen embrittlement.

Based on a fine and precise fracture surface analysis, recent works have shown in particular that hydrogen embrittlement of a martensitic high strength low-alloy steel, manifested by intergranular cracking and “quasi-cleavage” transgranular fractures, can be modelled by a physically-based statistical micro-mechanical model [26], [27] which relies on the synergistic

action of **H**ydrogen-**E**nhanced **L**ocalized **P**lasticity (HELP) [28], [29] and **H**ydrogen-**E**nhanced **D**ecohesion (HEDE) [30], [31] mechanisms. In these studies, the samples were thermally precharged in an autoclave at various hydrogen gaseous pressures for a duration of several weeks. The embrittlement of the material during loading of the specimens was thus linked to internal hydrogen redistribution dictated by chemical potential gradients, themselves linked to hydrostatic stress gradients, and changing demands for trapping as dislocation traps were increasing with plastic straining.

When the hydrogen source is external, for cathodic hydrogen chargings during the mechanical loading for instance, the phenomenon of adsorption and absorption at the subsurface of the material must also be taken into account. Lynch's AIDE model (**A**dsorbed **I**nduced **D**islocations **E**mission), based on the effect of hydrogen adsorbed or located on the interstitial sites of the first atomic layers of the material, assumes that these populations of hydrogen locally decrease the cohesion energy of the metal and facilitates nucleation and emission of dislocations from the surface [32].

Other mechanisms such as HESIVE (**H**ydrogen **E**nhanced **S**train **I**nduced **V**acanci**E**s), proposed by Nagumo [33], is in turn based on the hypothesis that hydrogen promote the formation of vacancies during plastic deformation. The embrittlement is then due to their overconcentration in the material and not directly by the presence of hydrogen. These four models, given in example here to introduce the complexity of the hydrogen embrittlement, will be described in more details later, in the following paragraphs.

To this, are added recent results on the effects of hydrogen on damage depending on whether it is trapped or mobile in the lattice. Wang has shown that the cohesion energy was more lowered by mobile hydrogen than trapped one [34]. The work of Guedes *et al.* confirms the deleterious effects of mobile hydrogen on the ductility of a quenched and tempered low-alloyed steel, favouring a quasi-cleavage mode of rupture, while no significant effect is observed with the trapped hydrogen [35]. The distinction between these two populations of hydrogen is not clearly done in some of the models of hydrogen embrittlement. Furthermore, the hydrogen transport by diffusion is considered as a whole, by taking into account an apparent diffusion coefficient with no distinction between diffusion along grain boundaries

and/or dislocations and interstitial lattice diffusion, which are occurring simultaneously but at different kinetics, several orders of magnitude separating the respective diffusion coefficients.

Some authors have attempted to model the intergranular cracking by simplifying this difficult problem with only intergranular hydrogen diffusion in a flat volumic interface between adjacent grains, and using a traction-separation laws with irreversible damage and hydrogen-concentration-dependent cohesive energy [36]. Although these works have already resulted in valuable tools in the study of the damage of polycrystalline materials with quite large grains, they remain rather far from the complexity of the martensitic microstructures of high strength steels. In such microstructures, trapping with the presence of hydrogen sources or sinks in the adjacent old γ-grains, supplying or impoverishing the hydrogen in the grain boundaries strongly influences mechanical properties at a local scale.

To illustrate this complexity, a preliminary work to this study is presented here. Based on our previous work on a duplex stainless steel, an attempt has been done in this study on the grade 350 maraging steel (M350) to highlight the local flux of hydrogen in the martensite microstructure using SKPFM analysis. In the first part of the document, the SKPFM analysis clearly highlighted in the two-phase stainless steel the effect of the difference of hydrogen-diffusion properties between the α-phase and the γ-phase, on the local hydrogen-distribution in the palladium layer. Wishing to obtain this type of information at a finer scale of the martensite microstructure, analyzes were also undertaken on the maraging steel 350. Figure 32 shows an example. The same procedure was used: the sample of 320µm thick M350 was coated with 5nm of palladium on the detection side before being hydrogen charged for 24 hours at -1200 mV/SCE in 30 g/L NaCl solution. Figure 32a shows the topographic AFM image on an area covering at least two old γ-grains in the microstructure. On Figure 32b, the SKPFM signal of the same area after 30 hours of desorption shows a heterogeneous distribution of its intensity, which can be correlated to a heterogeneous distribution of hydrogen taking into consideration the results presented in the previous chapter. In addition, the distribution seems to draw features related to the complex microstructure which suggests that this technique would easily track local variations in hydrogen during damage. Unfortunately, it is quite complicated to correlate without doubt these features to the sub-surface microstructure, the lateral resolution of the available device being limited compared to the very fine microstructure of the martensite. All our attempts were fruitless. To embark on a

crack initiation and propagation study based on measurements of local variation of hydrogen in the microstructure of a maraging steel using this technique seemed too risky. Although this technique has revealed its potential in the duplex SS in the previous chapter, it has been finally abandoned for hydrogen investigation in the maraging steel 350 in this part of the study.

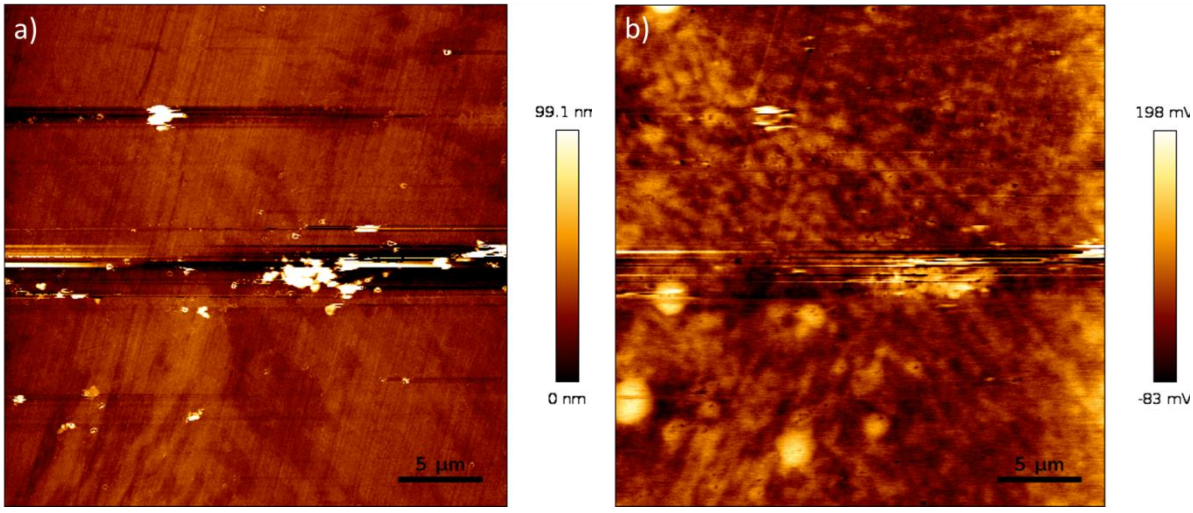

Figure 32 AFM images of maraging steel 350 after being H charged for 24 hours taken on the desorption side showing in a) the topography and in b) the respective SKPFM signal.

To study and identify the main mechanisms involved in the hydrogen embrittlement of the grade 350 maraging steel, an experimental methodology based on the combination of various mechanical tests under hydrogenating conditions has been used to explore the behaviour of the material. The methodology aims to determine the role and the importance of each of these mechanisms and to identify the limiting factors during the damage processes in order to streamline and simplify the models in a representative way.

The objective of the study is thus to develop an experimental methodology allowing highlighting the role of the redistribution kinetic of hydrogen in the material on the processes of damage, and particularly the different effects of GB/dislocation diffusion and the lattice diffusion of hydrogen. To separate the effects of hydrogen-dislocation interactions from the pure decohesion mechanisms at the interfaces in the microstructure linked to hydrogen concentration dependency, a very high strength steel was chosen among the 18wt.% Ni maraging steels. Its high properties allow to load grain boundaries at high level of stress and

to increase the interatomic volume, which affects both the diffusivity and the trapping of hydrogen, without triggering plasticity. The role of plasticity can then be explored at higher stress levels. Furthermore, its very low content of S and P excludes any embrittlement due to segregation effects. Different conditions of hydrogen charging during mechanical loading or beforehand, as well as the hydrogen entry conditions made it possible to explore the effects of trapping alone and the effects of diffusible hydrogen on the damage. To favour stress triaxiality and enhance hydrogen diffusion, conventional mechanical tests on axis-symmetrical notched specimens at various load rates were performed.

This chapter is divided in six parts. Just after the present introduction, the second part of the study is dedicated to a literature review of the material studied and its behaviour in hydrogenating environments. Then the description of the material used in this study, followed by the presentation of the experimental method are presented in the third part. Fourth paragraph explores the mechanical testing procedures of the grade 350 maraging steel. Numerical simulations necessary to explain some results are presented in the fifth paragraph. Then, results and discussions are presented in the last paragraph, and followed by a set of conclusions.

2. Literature review.

2.1. Metallurgical aspects of 18% Ni maraging steels

18% Ni maraging steels are a family of high-alloyed steels, which have ultra-high strength due to solid-state transformations, martensitic transformation on cooling (γ -> α') followed by aging which refers to the extended heat-treatment allowing strengthening of the matrix with intermetallic precipitation. Their name derived from these two transformations. They are available in four grades, 200, 250, 300 and 350, referring to their respective yield strength (YS) in ksi (the corresponding YS in MPa are 1380, 1720, 2070, and 2410 MPa). The principal alloying element is nickel. On the contrary, they contain a very low percentage of carbon. Secondary substitutional alloying elements are added to form intermetallic precipitates in the iron-nickel martensitic matrix, which include cobalt, molybdenum and titanium.

2.1.1. Martensite formation

The metallurgical behaviour of maraging steels is linked to the thermal hysteresis in the Fe-Ni alloys between martensite formation on cooling and its reversion to austenite on heating Figure 33 [37]. A typical heat treatment for maraging steels consists of solution annealing for 1 hour at 815-820°C in the austenite domain, followed by cooling to room temperature. Due to the high nickel content and low carbon content, the hardenability after annealing is independent of the cooling rate. The alloys are therefore cooled in air [38].

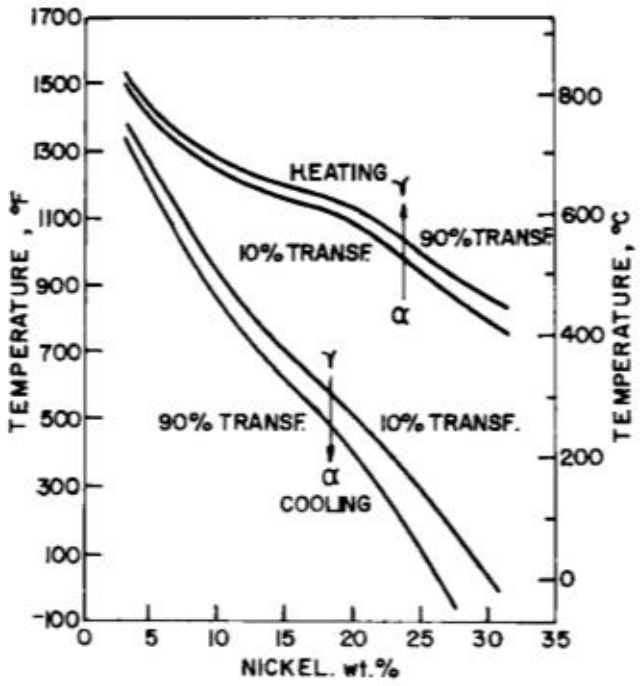

Figure 33 Metastable Iron-Nickel Phase diagram [37].

The martensite-start temperature (M_s) on cooling depends on the Ni content. The higher the latter, the lower the M_s temperature. In addition, the increase in nickel content lowers the cooling rate required to form martensite. For content higher than 10 wt.% Ni, a fully bcc martensitic structure is obtained even at very low cooling rates. The typical morphology of this martensite is called lath martensite (or massive martensite) and is obtained up to 28 wt.% Ni. Above this content, the martensite formation occurs below room temperature ; the microstructure obtained in this case is called twinned martensite [38].

The orientation relationships between the martensite laths formed and the austenite matrix are believed to follow the Kurdjumov-Sachs ones [39]:

$$(111)_\gamma \,||\, (011)_\alpha, and\ [1\bar{1}0]_\gamma \,||\, [1\bar{1}1]_\alpha, \qquad \text{[K-S]} \qquad \textbf{(4)}$$

Concerning mechanical properties, the presence of martensitic microstructure ensures the relatively high strength of the matrix. If the cooling rate has no effect on the hardenability, the effects of refinement of prior austenite grain size are remarkable. The literature review showed an improvement on both ductility and fracture strength on notched samples, and also on Charpy impact energy [40]. However, no effect was found on fracture toughness K_{IC} [41]. Due to that, several ways for prior γ-grain refinement were proposed either by thermomechanical treatment, cold working or also by making several austenite-martensite transformation treatments.

2.1.2. Morphology of martensite crystals

The microstructure of bcc-lath martensite in alloys 10-25 wt.% Ni differs from that of quenched carbon steels or alloys with Ni content higher than 28 wt.% in which martensite transformation occurs below room temperature. It is characterized by areas of variants that are parallel to one another and of similar size, with a well-organized morphology forming rectangular blocks and packets (Figure 34a). There are 24 variants obtained from an austenite grain, and these variants follow Kurdjumov-Sachs orientation relationships with respect to the parent crystal. Here is the organization as shown in Figure 34b, and described as follows in Table 3 [42], [43]:

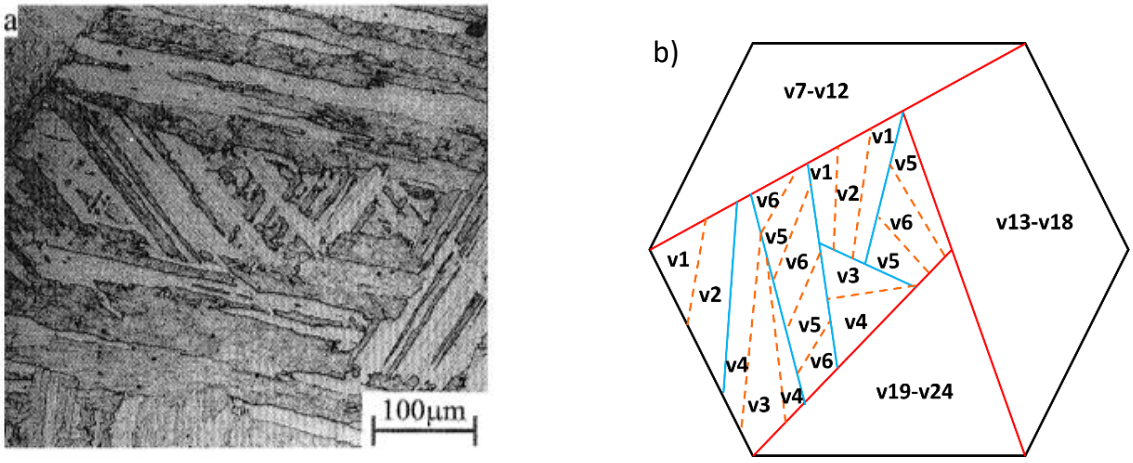

Figure 34 (a) Optical micrograph of typical lath martensite in a 18 wt.%Ni maraging steel [43]. (b) Schematic organisation of variants in a former γ-grain: former austenite GB in black, packets GB in red, blocks GB in blue, and sub-blocks GB in orange.

Each group of following variants, V1 to V6, V7 to V12, V13 to V18, and V19 to V24, belongs to a single packet which has the parallel relationship of close packed planes for the same $\{111\}_\gamma$ plane. For each habit plane, there is 6 possible orientations for α'-crystal with respect to the initial γ-crystal. These 6 orientations are grouped into 3 pairs of variants, and each of these pairs of variants form a block. Each variant inside a block is called a sub-block. Sub-blocks are weakly misoriented inside the same block (10.53°). The sub-blocks are composed of laths which are mono-crystals with small misorientation to each other (< 3°) [44].

In total, there is 10 possible angles of misorientation along $[011]_{\alpha'}$ between 2 variants following the Kurdjumov-Sachs relationships of orientation: between sub-blocks (10.53°), between blocks (70.5°, 60°, 49.47°), and between packets (10.53°, 14.88°, 20.61°, 21.06°, 47.11°, 49.47°, 50.51°, 51.73°, 57.21°).

Table 3 The 24 variants following the K-S orientation relationships in lath martensite.

Variant n°	Plane parallel	Direction parallel [γ] // [α']	Variant n°	Plane parallel	Direction parallel [γ] // [α']
V1	(111)γ // (011)α'	[-101] // [-1-11]	V13	(-111)γ // (011)α'	[0-11] // [-1-11]
V2		[-101] // [-11-1]	V14		[0-11] // [-11-1]
V3		[01-1] // [-1-11]	V15		[-10-1] // [-1-11]
V4		[01-1] // [-11-1]	V16		[-10-1] // [-11-1]
V5		[1-10] // [-1-11]	V17		[110] // [-1-11]

V6		[1-10] // [-11-1]	V18		[110] // [-11-1]
V7		[10-1] // [-1-11]	V19		[-110] // [-1-11]
V8		[10-1] // [-11-1]	V20		[-110] // [-11-1]
V9	(1-11)γ //	[-1-10] // [-1-11]	V21	(11-1)γ //	[0-1-1] // [-1-11]
V10	(011)α'	[-1-10] // [-11-1]	V22	(011)α'	[0-1-1] // [-11-1]
V11		[011] // [-1-11]	V23		[101] // [-1-11]
V12		[011] // [-11-1]	V24		[101] // [-11-1]

The characteristic sizes of these constituents and the changes in the morphology of lath-martensite have been studied in the 18wt.% Ni maraging steels, particularly the effect of austenite deformation at temperature below the recrystallization temperature (thermo-mechanical treatment of ausforming) insofar as packets and blocks are fundamental microstructural units which control the mechanical properties, especially the toughness [43], [45]. Table 4 summarizes the sizes of each substructure and dislocation density obtained in lath martensite with or without 60% ausforming [43]. Packet size and block width decrease significantly by ausforming while almost no change is observed in lath width, which remain around 0.60-0.80 µm. Other works found these approximately 1 µm-thick for lath width in 18wt.% Ni maraging steels [46], [47]. In addition, dislocation density in lath-martensite increases by ausforming. The authors concluded that dislocations in deformed austenite are inherited into lath-martensite, resulting in the increase of dislocation density in martensite.

Table 4 Dimensions of the microstructural units and dislocation density in lath-martensite with or without 60% ausforming thermomechanical treatment in 18%Ni maraging steel [43].

Ausforming treatment	Packet width (µm)	Block width (µm)	Lath width (µm)	Dislocation density ($10^{15}/m^2$)
0%	142	18.6	0.80	0.91
60%	67	2.5	0.64	1.30

The lath-martensite is characterized by a high density of dislocations uniformly distributed in the matrix. They are predominantly of the screw type and have a tendency to orient themselves along the <111>α' directions [48]. If the benefit of this microstructure is favourable to the good distribution of hardening precipitates, it is also for ductility. Lath-martensite of

18% Ni maraging steels shows a much higher ductility than iron even when tested at very low temperatures [49]. The reason seems to be in the fact that the number of mobile dislocations in lath martensite is much higher than in iron, which improves the ductility and reduces the propensity to cleavage.

2.1.3. Role of alloying elements in martensite formation and aging

Alloying elements used in maraging steels generally lower the M_S temperature with the exception of cobalt for which the addition up to 8 wt.% increases it. This effect is beneficial to ensure the formation of lath martensite even at higher concentrations of other alloying elements insofar lath martensite, characterized by high density of dislocations uniformly distributed, favours uniform nucleation and growth of intermetallic precipitates during the age-hardening process [48]. This homogeneous precipitation is also decisive for obtaining good plastic properties and high ductility [38].

Before aging treatment, the direct contribution of martensite microstructure to the strength in maraging steels is relatively small. The hardening is mainly due to solid-solution-strengthening by Ni, which represents more than 70% of the overall value of the yield stress in Fe-Ni alloys with less than 30wt.% Ni.

The very high strength of these steels is thus obtained by aging. It is realized in the range of 450° to 700°C during several hours, and leads to two main processes, the precipitation of various intermetallic precipitates and the ordering in the cobalt-containing solid solution. When precipitates grow too large, and the hardness decreases, the alloy is said to be overaged. Generally, this phenomenon is also accompanied by a conversion of martensite into austenite, called reverted austenite.

In addition to Ni, the main elements associated with precipitation are titanium, molybdenum and cobalt:

2.1.3.1. Titanium (Ti)

Titanium is a very active element and is considered as a fast diffusing element. The totality of the titanium in the system forms the precipitates such as Ni_3Ti and $Ti_6Si_7Ni_{16}$ at a very beginning of the aging process and what is left in the matrix is undetectable. Apart from being

a hardener, titanium refines the steel by forming carbonitrides with the residual carbon, which usually precipitates in the old austenite grain boundaries [38]. Titanium plays also an important role on the austenite reversion behaviour [50].

Addition of titanium increases the tensile strength and decreases the reduction of area [51].

2.1.3.2. Molybdenum (Mo)

The molybdenum effects concern also the precipitation processes, but they are strongly affected by the presence of titanium and cobalt. Generally, the cobalt enhances the activity of the molybdenum and increases the driving force for the precipitation of Mo. On the other hand, as seen before, Ni_3Ti nucleates quickly which will prevent the formation of a metastable Mo-based phase, called ω, because the Mo will preferentially segregate toward the Ti-based phase so the ω cannot get formed. In all cases, with or without the effect of Ti, Mo will end up forming the stable phase Fe_7Mo_6 [50].

The addition of molybdenum showed an increase in the tensile strength, but at the expense of fracture toughness. In addition to that, molybdenum decreases the area reduction with the increase of the strength. It favours however the suppression of grain refinement which ultimately counteracts its effects on ductility [51].

2.1.3.3. Cobalt (Co)

The main role of cobalt is that it decreases the solid solubility of the hardening components in the martensitic matrix, such as molybdenum and titanium [49]. This happens by the fact that cobalt does not form precipitate by itself but contributes to the reduction of work of formation of a nucleus by substituting itself with nickel and/or iron [50]. In this way, it leads to both an increase in the number of nuclei capable of growth, thereby reducing the distance between the precipitates, and an increase in the volume fraction of these particles.

Addition of cobalt increases the tensile strength of maraging steels but, in contrast to Mo and Ti, it does not decrease the reduction of area. In addition, cobalt promotes grain refinement which actually increases the ductility [51].

2.1.3.4. Nickel (Ni)

Nickel is the main alloying element in maraging steels. Of course, it ensures the martensite formation, but it also reduces the solubility of other alloying elements in the martensitic

matrix and participates to the precipitation process. Nickel has also a strong influence on the austenite reversion process. Due to rapid precipitation of nickel-based intermetallic precipitates for kinetic reasons, the depletion of the nickel in the matrix makes it possible to increase the reversion temperature of the austenite (A_s) [50].

Besides, Ni reduces the resistance to dislocation motion in the lattice and the energy of interaction with the interstitials. It promotes stress relaxation, which in turn decreases the trend to brittle fracture [52].

Many investigations on precipitation reactions and identification of the precipitates in 18wt.% Ni maraging steel have been done. An earlier literature review of B.-Z. Weiss gives the main results in [38], reported partially in the Table 5 below. The shape of the precipitates was found to be needles, disks, ribbons and spherical-likes, the most often reported, the Ni_3Mo intermetallic, having a rod-shape morphology parallel to the <111> directions of the martensite matrix. In the initial stage of the aging, the Ni_3Mo is favoured because of the low lattice misfit between the precipitate and the matrix. Aging for longer time or at higher temperature (> 480°C) leads to an increase in coherency stresses and the Ni_3Mo is replaced by a more stable Mo-containing precipitate such as Fe_2Mo [38].

Table 5 Data of phases precipitating in maraging steels in the course of aging (from [38])

Precipitating phase	Crystal structure	Lattice parameter (Angstrom)			
		a	b	c	a/c
Ni_3Mo	Orthorhombic	5.06	4.22	4.45	-
Fe_2Ti	Hexagonal	4.81	-	7.85	1.63
Fe_2Mo	Hexagonal	4.74	-	8.31	3.26

These results have been confirmed by more recent studies on maraging steel 350 using complementary techniques such as small angle X-ray scattering (SAXS) and transmission microscope [53]. The authors' investigations allowed to draw the schematic representation of the TTT curves corresponding to the start of transformation of various phases (Figure 35). At temperature above 450°C, precipitation of A_3B types of phases $Ni_3(Ti, Mo)$ takes place through the mechanism of clustering and ordering of atomic species.

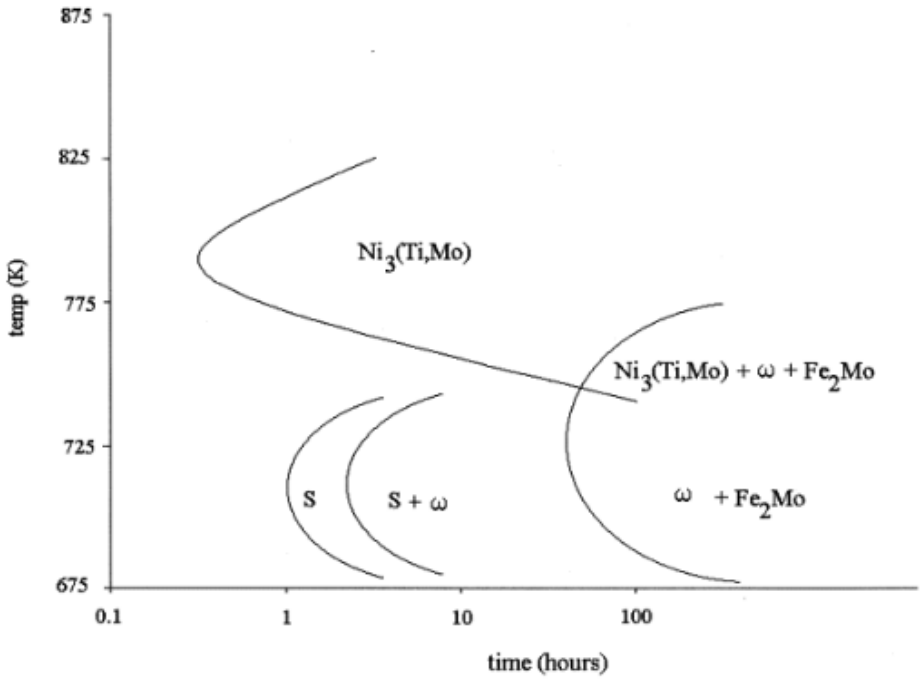

Figure 35 TTT curves corresponding to the start of transformation of various phases in maraging steel 350 [53].

Precipitations size and distribution is dependent on the aging time and temperature. For an 510°C-aging (783 K) for three hours, the average precipitate size, determined by hand counting on TEM images, was found to be around 40 nm long and 2.5 nm thick [54]. These rod-shaped geometry precipitates were found to contain Mo and to have a hexagonal structure, so it is believed to be Ni_3(Ti, Mo); the lattice parameters were found to be a = 0.5101 nm and c = 0.8307 nm. Moreover, some nearly spherical precipitates were found and are believed to be Fe_2Mo with also hexagonal structure with lattice parameters: a = 0.4745 nm and c = 0.7754 nm [54]. Small angle X-ray analysis used by other authors allowed to determine the variation of the first moment (number average particle diameter) of the size distribution of precipitates, R_1, with ageing time at 510°C [53]. As seen in Figure 36, after four hours of aging we end up with precipitates with a radius close to 10 nm [53].

While the Ni_3(Ti, Mo) precipitates seem to appear very early in the aging process, the Fe_2Mo precipitates appear later [53], after at least 3 hours of aging according to [54]. Furthermore, based on the analysis of the fringes contrasts that could be seen clearly in the dark-field TEM images obtained by using precipitate reflections, the authors showed that for certain electron beam directions, these fringes were found to be parallel to the length of the precipitates, so these precipitates can be considered as coherent with the matrix.

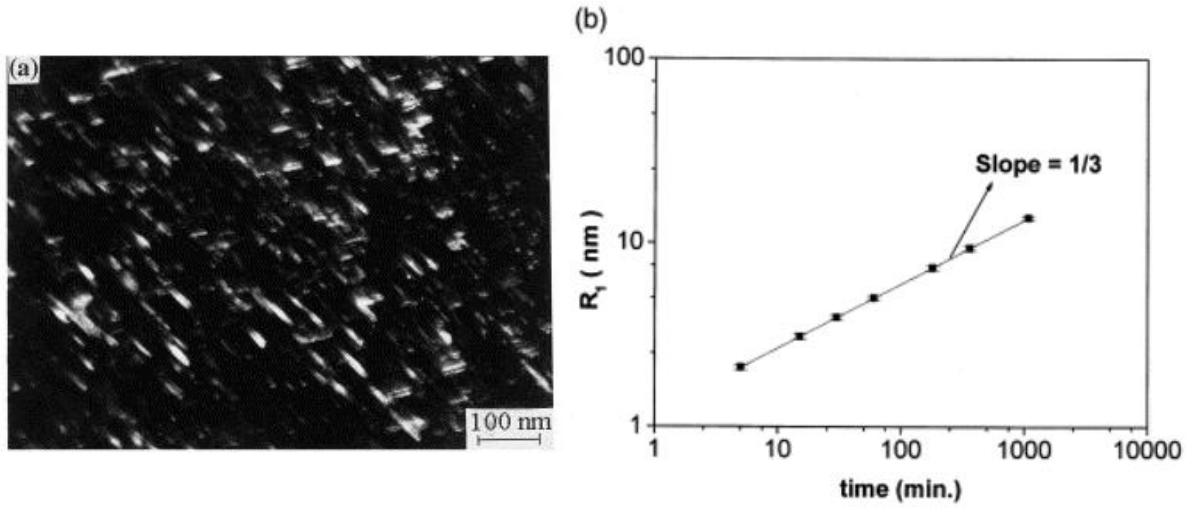

Figure 36 (a) Dark-field micrograph (g=1-10-1) showing the presence of ellipsoïdal Ni_3(Ti, Mo) precipitates in a maraging steel 350 aged at 510°C for 30 min [53]. (b) Variation of first moment of the size distribution of precipitates, R_1, with ageing time [53].

2.1.4. Reverted austenite

18wt.%Ni maraging steels have a tough martensitic structure with a high austenite reversion temperature, which depend on the Ni content after aging treatment.

The maraging steel 350 grade contains both cobalt and titanium in a substantial amount. A high-titanium concentration leads to a larger volume fraction of the Ni_3Ti type of phase, and the presence of cobalt makes the formation of the Fe_2Mo type of phase easier. The initial strength of these steels is achieved by the precipitation of a Ni_3(Ti, Mo) type of phase. This is then followed by precipitation of the Fe_2Mo phase which is responsible for the peak strength and also for maintaining high strength on prolonged aging.

The larger amount of Ni consumed in Ni_3Ti precipitates reduces the Ni content in the matrix making the high-Ni reverted austenite difficult to nucleate [50]. On the other side, the Fe_2Mo phase formation consumes Fe thus depleting the matrix in favour of Ni. These two precipitate formations lead to opposite effects on the reverted austenite nucleation during aging treatment. Nevertheless, Fe_2Mo precipitation taking more time according to Figure 35, a strict control of the duration of the aging treatment makes it possible to control and to avoid the formation of reversion austenite, if necessary.

Figure 37 shows the effect of the temperature and the aging time on the formation and the content of the reverted austenite in a maraging 350 steel [55]. It shows that for aging temperature below 950°F (< 510°C), reverted austenite does not form before 5 hours of aging while at 1000°F, less than 1 hour is sufficient.

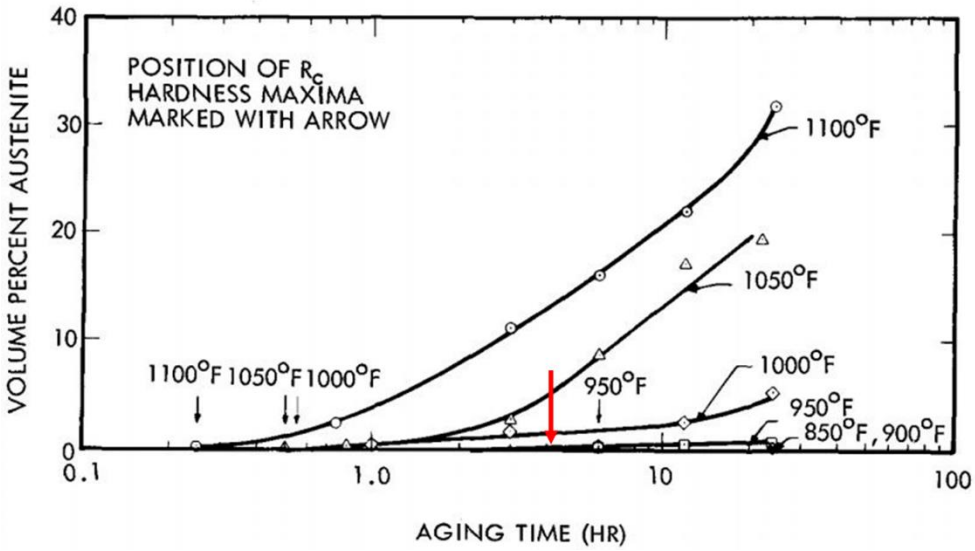

Figure 37 Influence of the ageing time on the content of the reverted austenite formed in a maraging 350 steel [55].

Reverted austenite starting to form at 510°C for long aging time is a lath-like austenite having a size of around 5 nm, and mainly localized on the laths boundaries of martensite and prior austenitic grain boundaries [56]. Following longer ageing, lath-like austenite starts to grow at a bigger rate than the precipitates and surrounds the martensite laths. The reverted austenite can grow to around 100 nm and have a plate-like shape within the laths as shown in Figure 38 for an overaged maraging [39].

For long aging duration, precipitates grow in size and increase their inter-particle spacing. In over aging, the strength decreases from its maximum value. Three different processes are involved. First, there is the coarsening of Ni_3Mo and Ni_3Ti precipitates. Next, is the formation of large stable Fe_2Mo precipitates, and finally, there is austenite reversion. The Ni_3Mo and Ni_3Ti precipitates are metastable [57], so they ultimately coarsen and dissolve back into solution [55].

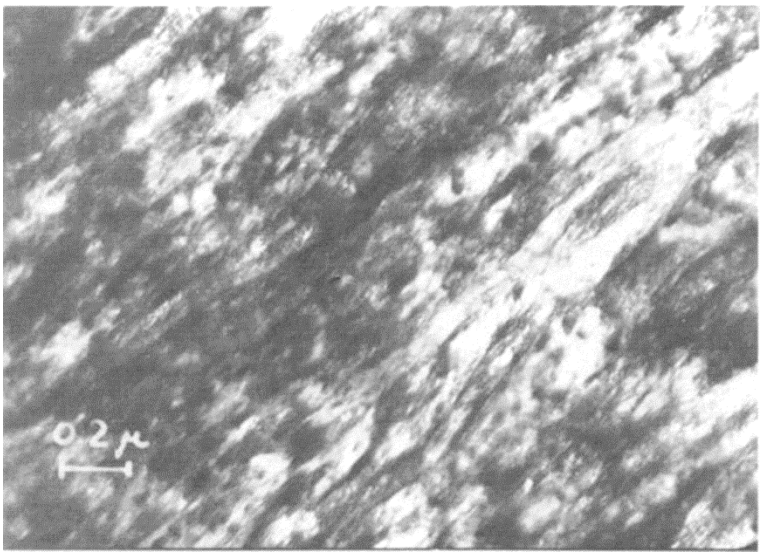

Figure 38 Bright field TEM image showing maraging structure with reverted austenite. The steel here was overaged for 3 hours at 675°C, reduced 28% by rolling at room temperature then aged again for 3 hours at 490°C [39].

2.2. Hydrogen interactions with metals.

The hydrogen embrittlement of metallic materials is very dependent on the microstructure and its evolution with stress and strain during mechanical loadings. Martensitic alloys in particular, present a complex microstructure with numerous metallurgical heterogeneities having each one specific interactions with hydrogen, including consequences on the hydrogen transport by diffusion and its trapping.

In this part, we will describe the main elements of the metallurgy of these martensitic steels involved in the interactions with hydrogen and playing a role in the hydrogen induced (or assisted) cracking.

2.2.1. Reactions of hydrogen adsorption and absorption.

Hydrogen is an atom usually present in environments encountered in service operation of structural materials. Due to its small size and mainly to its electronic structure which has a good compatibility with metals, it can penetrate metallic materials easily and diffuses through the microstructure.

In gaseous hydrogen atmosphere, molecules of hydrogen can be adsorbed on the surface, dissociated and atomic hydrogen absorbed in the material. The Sievert's law (5) that relates its concentration in the first atomic sites of surface C_H to the square root of the gaseous hydrogen partial pressure p_{H_2} at thermodynamic equilibrium introduces the notion of solubility *S*.

$$C_H = S\sqrt{p_{H_2}} \quad \textbf{(5)}$$

In aqueous environments and low pH, cathodic polarization allows the reduction of the proton (or H_3O^+) on the surface, following the Volmer reaction of hydrogen evolution, as shown in (6) [58]–[60].

$$M + H^+ + e^- = MH_{ads} \quad \textbf{(6)}$$

In basic aqueous environment, the reaction of hydrogen adsorption is the following:

$$H_2O + M + e^- \rightarrow MH_{ads} + OH^- \quad \textbf{(7)}$$

The hydrogen evolution reaction (HER) on the surface is then followed by two other possible reactions, the electrochemical desorption (Heyrovsky reaction (8)) and the chemical desorption (Tafel reaction (9)):

$$MH_{ads} + H^+ + e^- \rightarrow H_2 + M \quad \textbf{(8)}$$

$$2MH_{ads} \rightarrow H_2 + 2M \quad \textbf{(9)}$$

The hydrogen transfer from the surface to the bulk is realised by a pure chemical reaction (HAR):

$$MH_{ads} = H_{abs} + M \quad \textbf{(10)}$$

The kinetics of absorption, adsorption and desorption of hydrogen at the surface depend on:

- the electronic transfer during electrochemical reactions of Volmer and Heyrovsky,
- and the evolution of the hydrogen coverage rate θ of the metallic surface by the adsorbed hydrogen H_{ads}.

They are described by the conventional quantities r_o and r_1 [61]:

$$r_0 = -\frac{j}{F} = \nu_V + \nu_H \quad \textbf{(11)}$$

$$r_1 = \frac{q}{F}\frac{d\theta}{dt} = \nu_V - \nu_H - \nu_T - \nu_{abs} \quad \textbf{(12)}$$

j is the quantity of faradic current, ν_i the rates of each reaction stage i (Volmer, Heyrovsky and Tafel), F the Faraday constant, q the charge of a H_{ads} monolayer.

Under cathodic polarization, the reactions of adsorption and hydrogen release are dominant and can lead to the phenomenon of hydrogen embrittlement.

2.2.2. Role of hydrogen in cracking mechanisms

Due to the small size of its atomic radius that is of the same order of magnitude than the size of the interstitial sites in the metallic crystal lattice, hydrogen can easily enter into the tetrahedral sites of a metal with a cubic centered structure. The mobility of the hydrogen atom is very high. It diffuses from one interstitial site to another. The diffusion coefficient of hydrogen in ferrite for instance is of the order of 5.10^{-5} cm² s^{-1} at 25 ° C. Hydrogen also has low solubility in iron, which leads to a tendency to segregate into microstructural defects. The apparent diffusion coefficient is much weaker. For high strength low alloy steel for example, we found a value of 5.10^{-6} cm² s^{-1} at room temperature [62]. A particular electronic properties give to hydrogen a high partial molar volume despite its small size, which tends to generate distortions of the crystal lattice [61], [63], [64].

2.2.2.1. Mode of hydrogen transport

Stress assisted diffusion

Troiano [65] has observed a correlation between the position of the maximum of the triaxial stresses and that of crack initiation under hydrogen. In areas of high hydrostatic tension stress, the chemical potential of hydrogen in solid solution is decreased which causes an increase in the flow of diffusible hydrogen to these zones and a local increase in the hydrogen concentration. Thus, the flow of hydrogen *J* can be expressed by [66]:

$$J = D\nabla C + \frac{DC\overline{V_H}}{RT}\nabla\sigma_h \quad \textbf{(13)}$$

with D the hydrogen diffusion coefficient, C the hydrogen concentration, $\bar{V}_H$ the molar volume of hydrogen, R the gas constant, T the temperature and σ_h the hydrostatic stress defined as follows:

$$\sigma_h = \frac{1}{3}\left(\sigma_{xx} + \sigma_{yy} + \sigma_{zz}\right) \quad \textbf{(14)}$$

The diffusion coefficient is measured experimentally using permeation tests by analyzing the evolution of the hydrogen flow through a thin metallic membrane as a function of time.

Figure 39 shows the different steps of hydrogen entry and its transportation by diffusion from the crack tip or surface defect of a metallic material immersed in an aqueous environment [67]: (1) adsorption of H_2O, (2) reduction of water, (3) absorption of atomic H, (4) H transport by diffusion. The area of high hydrostatic tension stress is located at some micrometers ahead of the crack tip.

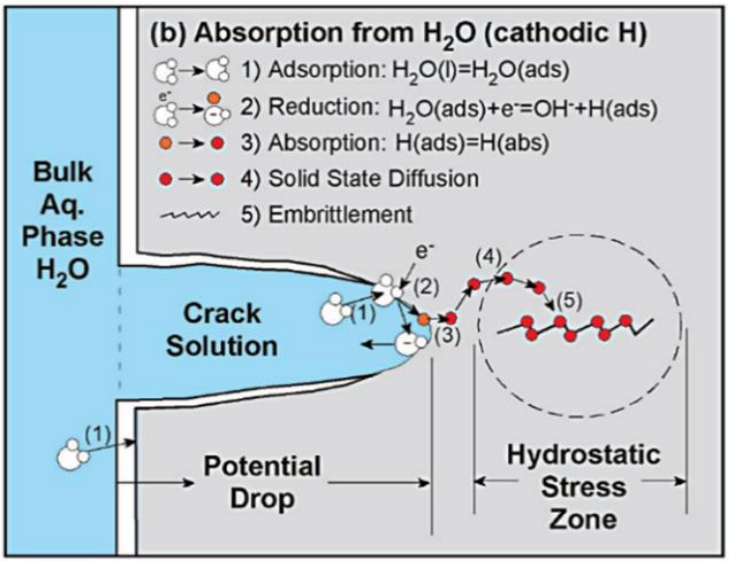

Figure 39 Hydrogen transportation mechanisms from aqueous environments [67].

Transport by dislocations

Hydrogen transport by dislocations has been suggested for the first time by Bastien and Azou [68]. Kumnick and Johnson [69] have shown by means of permeation tests that the trapping of hydrogen depends on the plastic deformation of the material. The increase in the density

of dislocations associated with the plastic deformation of a material put in contact with hydrogen is reflected by a significant increase in the hydrogen concentration in the plastic strained zone. This mode of transport was evidenced by the measurement of the desorption flow of pre-introduced tritium in a specimen subjected to a tensile test [70], [71]. Tien shows that dislocations in motion must not exceed a critical velocity v_c depending on the trapping energy, the diffusion coefficient and the temperature for the hydrogen transport to be effective [70].

The stronger weakening effect of hydrogen at low deformation rates is explained by the activation of the hydrogen transport mechanism by dislocations. The transport of hydrogen by dislocations can locally lead to over-concentrations of hydrogen in the material at obstacles such as precipitates, which block the movement of dislocations [72].

2.2.2.2. Trapping of hydrogen in martensitic high strength steels

The low solubility and the high mobility of hydrogen are at the origin of hydrogen trapping phenomena in ferritic and martensitic steels. The trapping of hydrogen is associated with a decrease in its mobility, which depends on the trapping energy. The trapping phenomenon has the effect of increasing the apparent solubility of hydrogen, reducing its apparent diffusivity and promote phenomena of local concentration that are causing hydrogen embrittlement. The distribution of hydrogen in the traps will depend on the binding energy and the concentration of hydrogen in the sites of the crystal lattice surrounding the trap.

Figure 40 shows a schematic representation of trapping sites as a function of their binding energy. Whereas the activation energy needed during lattice diffusion for the hydrogen to jump from a normal interstitial lattice site to another is E_a, when it is trapped in a lower energy site, the energy barrier needed for the hydrogen to get un-trapped increases. It is the addition of the saddle point energy E_s (equal to E_a + E' in Figure 40) and ΔE_x, the trap binding energy [63]. The de-trapping activation energy is equal to $E_s + \Delta E_x$.

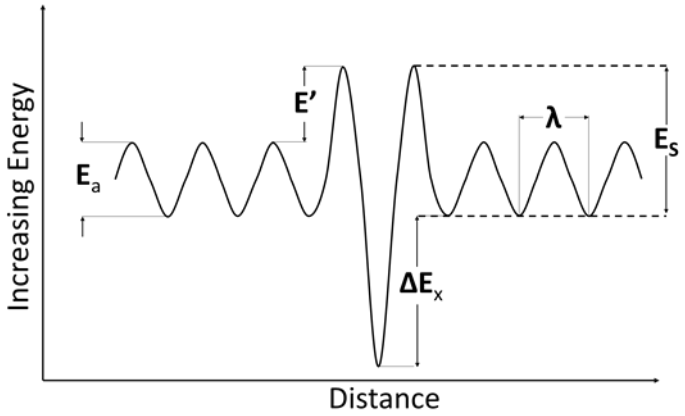

Figure 40 Schematic representation of trapping site.

Traps are classified according to their trapping energy as reversible or irreversible. Conventionally, this distinction is arbitrary and depends of course on the temperature. Reversible traps have low trapping energy. This type of trap releases the hydrogen trapped in the matrix as soon as the external activity of hydrogen decreases. Irreversible trapping sites are characterized by high trapping energy (ΔE_x); the trapped hydrogen has a very low probability of being released into the matrix at room temperature. From a kinetic point of view, the equilibrium between a trapping site and an interstitial site is defined by trapping rate (k_{LT}) and de-trapping rate (k_{TL}) constants. Knowing that $k_{LT} > k_{TL}$, the jump in the "trap towards lattice" direction is less likely. According to Pressouyre [73], reversible traps would have a trapping energy lower than 0.6 eV. Hirth suggests that trapping energy of 0.8 eV is even possible for reversibility [74].

In martensitic microstructures, the different traps are dislocations, precipitates, grain boundaries, vacancies and all the various interfaces inside the martensite microstructure (martensitic laths, blocks and packets boundaries). Figure 41 illustrates all these traps, the red dots representing the hydrogen. Their trapping energy vary from one to another. During the process of diffusion, these traps should become full of hydrogen in order to make it possible for the latter to move to the next site, which delays the hydrogen transport and reduces the apparent hydrogen diffusion coefficient [75]. This is the reason why what is measured usually during permeation tests is the apparent or effective hydrogen diffusion coefficient, and not the lattice diffusion one. However, these sites increase the solubility of the hydrogen in the defect itself as compared to the lattice or around them [75]–[77]. For instance, the core of dislocations is a deep trapping site for hydrogen while the elastic field around them is less

deep, the same for the precipitates and their interface with the matrix. The presence of these defects can be in the favour of the material by reducing the hydrogen diffusion coefficient, but it can also be detrimental for the material by being a potential region for crack initiation. The best example for that is hydrogen diffusion in plastically deformed materials, where it was seen that the higher the plastic deformation, the higher the dislocation density [69] and consequently, the lower the hydrogen diffusion coefficient [75].

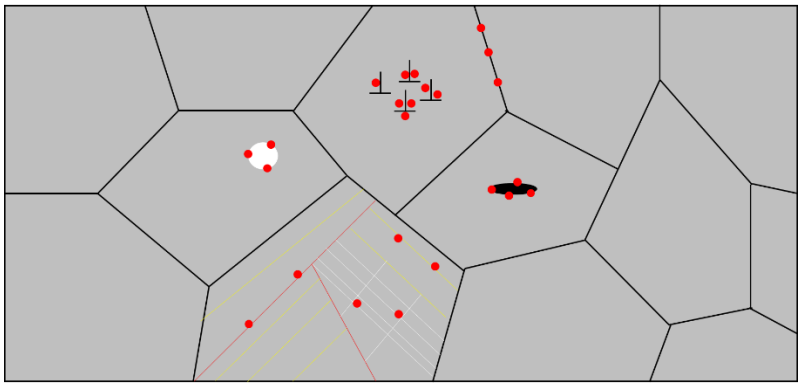

Figure 41 Potential trapping sites in the martensitic microstructure.

Experimental techniques can identify trapping sites and determine the characteristic quantities. In particular, there is tritium autoradiography and permeation and thermo-desorption techniques. The table 6 extracted from the reference [61], [78], [79], gathers some trapping energy data with a variability that depends on the method used to determine them. The trapping energies of dislocations are very close to those of γ-grain boundaries, packet and block boundaries. TiC carbides trapping energies depend on their coherency with the matrix. Given the low carbon content in maraging steels, these are not expected, although they may exist and participate in trapping. Intermetallic particles appear like weak traps with level of energies slightly higher than the ones linked to elastic fields of the crystal lattice. This indicates that $Ni_3(Mo,Ti)$ have a high degree of coherency with the matrix, particularly after the heat treatment corresponding to the peak hardness. Besides, Viswanathan *et al.* have shown from TEM microstructural examinations that the dislocation-precipitate interaction is by precipitate shearing, supporting the fact of a strong coherency of these intermetallics [54].

Table 6 Potential traps in martensitic microstructure and their corresponding energies.

Nature of the traps	**Trapping energies (eV) from** [61]
Old γ-grain boundaries	0,52
Packets boundaries	0,64
Martensite laths	0,28 0,50-0,62
Elastic field	0,28 0,36 0,3 0,2
Core of dislocation Screw dislocation Edge dislocation Dislocation (GND)	0,47-0,60 0,45 0,49 0,50-0,62
Vacancies	0,36 0,57-0,60 0,63
Interstitial site (octahedral)	0,34
Interstitial site (tetrahedral)	0,31
TiC coherent TiC semi-coherent TiC incoherent	0,3-0,4 0,56 0,68-1,4
Intermetallic particles Ni_3Mo, Ni_3Ti, FeTi	0,4* * from ref. [78], [79]

2.2.3. Intergranular hydrogen diffusion

The diffusion of hydrogen can be disturbed by the presence of microstructural heterogeneities. They have an important role in trapping but can also be at the origin of an increase in the apparent diffusion coefficient. Indeed, plane defects such as grain boundaries or linear defects such as dislocations allow in some cases to accelerate the transport of hydrogen by effects of diffusion short-circuits.

An abundant literature exists, particularly for cubic face-centered crystallographic structures. Preferential hydrogen mobility along the grain boundaries has been shown on nickel [80] while others authors have shown that grain boundaries are not high diffusivity paths [81]. Brass *et al*. studied the effect of grain size on the apparent hydrogen diffusion coefficient. They found that for smaller grains, the hydrogen diffuses faster. They related it to the fact that for smaller grains, the grain boundaries density is more important. They supposed that random grain boundaries could behave as a short-circuit for hydrogen diffusion. They determined the hydrogen diffusion coefficient in grain boundaries and calculate the ratio of $D_{Grain\ Boundary}/D_{Lattice}$ which varies between 3 to 100 in pure Nickel [80]. Yao *et al.* found nevertheless that there is a critical grain size above which no effect on hydrogen diffusion is detectable by conventional experiments; the limit in grain size they found was about 100 µm [81].

This variability of the effects seems to be related to the nature of the grain boundaries (degree of misorientation, twist or tilt grain boundaries) which depends on process forming. Simulation works have demonstrated the effects of twist and tilt grain boundaries, or the combination of both of them, on the hydrogen diffusion [82]. The work of Ichimura *et al*. on pure aluminum showed a phenomenon of acceleration of hydrogen diffusion with the decreasing grain size down to a critical size below which trapping at grain boundaries would be the predominant phenomenon [83]. Same results were obtained on polycrystalline nickel [84].

Nonetheless, the phenomenon of short-circuit by the grain boundaries does not seem to be observed when the interstitial diffusion coefficient is high as in α-iron [85], [86]. This fact may be explained by the difference between the levels of the saddle point energy at the grain boundary in bcc and fcc crystallographic structure. On Figure 42 are represented the energetic factors that explain the reversible character of grain boundaries as traps in bcc structure as compared to fcc structure [87]. The saddle point energy of hydrogen around grain boundaries in bcc is lower than the activation energies for lattice diffusion, so that trapping and detrapping of hydrogen at grain boundaries should therefore be easy. In addition, the activation energy of hydrogen diffusion inside the grain boundary is similar to that of the diffusion from a normal interstitial site to another (respectively 17.2 kJ/mole (0.18 eV) and 16.8 kJ/mole (0.17 eV) in Figure 42a. In Ni fcc crystallographic structure, the schematic diagram of energy levels for the diffusion of a hydrogen atom through a grain boundary can

be represented by Figure 42b. Trap activation energy is lower than that for bulk diffusion. The trapping effects appears thus to be weak, that is, hydrogen trapping and detrapping occur easily compared with bulk diffusion and contributes to favor intergranular diffusion.

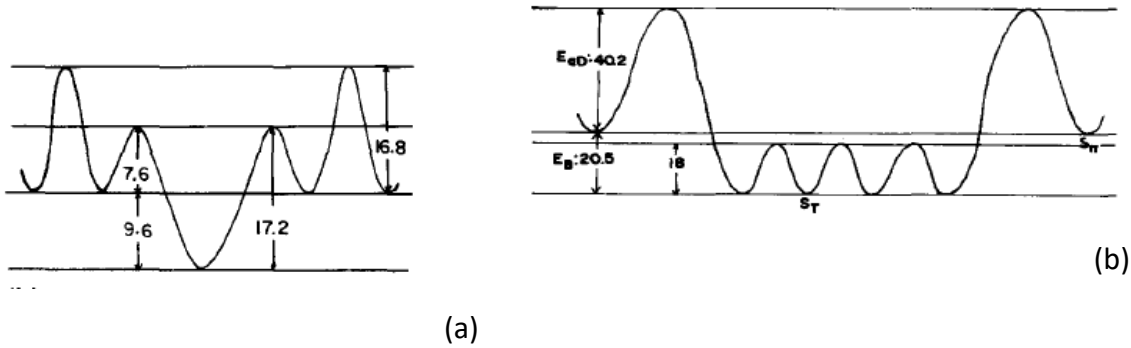

Figure 42 Energy levels of hydrogen around a grain boundary (in units of kilojoules per mole) in bcc structure (a) anf fcc structure (b) (from ref. [87]).

Short-circuit effect can also be envisaged with the hydrogen transport by dislocations. Some authors highlight the dragging of hydrogen by dislocations by varying the strain rate of a specimen pre-charged with hydrogen on steels [88] or nickel [71], [89].

Grain boundaries are categorized according to the extent of misorientation between the two adjacent grains. Low-angle grain boundaries or subgrain boundaries are those with a misorientation less than about 15 degrees. They are composed of an array of dislocations and their properties and structure are a function of the misorientation. In contrast, the properties of high-angle grain boundaries whose misorientation is greater than about 15 degrees are normally found to be independent of the misorientation. However, there are special grain boundaries at particular orientations whose interfacial energies are markedly lower than those of general high-angle grain boundaries.

The majority of boundaries are of a mixed type, combining twist and tilt boundaries and containing dislocations of different types and Burgers vectors, in order to create the best fit between the neighboring grains. If the dislocations in a boundary remain isolated and distinct, the boundary can be considered to be low-angle. If the density of dislocations is higher with reduced spacing between neighboring dislocations and even overlapping of their cores, the nature of the boundary is no longer ordered. The boundary is then considered to be high-

angle. In comparison to low-angle grain boundaries, high-angle boundaries are considerably more disordered, with large areas of poor fit and a comparatively open structure.

The excess volume of grain boundaries is another important property in the characterization. It was first proposed by Bishop [90]; it describes how much expansion is induced by the presence of a grain boundary. It is thought that the degree and susceptibility of segregation is directly proportional to it.

2.2.4. Concept of critical concentration in hydrogen

Pressouyre [91] introduced the notion of critical concentration in hydrogen. He hypothesized that cracking occurs at the tip of a defect when a critical hydrogen concentration is reached. This is the minimum hydrogen concentration from which the cohesive force becomes less than the total stress (sum of applied and residual stresses). This notion could be useful to explain the role of certain metallurgical parameters. Unfortunately, measuring the amount of total hydrogen cannot account for what is happening locally at the tip of a defect.

2.2.5. Models of hydrogen assisted cracking mechanisms

Three major classes of hydrogen assisted cracking mechanisms are described in the literature: rupture of a brittle phase (hydride), failure by reduction of cohesive forces (HEDE) and rupture by localization of plasticity (AIDE - HELP). These models are notably presented and analyzed by Lynch in a review article [32]. The model based on brittle phase failure will not be discussed here. Indeed, this model is based on the formation of hydride that cannot be formed in the type of steel studied. Hydrides are only formed in the Vb materials of the Mendeleiv periodic table and for titanium and zirconium alloys [92]. A fourth model concerns the formation and stabilization of vacancies (HESIVE).

*2.2.5.1. HEDE (**H**ydrogen **E**nhanced **DE**cohesion)*

This mechanism is based on the work of Troiano [65]. This theory is based on the fact that cathodic hydrogen introduced at the tip of crack during corrosion processes accumulates and reduces the forces of interatomic cohesion. Decohesion models are based on a basic principle: brittle fracture occurs when local stresses exceed interatomic bond forces, the latter being reduced by the presence of atomic hydrogen in the crystal lattice. By this model, it is possible

to explain brittle behaviors and it concerns both crystalline planes and grain boundaries or interfaces between two phases [93]. The accumulation of hydrogen on atomic planes or interfaces, induces a decrease in the interatomic cohesion forces, by modifying the electronic environment of neighbouring metal cations. As a result, the required stress to initiate a crack decreases. When local stresses exceed those of cohesion, a brittle fracture can occur [94]. The segregation of hydrogen along preferred planes is therefore an essential factor for the rupture according to this mechanism.

*2.2.5.2. HELP (**H**ydrogen **E**nhanced **L**ocalized **P**lasticity)*

This model proposed by Beachem and Birnbaum [28], [95] suggests that hydrogen increases dislocation mobility and locally decreases the flow stress. Located at the crack tip where the hydrostatic stresses are highest and where the entry of hydrogen into the material is facilitated by the emergence of sliding planes, hydrogen leads to a localized plastic deformation and a reduction of the critical stresses for crack initiation [96]. The phenomenon is based on the redistribution and the accumulation of the hydrogen around dislocations, which causes the increase in dislocation mobility and leads to a decrease in the elastic interaction energies between the dislocations and the obstacles. The minimum stress needed for dislocation displacement decreases. The fracture is ductile and occurs by successive shearings along the sliding planes in these softened regions. The crack may be transgranular or intergranular depending on whether the hydrogen is localized within the grains or at the grain boundaries. This idea is supported by observations that have shown ductile fractures attributable to embrittlement by hydrogen. The material does not become brittle but suffers a loss of elongation [97], [98].

*2.2.5.3. AIDE (**A**dsorption **I**nduced **D**islocation **E**mission)*

This model has been proposed by Lynch [94]. It is based on the weakening of atomic bonds at the crack tip, due to the adsorption of hydrogen. The adsorbed hydrogen at the crack tip reduces the formation energy of dislocations and facilitates their emission. Hydrogen thus has the effect of reducing the blunting of the crack by localizing the shearing [94]. Added to this is the formation and growth of micro-cavities at the crack tip, the coalescence of which causes a crack advance. The dimples resulting from this type of cracking appear smaller than those due to the ductile rupture of the material in an inert environment.

*2.2.5.4. HESIVE (**H**ydrogen **E**nhanced **S**train **I**nduced **V**acanci**E**s)*

The approach is based on the ability of absorbed hydrogen to form and stabilize new "superabundant" vacancies called "Superabundant Vacancy" (SAV) [99]–[101]. From a thermodynamic point of view, the interactions of absorbed hydrogen with the vacancies already present in the material are correlated with the formation of SAV vacancies. At room temperature, a vacancy can be a trap for hydrogen and it can trap up to six atoms of H, they are mainly localized on the grain boundaries [101], [102]. According then to the Gibbs model, the resulting vacancy-hydrogen interaction energies will decrease the vacancy formation energy. The increase in the number of formed vacancies will then lead to the formation of microcavities, generally at the level of the grain boundaries or the crack tip.

2.2.6. Hydrogen embrittlement of 18 wt.%Ni maraging steels

Generally, the hydrogen is believed not only to enhance crack propagation, but also to initiate it. The incubation of the crack caused by hydrogen was explained by several theories. Zapffe proposed for instance that a pressure could be built up enough to initiate a premature crack, and this could happen following a precipitation of the hydrogen in internal voids [103]. On the other hand, Petch and Stables suggested that hydrogen can be absorbed inside micro-cracks causing a decrease in the necessary critical stress to propagate the crack [104].

It is suggested that hydrogen cannot cause embrittlement if it is not localized in a relatively small region. However, that transport of hydrogen toward the brittle region is controlled only by the diffusion of the hydrogen. On the other hand, if the concentration of hydrogen is not high enough to initiate a crack, a precise period of time (incubation time) is necessary to cumulate and increase hydrogen concentration. Crack initiation period is then highly dependent on the hydrogen accumulation rate [105]. This is why it is more likely to trigger hydrogen embrittlement in low strain-rate tests rather than at high strain-rates, due to the short time to reach the necessary concentration in the latter.

As an illustration of hydrogen embrittlement phenomenon on high strength maraging steels, one can cite the work of Wang *et al*. [106]. Their works were focused on a TM210 maraging steel studied by slow strain rate tensile and constant load tests performed in electrolytically hydrogen chargings, and aged in various conditions to modify the reverted austenite in the

microstructure. In fact, they reported that when constant mechanical load is applied on a sample, and hydrogen is being absorbed, the concentration of the latter in the grain boundaries emerging on the surface would be on its maximum. When the hydrogen concentration reaches a critical amount in the grain boundaries, a crack will propagate following the grain boundaries taking into consideration that the cohesive strength holding two grains together would decrease. Nevertheless, if the applied load is less than the cohesive strength of the grain boundaries, even if the critical hydrogen concentration is reached, no hydrogen induced cracking would occur. When the concentration and the load applied are both critical, then a crack will propagate predominantly on the grain boundaries and lath boundaries. This will create a stress concentrated region ahead of the crack, this will also induce cracking along the lower hydrogen concentrated region (such as martensitic laths) resulting in a quasi-cleavage fracture. The stress ahead of the crack will continue to increase until the high hydrostatic stress zone will induce a crack connecting the micro-voids and resulting in a ductile dimples-like mode [106].

Other authors studied the effect of old γ-grain boundaries [107]. This reference mentioned that in a highly embrittling environement (H_2S containing aqueous environment) and for peak-aged conditions, the coarse grains-maraging steels showed intergranular mode of cracking, while in less severe hydrogenating conditions (gaseous H_2 environement), the cracking mode was quasi-cleavage fracture. For the maraging steel with fine grains, the intergranular mode was completely absent [107]. The authors explain that the change in mode of cracking is highly related to the transport paths towards the process zone ahead of the notch, and the supply of hydrogen into the plastic zone and/or the process zone.

Several parameters can affect the cracking mode in maraging steels. As seen before, hydrogen concentration is an essential factor in the triggering of crack initiation and propagation damage. The kinetics of hydrogen adsorption and then, hydrogen flux which diffuses inside the material, are strongly related to the nature of the environment and boundary conditions. The crack growth rates seems also dependent on the conditions of hydrogenation, and certainly, on the properties of diffusion inside the microstructure. Extracted from the works of Gangloff et al., Figure 43 shows intergranular fracture of a maraging steel caused by gaseous hydrogen atmosphere [108] [109]. It clearly shows the relation between the crack growth rate and the stress intensity factor where two stages can be highlighted. A first one, where the

crack propagation is very dependent on the stress intensity factor. It is explained by the fact that the damage at the crack tip is assisted by mechanical control. This stage is limited by a threshold stress intensity K_{Ith}, below which the crack growth is not explored. Then, a second stage shows the crack growth rate becomes independent of the mechanical parameters; it can be seen as a steady state stage. This can be explained by the hydrogen diffusion controlled cracking. A last part, which is not presented in most of the figures, shows the crack velocity again dependent of the stress intensity when mechanism of crack propagation are controlled by mechanical damage, close to the fracture toughness K_{IC}, with ductile mode of cracking.

These behaviors are often observed in the phenomena of environmental-assisted cracking, as mentioned in the overview of Lynch publication [94].

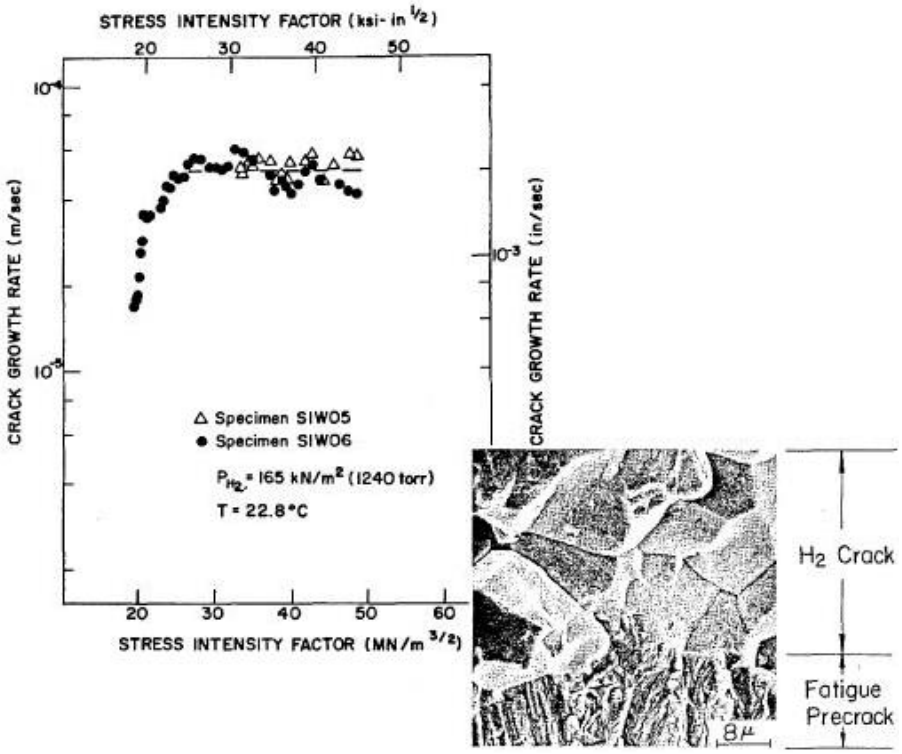

Figure 43 The crack growth rate variation with respect to the stress intensity in a maraging steel while being exposed to a low pressure hydrogen gas [109], [110].

The different effects of hydrogenating conditions and boundary conditions are well illustrated on Figure 44, which shows on the same high strength steel, but in different environmental conditions, both the level of the constant crack growth rate on the plateau and the stress intensity factor threshold. H_2S-containing aqueous environment is supposed to impose the highest hydrogen activity compare to gaseous hydrogen environment and NaCl aqueous

solution at open circuit potential. In these last conditions besides, the formation of oxide or corrosion product limits the hydrogen ingress and thus, the content inside the material. These conditions are less severe than the conditions used in pure hydrogen with higher activity.

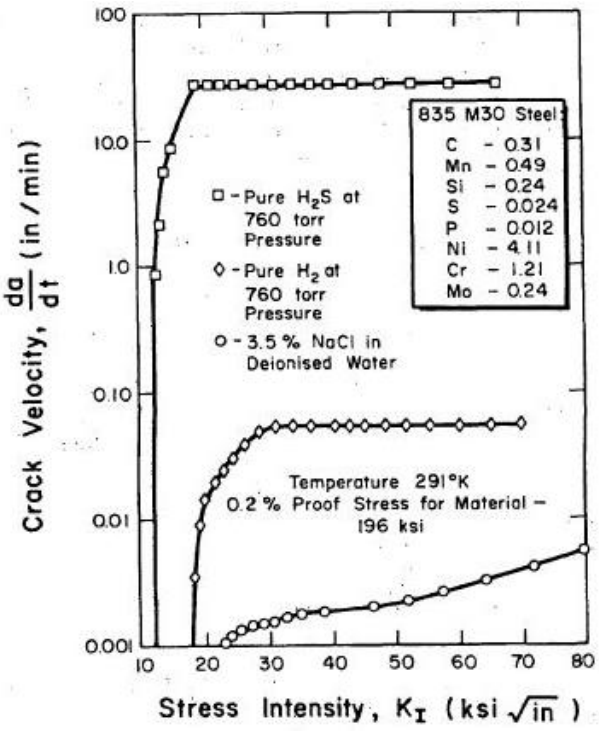

Figure 44 Crack growth rates *vs* stress intensity factors in a tempered martensitic steel in three different hydrogenating environments [111].

2.2.7. Model of hydrogen induced intergranular cracking in high strength steels

This short part is devoted to recent works on modeling of these hydrogen embrittlement processes which point out the fact that taking into account the intergranular hydrogen diffusion, and separation of these interfaces using cohesive laws, the hydrogen embrittlement can be quite well reproduced, at least on simple materials.

Benedetti *and al*. managed to model a hydrogen assisted stress corrosion cracking [36]. By applying Fick's second law to model the interfacial concentration evolution due to intergranular hydrogen diffusion, they connected the mechanical behaviour to the diffusion process and found a link between degradation of the mechanical strength of the intergranular cohesive interface by the concentration of the hydrogen.

Rimoli *et al.*, for their part, managed to model cracking in the process zone of a hydrogenated specimen [112]. They found, as seen below, a relation between the crack growth rate and the stress intensity factor similar to the experimental relation. It shows a kind of plateau where the crack growth rate increases slightly, almost independently from the stress intensity factor.

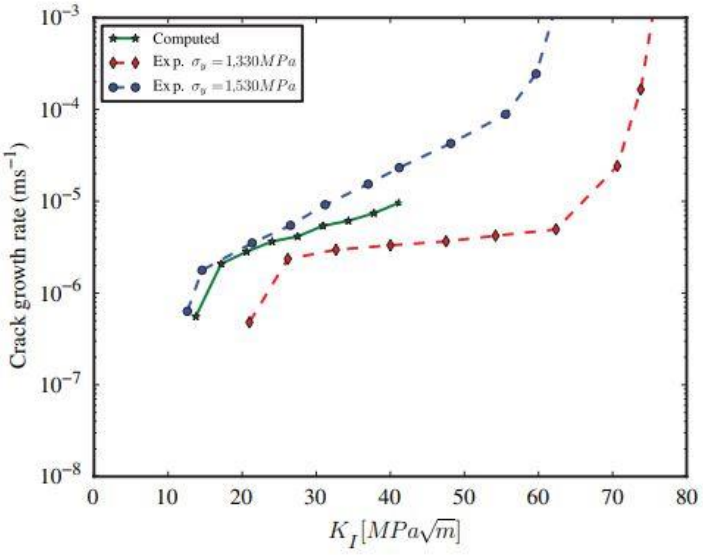

Figure 45 Crack growth rates *vs* K_I of AISI 4340 steel subjected to a constant load in an aggressive environment. Comparison of computed initiation crack-growth curves (green circles) and experimental data of Hirose and Mura [113] over a range of applied stress-intensity factors and showing the plateau.

The next paragraph presents the material chosen for the study; microstructure and mechanical properties will be presented and discussed with regards to hydrogen effects.

3. Material: microstructure and mechanical behaviour

3.1. Microstructural characterization

The studied material is a grade 350 maraging steel, provided by Aubert & Duval. It belongs to the series of 200, 250 and 300, the most common maraging steels with low carbon content and 18 wt.% Nickel, strengthened by a fine precipitation controlled at aging temperatures in the range of 450°C to 600°C. The numbers correspond to the yield strengths in ksi obtained by the aging treatment. Table 7 shows the specifications of the different maraging grades. The studied maraging steel 350 corresponds to the 12 wt.% cobalt grade. It is a vacuum melted

and consumable electrode remelted steel, with a very low sulphur and phosphorus content. Its complete chemical composition is shown in Table 8. Its yield strength at peak hardness is equal to about 2400 MPa.

These maraging steels combine high resistance and good fracture toughness in comparison with other ultra-high strength steels.

Table 7 Chemical composition specifications of maraging steel grades from 200 to 300 (%wt)

Maraging 200									
C	Si	Mn	S	P	Ni	Co	Mo	Al	Ti
<0.03	<0.1	<0.1	<0.01	<0.01	18.5	8.5	3.25	0.1	0.2
Maraging 250									
C	Si	Mn	S	P	Ni	Co	Mo	Al	Ti
<0.03	<0.1	<0.1	<0.01	<0.01	17-19	7-8.5	4.6-5.2	0.05-0.15	0.3-0.5
Maraging 300									
C	Si	Mn	S	P	Ni	Co	Mo	Al	Ti
<0.03	<0.1	<0.1	<0.01	<0.01	18-19	8.5-9.5	4.6-5.2	0.05-0.15	0.5-0.8

Due to the high content of nickel and the very low carbon content, the microstructure obtained with a natural air-cooling after solution annealing is martensitic. The steel is generally delivered under this condition to facilitate machining operations.

Table 8 Chemical composition of the grade 350 Maraging steel studied (%wt.)

Fe	C	Si	Mn	S	P	Ni	Cr	Mo	Al	Co	Cu	Ti	N
Base	0.001	0.06	<0.02	<0.0015	<0.005	17.71	0.07	4.39	0.21	12.56	0.03	1.8	0.001

Figure 46a to Figure 46d present the martensitic needle microstructure after the air-cooling of the solution annealed steel. The EBSD map where the sub-grain boundary misorientations have been chosen lower than 3° and the grain boundary misorientations higher than 15°, shows clearly the former austenite grains. Their average size, measured by image analysis software, is about 50 µm. The statistical analysis on the different components of the

microstructure shows that packets have a mean size of around 20 µm, blocks 3 µm and sub-blocks around 1.5 µm at the annealed state (Figure 47).

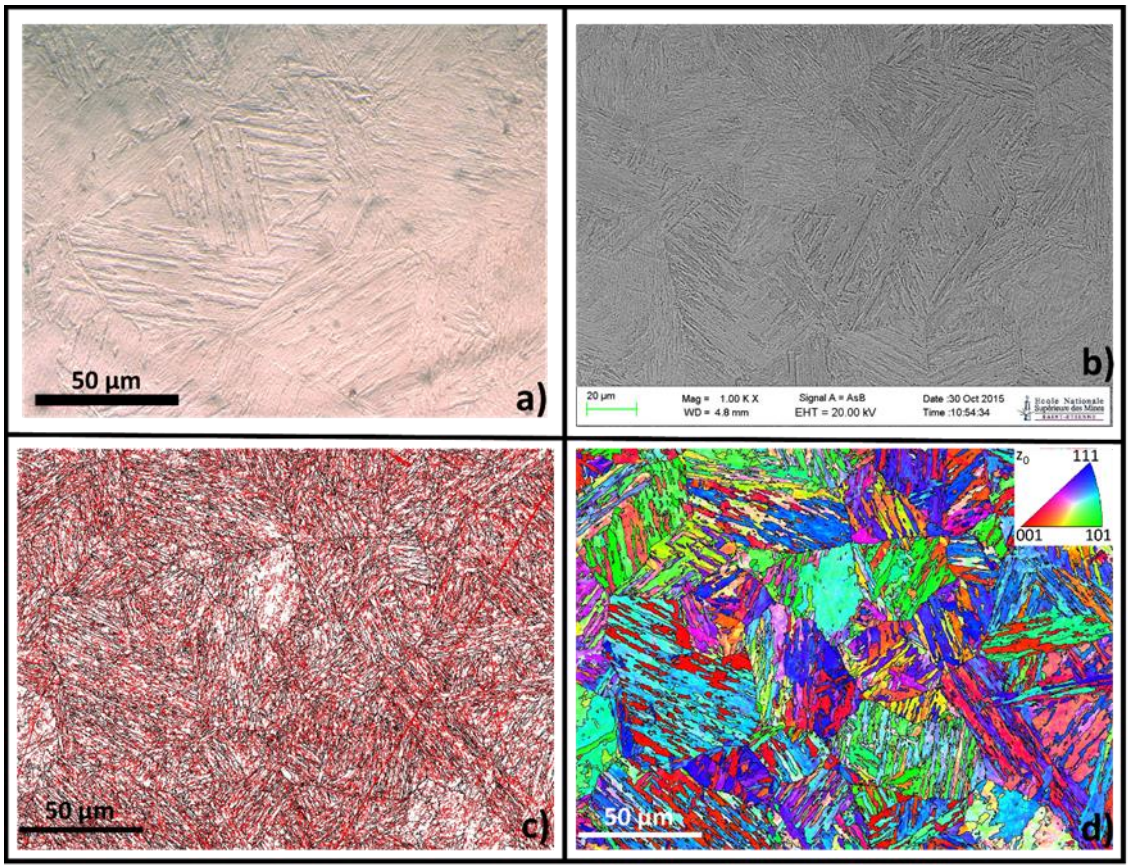

Figure 46 Microstructure of the solution-annealed steel. a) optical microscopy, b) backscattered electron microscopy, c) EBSD grain boundary and sub-grain boundary map and d) IPF EBSD map.

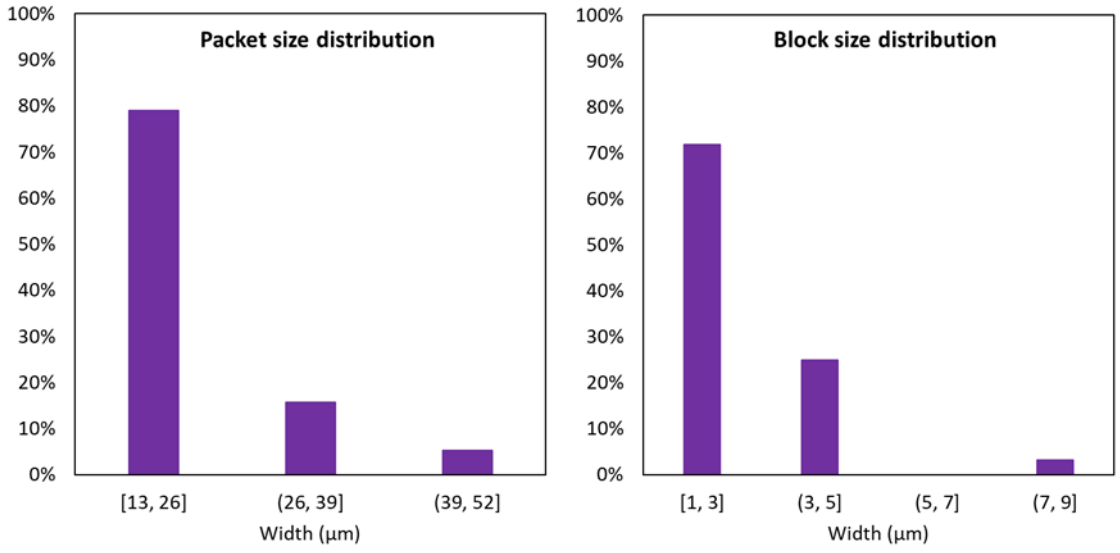

Figure 47 Histograms showing the distribution of the different sizes of packets and blocks in the as-annealed condition microstructure.

All machining operations were done in the annealed state. Then, an aging treatment of 4 hours at 510° has been performed before the last stage of cooling in calm air, as shown in Figure 48.

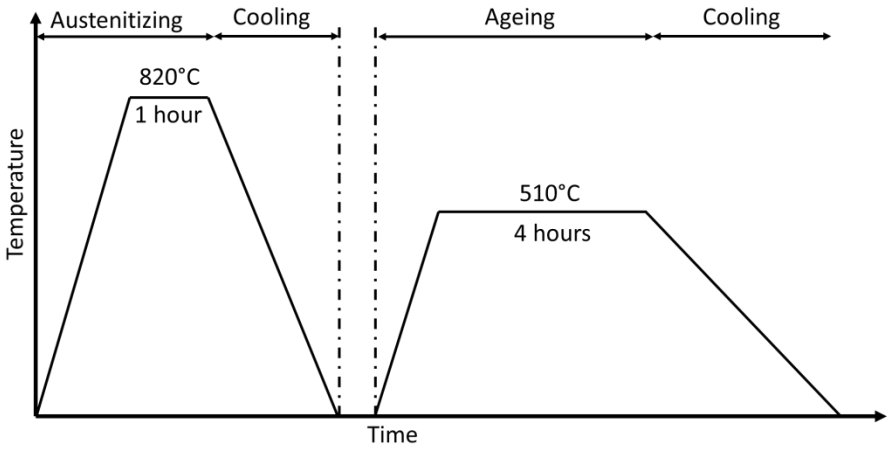

Figure 48 Heat treatement history to get Maraging 350 grade.

The standard treatment time at 510°C (950°F) is 6 hours for this steel grade, which gives the material its highest hardness while initiating the onset of over-aging, that is, austenite reversion could appear as seen in Figure 49 [55]. To avoid any formation of reverted austenite in this study, a duration of 4 hours at 510°C was preferred. Actually, no austenitic phase was detected by X-ray analysis as shown in Figure 50, even after 5 hours of aging, which is consistent with the results of H. J. Rack and D. Kalish [55].

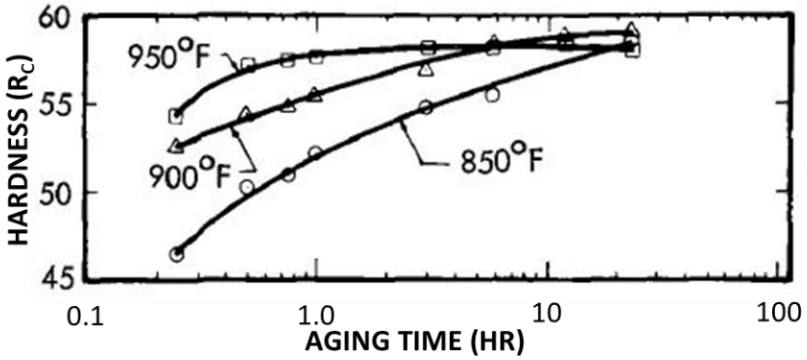

Figure 49 Influence of aging time on hardness of maraging 350 steel [55].

Due to the low carbon content, carbide precipitation is extremely low or non-existent during aging. The heat treatment leads on the contrary to the formation of hardening intermetallic precipitates such as $Ni_3(Ti,Mo)$ and Fe_2Mo [54].

The aging treatment did not change the characteristic dimensions of the components in the microstructure. Figure 51a to Figure 51d show the microstructure after aging at 510°C. The EBSD images were plotted with the same misorientation parameters for sub-grains and grain boundaries than previously. Here again, a fine analysis of the microstructure by image processing allowed quantifying the size of the different components. The mean size of former austenitic grains was found equal to around 50 µm, and the packets, blocks and sub-blocks around respectively 20 µm, 3 µm, and 1.5 µm (Figure 52). The width of the martensite laths is around 200 nm. Figure 51c and Figure 51d show the same complex microstructure of the solution annealed material on these EBSD images with the same misorientation parameters.

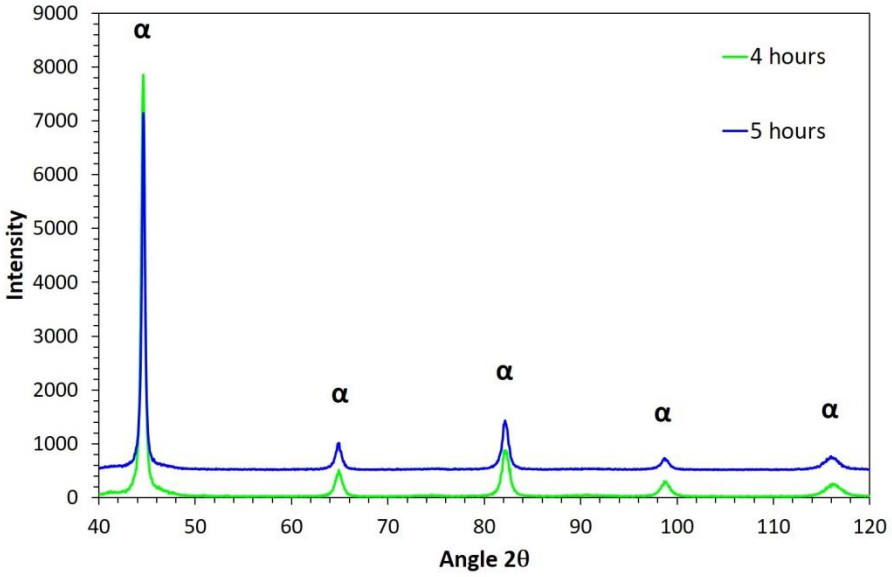

Figure 50 DRX analysis of maraging steel 350 after heat treatement durations of 4 and 5 hours at 510°C, showing the abscence of austenitic phase.

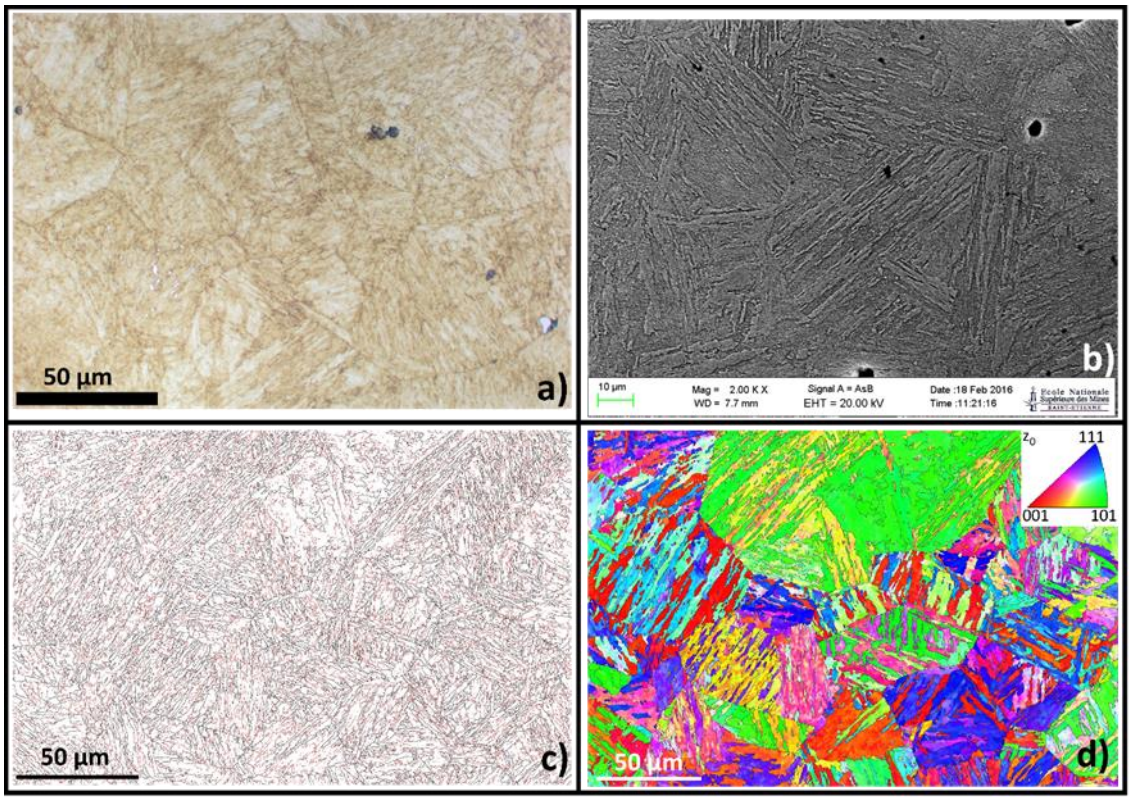

Figure 51 Microstructure of the maraging steel after heat treatment (4 hours at 510°C). a) optical microscopy, b) backscattered electron microscopy, c) EBSD grain boundary and sub-grain boundary map and d) IPF EBSD map.

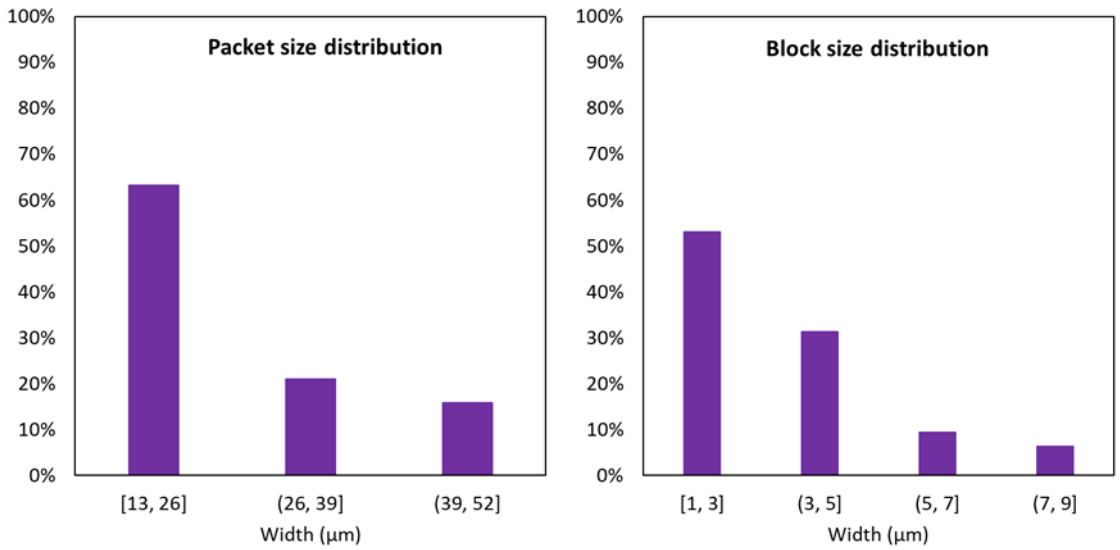

Figure 52 Histograms that shows the distribution of the different sizes of packets and blocks in the aged condition.

No specific analysis of the precipitation state at nanometric scale was done on the studied maraging steel 350. The precipitates in presence are considered to be those identified in the scientific literature previously presented.

3.2. Mechanical behaviour

The mechanical properties of the steel in solution-annealed condition are reported in Table 9. Insofar tensile tests have been carried out only after the aging heat treatment, properties for annealed condition reported in the Table 9 correspond to the specifications given by Aubert & Duval. Tensile tests were done on a 5 mm diameter and 10 mm gauge length smooth specimens, and at a strain rate equal to 10^{-4} s^{-1}.

Table 9 Mechanical properties before and after aging heat treatment of 4 hours.

	solution-annealed condition (A&D specifications)	**after aging heat treatment**
Heat treatment	820°C + air-cooling	510°C/4 hours + air-cooling
$R_{p0.2\%}$ (MPa)	817-895	2413
UTS (MPa)	1102-1158	2600
Elongation, %	15-16.9	3.5
Area reduction, %	71-82	-
Hardness, HV	329-373	-

Stress-strain curve

The stress *vs* strain curve is reported on Figure 53. It shows the very high mechanical characteristics of the steel but also its low work hardening ability. Compared to the solution annealed state, the material after 4 hours-aging at 510°C shows remarkable increase in the yield and tensile strength while uniform elongation at UTS and total elongation decrease drastically from around 16% to 3.5%.

From a general point of view, the mechanisms contributing to the stress of metallic materials are: the lattice and solution shear resistance $\tau_{l.s}$, the precipitate shear resistance τ_p and the dislocation shear resistance τ_d. The relation which expresses the flow strength s is an additive contribution of each of these elements:

$$s = m_T.\tau_t + s_b \qquad \text{where } \tau_t = \tau_{l.s} + \tau_p + \tau_d \tag{15}$$

m_T is the Taylor factor, τ_t the total shear resistance, and s_b the additional grain boundary resistance. In 300 maraging steel, P.J. Raboin and al. [114] have shown that the solute concentration containing both interstitial and substitutional elements contributes in 38% of the tensile strength. The precipitate shear resistance which is optimized when both particle width and fraction of intermetallic phases containing Mo and Ti reach optimum values ([49]–[51], [53]) contributes to 51% of the total flow strength for maraging steel 300 [114]. On the contrary, the flow stress contribution due to dislocation shear resistance is quite low. Raboin and al. have estimated it to only 4% by considering the difference between the tensile and the yield strength [114]. This is mainly due to the initial high dislocation density. L.F.P. Van Swam and al. have measured a dislocation density of 10^{15} to 10^{16} m^{-2} after only 0.1% plastic strain on a 300 maraging steel [115], while it is only around 10^{15} m^{-2} at 10% of total deformation on a quenched and tempered low alloy steel [62]. For comparison, the dislocation density in pure α-Fe is in the range of 10^{13}-10^{14} m^{-2} for plastic deformation of 37% [116], [117]. Transformed martensite thus contains an initial high dislocation density, which actually does not increase much with additional plastic deformation and therefore does not participate a lot in increasing the flow strength.

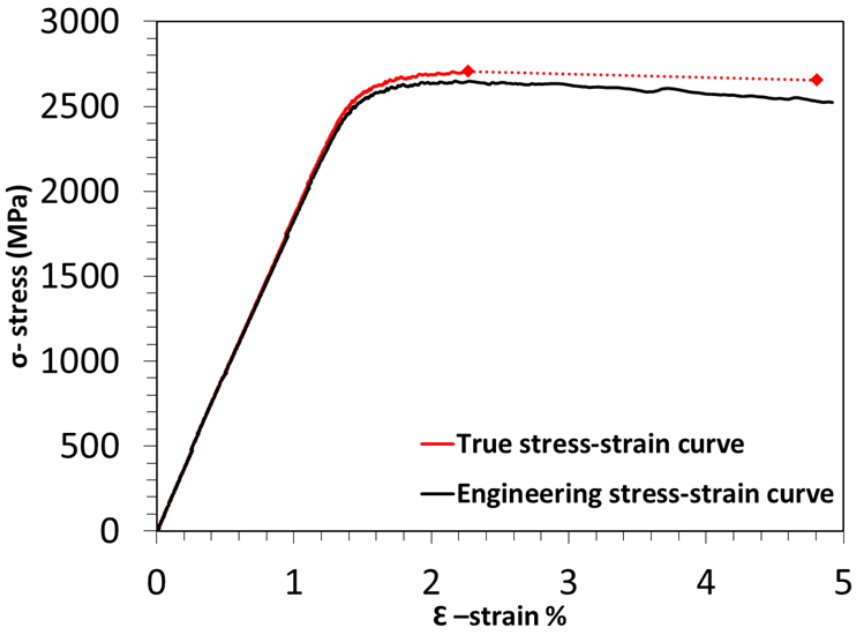

Figure 53 Stress vs strain curve for tensile test at strain rate of 10^{-4} s^{-1} on smooth specimen.

The precipitate shear resistance is given by the Orowan-Ashby equation [118]–[120]:

$$\tau_p = \left(\frac{0.538Gb\sqrt{f_v}}{2R}\right).\ln\left(\frac{R}{b}\right) \ \text{(mode I)} = cGb/\lambda \ \ \text{(mode II)} \qquad \textbf{(16)}$$

where G is the shear modulus, b is the Burgers vector, f_v is the volume fraction of precipitates, R is the radius of the precipitate, c is a correction coefficient and λ is the precipitate spacing. In maraging steels, the nanoscale precipitates are the main contributors to strength. The two mechanisms through which the dislocations can move across them are shearing (mode I in the equation (16) and by-passing (mode II) based on radius and inter-particle spacing, as illustrated in Figure 54.

If R/b < 15, the dislocation moves by shearing the precipitate, where f_v and R are the dominant factors influencing the strength. If R/b ≥ 15, the dislocation moves via by-passing the precipitate forming a dislocation loop around the precipitate, where λ is the dominant factor influencing the strength [121]. Considering the system {110} <111> for gliding dislocations in the CC martensite matrix, the Burgers vector b is equal to 0.24 nm. R. Tewari *et al* have measured the size of spherical hardening precipitates equal to about 10 nm for aging treatment duration higher than 4 hours [53], while Viswanathan *et al* showed that the average precipitate size was found to be around 40 nm long and 2.5 nm thick [54]. Without having been able to measure the size of the precipitates on our study material, we can thus consider that the two modes of hardening are possible, each one modifying the microstructure with regard to the trapping of hydrogen.

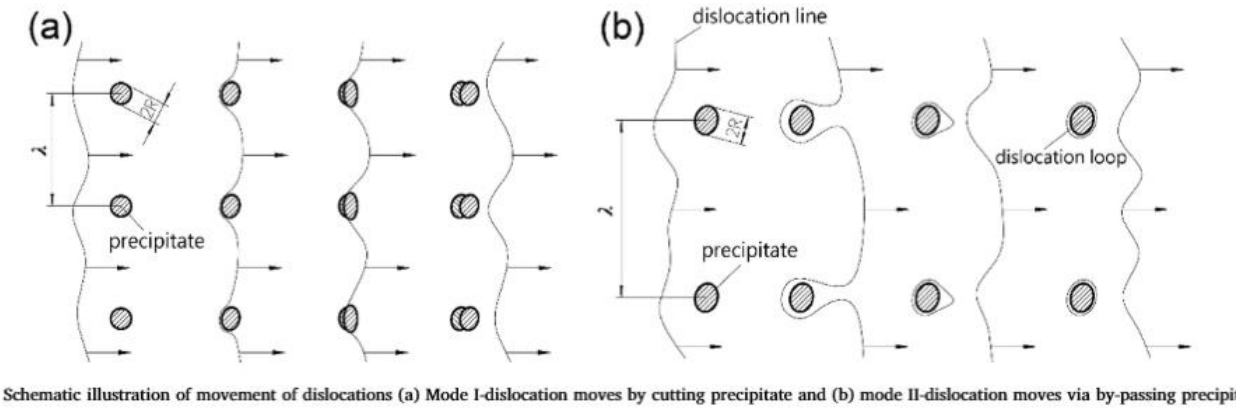

Schematic illustration of movement of dislocations (a) Mode I-dislocation moves by cutting precipitate and (b) mode II-dislocation moves via by-passing precipi

Figure 54 Illustration of dislocation movement (a) by shearing the of precipitates (mode I) and (b) via by-passing precipitates (mode II) [121].

The true-stress vs true-strain curve shows a first stage where the work hardening rate decreases with increasing strain, and then a second stage where it is constant or slightly increasing. The second stage is attributed to the contribution of nanoscale precipitates on uniform deformation, while the first stage is associated with the deformation of the martensite matrix [121]. The high density of nanoscale precipitates plays an important role in uniform deformation because of a near homogeneous distribution of precipitates in the matrix. Furthermore, the high coherency of nanoscale precipitates with the matrix makes difficult for the dislocation to cut or by-pass the precipitates. The ultrahigh strength and toughness of maraging steel is obtained via a high density and low lattice misfit nanoscale precipitates with the martensite matrix. The presence of the nanoscale particles in the ductile matrix hinder the movement of dislocations for long distances, but they retain the freedom of motion for local displacements (between particles).

Fracture surface analysis

Figure 55 shows a general view of the fracture surface of the specimen. The fracture shows a ductile character. Firstly, we can observe a macroscopic shearing zone all around the specimen, with a 200 µm width. At higher magnification, little dimples are clearly visible and attest of the ductile fracture of the maraging steel. They are very small, about 0.5 to 1 µm in diameter, but no precipitate is visible even at very high magnification. It must be notified that some smooth facets are also seen on the fracture surface and can be the result of fracture along shearing plans (Figure 55c and Figure 55d).

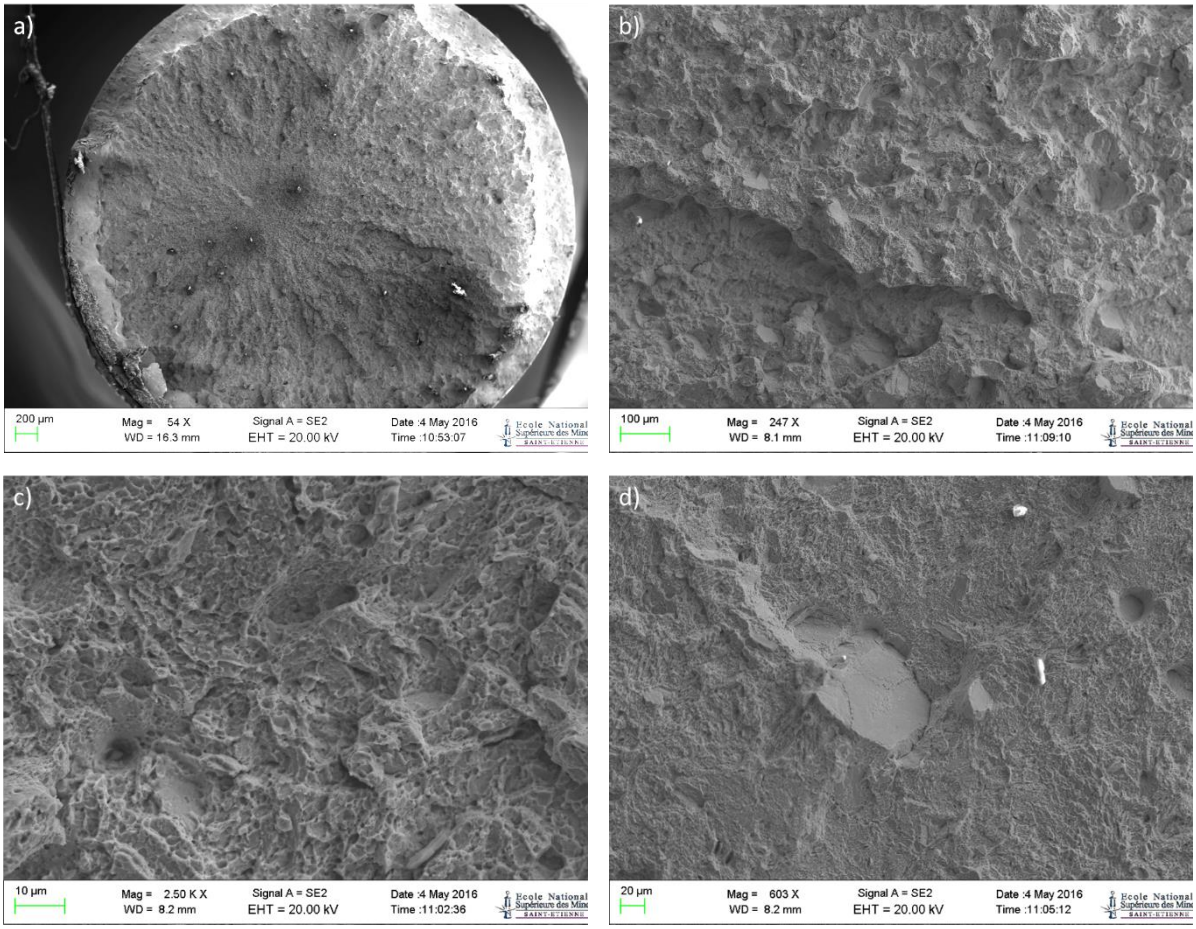

Figure 55 Fracture surface of the smooth tensile specimen at various magnifications.

4. Experimental procedures

4.1. Mechanical tests under hydrogenating environment

The mechanical tests were performed to discriminate the different mechanisms involved in the H-induced damage in the maraging steel. They consist firstly of estimating the "intrinsic" brittleness of the steel in the presence of trapped hydrogen using resilience tests (Charpy-toughness tests), where no effect related to the diffusion of hydrogen is expected. The examination of these tests gives data on the fracture energies and the modes of cracking. Secondly, to exacerbate the hydrogen/plasticity interactions, the susceptibility to hydrogen embrittlement was assessed using slow tensile tests on notched specimens at sufficiently low strain rates with respect to the hydrogen diffusivity. The notch makes it possible to favour the hydrogen plasticity interactions at its tip and allows estimating crack growth rates more easily insofar only one crack is initiated. Fracture stress and mode of cracking are also examined from these tensile tests. Finally, delayed fracture tests have been performed using either constant load tests at various loadings, or constant displacement tests on notched specimens also.

4.1.1. Specimens

- **Charpy tests**

Fracture toughness tests were done using Charpy hammer shown in Figure 56. These tests were carried on samples cathodically hydrogen-precharged at different durations, the hydrogen content increasing with time. The geometry of the sample is not standardized in the sense that they have smaller size to keep the same diffusion distance from the surface to the bulk than axisymmetric specimen. They are of parallelepipedic shape of square section 5x5 mm^2 and length 48 mm, with a V-notch of depth 1 mm and an angle of 45° as shown in Figure 57. The hydrogen charging was performed at cathodic potential E_c=-1200mV/SCE in a 30 g/L NaCl solution using the same device shown Figure 4 for SKPFM study. Four hydrogen charging different durations were applied: 4, 13, 24 and 48 hours, the reference test being on a no H-charged specimen.

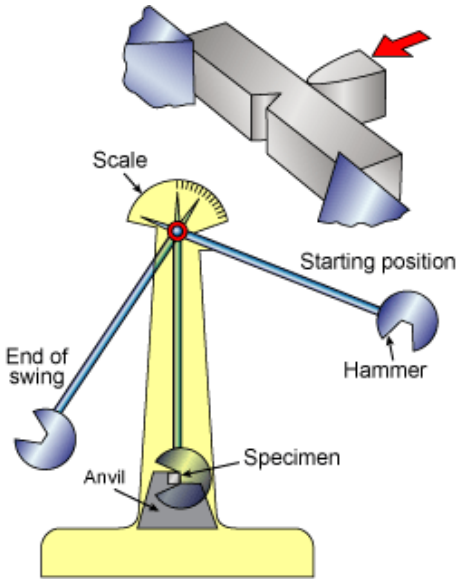

Figure 56 Pendulum impact tester for Charpy tests [122].

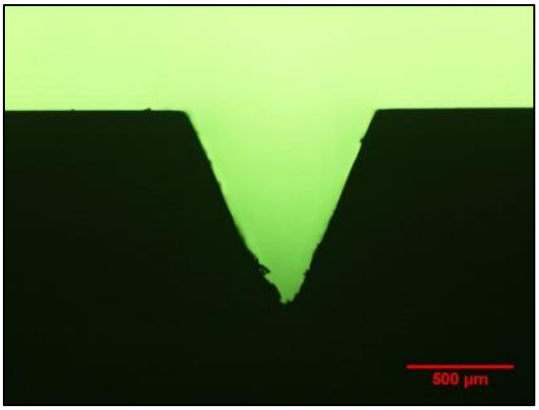

Figure 57 Profile of the Charpy-V notch specimen.

- **Tensile tests: slow strain rate tests and constant load tests**

Figure 58 shows the geometry of the axisymmetric notched tensile test specimen with dimensions in mm. The notch has an angle of 45°, 1 mm depth, and a tip-radius of 0.4 mm, less severe than the sharpy V-notch specimen. The specimens were machined before the aging treatment, so that no strain hardening in the notch tip persists thereafter.

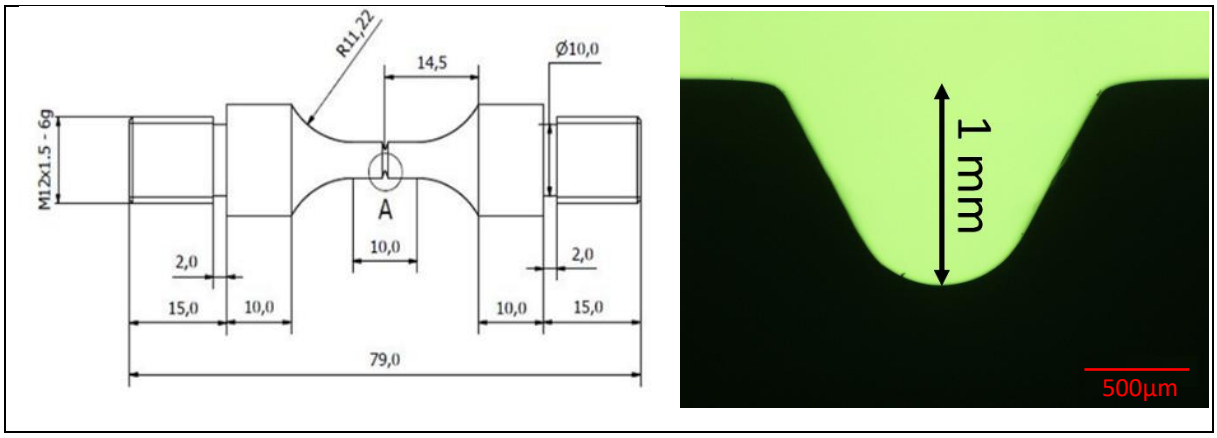

Figure 58 Dimensions of the tensile sample in mm and a magnification of the notch.

The notch was designed in a way to optimize the stress concentration factor K_t and stay under the yield strength of the steel at the tip of the notch for some of the tests. According to Peterson's [123], the stress concentration factor k_t for a tension bar of circular cross section with a U-shaped groove to the dimensions of our test specimen is around 3. The displacement rates for slow tensile tests were ranged from 10^{-3} to 10^{-6} mm.s^{-1}. The effect of a pre-deformation was explored on a slow tensile test at 10^{-5} mm.s^{-1}.

The same design of specimen was used for constant load tests. Three levels of load were applied for these tests were: σ = 1500, 1000 and 550 MPa, where σ is F/So, So is the section of the specimen to the right of the notch, F the load applied.

For these series of tests, two different ways of hydrogen charging were used. For some tests, a protective silicone layer was applied at the bottom of the notch to isolate it from direct cathodic hydrogen charging, while for others, no protection was used (see next paragraph § 4.1.3).

- **Constant displacement test**

Only one test was done in these conditions. Figure 59 shows the geometry of the notched sample that was used. The notch was done with a wire saw using a 150 µm-diameter wire on 1 mm-depth. This type of notch aims to apply the most sever conditions by approaching a crack geometry. The sample was mirror polished from all its sides, then a constant displacement of 12 µm was applied by two screws as seen in the Figure 59. This displacement was previously determined on the same sample and corresponds to a loading of 500 MPa on the ligament remaining between the two symmetric notches (loading of 7.5 kN on the 15 mm^2-

remaining section). The sample was then immersed in 30 g/L NaCl solution and a cathodic potential of -1200 mV/SCE was applied. Hydrogen-assisted cracking was initiated and has propagated on a part of the section. The specimen was finally mechanically opened to perform fractographic analysis.

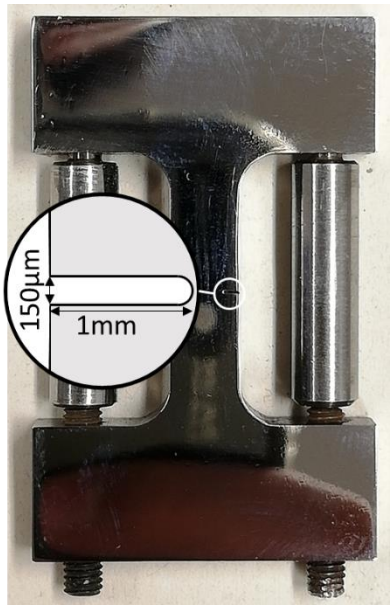

Figure 59 The specimen used to perform constant displacement test.

4.1.2. Machines used and assemblies

- **Tensile machines**

The tensile machines used are four columns electro-mechanical machines INSTRON controlled by a position control loop. After the sample is mounted, the top part of the machine stays fix while the traction is achieved by moving the crosshead down at the targeted displacement rate. The displacement of the sample is measured usually by an extensometer (which was done for tensile test in air on the smooth sample) which allows measuring the deformation of the gauge length of the test specimen. However, it was not possible to install one on the notched samples cathodically H-charged, due to the fact that the tests are held in an aqueous solution. This is why LVDT sensors were used in these conditions with a range of measurement of $\pm 1\ mm$ (Figure 60). The loading conditions for these tests are given by referring to the displacement and displacement rate applied. Then, finite element calculations estimate for each condition the corresponding strain rate at notch-tip (see below section 5).

The displacement rates explored for tensile tests are: 10^{-3}, 10^{-4}, 10^{-5} and 10^{-6} mm/s.

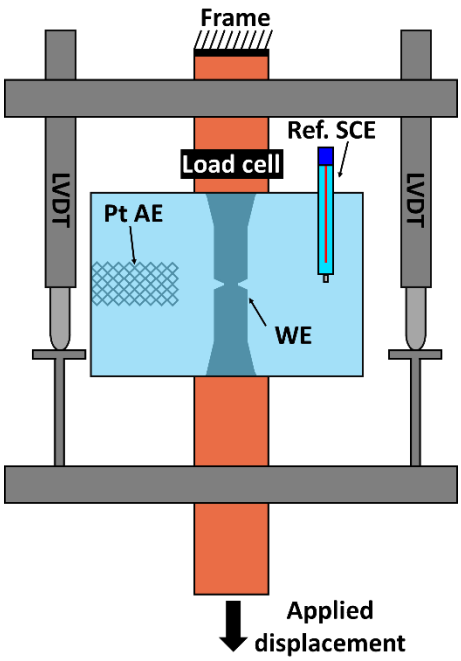

Figure 60 Assembly of the tensile test under hydrogenating conditions.

- **Constant load tests**

The constant load tests were held using a compression ring load cell (Figure 61). The load was applied gradually with a rate of 1.2 kN/min. Once the load value is reached, a delay of two hours is left before the load is readjusted again and the test itself is started. During this delay, one could note a slight decrease of the load, corresponding to a stress relaxation. Deaeration of the cell was done during the delay time using flux of nitrogen gas. Then, cathodic charging started using the same environmental conditions and applied potentials as the ones used for the slow strain rate tensile tests.

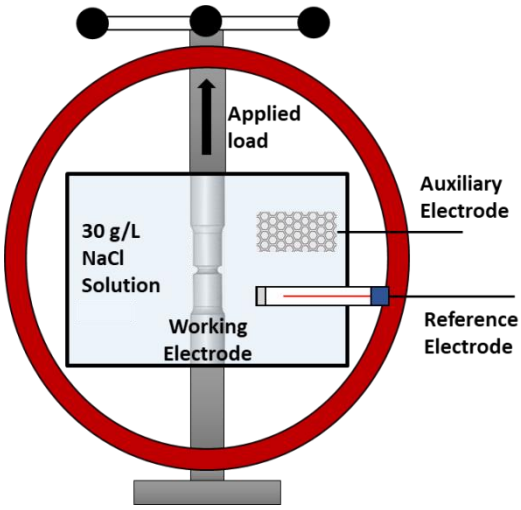

Figure 61 Constant load test assembly.

4.1.3. Experimental procedure for hydrogen cathodic chargings.

In order to evaluate the cathodic potential for hydrogen charging, a polarization test was done on the maraging steel in a 30 g/L NaCl solution. Figure 62 shows the curve done at 1 mV/min scan rate. One can see in the range of -300 to around -900 mV/SCE, the plateau corresponding to the reduction of oxygen, then the cathodic branch related to the hydrogen evolution reaction. The cathodic potential chosen is E_c=-1200 mV/SCE which ensures a proton discharge current of about 1 mA/cm^2 in the kinetic control domain of the reaction.

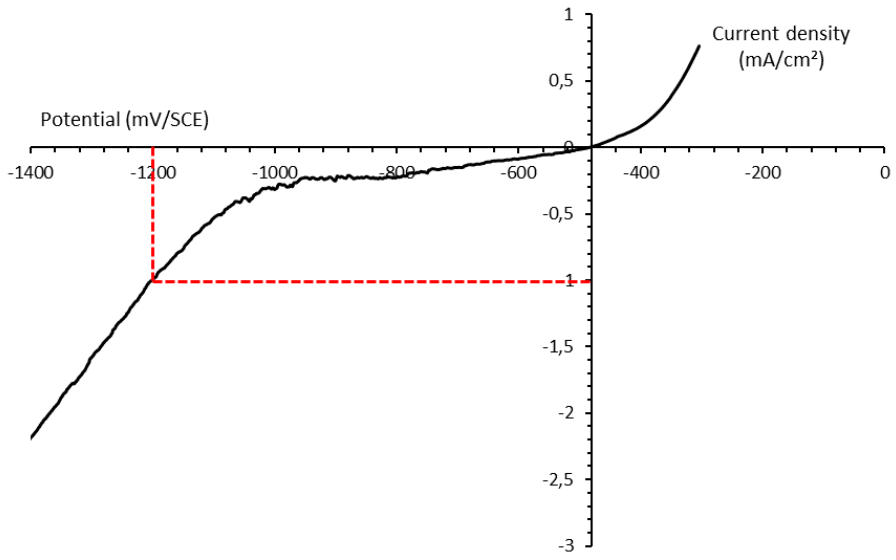

Figure 62 Polarization curve of the grade 350 maraging steel in a 30 g/L NaCl solution at ambient temperature.

- **Specimen surface preparation for hydrogen**

To separate the effects of hydrogen adsorbed on the notch surface, and diffusing in the process zone, from the one provided only by the bulk around the process zone, two different preparations of the samples were proposed for mechanical tests (Figure 63). The first corresponds to the exposition of all the free surface of the sample (Figure 63a), in which the hydrogen can penetrate from all the surface, including the notch. The second corresponds to the deposition of a silicon protection on the total surface of the notch (Figure 63b). In the latter case, no direct entry of hydrogen is possible at the bottom of the notch. The hydrogen that reaches the zone comes from diffusion from the surface of the sample.

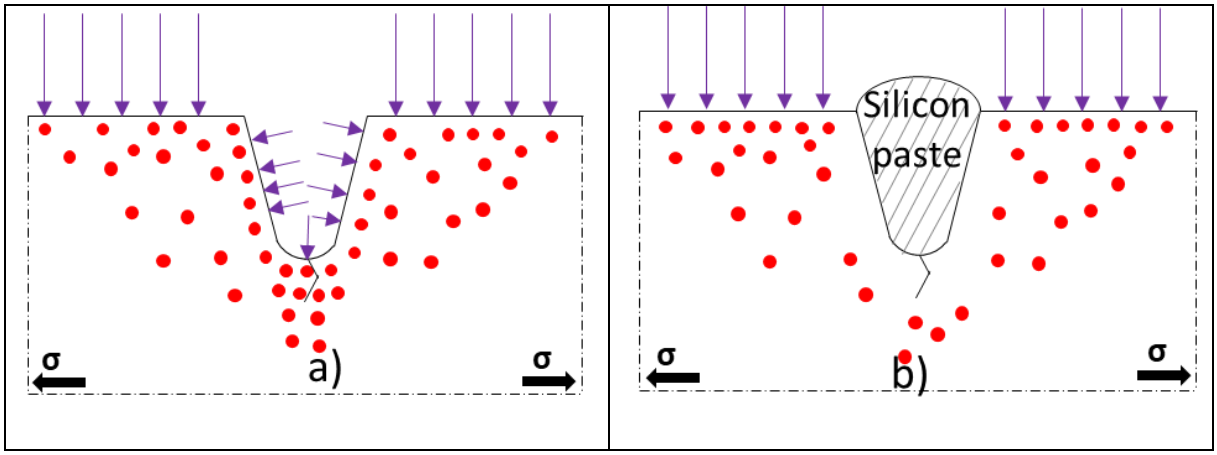

Figure 63 Two types of hydrogen charging, a) with uncovered notch, b) protected notch with silicon paste.

4.1.4. Grid of mechanical tests.

All the mechanical tests and their parameters for environmental conditions are shown in the following Table 10:

Table 10 List of mechanical tests and their parameters.

Charpy tests				
Duration of H-precharged at E_c=-1200 mV/SCE				
0 h	4 h	12 h	24 h	48 h
X	X	X	X	X

Slow displacement rate tensile tests				
Displacement rate V_t (mm/s)	Air	H-precharged 24h at E_c=-1200 mV/SCE + Cathodic H-charging during tensile test		H-precharged 24h at E_c=-1200 mV/SCE + Tensile test in air
		Unprotected surface notch	Silicon protected surface notch	
10^{-3}	X	X	-	-
10^{-4}	X	X	-	-
10^{-5}	X	X	X	X
10^{-5} (after a pre-strain)	-	X	-	
10^{-6}	X	X	X	X

Constant load tests			
Applied load (MPa)	Air	Preloading in air + Cathodic H-charging during loading	
		Unprotected surface notch	Silicon protected surface notch
550		X	
1000		X	X
1500	X	X	X

Constant displacement test		
Displacement (mm)	Air	Preloading in air + Cathodic H-charging during loading without silicon protection
12 (corresponding to initial loading of 500 MPa)	-	X

4.1.5. Fracture surface analysis

After the mechanical tests, fracture surfaces and modes of cracking were characterized with a ZEISS SUPRA scanning electron microscope. Crack paths were also studied on cross sections; additional EBSD analysis on these cross sections complete these examinations.

Different features appeared on fracture surfaces as a function of the loading and environmental conditions. They were quantified by image treatments and measurements of their surface fractions (for instance, intergranular and transgranular mode of cracking). These analyses were based on a reference surface of 0.5 mm^2 for each specimen.

It allowed to distinguish subcritical cracking induced by environment from mechanical final rupture. The mean crack growth rates corresponding to environmental effects were estimated by dividing the subcritical crack length to the total duration of the tensile test. This approximation could be made since the initiation of the crack occurred very early compared to the total duration of the test. Crack length measurements were done using the ImageJ software.

4.1.6. Calculation of stress intensity factor.

Some tests were analysed by considering not only the fracture load, but also the stress intensity factor K_I, taking into account the crack length measured post mortem on the fracture surface. The calculation of K_I is based on the work of [124], [125]. From an axisymmetric notched specimen model, the authors proposed the following equation (17).

$$K_I = \Sigma * (\pi a)^{1/2} * Y(a, D_0) \quad \textbf{(17)}$$

$$\Sigma = 4F/\pi D_0^2 \quad \textbf{(18)}$$

where Σ represents the stress far from the notch (equation (18)), D_0 the diameter of the specimen, Y the dimensionless function (equation (19)). In our case D_0=5 mm (D_{net}, the net diameter of the sample at the notch tip is equal to 3 mm). The equation of *Y (a, D_0)* is:

$$Y(a, D_0) = \frac{1.121 - 3.08(a/D_0) + 7.344(a/D_0)^2 - 10.244(a/D_0)^3 + 5.85(a/D_0)^4}{[1 - 2(a/D_0)^2]^{3/2}} \quad \textbf{(19)}$$

where a is the crack length measured experimentally, including the initial notch length [125].

These values will be compared to the plain strain fracture toughness K_{IC} found in the work of several authors. For recall, these values ranged from 30 to 55 MPa√m according to [55], [126]–[128].

4.2. Characterization of the material with respect to hydrogen

Diffusivity and solubility of the hydrogen in the material were estimated using electrochemical permeation method, and direct hydrogen content measurements by total fusion.

This paragraph explains the experimental procedures for permeation tests and the calculations performed.

4.2.1. Electrochemical permeation tests

- **Experimental setup and specimen preparation**

Permeation tests were performed using a Devanathan cell as represented in Figure 64. The experimental protocol is based on two cells, one is called “Entry cell”, by which hydrogen is introduced by imposing a cathodic potential. The other cell called “Exit cell”, where hydrogen is oxidized by imposing a slightly anodic potential around +50 mV/OCP (OCP=Open Circuit Potential). Both cells contains a 0.1 M NaOH solution.

The samples were initially cut from a 20 mm diameter rod of raw material. The samples had at the beginning 500 µm thickness. They were mirror polished before aging as mentioned before and then polished with finishing step to remove the oxide layer. The polishing was done on both faces of the sample, starting with a polishing paper of P600 and finishing with 1 µm-diamond paste and with silica. The final thickness was around 335 µm.

The face that was used to detect hydrogen was then cleaned and dried very well and coated with around a 50 nm layer of palladium to avoid any potential evolutions of the surface that

might affect the measurements, and then a nickel wire was welded on it to make the electrical contact in a part outside the cell.

The two faces of the sample are plugged to the working electrode connection. In each cell, the auxiliary electrodes were made of sheets of platinum and the reference electrodes used were saturated calomel electrodes (SCE).

- **Experimental procedure**

Permeation tests were held in a 0.1 NaOH solution both in the half-cells, in the charging and detection sides. In order to choose the potentials of cathodic polarization and anodic oxidation of hydrogen, a polarization test was done on the maraging 350 steel in the solution. Figure 65 represents the polarization curve done with a 1 mV/min scan. The open circuit potential is measured to be -420 mV/SCE, several cathodic potential were chosen to perform the hydrogen charging: -1200; -1300; -1400; -1500 and -1600 mV/SCE. These potentials were chosen in order to perform a test with several step of transitory phases and steady stages. It will allow to determine several hydrogen diffusion coefficients, each one by increasing the potential approaching the lattice diffusion coefficient [18].

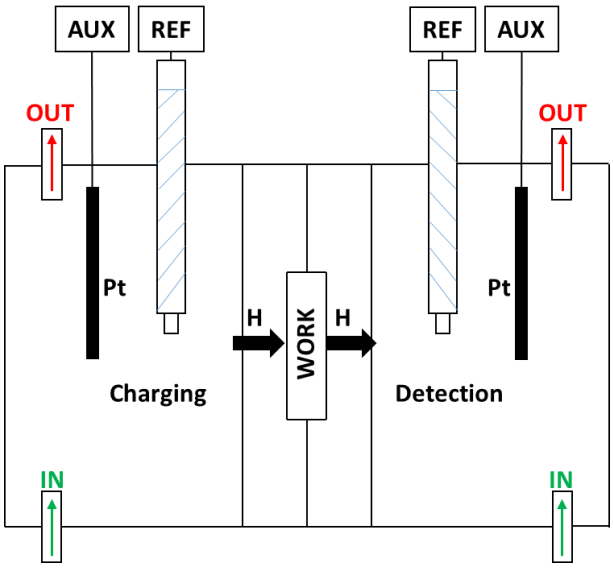

Figure 64 Schematic representation of the electrochemical permeation cell used.

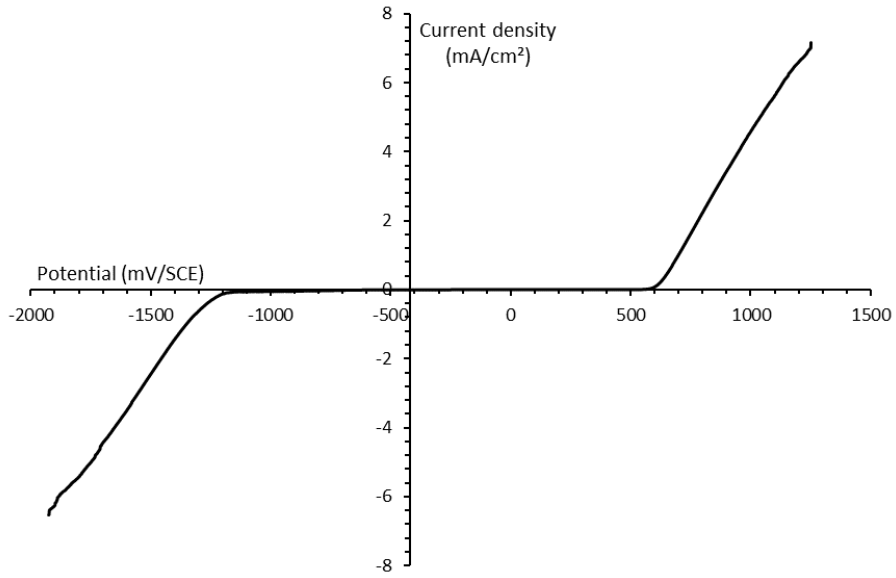

Figure 65 Polarization test done on the 350 grade maraging steel in a 0.1 NaOH solution.

After mounting the sample as a working electrode, the detection side was filled with solution and the open circuit potential (OCP) was measured on the Pd-coated side. Then a potential equal to OCP+50 mV/SCE was applied to slightly anodize the sample and allow the hydrogen oxidation when it will reach the surface. In our case the value was around +30 mV/SCE. Then the charging cell was filled and the program was launched.

4.2.2. Determination of the diffusion properties

Using this experiment, diffusion coefficient and hydrogen surface concentration were determined. These parameters can be calculated by using data extracted from the curve of the current density as a function of time (Figure 66).

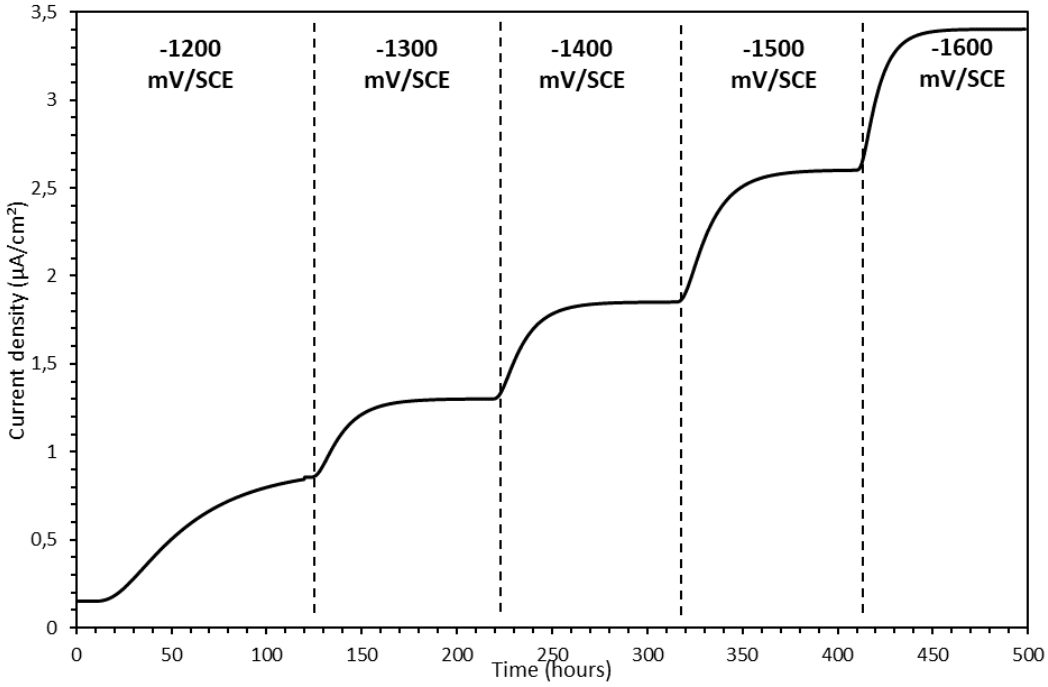

Figure 66 Permeation transients performed on a Pd-coated sample for different cathodic potentials.

Based on the results obtained and shown in Figure 66, and by applying the time lag method according to the standard ISO 17081:2004 [129], the apparent hydrogen diffusion coefficient and hydrogen surface concentration were calculated according to equation (20) and equation (21):

$$D_{eff} = \frac{L^2}{6t_l} \quad \textbf{(20)}$$

$$C_H = \frac{I_\infty L}{FD} \quad \textbf{(21)}$$

where D_{eff} is the diffusion coefficient, L is the thickness of the sample, t_l is the time lag value (time corresponding to the value of 63% of $I_\infty - I_0$ interval), I_∞ is the steady state current density, I_0 the initial current density and F is the Faraday constant.

Table 11 shows the diffusion coefficients and the surface hydrogen concentration calculated from different transients. It presents also the overpotentials ($\eta[V]=E_c-E_0$) where E_c is the applied cathodic potential and E_0 is the open circuit potential.

Table 11 D_H and C_H values extracted from the permeation tests shown on different increasing overpotentials

Potential (V/SCE)	Overpotential (V)	I_∞ (µA.cm^{-2})	D_{eff} (m^2.s^{-1})	C_H (mol.m^{-3})
-1.200	-0.777	0.912	6.38x10^{-14}	0.0439
-1.300	-0.877	1.300	1.90x10^{-13}	0.0210
-1.400	-0.977	1.850	2.02x10^{-13}	0.0281
-1.500	-1.077	2.600	1.80x10^{-13}	0.0443
-1.600	-1.177	3.400	2.80x10^{-13}	0.0373

The average diffusion coefficient is equal to D_{eff} = 1.83x10^{-13} m^2.s^{-1}.

Several transients of permeation were performed with increasing cathodic potentials. This method results in filling all possible traps and allows approaching a lattice diffusion coefficient.

4.2.3. Hydrogen content measurements

Hydrogen contents introduced during various hydrogen charging were evaluated by the total fusion method; the outgoing hydrogen flow was measured by catharometry. The specimens used were machined as cylinders 6 mm in diameter and 6 mm in height. Various conditions of hydrogen charging were explored:

- no H charging,
- H cathodically charged for 24 hours,
- H cathodically charged for 24 hours followed by 12 hours of storage in dry air.

These measurements were done twice. The Table 12 shows the average value.

Table 12 Hydrogen content measurements.

Charging conditions	No H charging	H charged 24 hours	H charged 24h followed by 12h dry air storage
mass ppm	0.62	1.9	1.06

5. Numerical simulation of the mechanical behavior of notched specimen

5.1. Constitutive relation

In this section, a numerical simulation of the mechanical behavior of the tensile notched specimen is done in order to have a better assessment of the mechanical quantities in the vicinity of the notch tip according to the various loadings applied during the tests. The software used in this case is COMSOL Multiphysics. The elastoplastic model used is divided in two parts: first part a linear relation between the stress and the deformation describing the elastic domain (see equation (22)), where E is the Young modulus.

$$\sigma = E.\varepsilon \tag{22}$$

Second part represents the plastic domain, based on the relation (23).

$$\sigma_{ys} = \sigma_{ys0} + \left(\sigma_{\infty} - \sigma_{ys0}\right).\left(1 - exp^{-m\varepsilon_{epe}^{n}}\right) \tag{23}$$

Where σ_{ys} is the hardening function, σ_{ys0} is the initial yield stress which is found to be 2300 MPa, σ_{∞} is the steady-state flow stress which is found to be 2647 MPa, m is the saturation coefficient chosen to be equal to 1100 and n is the saturation exponent in this case equal to 1. These parameters were chosen in order to fit the simulated curve with the experimental one.

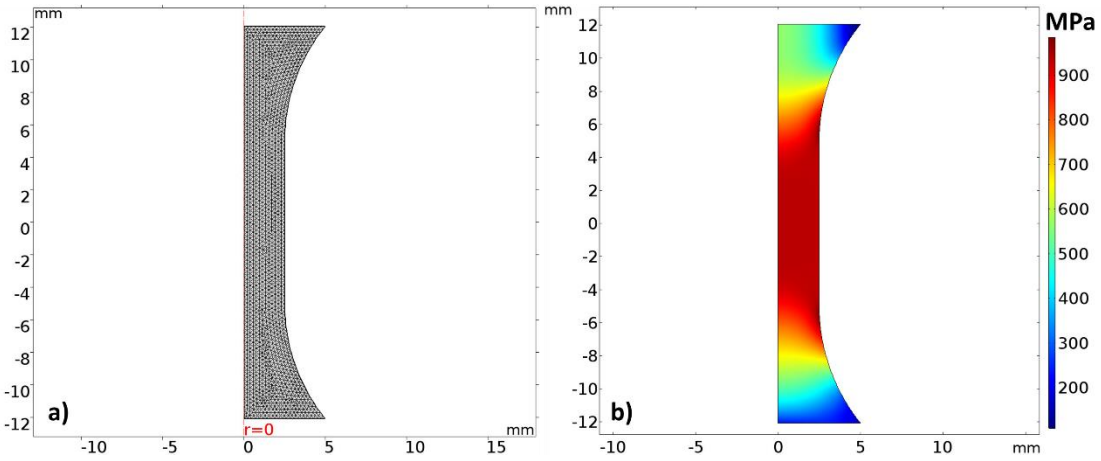

Figure 67 A presentation of a) the meshed geometry of the modeled sample, and b) the Von Mises stress distribution for 1% total deformation in the sample.

Figure 67a shows the geometry of the smooth sample without notch. This geometry was chosen to be identical to the geometry of the experimental sample and to fit the parameters of the model. The meshing was done using a triangular fine meshing automatically done by COMSOL. The bottom border was fixed and an imposed displacement of 0.3 mm was imposed on the top border, the point used for the measurements is located in the centre of the sample (here on r=0, z=0). Figure 67b shows the Von Mises stress distribution in the sample section. This distribution shown here corresponds to 1% total deformation.

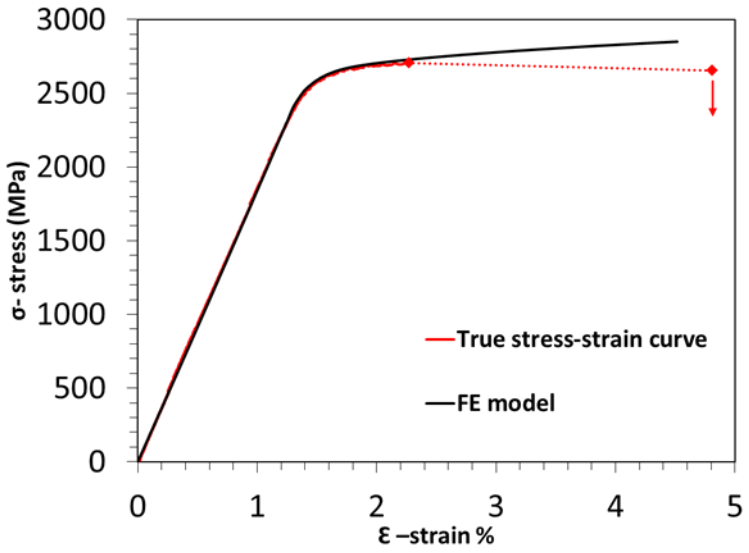

Figure 68 Comparison between the experimental true-stress *vs* true-strain curve in red with the COMSOL simulated curve in black.

Figure 68 shows a comparison between the experimental stress *vs* strain curve shown in red, and the one simulated by FE with COMSOL in black. It shows that the model is valid until around 2% of total deformation.

5.2. Modeled behavior

After adjusting parameters of the model on a smooth geometry, it was applied on a notched sample with the same parameters.

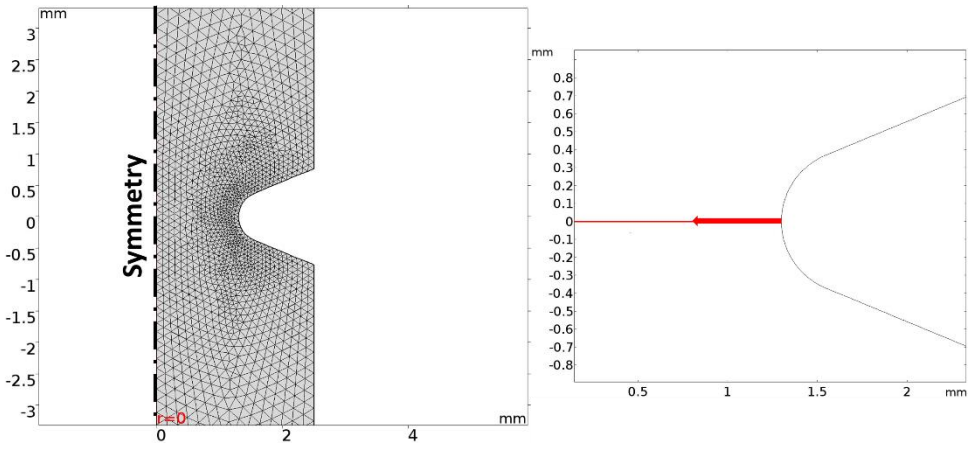

Figure 69 Presentation of the meshing on the notched sample geometry (on the left), and cutting plane for the profile representation of quantities calculated shown by a red arrow (on the right).

Figure 69 shows the geometry of the notched sample modeled with a 1mm-notch depth, an angle of 45° and a notch-tip radius of 0.4 mm. The meshing is also triangular with a refinement around the notch tip.

Figure 70a shows the distribution of the Von Mises stress after a displacement of 0.08 mm, Figure 70b the triaxiality distribution for the same displacement and Figure 70c the hydrostatic stress distribution. Figure 70d shows a magnification of plastic deformation in the notch tip region.

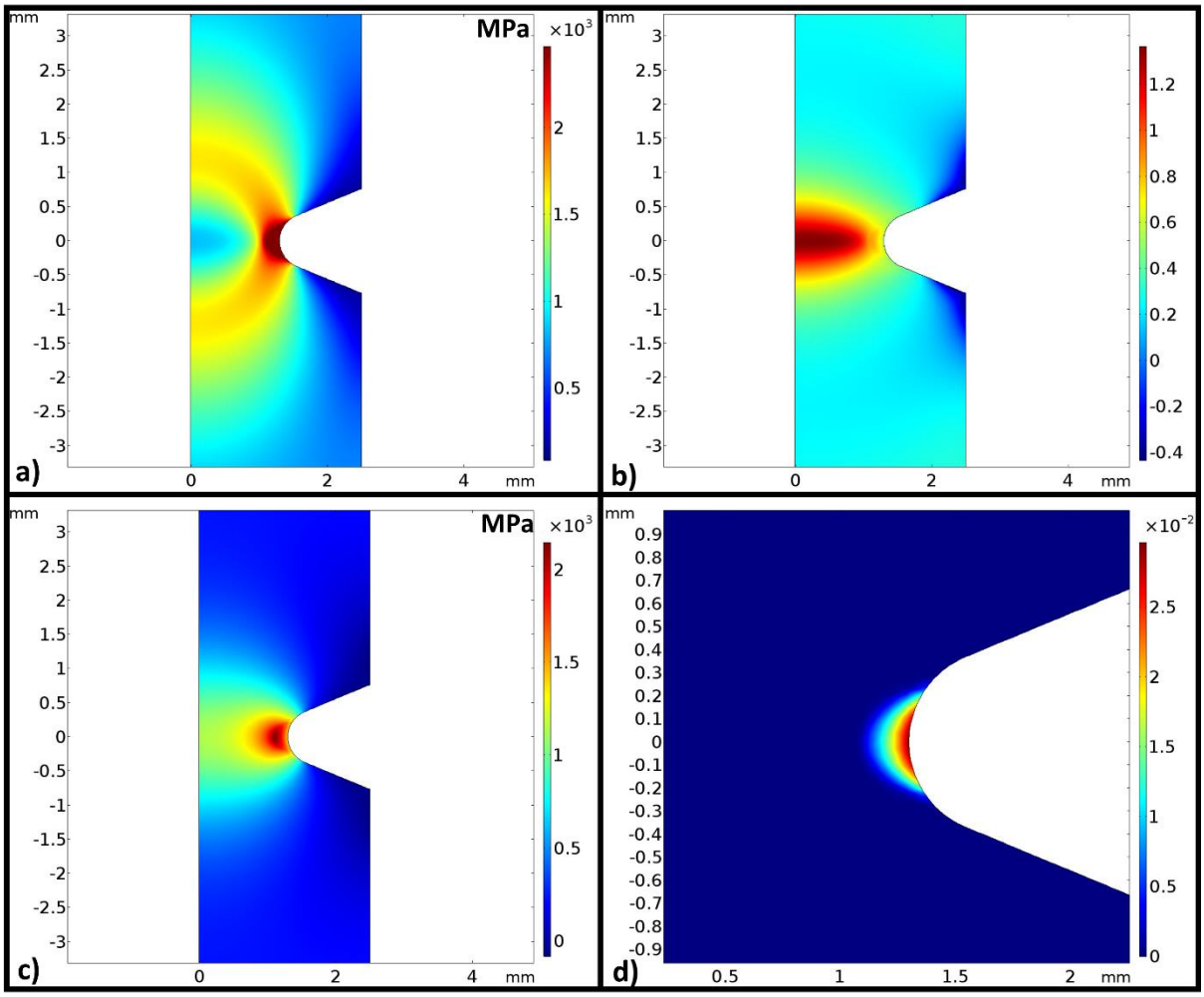

Figure 70 A presentation of the results exported after a displacement 0.08 mm showing in a) Von Mises stress distribution, b) stress triaxiality, c) hydrostatic stress distribution and d) plastic deformation distribution.

5.3. Mechanical parameters studied

The objectives of these FE calculations being to estimate the mechanical quantities obtained during the tensile tests on notched specimens, the simulations were done for the corresponding displacement values at rupture. These displacements are 0.025, 0.04, 0.055, 0.06, 0.08 and 0.23 mm.

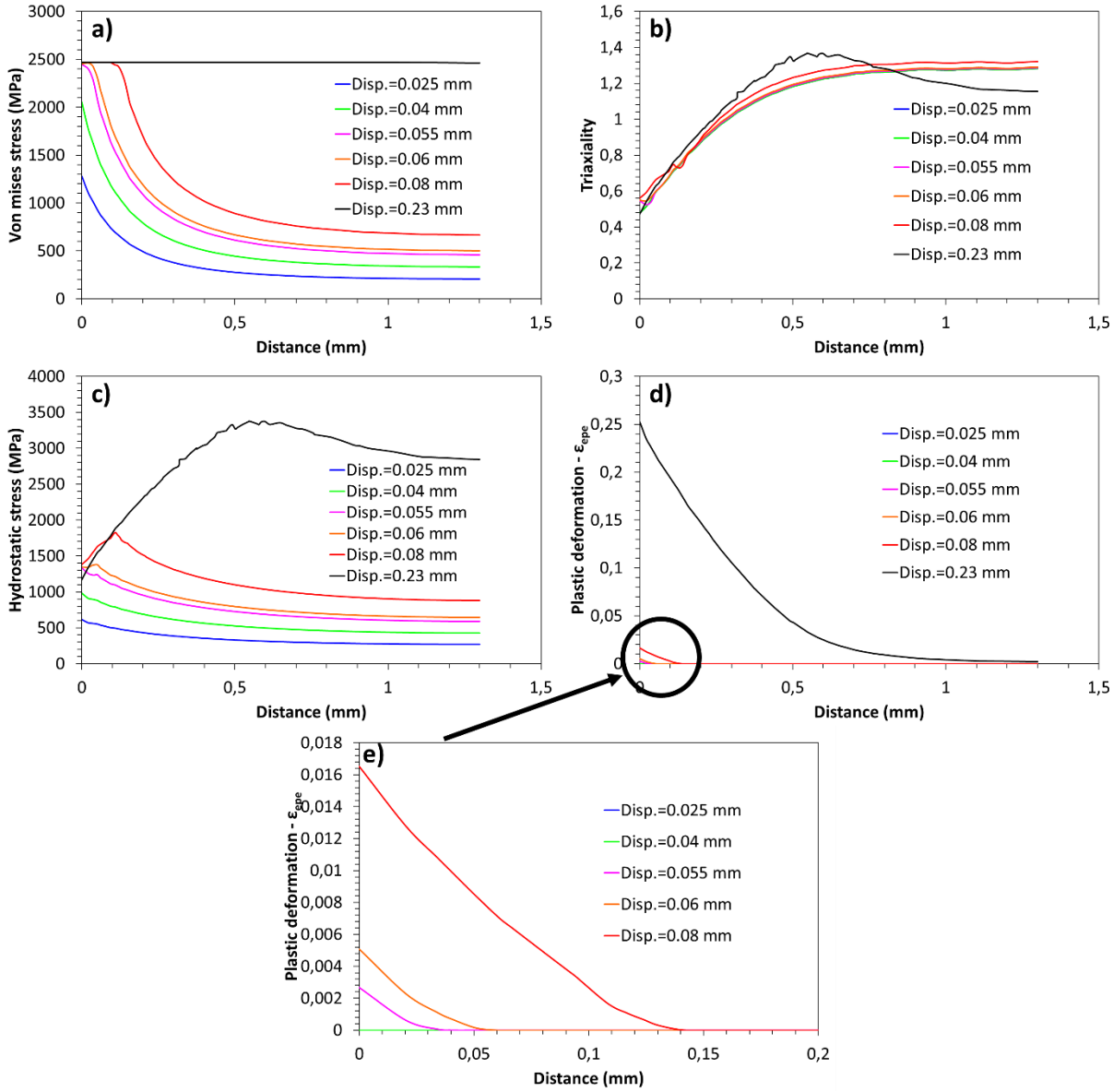

Figure 71 Profiles of the mechanical quantities variations from the notch tip to the centre of the sample for loadings corresponding to displacements equal to 0.025, 0.04, 0.055, 0.06, 0.08 and 0.23 mm. a) Von Mises stress, b) Triaxiality, c) Hydrostatic, d) and e) Plastic deformation.

Figure 71 shows the profiles of mechanical quantities varying from the notch tip to the symmetry axis of the specimen obtained by FE calculation for the different displacements. The Von Mises stress variations in Figure 71a show a full plastic deformation in the section for the 0.23 mm displacement test (simulating the tensile test held in air), in addition a plastic zone is present for the 0.08, 0.06 and 0.055mm displacement tests while no plastic deformation occurs for lower displacements. In Figure 71b an increasing stress triaxiality is observed for all the displacements from the notch-tip to the mid distance, with a peak at about 0.6 mm for the highest displacement. In Figure 71c, the expected peak of hydrostatic stress is observed,

it moves more to the notch tip while the displacements applied on the specimen are decreasing. However, for the 0.025 and 0.04mm displacement tests, the hydrostatic stress distribution decreases while moving deeper in the sample. In Figure 71d and Figure 71e, we show the absence of plastic deformation for the two lowest displacements applied. Considering that the model is correct and applicable up to 2% of total deformation, mechanical quantities calculated for displacements higher than 0.08 mm have to be taken with care.

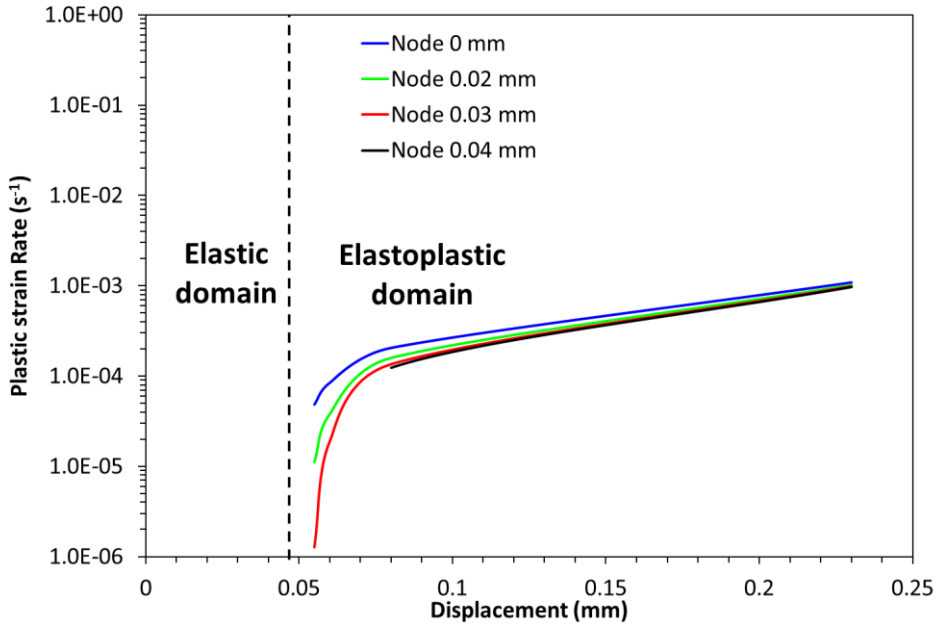

Figure 72 Plastic strain rate vs Displacement for a displacement rate of 10^{-3} mm.s^{-1} calculated for 4 different nodes in the section (node 0 mm is the notch tip).

Figure 72 represents the plastic strain rate ($\dot{\epsilon}_{epe}$) *versus* the displacement calculated for a displacement rate of 10^{-3} mm.s^{-1} on different nodes in the cross section of the geometry, from the node 0, at the exact notch-tip, to the node at 0.04mm-abscissa. The calculations show that the plastic strain rate tends to zero when the displacement is lower than 0.047mm (no plastic deformation). In addition, for larger displacements the plastic strain rate tends to converge to the value of 10^{-3}s^{-1}, corresponding to the strain rate that a specimen with a 1 mm gauge length should have for this displacement rate. We recall that the notch-tip radius equal to 0.4 mm allows this simplified representation.

6. Results and discussion

6.1. V-notch impact tests

6.1.1. Effect of hydrogen pre-charging

In this part, the specimens were pre-charged cathodically to assess the intrinsic effect of hydrogen located on various trapping sites of the microstructure of the maraging steel by avoiding H-transport effects using "shock" tests. Four different charging durations were applied: 4, 13, 24 and 48 hours. By increasing charging duration, we expect both a higher hydrogen content and a higher diffusion distance in the bulk from the specimen surface. The penetration distance of hydrogen is proportional to the square root of the product of diffusion coefficient and time. The calculation is based on the effective diffusion coefficient measured beforehand by permeation tests (D_{eff} = 6.38 10^{-14} m^2/s) and using the following relation that considers a hydrogen diffusion in a semi-infinite volume, the effect of traps being included into the effective diffusion coefficient [130]:

$$x = 2\sqrt{D_{eff}\, t} \qquad \textbf{(24)}$$

where D_{eff} is the effective diffusion coefficient and *t* the duration of hydrogen charging.

Table 13 shows the results for the four different H-charging durations. This simple calculation shows that the specimens are not completely H-charged in the middle, even after 48 hours.

Table 13 The hydrogen diffusion distance with respect to the different hydrogen charging times.

Time (hours)	4	13	24	48
Diffusion distance (µm)	60	110	150	210

We saw previously that after 24 hours of charging, hydrogen content reaches around 1.9 ppm, while for the non-charged samples, a residual content of around 0.62 ppm was found. Insofar the specimens were immersed in liquid nitrogen just after charging, the hydrogen content measured here covers both the diffusible and the trapped hydrogen, irreversible and reversible.

Figure 73 shows the average fracture energies calculated from the results of three different tests, as a function of hydrogen charging durations. It shows that while increasing the hydrogen content and depth penetration, the fracture energy decreases showing the weakening effect of hydrogen on the material. It seems that the embrittlement is more severe with a longer loading time as suggested by the calculation of diffusion distances presented in Table 13.

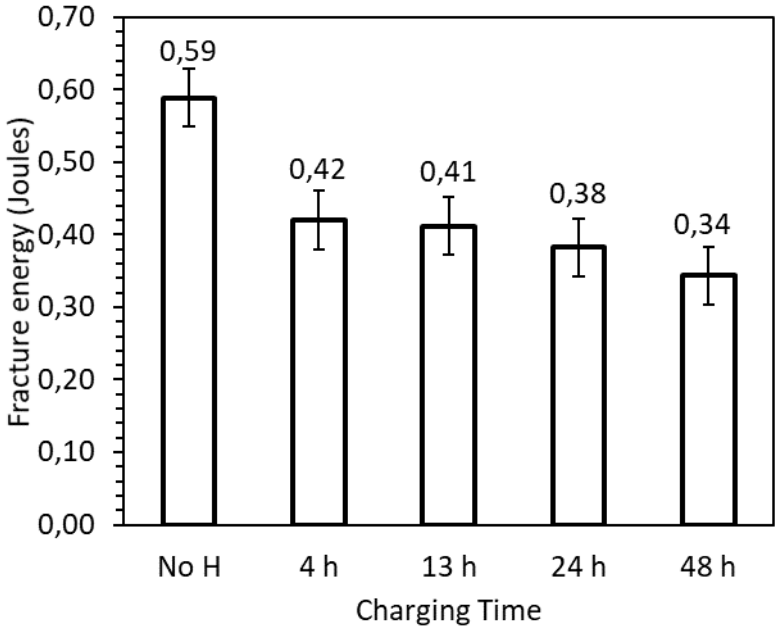

Figure 73 Fracture energies as a function of hydrogen charging time.

6.1.2. Fracture surface analysis

Figure 74 shows the fracture surface of the hydrogen-uncharged specimen. Figure 74a shows the notch tip followed by a shearing zone. Figure 74b shows at higher magnification the shearing zone with features of ductile fracture with dimples stretched in the shear plan direction.

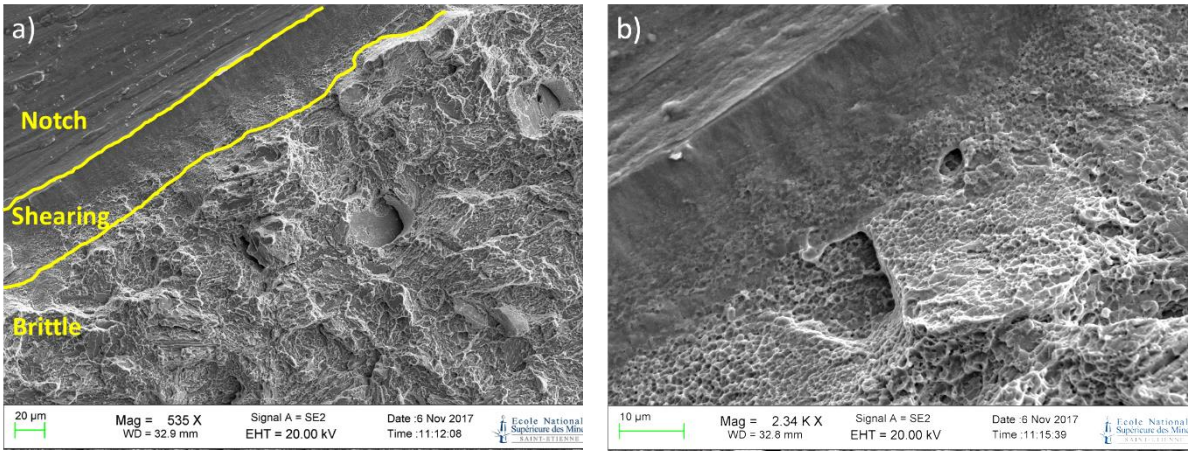

Figure 74 Fracture surface of the hydrogen-uncharged sample, broken after Charpy test.

Figure 75 shows the fracture surface of the sample cathodically hydrogen-charged for 24 hours. The surfaces show mainly a ductile character but some brittle facets appear along the notch tip, and some of them follow the former austenitic grains boundaries. Also, one can note the disappearance of the shearing zone. Figure 75c shows an example of grain boundary facet that was observed.

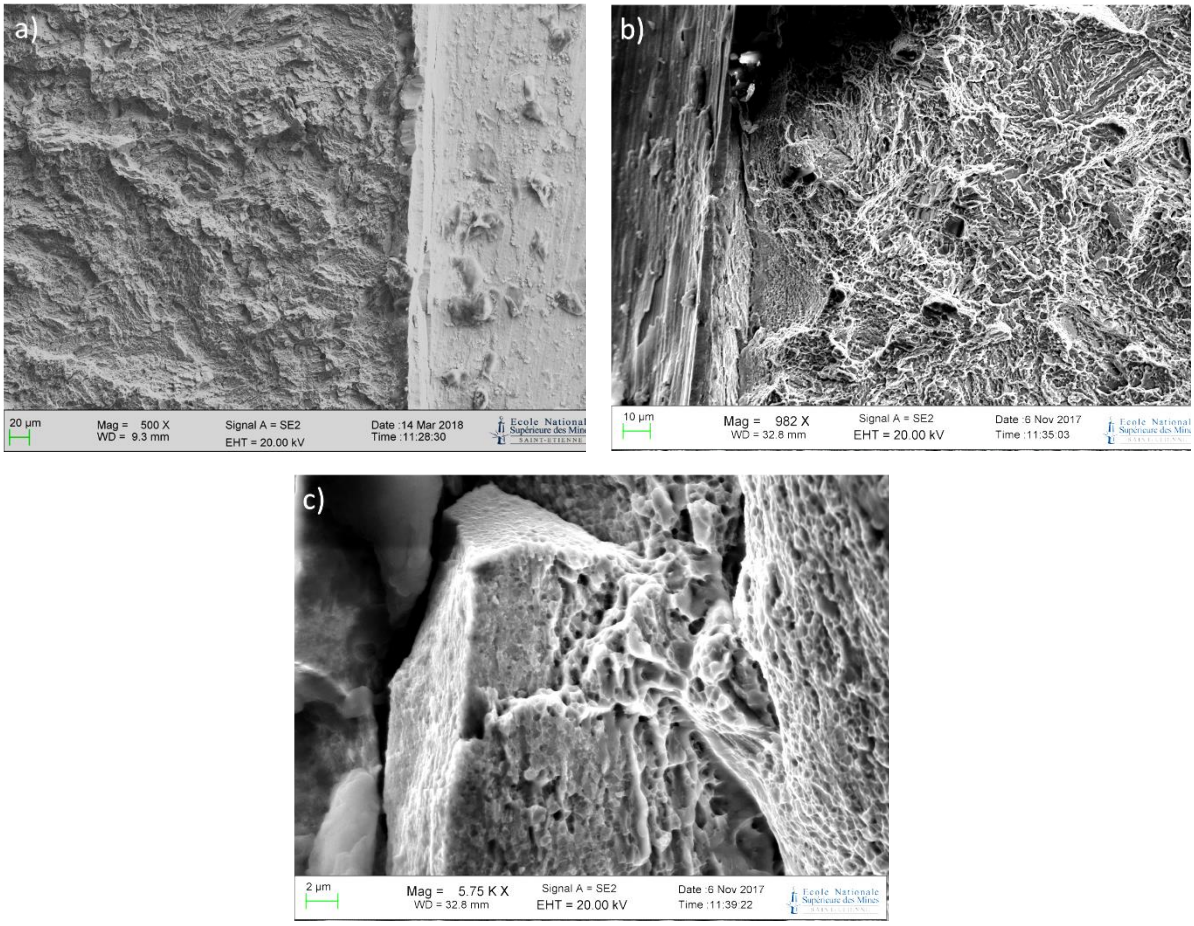

Figure 75 Fracture surface of the sample hydrogen-charged for 24 hours, broken after Charpy test.

Figure 76 shows the fracture surface of the sample hydrogen-charged for 48 hours. The same observations as on Figure 75 can be noted. The disappearance of the shearing zone is clear and the dominant ductile fracture is observed. Nevertheless, some brittle transgranular rupture zones close to the notch tip can also be seen in greater numbers, as seen in Figure 76b, while moving away from the bottom of the notch, the ductile mode becomes dominant again Figure 76c .

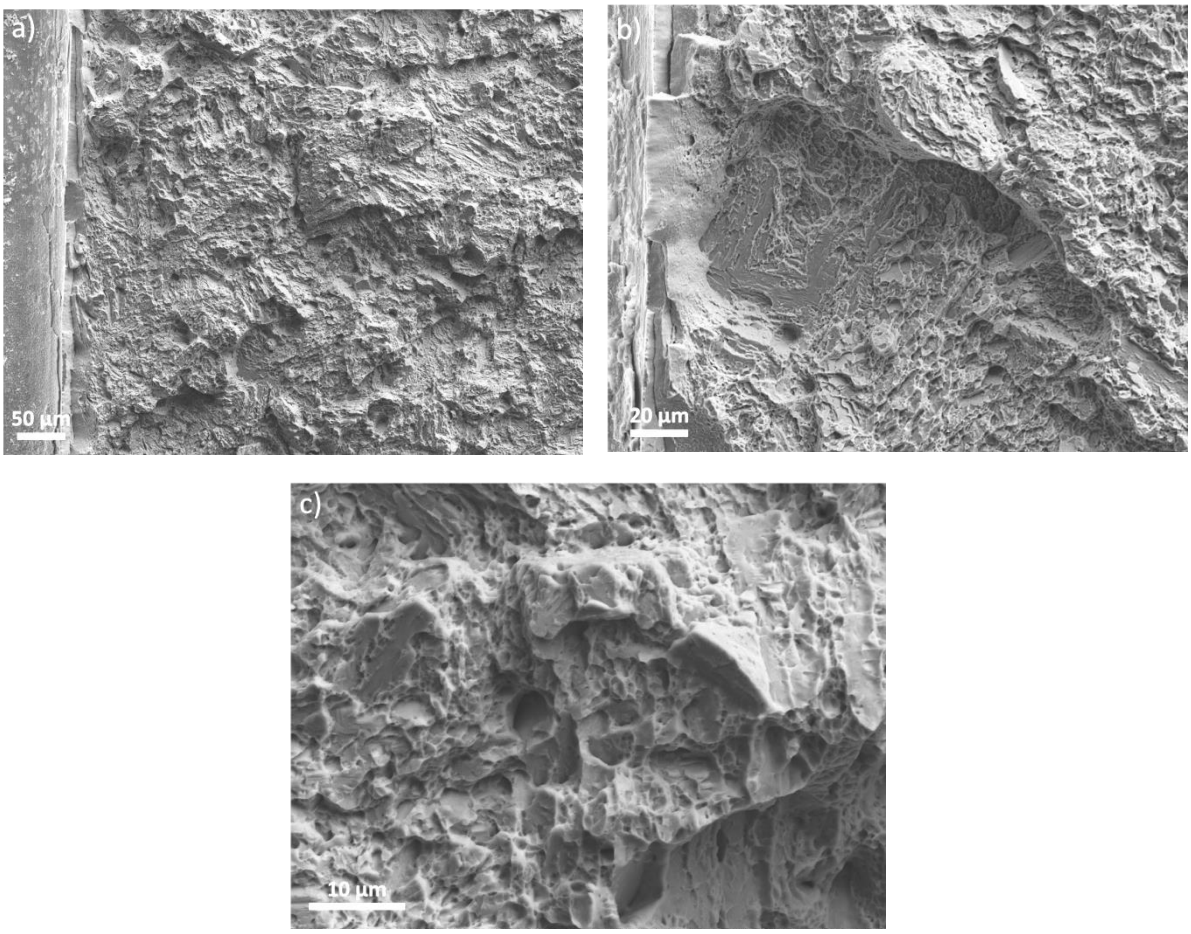

Figure 76 Fracture surface of the sample hydrogen-charged for 48 hours, broken after Charpy test.

Figure 77a and Figure 77b show the fracture surface of the two samples charged with hydrogen for 4 and 13 hours respectively. As before, the shearing zones at the notch tip are not present, while the ductile character remains dominant. Some crack initiations observed very close to the notch tip are oriented perpendicular to the surface (opening in mode I), suggesting a brittle cracking. Their depth is limited, of some micrometers.

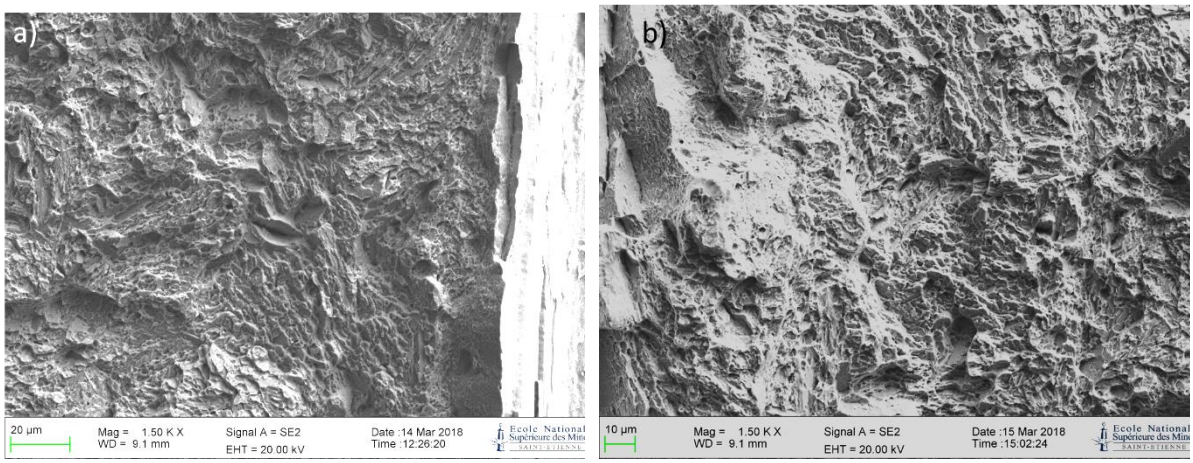

Figure 77 Fracture surfaces of the two samples hydrogen-charged for a) 4 hours and b) 13 hours, broken after Charpy test.

6.1.3. Summary

The fracture energy, even though it is generally low for the maraging steels, is clearly different between the hydrogenated samples and the non-hydrogenated one. There is a factor around 1.5 between their respective fracture energy. The greater the quantity of hydrogen introduced (duration of cathodic charging), the lower the fracture energy.

The fracture surface analysis for all hydrogen-charging conditions shows a mainly ductile fracture character. Although, for the two specimens charged the longest durations (24h and 48h), some transgranular and intergranular brittle zones can be found close to the notch tip, where the amount of hydrogen introduced is the most important. The presence of these brittle zones explains the lower fracture energies for these two samples. If we consider the hydrogen penetration distance for these two samples, that is respectively 150 µm and 210 µm, the hydrogen content in this zone seems to be sufficient to modify the behavior of the material, decreasing its fracture energy and favouring brittle crack initiation. However, the two other samples less hydrogen-charged have relatively close fracture energies. The hydrogen diffusion distance in their case is shorter, respectively 60 µm and 110 µm, but seems sufficient to affect the behavior of the material.

Considering that these tests do not allow hydrogen transport by dislocations, they show that the simple diffusion and trapping are enough to weaken the material. In addition, the presence of some intergranular and transgranular facets suggests that the hydrogen trapped at these sites is in sufficient quantity to weaken these bonds. Nonetheless, the hydrogen

diffusion distances are much deeper than the brittle cracks observed. This suggests that a critical hydrogen content is needed to trigger the cracking in this mode. Under this threshold, the mode of cracking remains ductile, with formation of microcavities with plasticity, their coalescence conducing to fracture with dimples. Nevertheless, no variation in dimple size could be demonstrated on the fracture surface specimens hydrogen charged, as compare to the one uncharged.

6.2. Slow strain rate tests

6.2.1. Effect of the strain rate on the material in air

Two different displacement rates were tested to explore this parameter on the mechanical behaviour of the bcc crystallographic structure of the maraging steel: $V_T = 10^{-5}$ mm/s and 10^{-6} mm/s. These two tests shows a very small variation of the fracture stress, which decreases slightly with decreasing strain rate (Figure 78). The strain measurement out of the notch during the test does not allow to highlight any work hardening nor plastic instabilities with necking. Nevertheless, the level of stress seems to indicate that fracture occurred during the uniform plastic deformation stage, i.e., during the stage of cutting or by-passing precipitates.

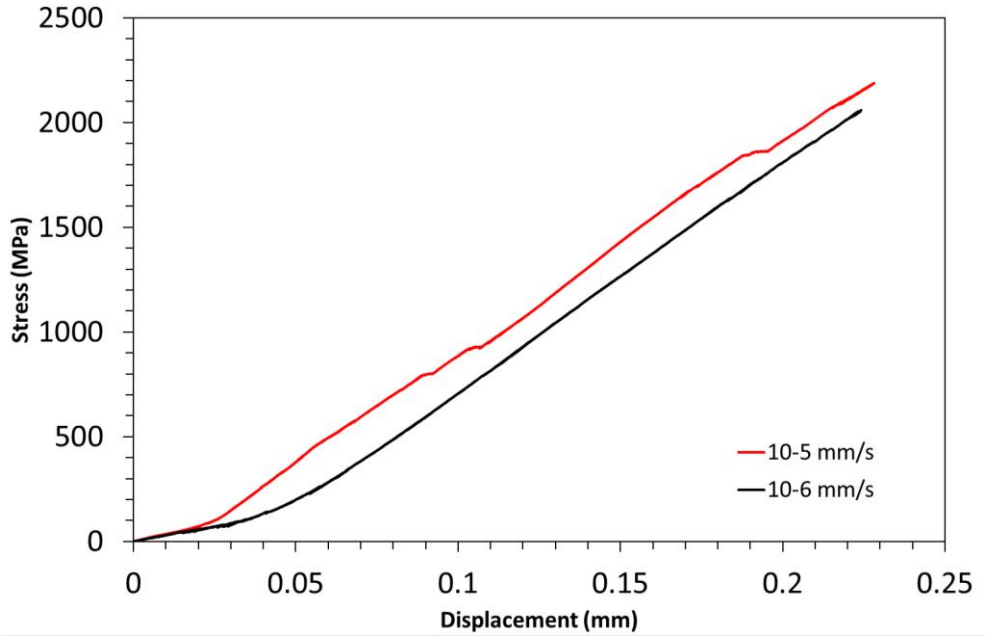

Figure 78 Stress *vs* displacement curves at 10^{-5} mm/s and 10^{-6} mm/s performed on uncharged samples.

The Figure 79 shows the fracture surfaces of the two tensile tests performed in air without hydrogen charging. The initiation of the crack happened in one localised place on the periphery. We can see a shearing zone on the remaining part of the perimeter of the notch, and at greater magnification, the fracture surface presents a mode entirely ductile with dimples. Nevertheless, we can observe some smooth planes that can correspond to ruptures by quasi-cleavage.

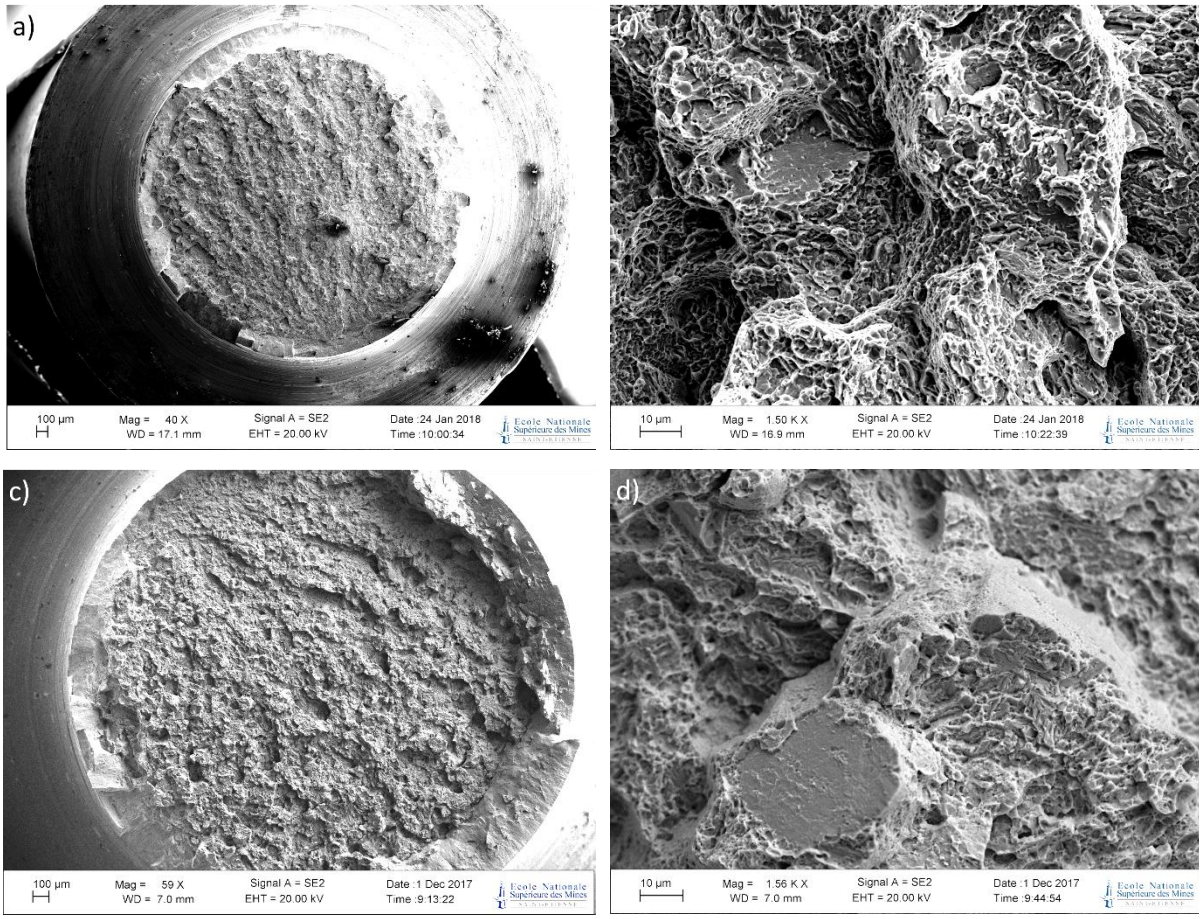

Figure 79 Fracture surfaces showing the fractured surface for: 10^{-6} mm/s in a) and b) and 10^{-5} mm/s in c) and d). Both of the tests are done on uncharged samples.

6.2.2. Effect of strain rate on hydrogen embrittlement

- **Stress *vs* displacement curves**

In this section, results presented concern effects of strain rate or displacement rate on the behaviour of the steel under hydrogen charging. The curves are shown on Figure 80 whilst Figure 81 shows the fracture stresses for the different tests. First of all, it should be noticed that if the curves are not linear this is linked to a measurement artefact of the elongation by

LVDT, which was realized outside the corrosion cell. When cracking occurs not perfectly all around the perimeter of the notch tip, a slight misalignment could appear and cause this non-linear evolution of the stress-displacement curve. Nevertheless, this information on the curve is not sufficiently precise to pinpoint exactly any crack initiation time. Our analysis focused only on the fracture stresses.

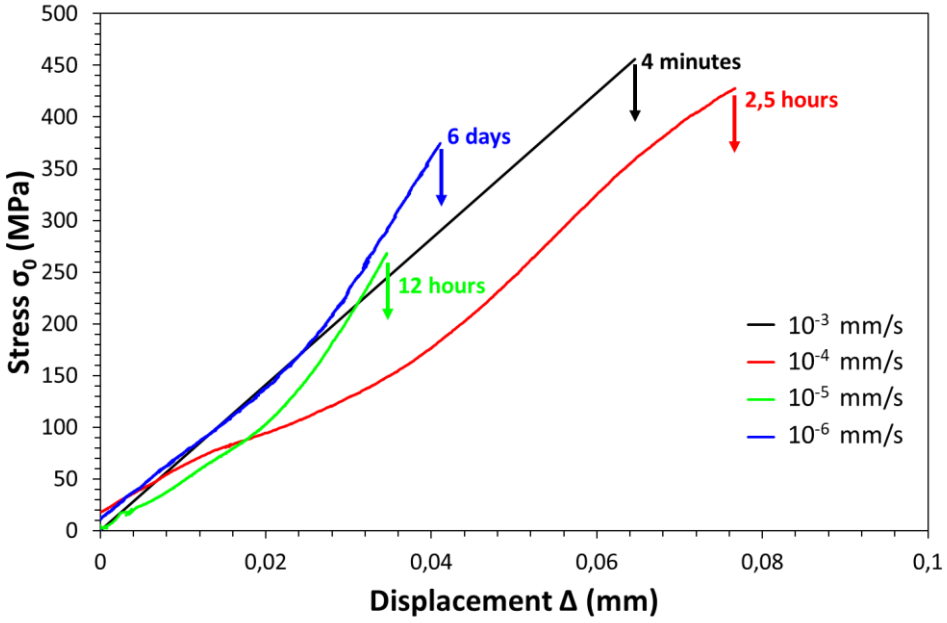

Figure 80 Stress-Displacement curves for cathodic tests at different displacement rates.

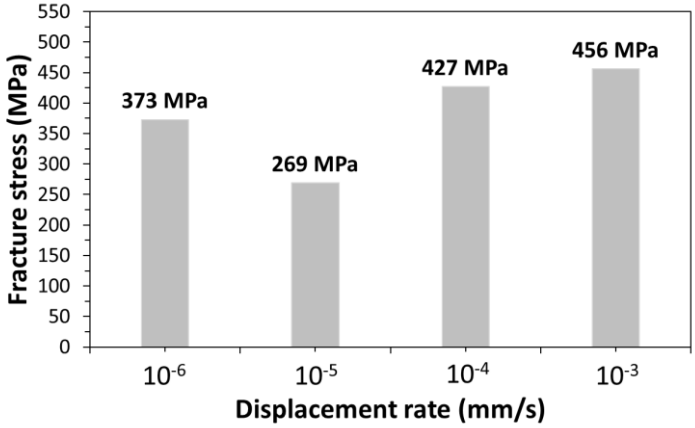

Figure 81 Test fracture stress for the different displacement rates under cathodic charging at -1200 mV/SCE after precharging 24h at the same potential. Fracture stress in air at 10^{-5} mm/s is equal to 2188 MPa.

A drastic effect of cathodic hydrogen charging was observed on the fracture stress as compared to the reference test performed in air. The stress is lowered by a factor 5 to 6.

The results show an effect of the strain rate on the fracture stress. By considering the notch tip strain rate at the node zero (see Figure 72), the displacement rates explored here correspond to strain rates ranged from 10^{-4} to 10^{-7} s^{-1} at the beginning of the test. The maximum embrittlement is observed at 10^{-6} s^{-1}, which is in accordance with literature [131], [132]. At lower strain rate, the fracture stress tends to rise again, indicating a reversible effect of hydrogen embrittlement in these particular conditions of straining.

- **Fracture surface analysis**

Figure 82 shows the fracture surfaces of the tensile test performed at the displacement rate of 10^{-3} mm/s. The fracture surfaces show a transgranular fracture mode with ductile tearings and dimples. For higher magnifications, we can observe some localized quasi-cleavage fractures with facet sizes corresponding to the ones of blocks (Figure 82b). At a finer scale, these facets corresponding to blocks are themselves marked by ligaments whose distance between them corresponds to the dimensions of the sub-blocks of the martensitic microstructure (Figure 82c). At very high magnification, Figure 82d shows the fracture at the scale of a martensite lath, where one can distinguish the fine precipitation inside them, while in the zone with dimples, some larger precipitates can be observed at their bottom. These various characteristics of the fracture mode underline the fact that no preferential path seems to guide the crack. On the contrary, it crosses the microstructure probably governed by effects dependent on mechanical factors.

The fracture aspect is comparable with what was observed on Charpy tests hydrogenated for 24 and 48 hours. The tensile curve shows a linear increasing loading with a brutal drop at the end of the experiment. On the other hand, the microscopic observations show that the initiation zone of the main crack in the Figure 82a, starts from the right of the sample (as presented) with a propagation directly towards the left, leaving shearing zones on the upper and bottom part and a more ductile ligament on the end of the propagation on the left. This similarity with the Charpy test suggests that these kind of cracking propagates fastly.

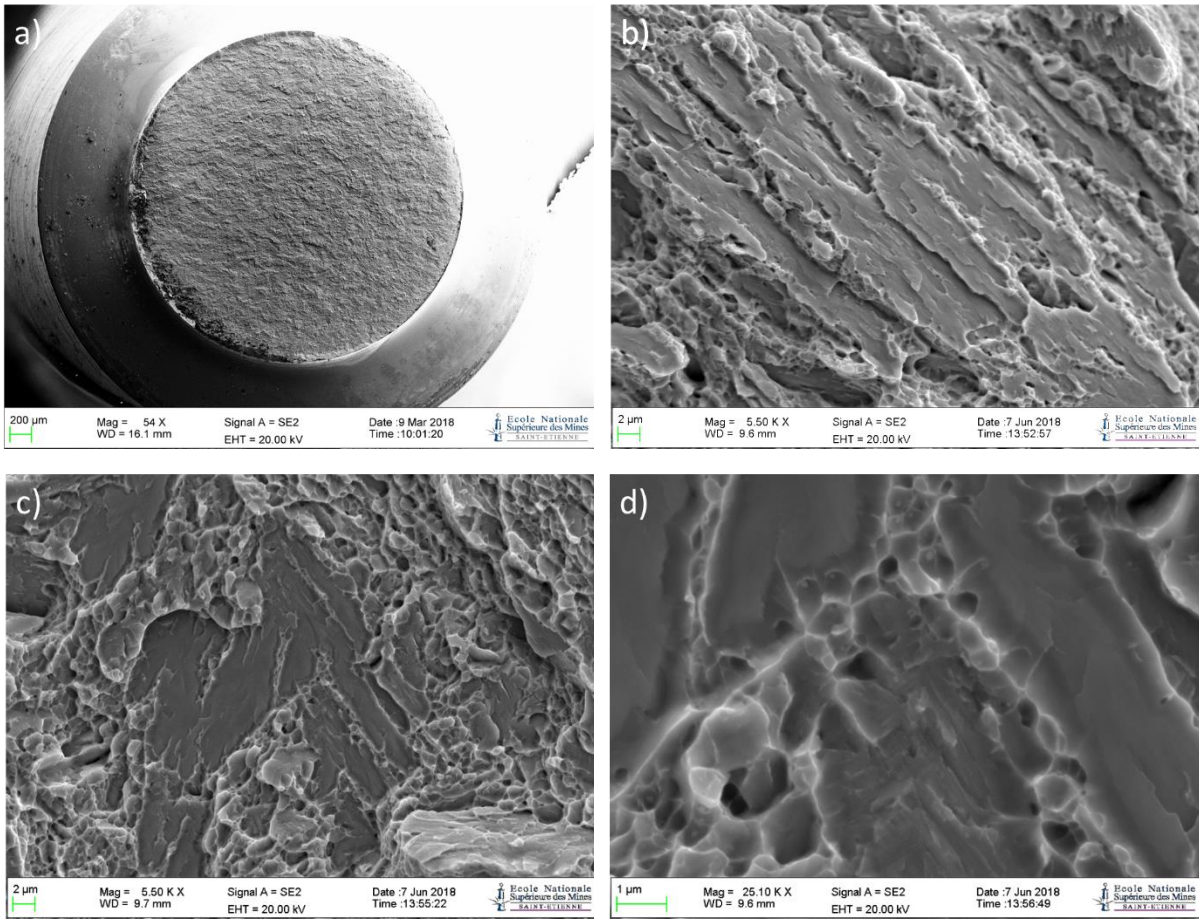

Figure 82 Fracture surfaces of a sample after tensile test under hydrogen cathodic charging and displacement rate of 10^{-3} mm/s.

Figure 83 shows the fracture surface of the tensile test at a displacement rate of 10^{-4} mm/s. The fracture surface in Figure 83a shows a large zone of a predominantly intergranular mode of cracking. It should be noticed that this mode nevertheless contains transgranular cracks distributed among the intergranular facets. It covers around 50% of the fracture surface. The maximum depth of the intergranular crack, measured in relation to the radius of the specimen (R), is around 60% of R. Whereas intergranular cracking started relatively early during tensile test, and finished at the transition to the final transgranular cracking, the crack propagation duration is around 2.5 hours. This gives a mean crack growth rate equal to around da/dt = 1.1×10^{-4} mm/s.

For greater magnifications, the examination of the intergranular zone shows the presence of transgranular parts (Figure 83b) that goes through one to two former austenitic grains. Finally, the area of this transgranular brittle zone is equal to around 22% of the IG/TG fracture surface. This zone is characterised by a “quasi-cleavage” fracture mode (Figure 83c). The transgranular

brittle crack initiates on specific crystallographic interfaces, as we can see the tiny cracks on the right of the transgranular zone on the same figure. If we compare the transgranular zone with the different “objects” of the microstructure, this transgranular rupture can correspond to packets or blocks separations. Compared to the purely transgranular zone where numerous features of ductility like tearings and dimples are present (see Figure 83d), this mixed intergranular/transgranular mode (IG/TG), which precedes the transgranular crack (TG), does not contain features of ductility.

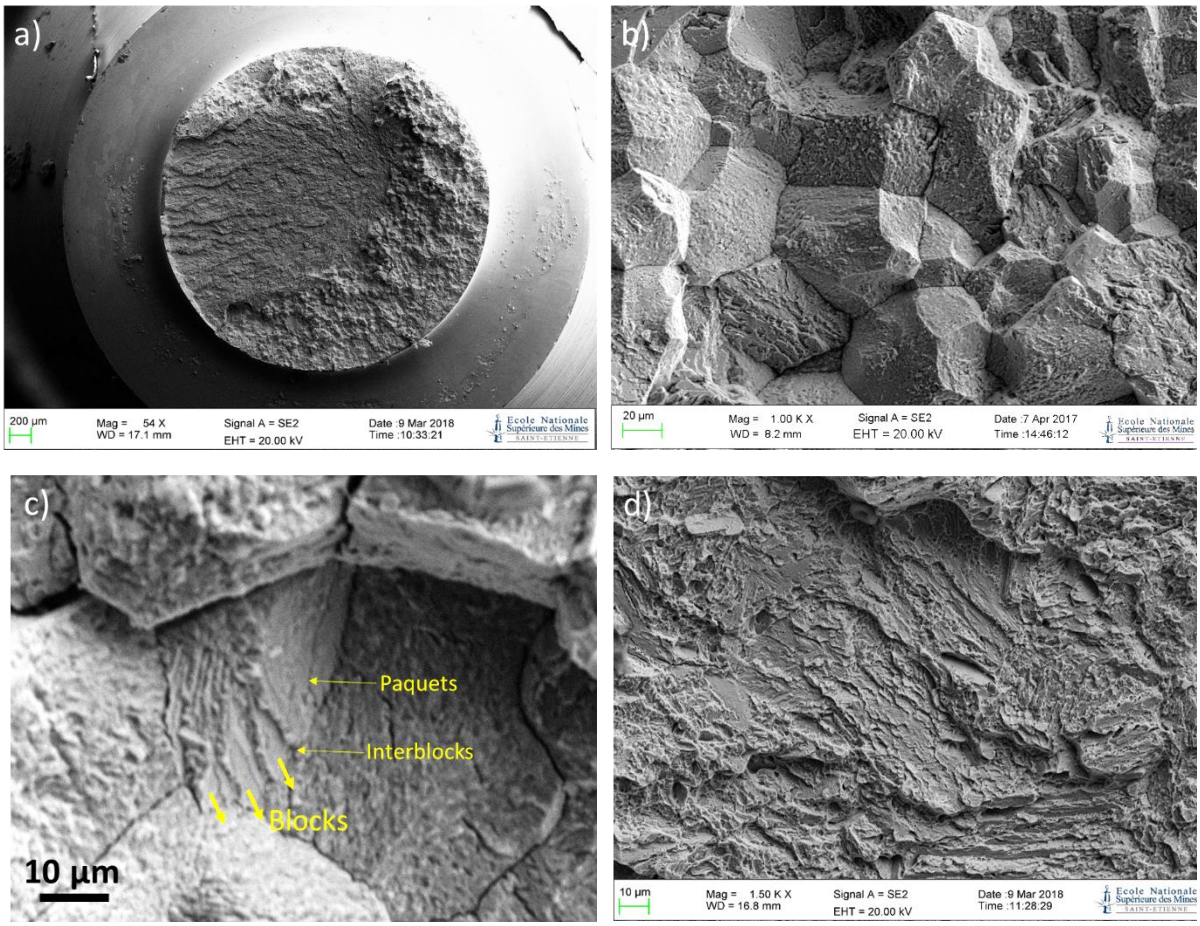

Figure 83 Fracture surfaces of the tensile test at displacement rate of 10^{-4} mm/s under hydrogen cathodic charging.

Figure 84 shows the fracture surface of the specimen corresponding to the displacement rate of 10^{-5} mm/s. The sample shows an intergranular initiation at the notch root on around two third of the perimeter, and has a depth of 64.8% of the radius equal to 972 µm. The mixed intergranular/transgranular zone occupies around 50% of the total surface (Figure 84a). On a larger magnification, we can note the same characteristics than the test before (10^{-4} mm/s): brittle transgranular/intergranular mixed mode, the transgranular mode covering around 15%

of the whole mixed mode. As previously, the transgranular brittle mode contains also small quasi-cleavage facets with a size that corresponds to the dimension of packets or blocks.

By considering the total duration of the test equal to the mixed intergranular/transgranular crack propagation time, the crack growth rate is equal to da/dt = 2.25×10^{-5} mm/s.

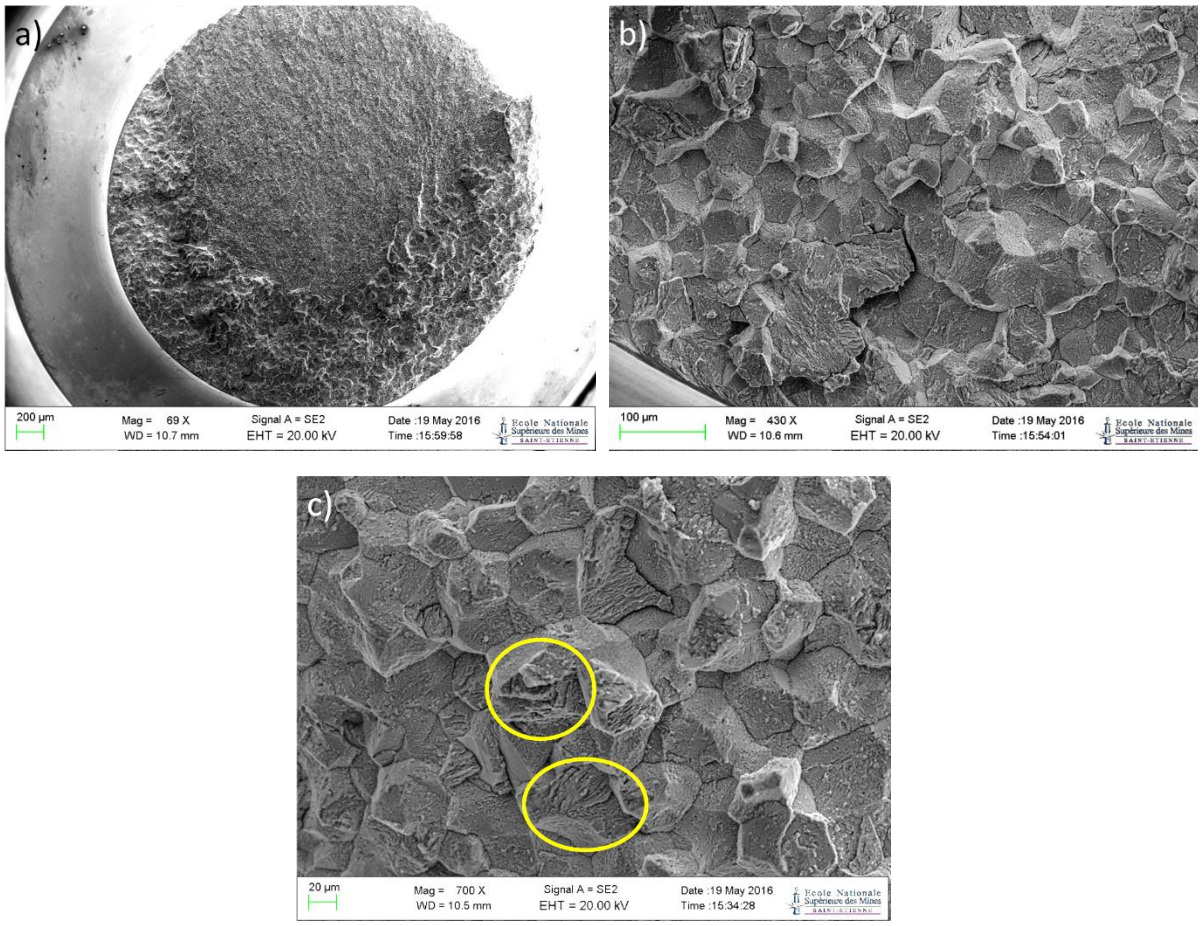

Figure 84 Fracture surface of the tensile test at displacement rate of 10^{-5} mm/s under hydrogen cathodic charging at different magnifications. Yellow circles on c) indicate transgranular mode in the mixed IG/TG fracture surface.

Figure 85 shows the fracture surfaces of the cathodic tensile test for the displacement rate of 10^{-6} mm/s. Although this test is the slowest in terms of displacement rate, it presents a resistance to cracking greater than the one performed at 10^{-5} mm/s. The general fracture surface, Figure 85a, shows a relatively small intergranular/transgranular mixed zone that covers around 1.6% of the total fracture surface. The depth of the mixed IG/TG crack propagation with respect to the radius was calculated to be 15.4% of R.

This mixed intergranular/transgranular zone is the initiation zone of the main crack which leads to the final fracture, although we can identify another transgranular initiation zone. The

transgranular parts in the mixed mode surface presents here again a quasi-cleavage type mode of fracture on a zone having the characteristic dimensions of packets. Each TG facets present smaller dimensions that can correspond to blocks (Figure 85d). The features of the mode of cracking present strong correlation with typical dimensions of constituents of the microstructure. One can identify for instance the blocks and sub-blocks on Figure 85f and compare then to ones on EBSD cartography on Figure 85g. Actually, the appearance of the fracture of the blocks by quasi-cleavage seems to be a decohesion between sub-blocks, along inter-block interfaces. This is clearly shown on Figure 85f, on the right in the middle, by successive decohesions of sub-blocks perpendicular to the main plan. Ductile ligaments, appearing white on the fracture surface, constitute actually the connecting areas between sub-blocks.

Zone with dimples are also present on the fracture surface outside the mixed IG/TG part; they show a mechanical fracture for some interfaces. On a lower magnification (Figure 85e), one distinguishes entirely ductile zones that could correspond to the ductile fracture of packets.

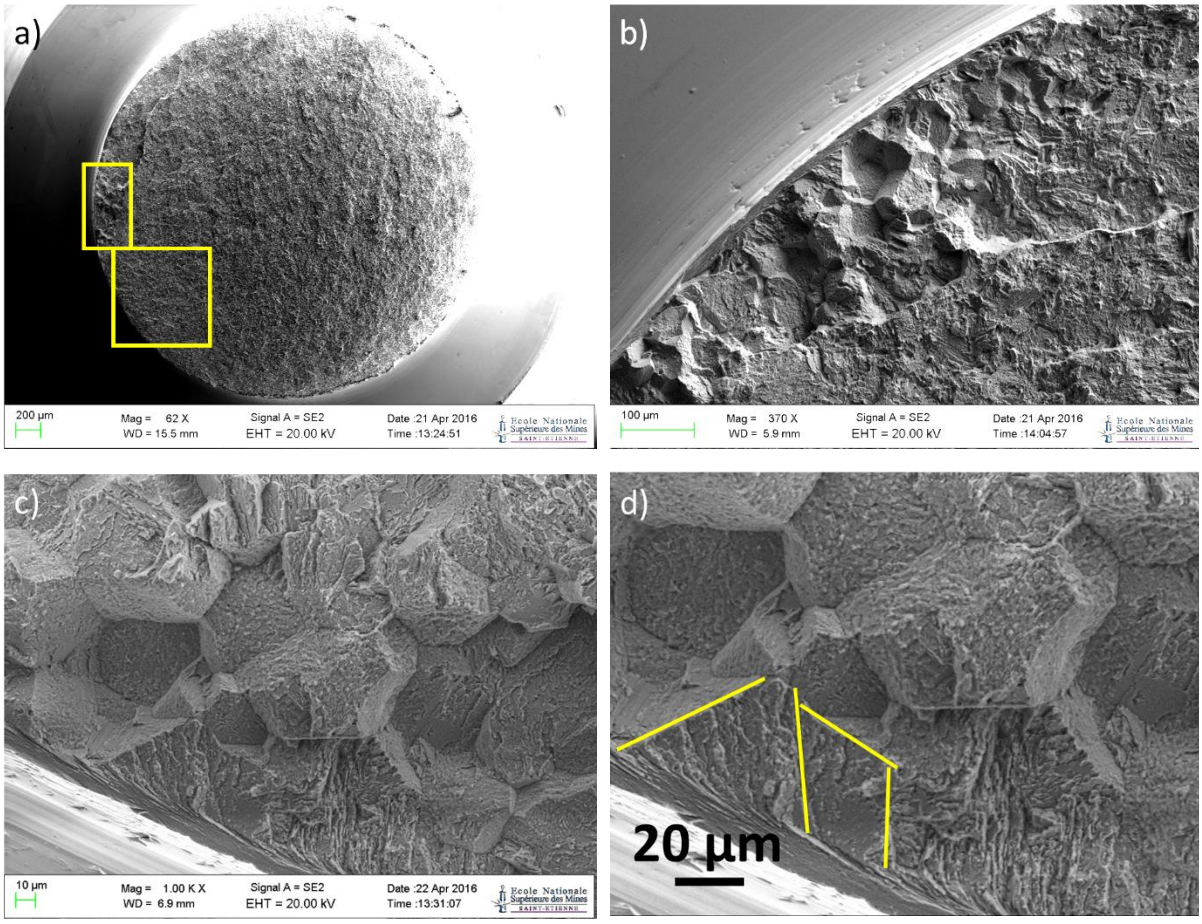

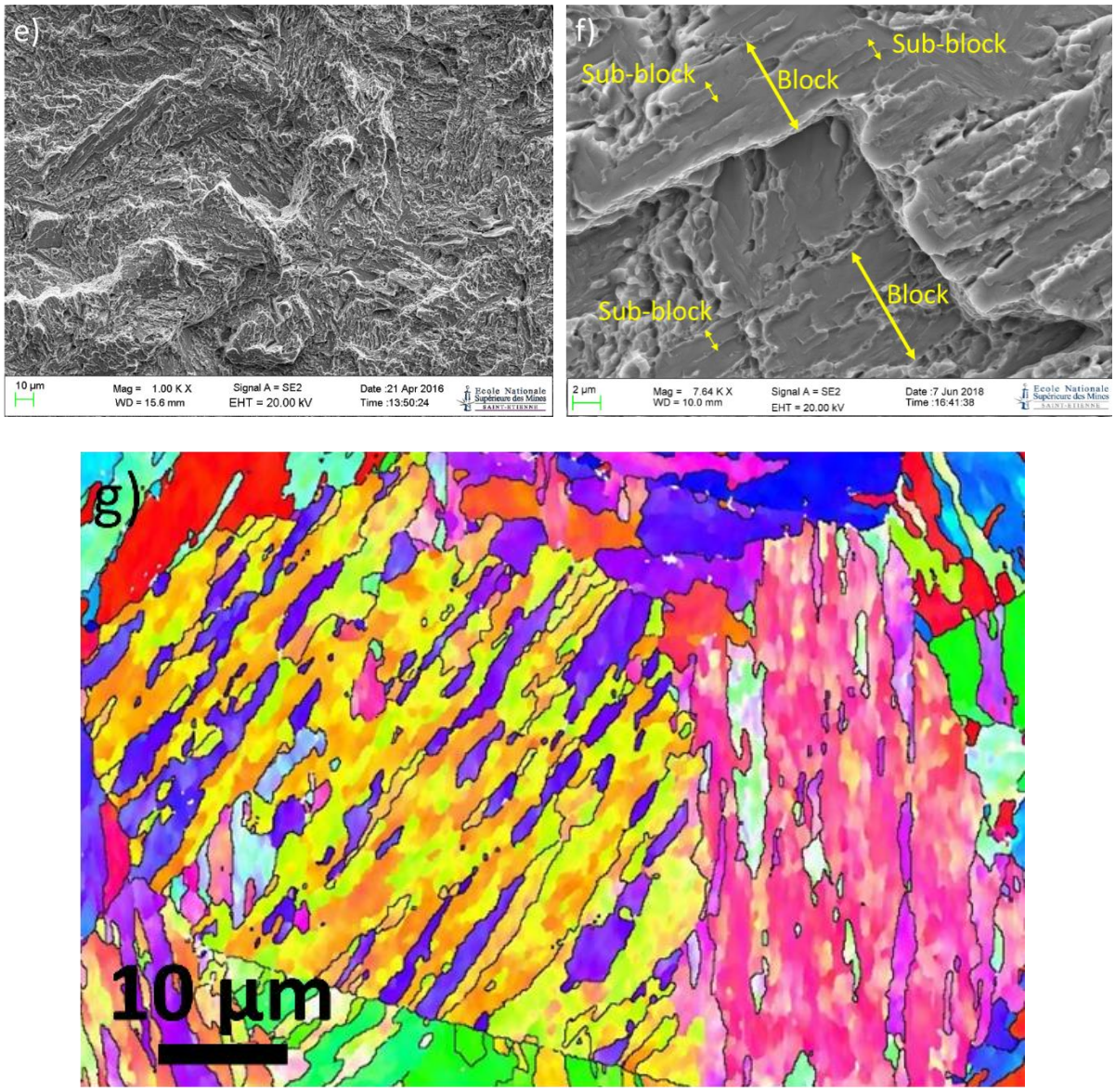

Figure 85 Fracture surface of the tensile test at displacement rate of 10^{-6} mm/s under hydrogen charging at different magnifications from a) to f). g) EBSD image at same magnification than f) for comparison.

6.2.3. Effect of pre-strain on the hydrogen embrittlement

The pre-strain was applied on the specimen just after the 24h-cathodic charging of hydrogen. The strain value applied corresponds to a fast loading up to 600 MPa on the specimen (few seconds at around $V_t = 10^{-2}$ mm.s^{-1}), which itself corresponds to a displacement of about 0.08 mm. At this value, the FE calculations have shown that the plastic deformation at the tip of the notch is around 1.6 to 2%, which still corresponds to the regime of plastic work hardening and the beginning of the uniform deformation plateau with moving of dislocations across nanoscale precipitates. Then, the specimen was unloaded, and the slow strain rate test under cathodic hydrogen charging at $V_t = 10^{-5}$ mm.s^{-1} was started.

It should be noted that at this displacement rate of $V_t = 10^{-2}$ mm.s^{-1}, the specimen did not break at this stress value, unlike the test performed at 10^{-3} mm.s^{-1}.

Figure 86 shows the tensile curve of this test in the stress-displacement graph with all the other curves. The pre-strain effect is detrimental, the maximum stress reached in these conditions, σ_R = 165 MPa, is lower by almost 100 MPa as compared to the test at 10^{-5} mm.s^{-1} without pre-straining. The long plateau after the peak of stress corresponds to the extended IG/TG crack propagation before the final rupture. In contrast to the other tests, subcritical propagation may have occurred up to significant crack depth given the low stress level.

Figure 87 shows the fracture surface of the specimen. One can clearly observe a predominant intergranular/transgranular propagation on almost the totality of the fracture surface (~ 87%). Several initiations of this crack took place all around the perimeter at the root of the notch and permitted a propagation relatively axisymmetric. The maximum depth of this crack with respect to the radius is 100% R, which is equal to 1.7 mm. If we consider that the subcritical propagation initiated early and propagation took place during the whole 0.045 mm-displacement (see Figure 88), one can get a propagation duration of 2000 seconds, and so assess a crack growth rate of 8.5×10^{-4} mm/s.

With a greater zoom, we can here again estimate the fraction of transgranular mode of cracking inside the mixed IG/TG fracture surface, which is equal to 22%.

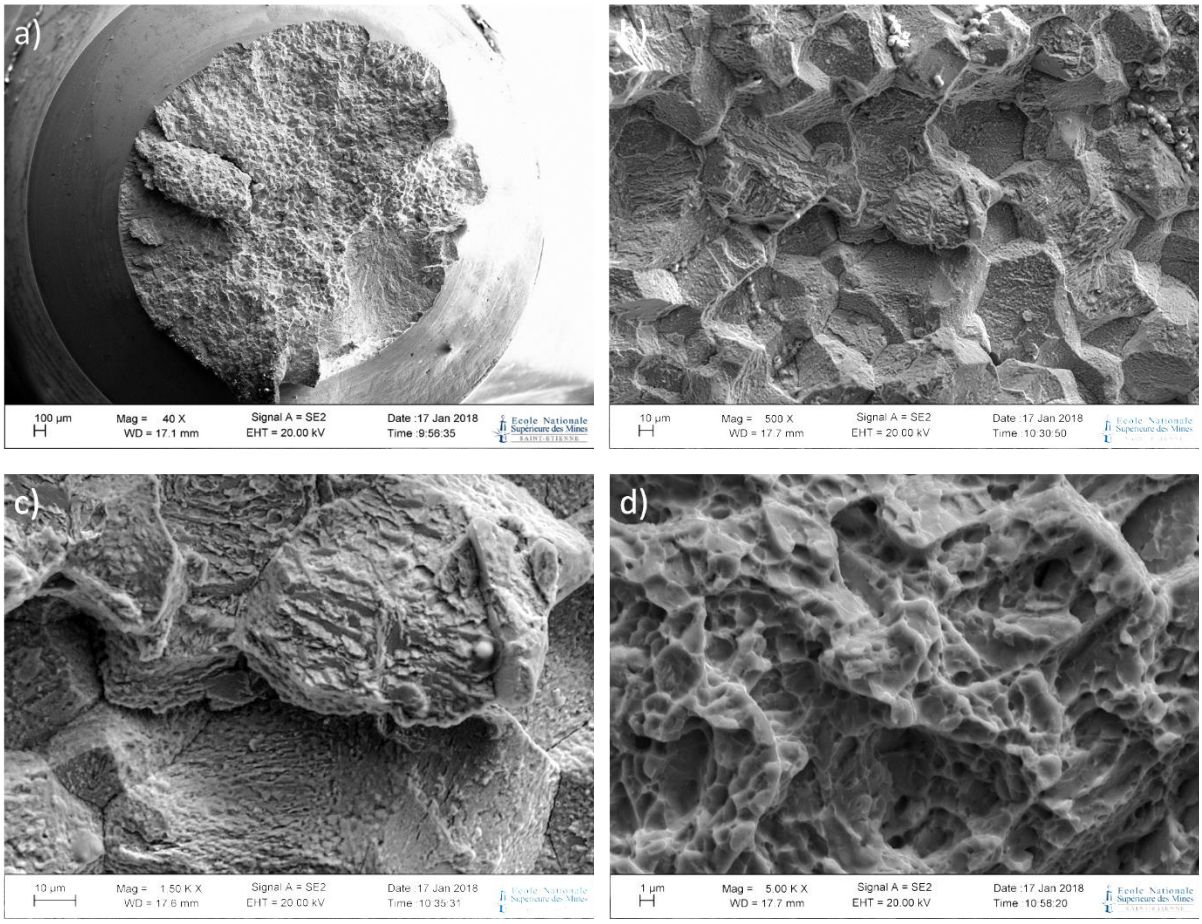

Figure 87 Fracture surface of the tensile test at displacement rate of 10^{-5} mm/s under hydrogen cathodic charging on the pre-strained specimen.

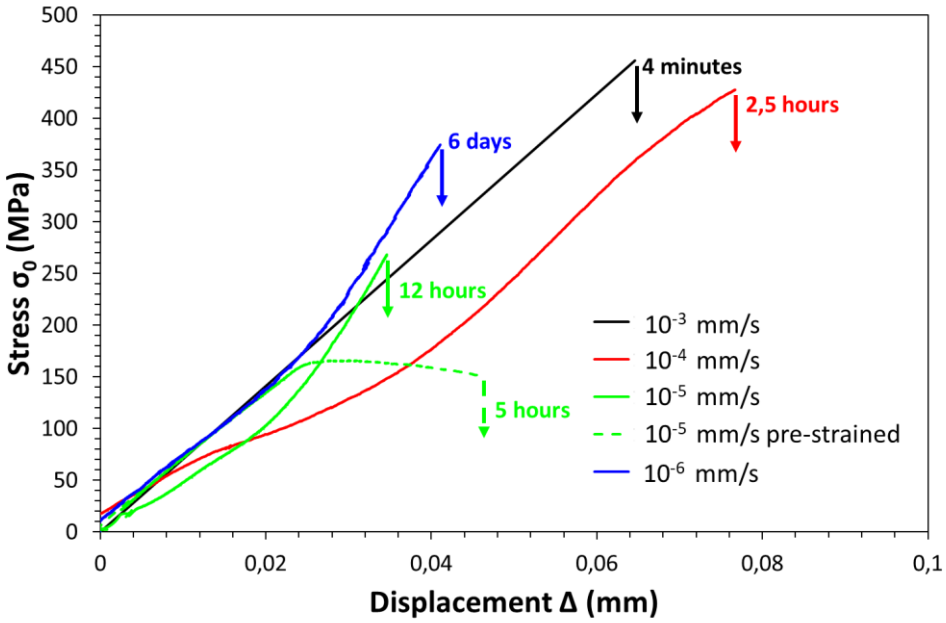

Figure 88 Stress-Displacement curves of tests at different displacement rates under hydrogen cathodic charging including the pre-strained specimen tested at 10^{-5} s^{-1}.

Table 14 summarizes the results obtained from slow strain rate tests in this part. Distances and areas were measured by ImageJ software. $f_{IG/TG}$ is the fraction of the mixed intergranular/transgranular fracture surface on the total fracture area, a_{max} is the deeper depth of the mixed mode crack through the specimen, and da/dt is the crack growth rate assessed from a_{max} and the total duration of the tensile test. The stress intensity factors in the last column are calculated from equation (17) in the 4.1.6 paragraph. The crack length considered here is the one of the mixed IG/TG mode of cracking which corresponds to the sub-critical regime of propagation. Since the crack is not axisymmetric, the values calculated here are certainly slightly overestimated.

Table 14 A table presenting for each displacement rate, the mixed intergranular/transgranular fracture percentage, the depth of the IG/TG crack with respect to the radius of the specimen, and the IG/TG crack growth rate. The stress intensity is calculated based on the IG/TG crack depth.

V_t (mm/s)	Fraction of IG/TG mixed mode of cracking $f_{IG/TG}$ (%)	TG fraction inside IG/TG mode f_{TG} (%)	a_{max} (µm and % of the specimen radius R)	da/dt (mm/s)	Duration	Stress intensity factor (MPa√m)
10^{-3}	0	0	0	0	4 minutes	-
10^{-4}	50.5	22	1016 µm (59.8% R)	$1.13x10^{-4}$	2.5 hours	13.8
10^{-5}	50.0	15	949 µm (64.8% R)	$2.25x10^{-5}$	12 hours	9.7
10^{-5} (pre-strained)	87.5	22	1700 µm (100% R)	$8.54x10^{-5}$	5 hours	10.8
10^{-6}	1.5	32	256 µm (15.1% R)	$4.80x10^{-7}$	6 days	8.3

6.2.4. EBSD analysis of crack path in the microstructure

EBSD analysis on the cracking path was carried out on the tensile specimens corresponding to displacement rates of 10^{-3}, 10^{-5} and 10^{-6} mm/s.

The cross section perpendicular to the fracture surface of the specimen tested at 10^{-3} mm/s is presented on Figure 89. It shows a little secondary crack of around 10 µm depth under the main fracture surface. According to EBSD data, the crack starts between two packets or blocks of strong misorientation then forks along a packet. The main crack seen in section passes through the packets of laths without following a preferential path of strong misorientation, for instance between packets, blocks or sub-blocks. The laths are broken within the packets or blocks, crossed by the crack.

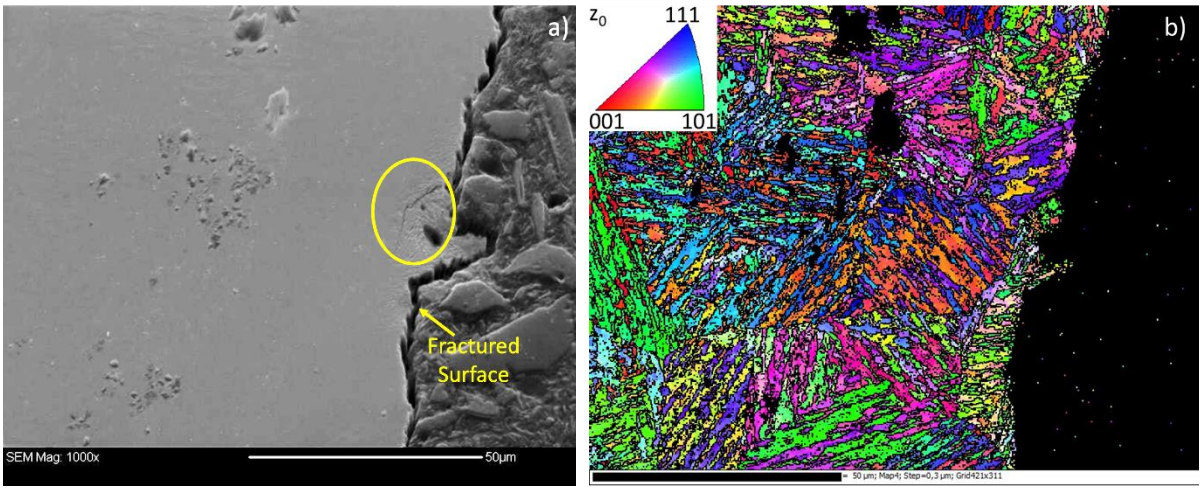

Figure 89 Cross section of the fracture surface of the 10^{-3} mm/s specimen showing in a) a TG crack in a secondary electron image, and b) EBSD IPF map of the same area.

On Figure 90 is presented the cross section that corresponds to the pre-strained specimen tested at the 10^{-5} mm/s; it shows the mixed intergranular/transgranular cracking mode along a secondary crack. The intergranular cracking path corresponds obviously to the former austenitic grain boundaries while the transgranular crack path corresponds to cracking between blocks and packets of the martensite microstructure. Figure 90c shows more precisely on a zoomed part of the fracture surface these two cracking modes. One should also remark that all stopped cracks under the main fracture surface correspond to this mixed inter/transgranular mode of cracking. It means that this mode of cracking is sub-critical while the entirely transgranular cracking mode corresponds to the last fast fracture stage of the specimen.

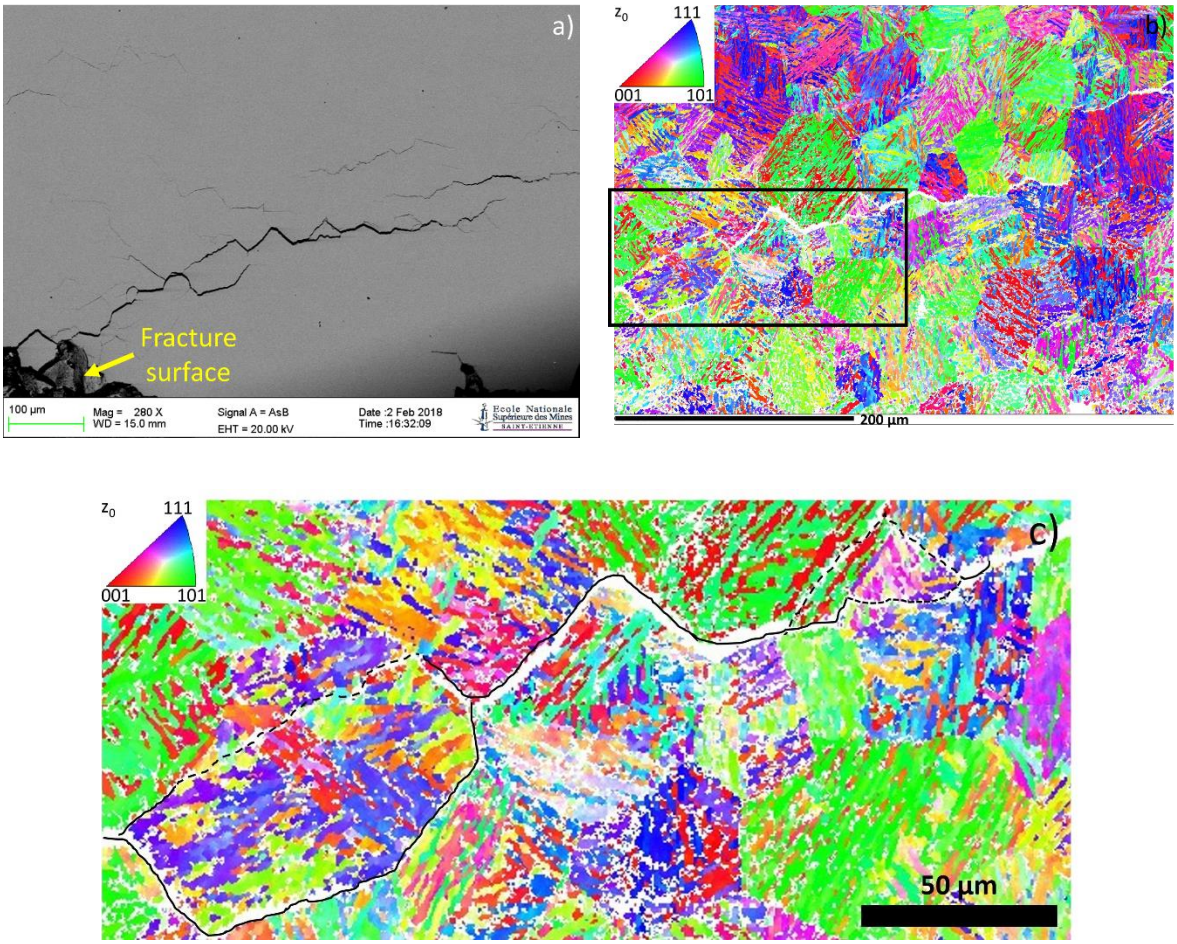

Figure 90 Cross section of the fracture surface of the 10^{-5} mm/s specimen showing in a) IG/TG crack path in a secondary electron image, and b) EBSD IPF map of the same area c) zoomed image on an intergranular (full lines) and transgranular (dashed lines) cracking path.

The distribution of crystallites misorientations on both sides of the cracking path was determined using EBSD data. Figure 91 shows the frequency of the point-by-point survey according to the classes of misorientation. One can notice that the most important frequencies concern the high angle misorientations. The class [4°, 8°] counts also a significant number of misorientations.

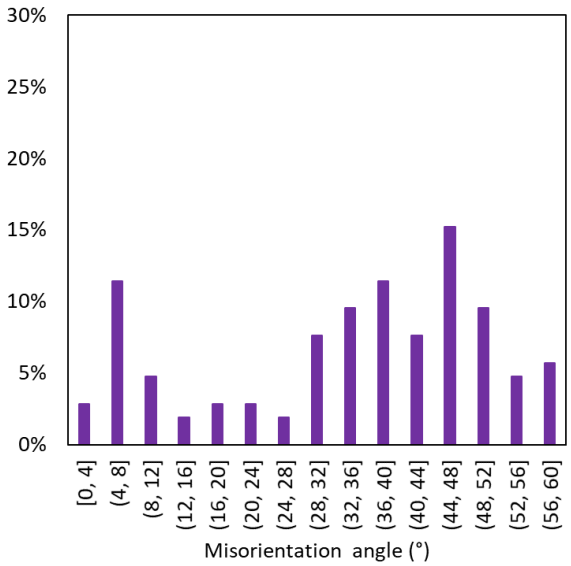

Figure 91 Misorientation angle distribution across the crack shown in Figure 90 of the 10^{-5} mm/s specimen.

While for the misorientation between blocks, the options are: 49.47°, 60° and 70.5°, the misorientation between packets can be characterized by more angles, as listed here : 10.53°, 14.88°, 20.61°, 21.06°, 47.11°, 49.47°, 50.51°, 51.73° and 57.21° [43] [42]. Our results thus show that the crack follows paths of strong misorientation, either they are old γ-grain boundaries or other types of interfaces of strong misorientation among packet boundaries, block or sub-block boundaries.

The last crack path analysed by EBSD is the one corresponding to the $V_T = 10^{-6}$ mm/s specimen which showed a very short mixed IG/TG cracking. Fracture surface presented on Figure 92 corresponds to the transgranular part after the short IG/TG crack. One can observe numerous features of ductility like tearings and dimples both with brittle TG facets. Secondary cracks are also visible here, and that is what we focused on with EBSD analyses.

A cross section was done and we identified six secondary cracks, here we present three of them (Figure 93). The cross sections show two secondary cracks following inter-packet and inter-block crack path, and one secondary crack propagated along inter sub-block path. These cracks are not deep, just as suggested by observing the secondary crack left on the fractured surface (around 10 µm). The point-by-point survey of misorientations along the cracking path and following a constant step is reported on Figure 91. It is obvious that cracks follow paths of high misorientation between crystallites, as noted in the IG/TG cracking mode. Based on the average size of the old γ–grain, extensive examination of the failure surfaces on the EBSD

mappings suggests that the crack has propagated through the inter-blocks and sub-blocks interfaces (Figure 93b, d, f). In contrast to the mixed mode, the pure transgranular propagation mode corresponding to the fast final fracture seems rather to correspond to a path of propagation independent of the different interfaces between "objects" of the microstructure (packets, blocks and sub-blocks), crossing the martensite laths within them. It is dependent on mechanical factors. Figure 82 corresponding to the test at 10^{-3} mm/s illustrates this result.

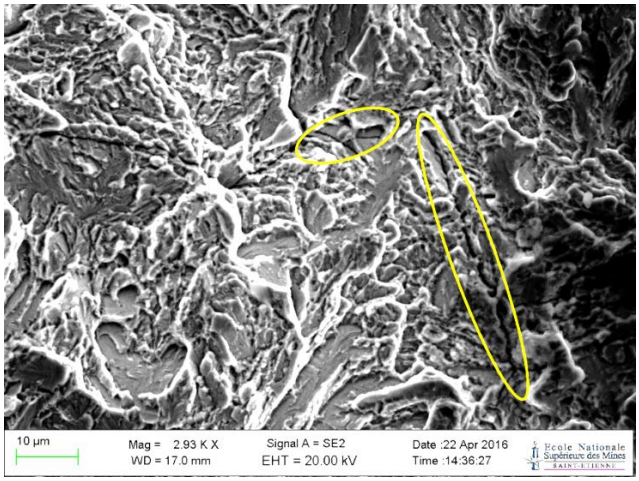

Figure 92 A transgranular fracture surface for the 10^{-6} mm/s tensile specimen, showing secondary cracks.

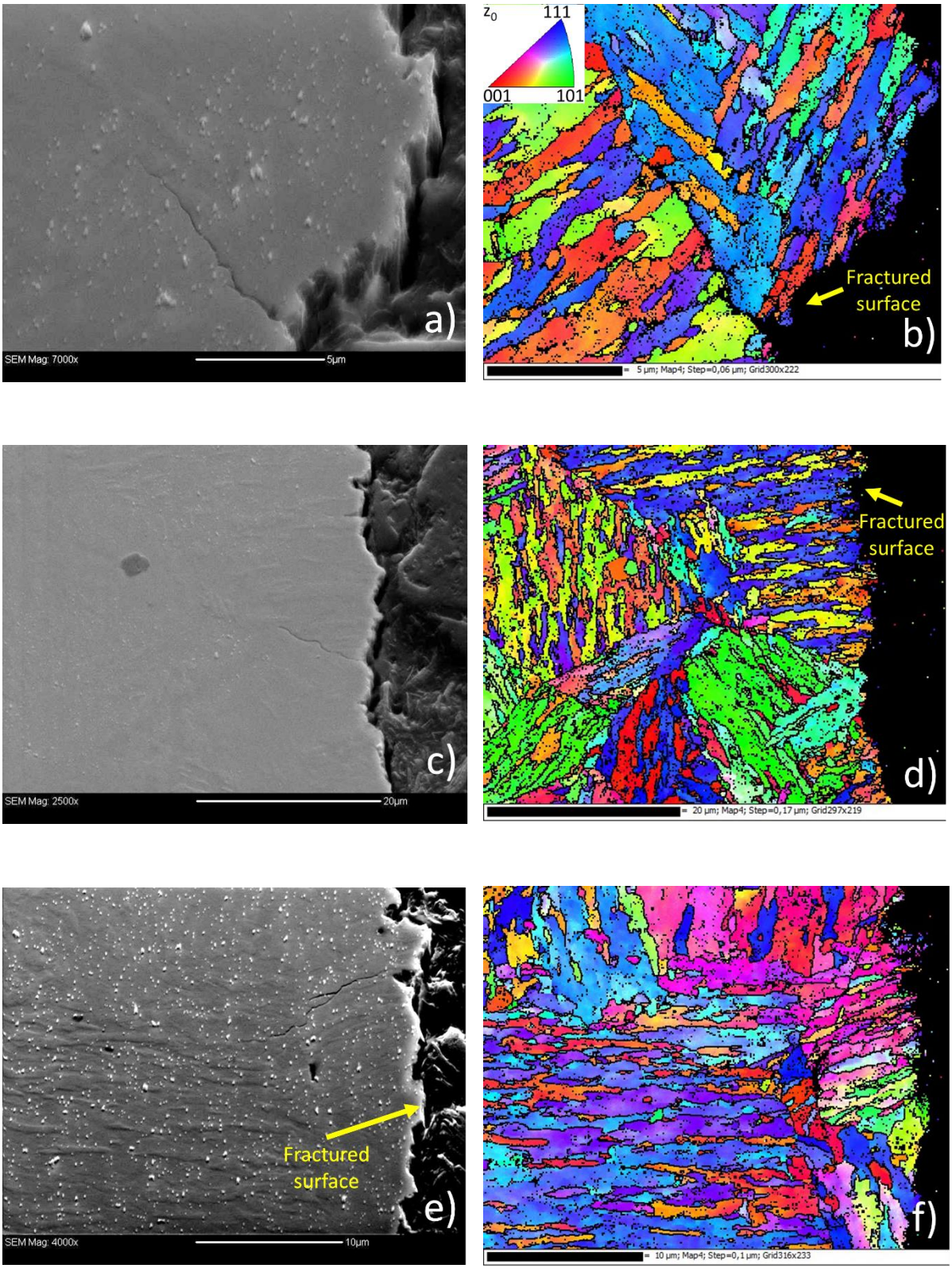

Figure 93 SEM images of the 10^{-6} mm/s specimen showing in a) c) and e) secondary electron images of the cross sections and the cracks, and in b) d) and f) their respective EBSD IPF maps.

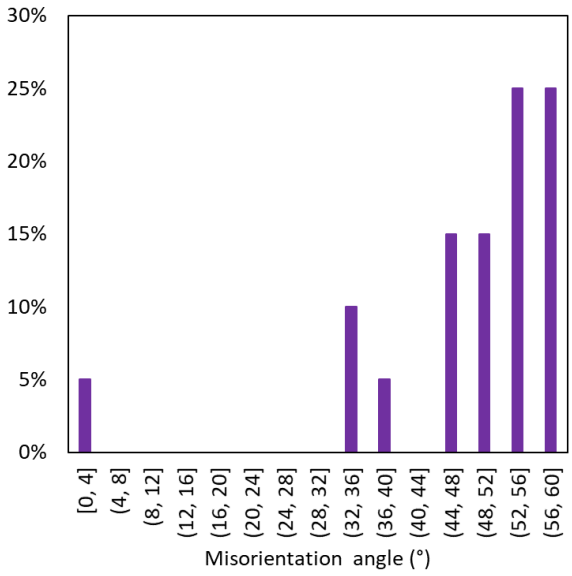

Figure 94 Misorientation angle distribution across the crack shown in Figure 93 of the 10^{-6} mm/s tensile test.

6.2.5. Summary

Slow strain rate tests on notched specimen showed a detrimental effect of hydrogen cathodic charging on the fracture stress, decreasing it by a factor of five or more, as compared to that in air. As expected, crack initiation occurred at the notch tip where both a high stress triaxiality rate and a plastic deformation develop in the process zone, favouring both hydrogen diffusion and trapping. However, crack initiation is not systematic throughout the periphery of the specimen. Only one or two sites are observed, the crack propagating thus asymmetrically.

Crack initiation is relatively fast, as compared to the total duration of the tensile test. This can be seen very well on the pre-strain test at 10^{-5} mm/s where the crack is very deep, and on the others, by the non-linearity of the curves, which finally occurs rather early at the beginning of the test. The crack advance occurs according to two regimes of propagation, a subcritical regime corresponding to a cracking mode both intergranular and transgranular, and a critical regime conducing to final fracture of the specimen. The later corresponds to a transgranular cracking with numerous ductile features at the same time as more brittle zones such as quasi-cleavage facets. The main characteristic of the transgranular mode in the mixed IG/TG is that cracking path follows mainly high misorientation interfaces, which suggests packet and block boundaries of high misorientations. Lower misorientations have nevertheless been also observed and should not be excluded. The mixed IG/TG mode of cracking can thus be defined

as a sub-critical mode of cracking, following high misorientation interfaces in the martensitic microstructure.

The IG/TG crack depth depends strongly on the strain rate applied. At 10^{-4} and 10^{-5} mm/s (which correspond to about 10^{-5} s^{-1} and 10^{-6} s^{-1} at the notch tip at the beginning of the test), the crack length reached about 1 mm, which is much greater than the theoritical diffusion distance previously calculated for the 24 hours hydrogen pre-charging, and adding up the duration of the traction itself (D = 6.38 10^{-14} m^2/s). Table 15 gives the value of hydrogen diffusion distance during these times. The discrepancy between values suggests that an alternative mechanism to the hydrogen diffusion takes part in the transport of hydrogen in the maraging steel. Nevertheless, by comparing the tests, in particular the two tests at 10^{-5} mm/s with and without pre-staining, but also with the others, the hydrogen transport by dislocations does not seem to explain by itself this alternative mechanism since no clear correlation is relevant with the strain rate of the tensile tests, particularly the mode of cracking. This point will be discussed later.

Finally, a pre-straining substantially increases the hydrogen embrittlement. The deepest mixed IG/TG crack was observed in these conditions.

Table 15 Theoritical diffusion distance of hydrogen during cathodic pre-chaging and tensile test duration, compare to brittle crack propagation.

V_t (mm/s)	10^{-3}	10^{-4}	10^{-5}	10^{-5} (pre-strained)	10^{-6}
Duration (H pre-charging + tensile test duration)	24 h + 4 minutes	24 h + 2.5 hours	24 h + 12 hours	24 h + 5 hours	24 h + 6 days
a_{max} (mixed IG/TG crack) (µm)	0	1016	949	1700	256
Hydrogen diffusion distance $x = 2\sqrt{D\,t}$ (µm)	150	156	182	163	392

6.3. Constant load tests

In this series of tests, the loads were applied before the cathodic charging of hydrogen. The loadings targeted the double aim: to slightly plastically deform the material at the notch tip

with relatively low levels of stress (σ = 550 MPa, with $\sigma = F/S_0$, F is the applied load and S_0 is the minimum section), and to gradually increase the load to high values but below the mechanical strength of the steel (σ = 1000 MPa and 1500 MPa), thus modifying the trap density in the material, and their nature. Finite element calculations have shown that at 550 MPa, the plastic strain at notch tip reached around 1.4% to 1.6%, which actually corresponds to the level of homogeneous plastic deformation where no mechanical damage are expected. At higher stresses, both large plastic deformation and mechanical damage, i.e., formation of micro-cavities, have certainly occurred.

6.3.1. Effect of stress on hydrogen embrittlement

Figure 95 shows the load *vs* time curves of the three tests at 1500, 1000 and 550 MPa. We recall that the load was applied 2 to 3 hours before hydrogen charging to allow stress relaxation without hydrogen effects at this stage. When the slight relaxation of the sample is achieved, the specimen is loaded again at the targeted stress value and the cathodic potential is applied. The vertical dashed line corresponds to the starting of the cathodic charging for all the tests (Figure 96).

The results show that the lower the applied stress, the more delayed the fracture.

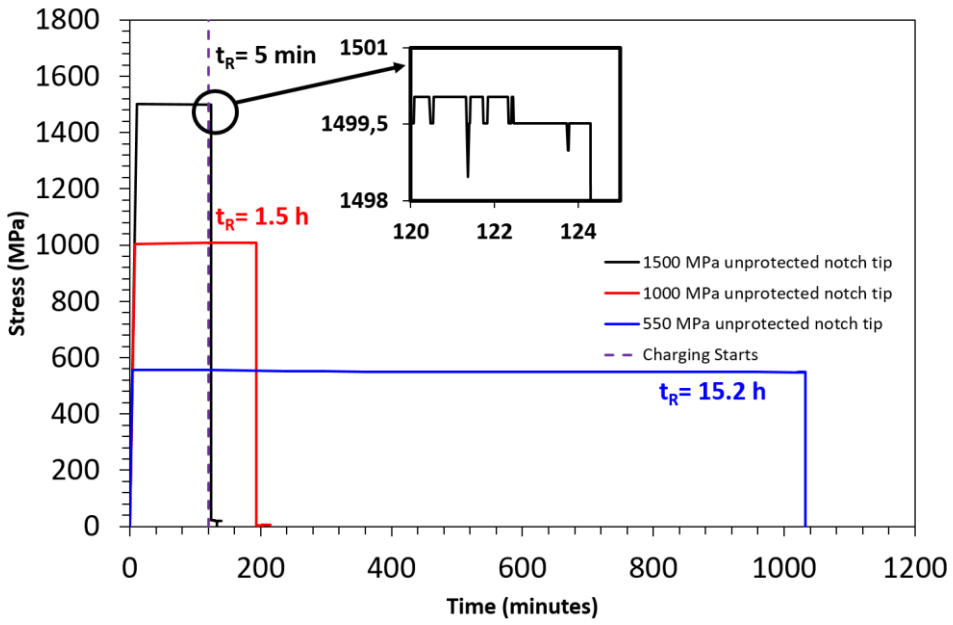

Figure 96 Stress vs time curves of constant load tests under cathodic hydrogen charging.

6.3.2. Fracture surface analysis

The fracture surface analysis of the specimen loaded at 1500 MPa is shown on Figure 97. A single initiation site is present. The crack has propagated following the mixed intergranular/transgranular mode on around 204 µm depth, suggesting a sub-critical crack propagation before the fast final fracture. The corresponding crack growth rate is equal to da/dt = 6.8×10^{-4} mm/s. The critical crack leading to the final fracture is purely transgranular with both brittle facets and ductile features just as observed on the slow strain rate tensile test specimens.

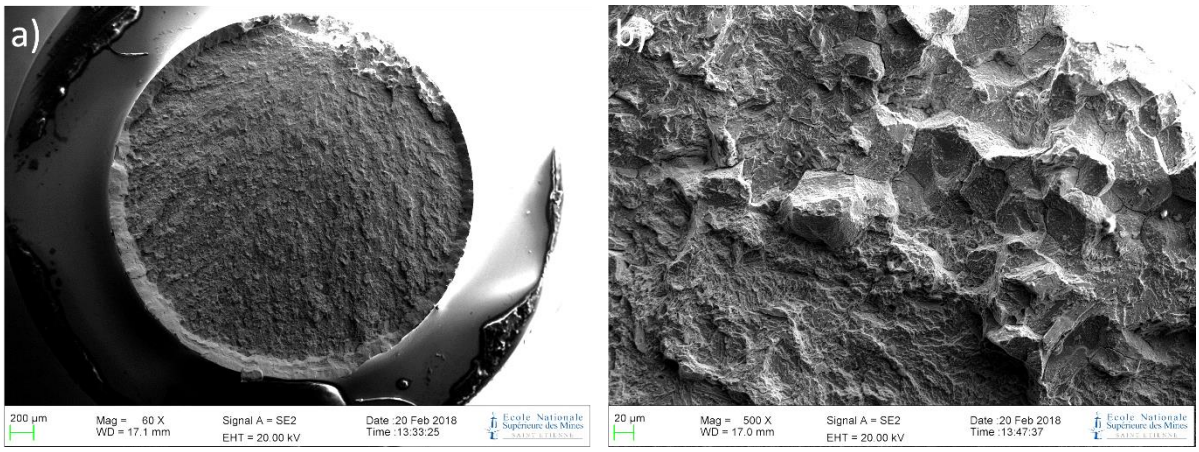

Figure 97 Fracture surfaces of the specimen loaded at 1500 MPa under cathodic charging of hydrogen.

For the 1000 MPa loaded specimen, the crack initiation is also localised on a single site and follows a sub-critical mixed IG/TG path on around 243 µm depth. The corresponding crack growth rate is equal to da/dt = 4.5×10^{-5} mm/s (Figure 98).

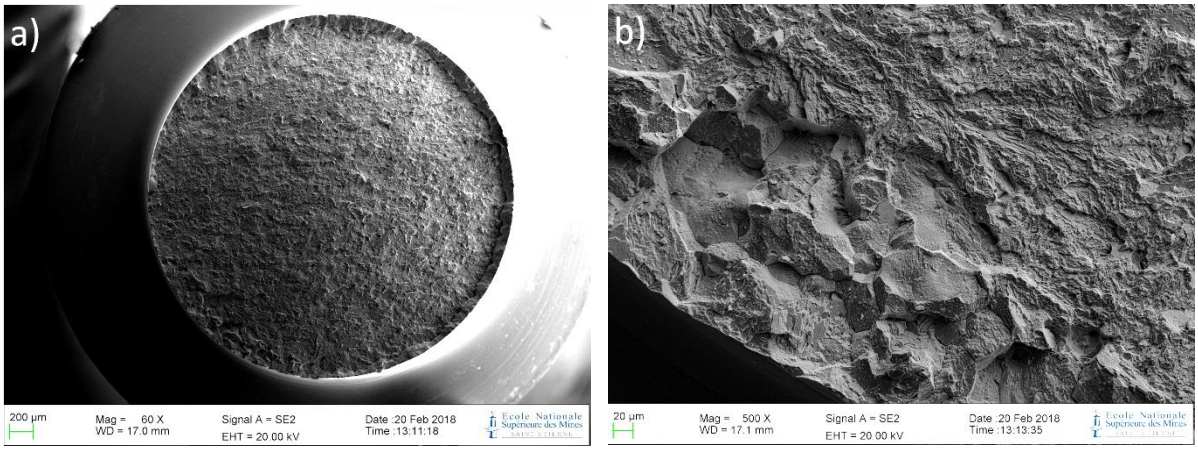

Figure 98 Fracture surfaces of the specimen loaded at 1000 MPa under cathodic charging of hydrogen.

Finally, the 550 MPa loaded sample presents a small mixed intergranular/transgranular zone located at the initiation site; the maximum crack depth is 80 µm (Figure 99b). The rupture is then predominantly transgranular, where ductile features like dimples and tearings appear mixed with brittle facets as previously described for slow traction tests (Figure 99c and d). The sub-critical crack growth rate in this case is equal to da/dt = 1.46×10^{-6} mm/s.

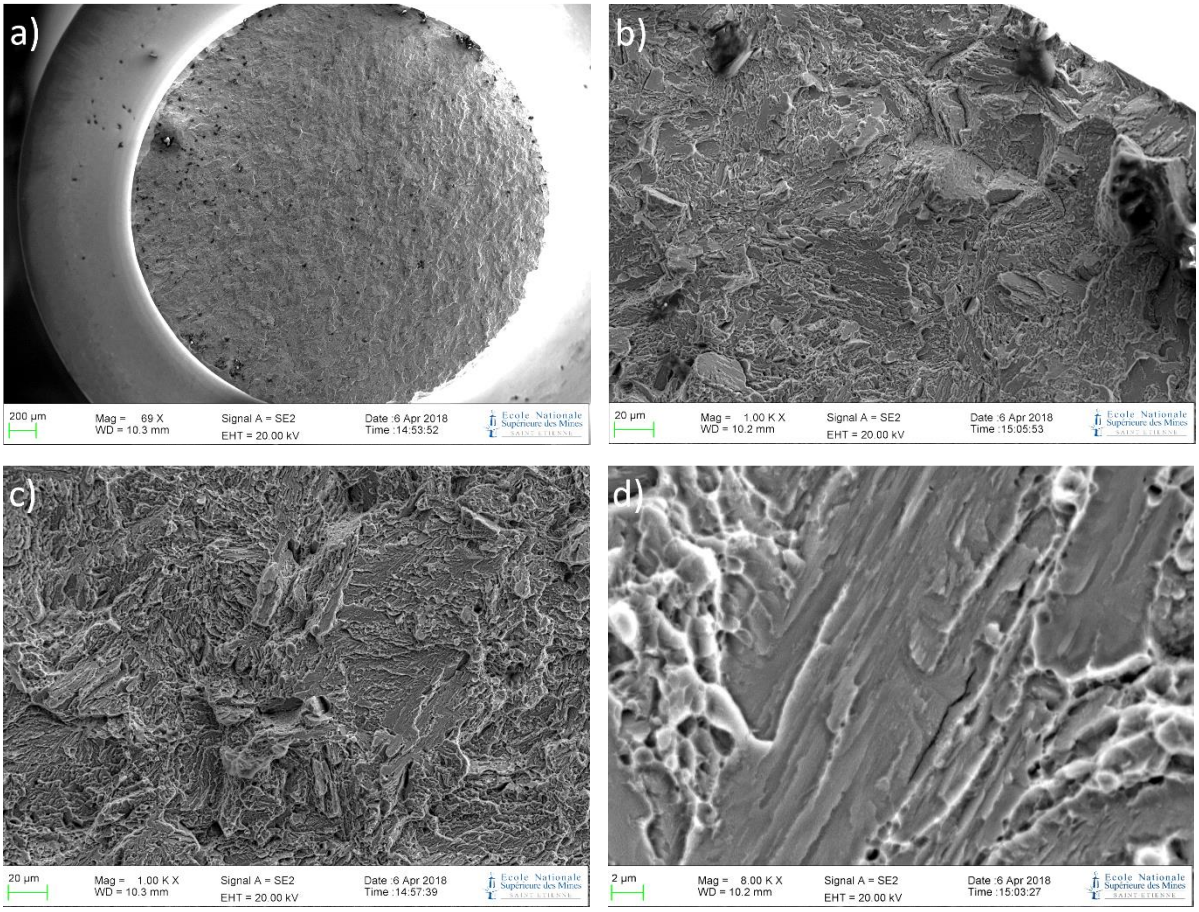

Figure 99 Fracture surfaces of the specimen loaded at 550 MPa under cathodic charging of hydrogen.

6.3.3. Summary

Constant load tests showed a less detrimental effect of hydrogen on IG/TG subcritical cracking than dynamic slow strain rate tests. The crack depths are reported in the Table 16 and compared to the theoretical diffusion distance of hydrogen in the material.

Table 16 Theoritical diffusion distance of hydrogen during constant load test duration, as compared to IG/TG subcritical crack propagation.

Loading (MPa)	1500	1000	550
Test durations	5 minutes	1.5 hours	15.2 hours
a_{max} (mixed IG/TG crack) (µm)	204	243	80
Hydrogen diffusion distance $x = 2\sqrt{D\,t}$ **(µm)** (with D=6.38 10^{-14} $m^2.s^{-1}$)	8	37	118

The IG/TG crack depth is higher than the simple diffusion distance of hydrogen in these conditions, which suggests an alternative mechanism of hydrogen transport here again to explain such a deep embrittlement. Moreover, compare to the test durations in slow strain rate tests, the crack length are smaller. The static conditions of loading thus seem to limit the hydrogen embrittlement. This result is well known in many material/environment systems. The dynamic strain conditions are favourable in particular to the entry of hydrogen.

6.4. Constant displacement test

We recall in this part that the specimen was pre-loaded by applying a small constant displacement with screws. The specimen was then hydrogen charged in the corrosion cell, and crack initiated and propagated without further follow-up. The time to failure was about 30 minutes.

The fracture surface analysis of the constant displacement specimen (Figure 100) shows a single initiation site with a subcritical intergranular/transgranular crack that covers almost the whole surface. Insofar the specimen has been entirely fractured in about 30 minutes, the corresponding crack growth rate was estimated to around 10^{-3} mm/s. The ligament-crack leading to the final fracture is purely transgranular with both brittle facets and ductile features just as observed on the slow strain rate tensile test specimens. Figure 100b shows cracking at a triple grain boundary, with a trace of transgranular cracking following the blocks (see white arrows). Figure 100d, shows the profile of the crack propagating ahead of the notch tip.

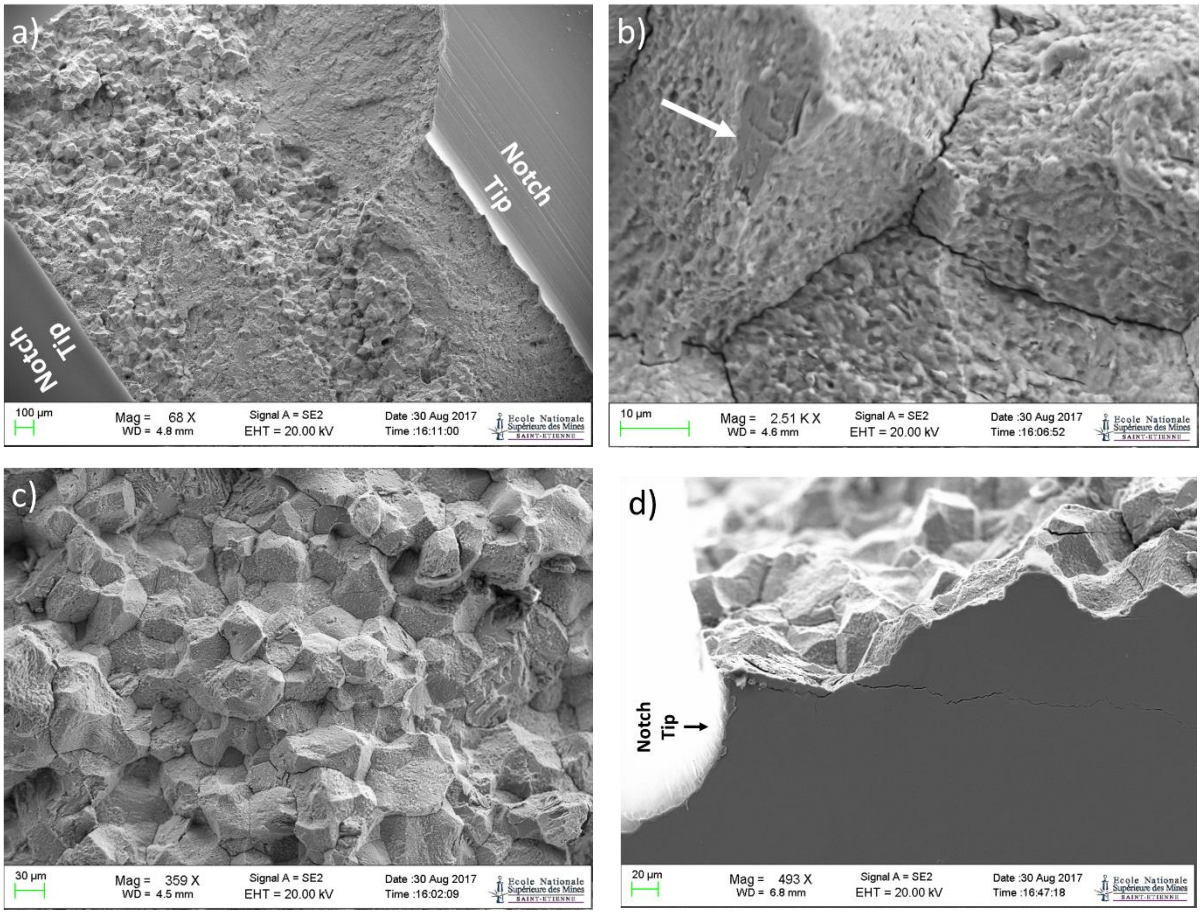

Figure 100 Fracture surfaces of the constant displacement specimen.

Figure 101 shows the EBSD IPF map of a selected area along the crack path. The maps show that the crack propagates preferentially following prior austenite grain boundaries. Transgranular crackings through and along blocks and sub-blocks are also observed. The distribution of the misorientation angles from either sides of the crack path is shown on Figure 102. Two groups of angle misorientation are observed, one containing angles from 0° to 12° and the other containing higher angles from 32° to 56°. The first group can correspond to crack path along blocks and sub-blocks, illustrated on the fracture surface by the transgranular part of the crack in the inter/transgranular mode of cracking. While the second group corresponds to the cracking along austenitic grain boundaries and block boundaries.

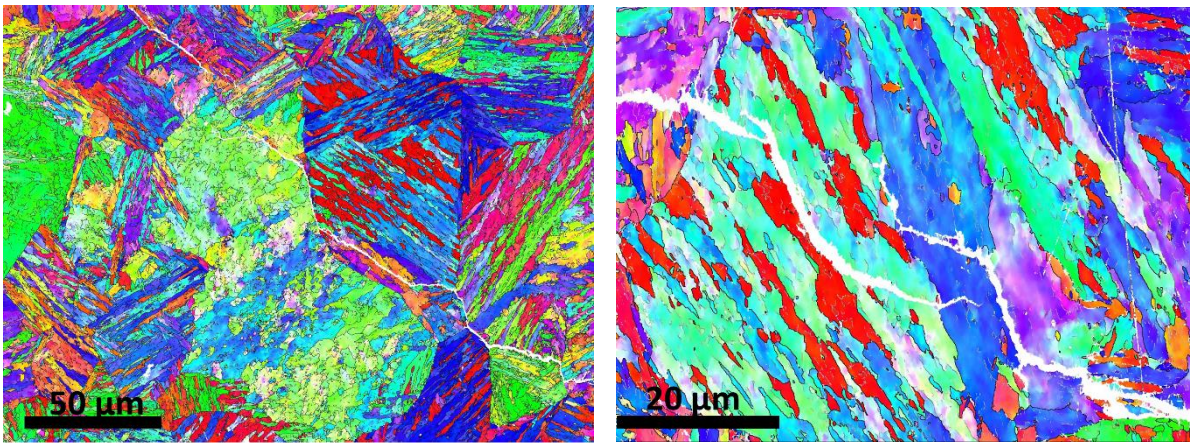

Figure 101 EBSD IPF maps in the cross section of the constant displacement specimen, highlighting the different cracking paths.

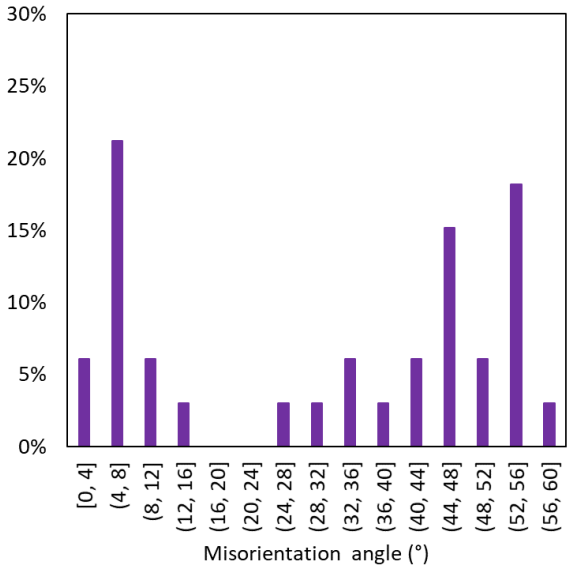

Figure 102 Misorientation angle distribution along the crack path shown in Figure 101.

6.5. Synthesis and discussion on effects of strain rate on hydrogen embrittlement

6.5.1. Hydrogen induced cracking paths

Effects of strain rate on hydrogen embrittlement were observed in many studies on maraging steels. Nageswara Rao *et al.* who conducted a study on a 18Ni2400 maraging steel in seawater and open circuit potential, have reported that notched tensile strength (NTS) decreases from 1086 MPa at $4.17x10^{-6}$ s^{-1} to 595 MPa at $2.10x10^{-7}$ s^{-1} [133]. This effect is visible to a lesser extent during slow tensile tests in air for the lower strain rates, less than $8.33x10^{-7}$ s^{-1}. In both conditions, these results are attributed to hydrogen effects, related to the relative humidity for tests in air and to the hydrogen cathodic discharge in aqueous solution. In seawater, regardless of the strain rate, the dominant fracture mode is intergranular in the region of EAC, while in the final region fractured by overload, microvoid coalescence and quasi-cleavage constituted the main characteristics of cracking.

In different hydrogenating conditions, Bradhurst *et al.* found the same trends on four commercial grades of maraging steels investigated in NaCl solution at slow strain rate [134]. They reported that the strongest steel was also the most susceptible to hydrogen induced intergranular cracking. Furthermore, when hydrogen was removed by baking steels found again their original properties.

Santos *et al.* studied the hydrogen embrittlement of the 300 grade maraging steel in 0.6 NaCl solution at 10^{-6} s^{-1} and cathodic potential. Three heat treatments were investigated: peak-aging, over-aging which induces austenite reversion, and as solution annealed [132]. They reported that the mode of cracking of annealed and over-aged samples tested during hydrogen charging changed from ductile dimples to a mixture of ductile dimples and quasi-cleavage planes. On the contrary, in peak-aged samples, intergranular fracture was observed. They explain that at a low strain rate, diffusion and concentration of hydrogen into the material is predominantly at grain boundaries, and promotes intercrystalline fracture. They rely for that on the results of Wang *et al.* [106] who correlate the hydrogen content and distance of diffusion during slow strain rate tests at 10^{-7} s^{-1} under cathodic charging to the

depth of the intergranular + transgranular crack ring-shape, using the following equation for hydrogen diffusion distance:

$$x = \alpha\sqrt{D\,t} \qquad \textbf{(25)}$$

where x is the diffusion distance, α is a constant , t is hydrogen diffusion time, and D is the diffusion coefficient.

Reddy *et al.* reported that tensile properties and fracture mode of 18Ni 250 maraging steel were correlated with the quantity of hydrogen absorbed in the steel during the tests. They observed a change in fracture surface from ductile dimples to a mixed mode, intergranular separation and transgranular cleavage as the amount of absorbed hydrogen increased [135]. The tensile tests were done at constant displacement rate corresponding to a strain rate of about 10^{-3} s^{-1}.

The results of slow strain rate tests obtained in this study are partially in accordance with the data of the literature. The evolution of the cracking mode from the mixed intergranular/transgranular mode to the transgranular mode, with ductile features such as dimples and tearings, and quasi-cleavage facets is well observed. Likewise, the fracture stress decreases with the decreasing of strain rate, which induces an increase of this brittle mode of IG/TG cracking. Nevertheless, at the lowest strain rate, V_t = 10^{-6} mm/s, the subcritical IG/TG mode of propagation disappears for the benefit to the other mode. FE calculations have shown that this displacement rate corresponds to a local strain rate at the notch root of about 10^{-7} s^{-1}. At this strain rate, Nageswara et al. [133] and Wang *et al.* [106] observed this typical mode of cracking. Nonetheless, their materials of study differ from ours in that a fraction of reverted austenite is present at the end of their aging treatment. Wang argues in particular that hydrogen prefers to concentrate at the martensite lath or grain boundaries, where the reverted austenite is prone to nucleating. The enrichment of hydrogen in these regions decreases the cohesive strength between the boundaries, so the hydrogen-induced cracks are more inclined to propagate along the martensite lath or grain boundaries [106]. In our case on the contrary, the aging treatment parameters were chosen to avoid any reversion of martensite in austenite. No hydrogen enrichment other than trapping should be considered in these sites of the microstructure, including the interfaces of strong misorientations, as observed in fractographics analysis. According to Pressouyre [73], [91], hydrogen traps can be

considered as reversible if their energy is lower than 0.6 eV. The various trapping energies listed in Table 6 for each trap in martensite microstructures show that old γ-grain boundaries can be considered as reversible traps. Thus at sufficiently low strain rate, hydrogen could be released from the grain boundaries, that would contribute to increase the resistance to hydrogen embrittlement.

6.5.2. Effects of dynamic strain rate on hydrogen ingress

Constant load test have shown a stress relaxation over time of some megapascals. This testifies to the fact that specimen continued to deform, its plastic strain replacing the elastic strain of the testing system. The load drops with time at a rate which depends on the stress dependence of plastic strain rate for the steel. The plastic strain rate is given by the Orowan equation [136]:

$$\dot{\epsilon_p} = \Phi\, \rho\, \mathbf{b}\, \bar{v} \qquad \textbf{(26)}$$

where ϕ is a geometrical factor, ρ is the density of mobile dislocations, **b** is their Burgers vector, and $\bar{v}$ is their average velocity.

Hydrogen charging on specimens under constant loading was performed after a complete stress relaxation, which assumes that no more plastic deformation occurred when cathodic hydrogen charging was started. The conditions of hydrogen ingress were thus very different of the ones during slow strain rate tests. It is well known that hydrogen adsorption and absorption is dependent on the surface state and the boundary conditions of the material [137], [138]. Authors [139], [140]–[142] showed that hydrogen absorption is promoted by plastic deformation, resulting in a higher hydrogen content in the materials. Permeation tests also showed that plastic deformation promotes flux of hydrogen desorption [139] [138].

The small IG/TG crack length obtained at constant loading should be due to slow hydrogen ingress in the material as compared to the slow strain rate tests. The crack for test at 500 MPa loading in particular has lasted long enough to allow hydrogen depletion from the grain boundaries and reduce the IG/TG crack growth to a few tens of micrometers.

From the analysis of cracking during slow tensile tests, the chronological description of the advance of the crack could be established. Crack initiation occurs in the IG/TG mode at root

of the notch when the hydrogen concentration exceeds a critical threshold. The propagation is then subcritical and follows a mixed intergranular and transgranular propagation path, the latter mode seeming to be linked to a strong misorientation of the crystallites on both sides of the crack. When the crack reaches a critical length, which depends on the load applied and the duration of the test, the cracking enters in a fast regime and a transgranular propagation mode in which both transgranular facets, dimples and ductile tearings are combined.

To rationalize the results and consider the behavior of the material containing a crack, a stress intensity factor (K_I) has been calculated for each specimen, using the equation (15) presented in part § 4.1.6. K_I values were assessed with the different IG/TG crack lengths, loaded at the fracture stress. They are certainly slightly over-estimated insofar the subcritical crack propagation initiated at a lower level of stress. Nevertheless, they give a good estimation of the crack loadings. They are plotted as a function of the test duration, which actually is the time to failure. Figure 103 shows the results for slow strain rate tests and constant load tests under cathodic hydrogen charging (respectively black round dots and blue square dots) expressed as a function of the duration of the tests. They are added to points taken from works of Carter on a 350 grade maraging steel in 3% NaCl solution at OCP (pink triangular dots), and Rack *et al.* on a 350 grade maraging steel and He *et al.* on a 2800 MPa-grade maraging steel for toughness values in air (red rectangle) [126], [127], [143], [144]. The others points will be discussed later.

The critical stress intensity factor values follow a decreasing slope with time, with a range of K_I where time to failure seems more independent on stress intensity factors. This quasi time independent behaviour can be correlated with an essentially constant crack growth rate. Otherwise, short test durations significates that K_I is close to the toughness in air, estimated here at an average value of 35 MPa$\sqrt{\mathrm{m}}$. Actually, the value of toughness is essentially dependent on the temperature aging, and directly correlated to the fraction of reverted austenite [126]. The graph shows also the existence of a threshold stress intensity factor, under which no sub-critical propagation occurs. It is estimated at $K_{I\ threshold}$ = 8 MPa$\sqrt{\mathrm{m}}$. These results are in good accordance with the ones of Carter *et al.* obtained in NaCl solution at OCP [126], with nevertheless a shift of the quasi “time-independent” region on the time-axis. This could be attributed to a lower constant crack growth rate on the plateau in their case, or an increase in the incubation time for crack initiation if crack velocity and fracture toughness

(hence the critical crack length for ligament rupture) are similar in this comparison. If we compare the tests at slow strain rate and the ones at constant load in this study, the slight shift to higher time to failure for constant load tests can be attributed to an extended incubation time due to hydrogen ingress. It is also interesting to note that the threshold stress intensity factors are close together. Actually, Carter has observed the same behavior with different aging treatments leading to different fractions of reverted austenite.

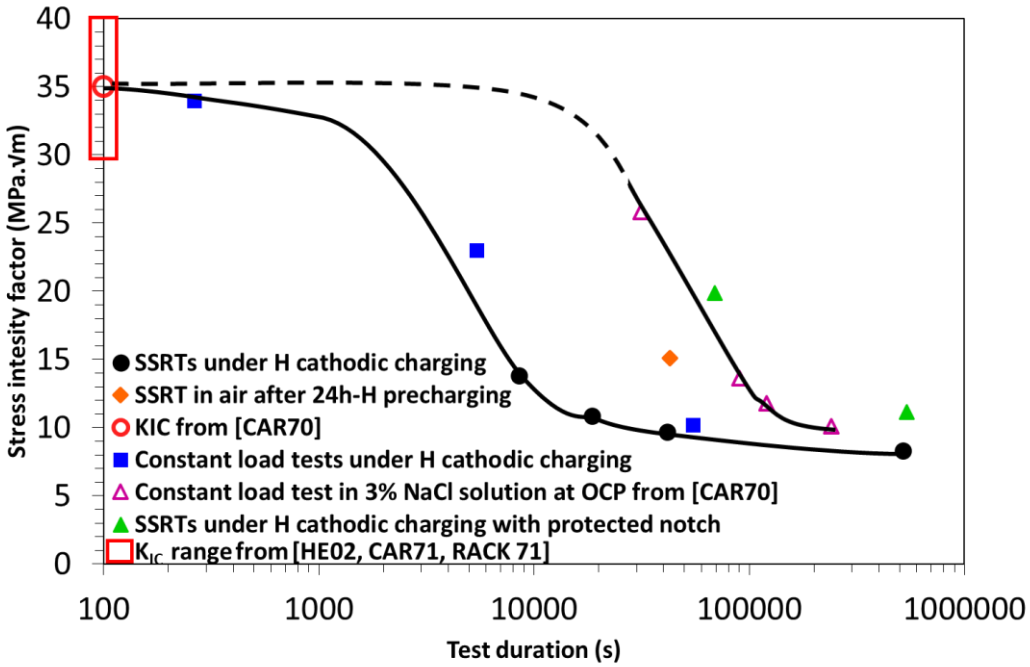

Figure 103 Stress intensity factor presented for different types of tensile tests and their corresponding durations (time to failure) in addition to the constant load tests, compared with the literature [126].

If we now consider our only test points in slow traction and constant load in Figure 103, the way in which the stress intensity factor was calculated can also be interpreted as the critical value K_{IH} from which the critical crack in pure transgranular mode is triggered. It is obvious that this critical value is even lower when the duration of hydrogen charging is long. On the other hand, the behavior of steel in these conditions does not seem to depend on the strain rate applied, but rather on the test duration.

The two Figure 104 and Figure 105 show the different cracking modes resulting from the hydrogen embrittlement of the 350 grade maraging steel: a subcritical IG/TG cracking mode for moderate at low strain rates governed by time-dependent factors, and a critical TG mode of cracking governed by mechanical-dependent factors.

At this stage, it is noted that the intergranular propagation mode is very rough. We will discuss a little further the reasons that can explain this "ductile" aspect of the grain boundaries and that has already been seen in the literature [94].

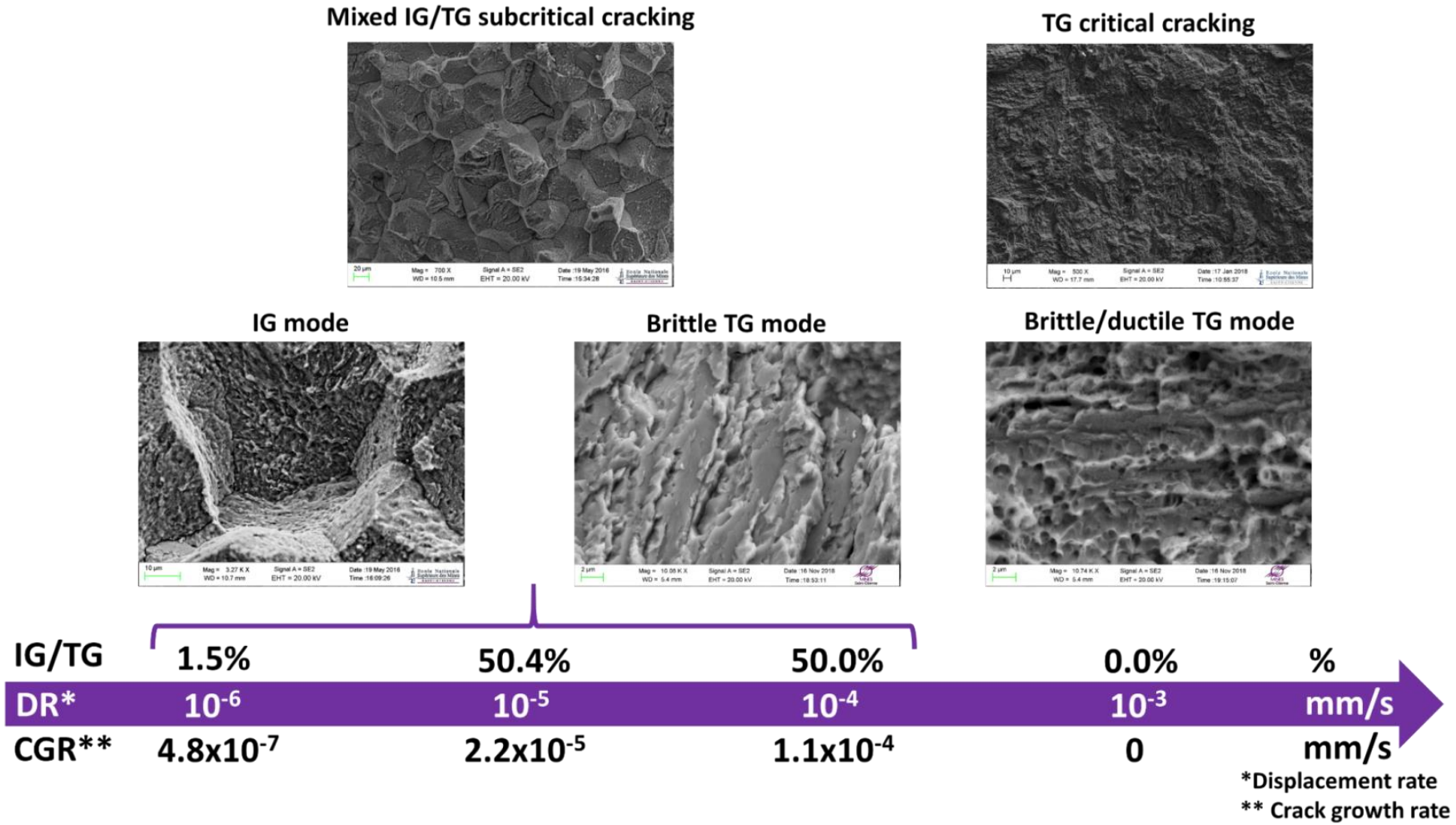

Figure 104: Evolution of cracking mode with displacement rate for slow strain rate tensile tests.

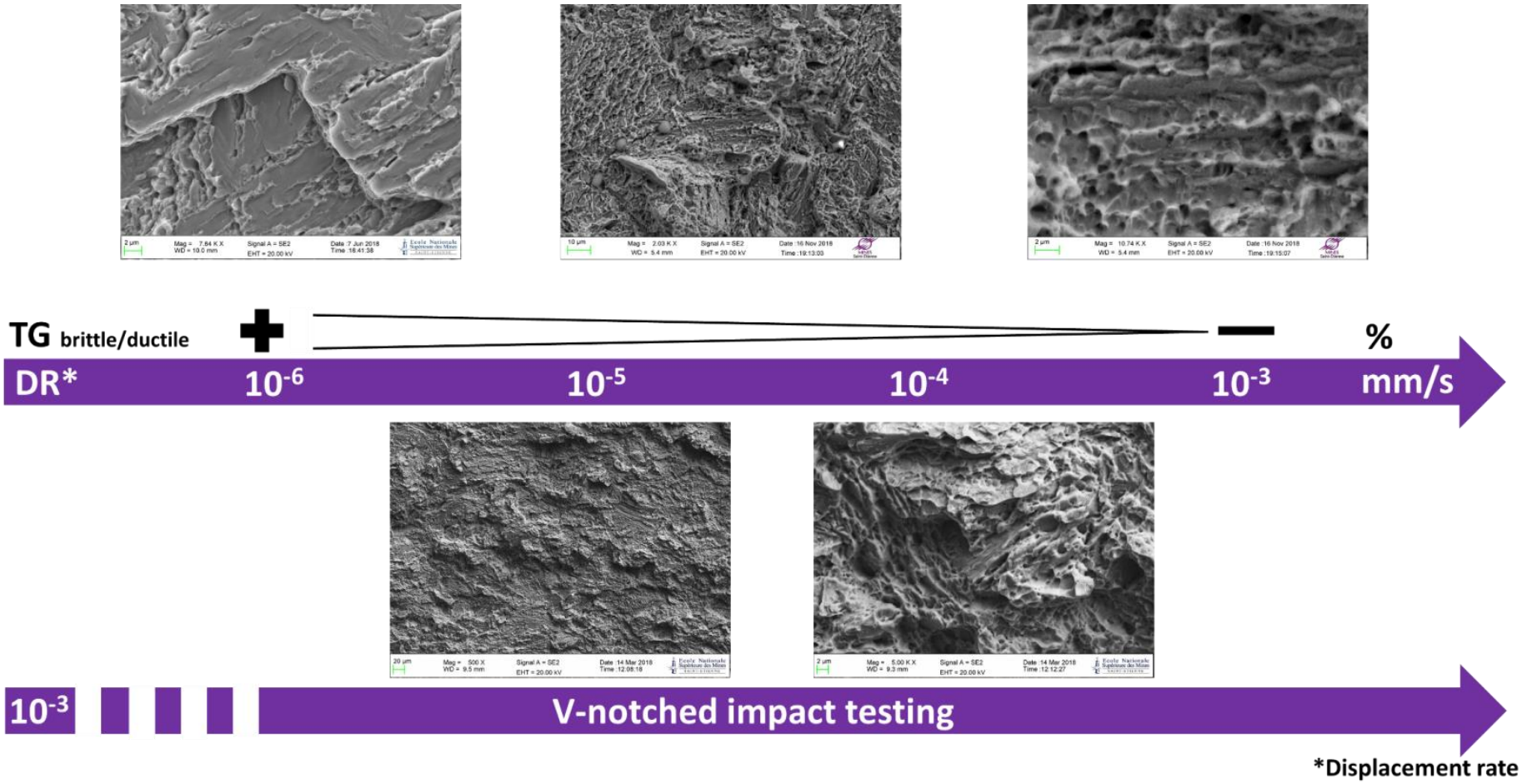

Figure 105: Evolution of critical transgranular cracking mode following the subcritical cracking mode at various displacement rates, from the lowest displacement rate (10^{-6} mm/s) up to V-notched impact tests.

6.5.3. Relation between crack growth rates and stress intensity factors

Figure 106 shows a range of stress intensity factors where time to failure seems more independent on this mechanical parameter. This quasi time independent behavior can be correlated with a constant crack growth rate. To verify this point, the crack growth rates assessed previously by considering both the length of IG/TG cracks and the total duration of the tests (we neglect the incubation time and the TG crack growth time) are plotted as a function of stress intensity factors in Figure 106. At dots corresponding to slow strain rate tests and constant load tests, are added the toughness values from the authors previously cited in Figure 103 [126], [127]. The duration of each test is indicated below each mark in brackets.

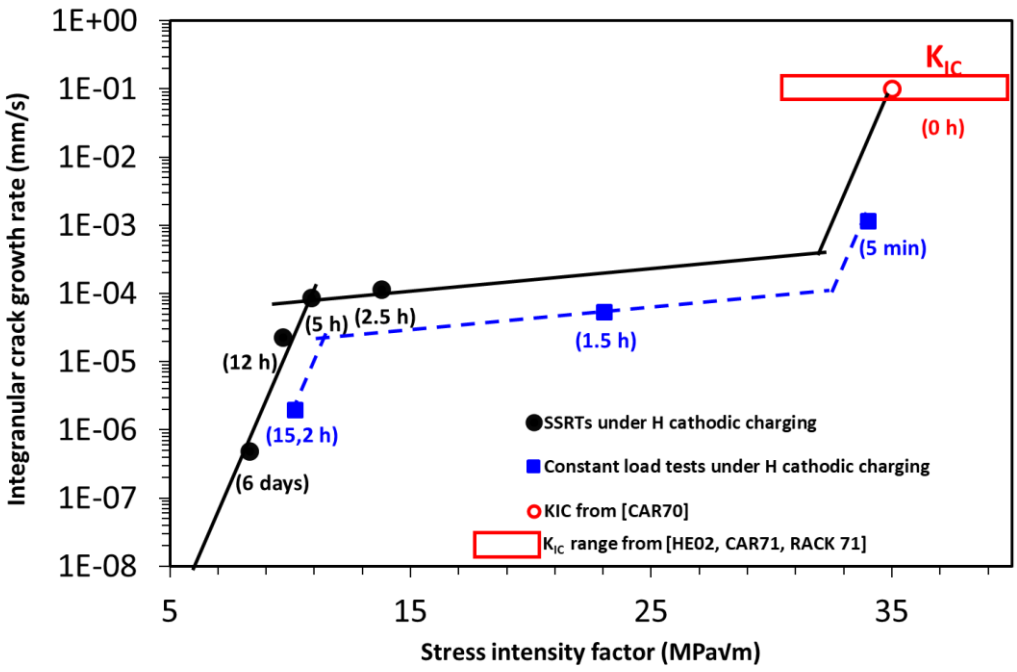

Figure 106 Mean intergranular crack growth rate versus stress intensity factor for different tests. Range of fracture toughness values in red.

The general shape of the curve is representative of environmental effects on crack growth rates in many systems material/environment. Three different stages appear beyond a threshold value of stress intensity factor $K_{Ith,}$ below which no measurable propagation is observed. In stage I crack growth rate rises sharply with increasing stress intensity factor due to mechanical control of damage in the process zone. In stage II, crack growth rate is

independent or slightly dependent of K_I due to reaction rates at the surface of the material and hydrogen diffusion in the bulk toward the process zone. Finally, in stage III, crack growth rate increases again with increasing stress intensity factor approaching the toughness of the material K_{IC}. In this last stage, mechanical ductile fracture damage adds up to environmental effect.

The behavior of the 350 grade maraging steel of this study is in good accordance with the literature. The works of Gangloff *et al.* in particular [108], [109], which are presented in the bibliographic review part, have also shown the existence of the crack growth rate plateau where time-dependent processes are more likely to occurs. The crack growth rates on the plateau in our case are ranged between 10^{-7} m/s and 10^{-6} m/s, which is one order of magnitude lower than in gaseous hydrogen [109] but quite similar to crack growth rates in NaCl solution [108].

6.5.4. Summary

We have demonstrated in this part that the mechanism of sub-critical crack propagation can be related to processes of hydrogen diffusion. The evolution of the crack growth rates with the stress intensity factor follows a classical behavior of environmental assisted cracking, with the existence of a plateau which can be the fact here of a hydrogen diffusion-assisted crack propagation mechanism. The slight difference between the crack growth rates measured in constant load tests and slow strain rate tests could be due to the conditions of hydrogen ingress, although the effect of hydrogen transport should not be ruled out. The existence of a threshold stress intensity factor is shown on the da/dt vs K_I curve. Likewise, the increase of crack growth rates with K_I at the end of the plateau seems to be related to the approach of the toughness, taken from literature data. By considering the fast final rupture of the remaining ligament, which follows a transgranular cracking mode melting brittle facets and ductile features, it has been shown that the critical stress intensity factor is dependent on the test duration, related to the hydrogen content in the material.

The next chapter is dedicated to a thorough study to explore the diffusion-assisted mechanism of cracking. The variation of cracking mode notably, suggests that intergranular hydrogen diffusion could play an important role, as trapping or de-trapping effects in grain boundaries.

6.6. Effects of hydrogenating conditions on hydrogen embrittlement

The objectives of this part is to highlight the role of intergranular diffusion of hydrogen in the embrittlement mechanism of maraging steel studied. For that, a series of slow tensile tests and constant load tests were performed again but with various hydrogen input conditions to explore on the one hand, the effects of internal hydrogen alone with hydrogen pre-charging before mechanical loading, and on the other hand, the effects of internal hydrogen while keeping of hydrogen source during traction. These conditions required a silicone protection inside the notch during the cathodic charging of the sample.

The same notched specimens were used to preserve the same effect of stress triaxiality on the "forced" diffusion of hydrogen towards the process zone. The two displacement rates chosen were $V_T = 10^{-6}$ mm/s and 10^{-5} mm/s.

6.6.1. Slow strain rate tests under internal hydrogen

- **Tests performed at displacement rate of 10^{-6} mm/s**

Figure 107 presents the stress *vs* displacement curves for the different charging conditions. The test named "24h precharged" refers to the test with the hydrogen pre-charging alone before the traction in air. The test named "24h precharged + cathodic with protected notch" refers to the test with silicone protection of the notch, while the other refers to a direct cathodic charging as seen previously. They are also compared with tensile test in air as a reference without hydrogen embrittlement.

Of all these hydrogenating conditions, the *in-situ* hydrogen charging condition is the most severe, while the test with a specimen only pre-charged for 24 hours gives a rupture stress of 900 MPa. Its fracture surface revealed no intergranular crack initiation; it showed transgranular mode of cracking with a lot of ductile features as presented in Figure 108.

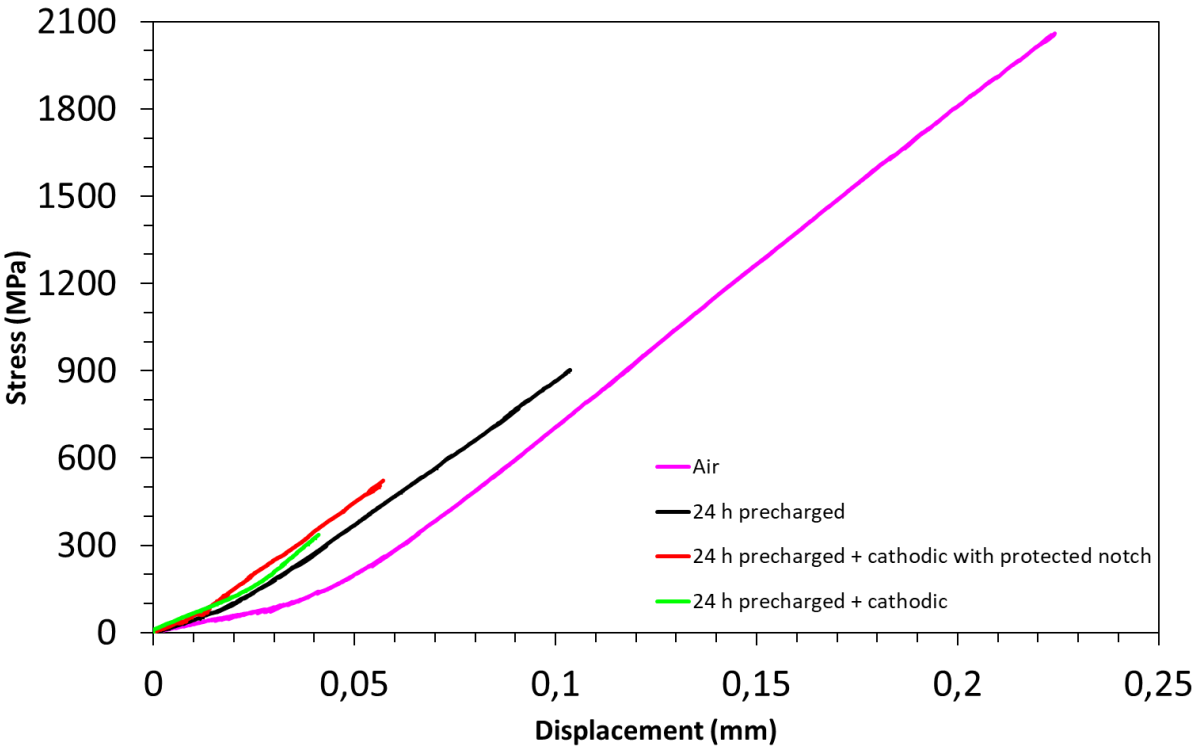

Figure 107 Effect of hydrogen charging conditions on fracture stress for tensile tests at 10^{-6} mm.s^{-1}.

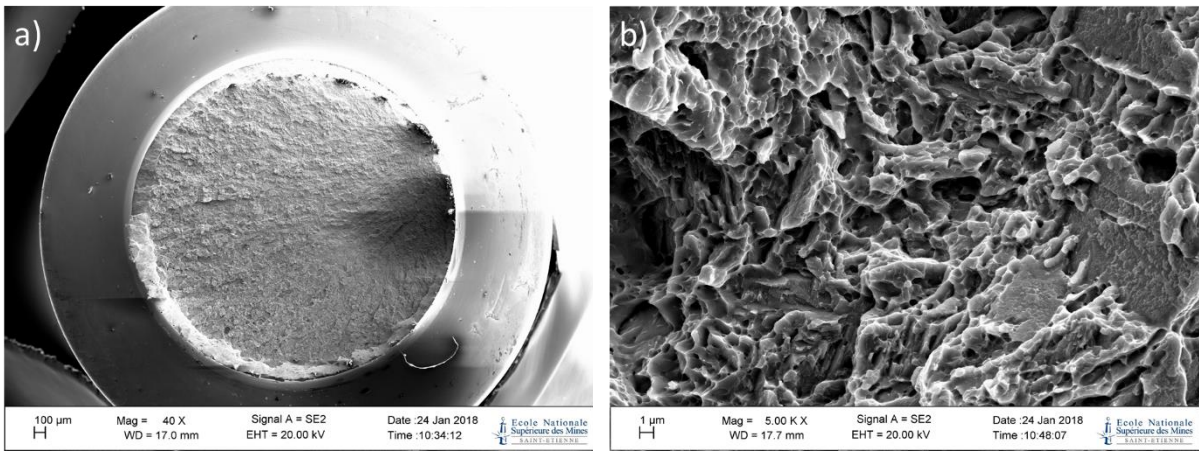

Figure 108 Fracture surfaces of the 10^{-6} mm/s test 24 h hydrogen pre-charged.

The sample "24h precharged + cathodic with protected notch" breaks at an intermediate stress equal to 512 MPa. The fracture surface shows a single initiation site on the periphery. It leads to the mixed intergranular/transgranular cracking mode on a relatively low depth of 150 µm, the surface of this mode covering only around 1 to 2% of the total surface. Considering the IG/TG failure mode as subcritical cracking and occupying most of the duration of the test, the crack propagation velocity was estimated to da/dt = 2.56x10^{-7} mm/s (see Figure 109). The transgranular mode of cracking shows a mixed ductile and brittle fracture as

previously described, with a larger proportion of decohesion zones at the beginning of propagation, which then decreases in favor of more ductile mode. On Figure 109e, one can measure the characteristic dimensions of a typical transgranular facet that seems correspond to the size of packets and blocks. Finally, these conditions lead to the same behaviour than the test done without notch protection in terms of cracking modes.

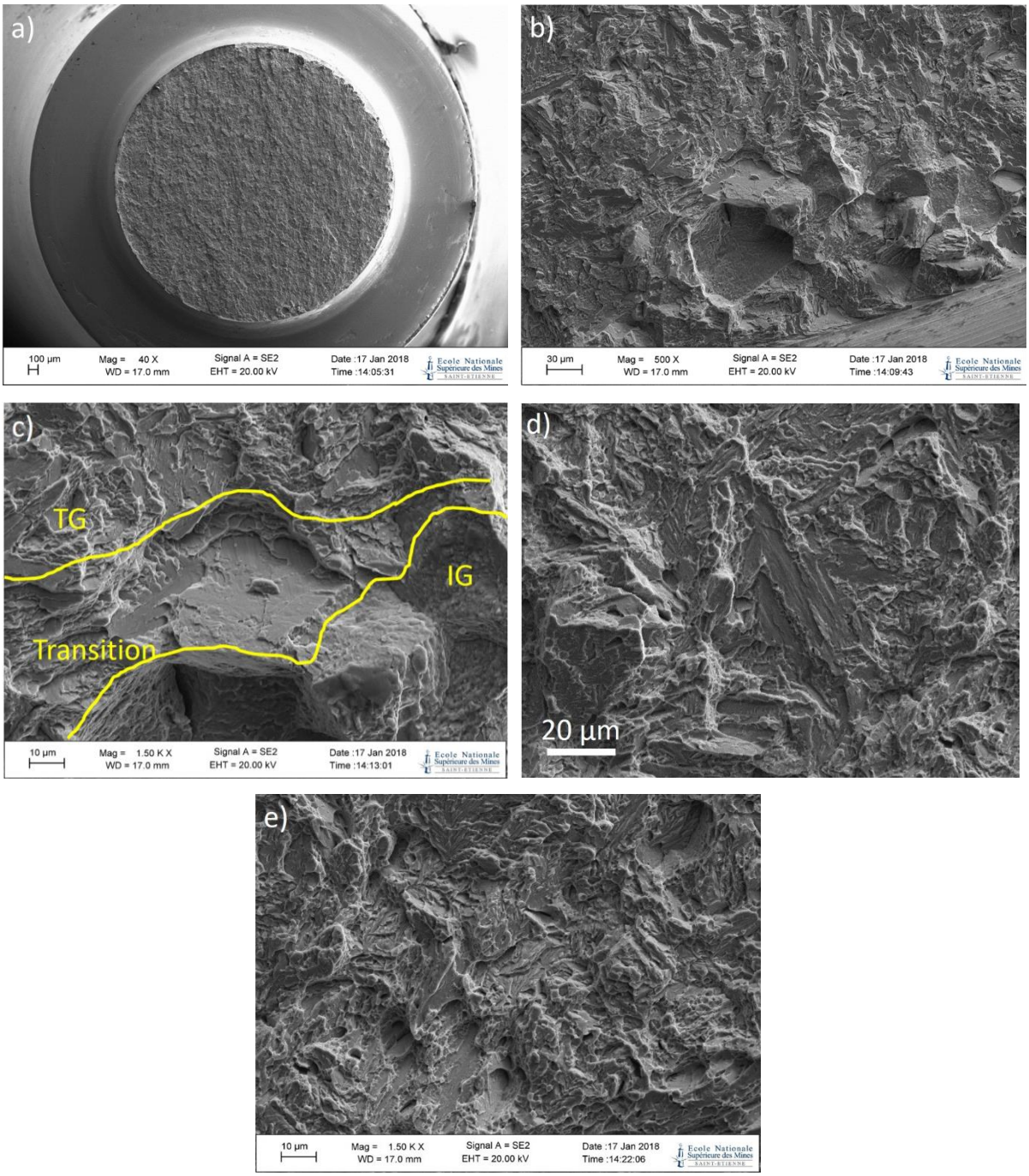

Figure 109 Fracture surfaces of the 10^{-6} mm/s test 24 h pre-charged + *in-situ* charging with protected notch. a) general fracture surface, b) IG/TG sub-critical crack initiation, c) magnification of the transition part, d) TG facet of the TG mode, e) ductile mode at the end of the TG crack (final ligament rupture).

- **Tests performed at a displacement rate of 10^{-5} mm/s**

Figure 110 shows the stress *vs* displacement curves at 10^{-5} mm/s. The same ranking than the one at 10^{-6} mm/s is found, but with lower rupture stresses.

The "24h precharged" specimen broke at 666 MPa and shows an intergranular crack initiation, as opposed to the 10^{-6} mm/s specimen. This mixed IG/TG crack propagated on a 140 µm-depth. The corresponding crack growth rate is equal to da/dt = 2.3×10^{-6} mm/s.

The pure transgranular crack, following the sub-critical crack, remains mostly ductile albeit facets of supposed inter-blocks and inter-packets decohesion are clearly visible as seen in Figure 111.

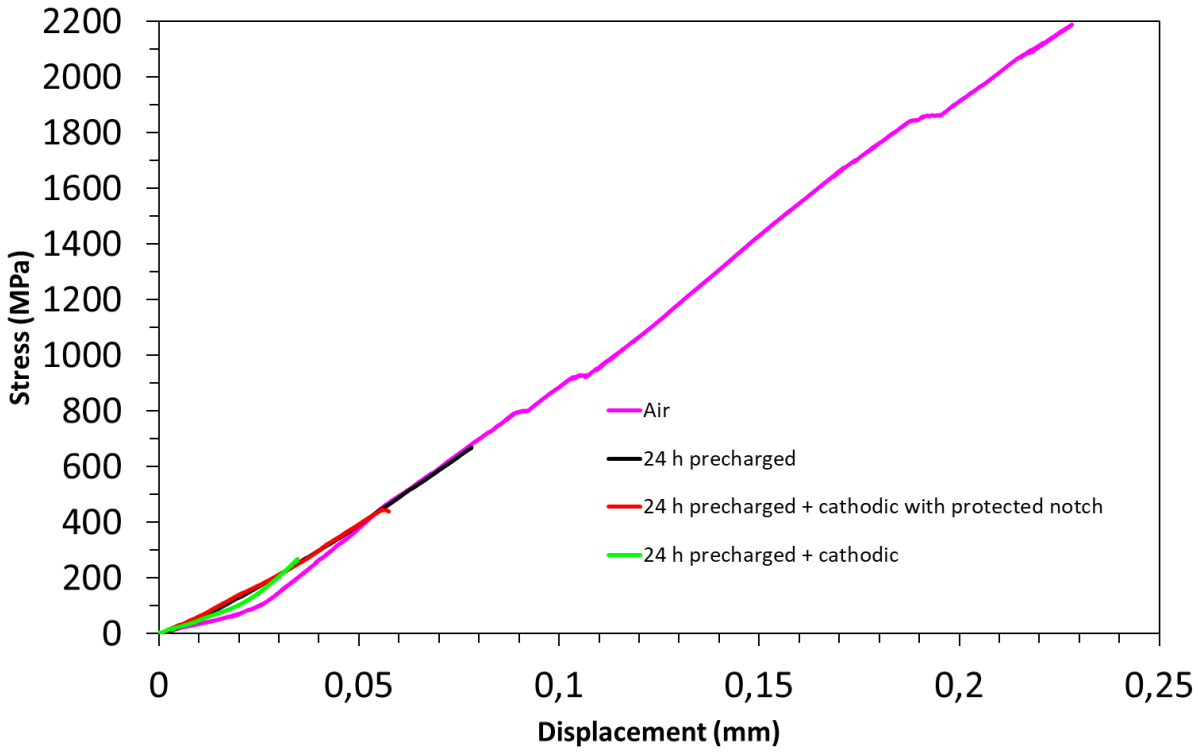

Figure 110 Effect of hydrogen charging conditions on fracture stress for tensile tests at 10^{-5} mm.s^{-1}

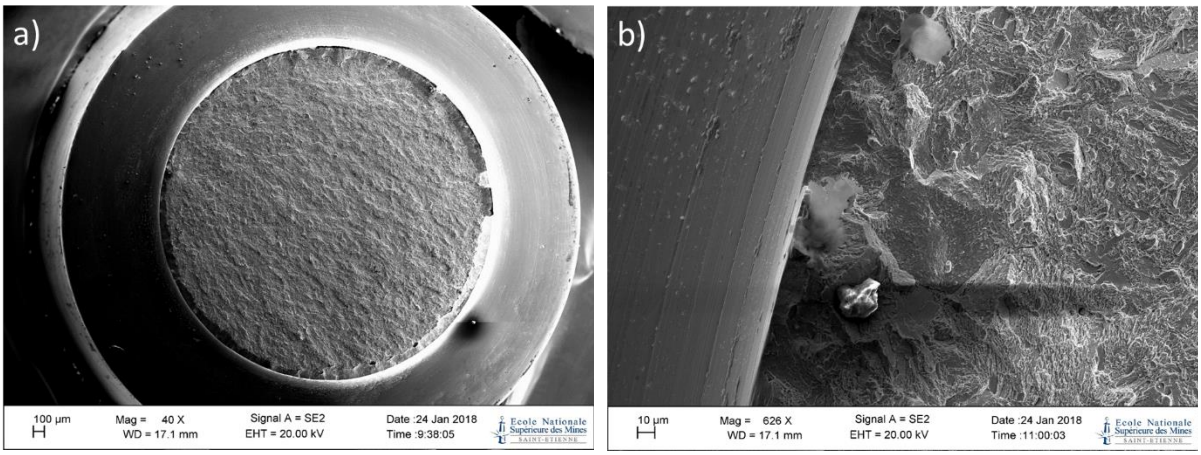

Figure 111 Fracture surfaces of the 10^{-5} mm/s test 24 h hydrogen pre-charged.

The test "24h precharged + cathodic with protected notch" presents a rupture stress higher than without protection, respectively σ_R = 439 MPa versus σ_R = 304 MPa. The fracture surface of the specimen presents a large mixed intergranular/transgranular fracture, covering around 30% of the total fracture surface. The maximum depth of this crack is equal to 1330 µm, which leads to a crack growth rate of around da/dt = 1.9×10^{-5} mm/s (by always considering the time of propagation as the total duration of the tensile test). The fraction of the transgranular mode in the mixed IG/TG mode covers around 16% of the zone, which suggests that these cracks correspond to the same decohesions of high angle misorientation interfaces characterized in the previous part. The final transgranular fracture zone here also presents an aspect relatively ductile inserted in brittle facets of decohesion as seen in Figure 112. Figure 112c shows clearly the transgranular rupture crossing the former austenitic grains where one can identify at least three packets. This again supports the fact that the crack path follows the inter-packet and inter-block interfaces.

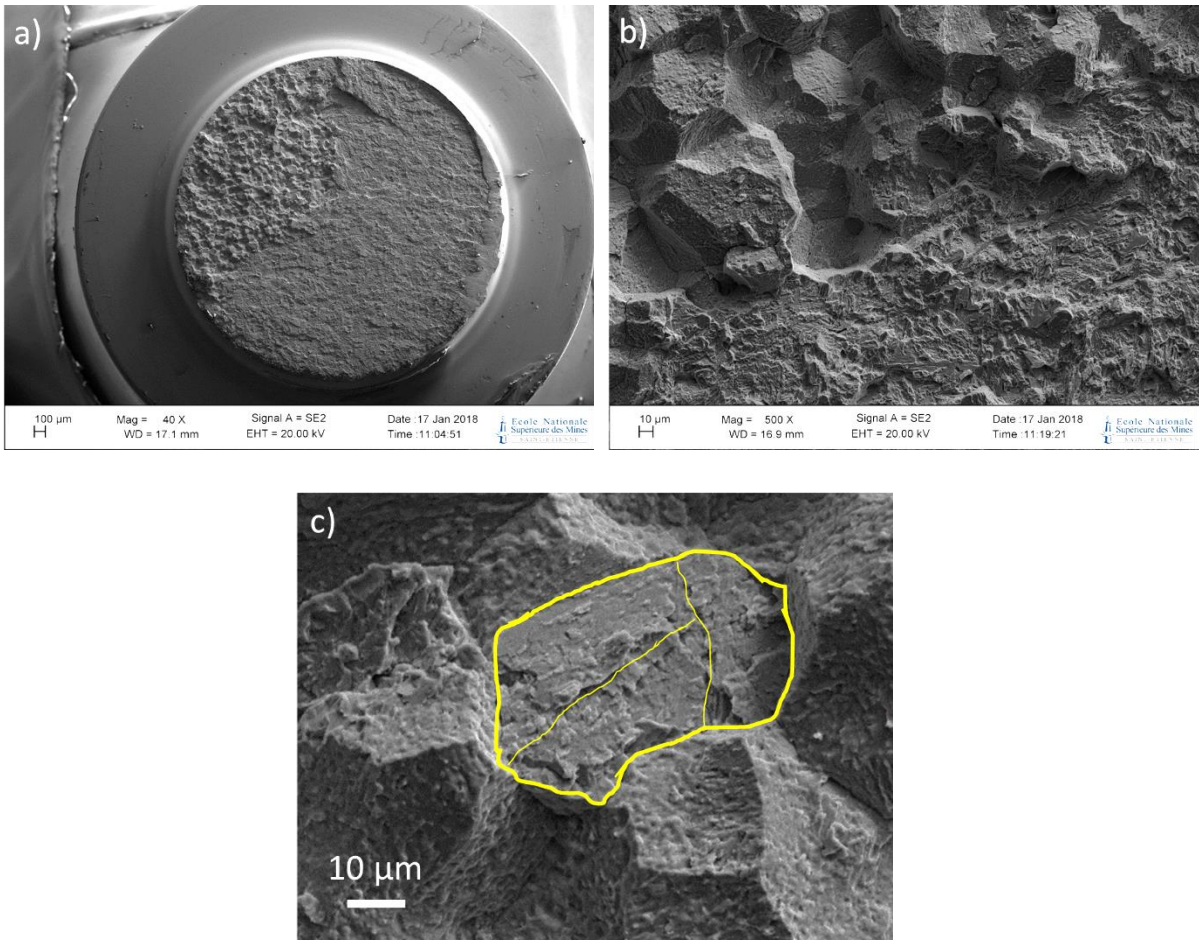

Figure 112 Fracture surfaces of the 10^{-5} mm/s test 24 h pre-charged + *in-situ* charging with protected notch.

Figure 113 summarizes the results of this series of tests as a function of the two displacement rates explored, for both the fracture stress and the extent of the mixed IG/TG sub-critical crack. Figure 114 presents the mean crack growth rates in these various test conditions.

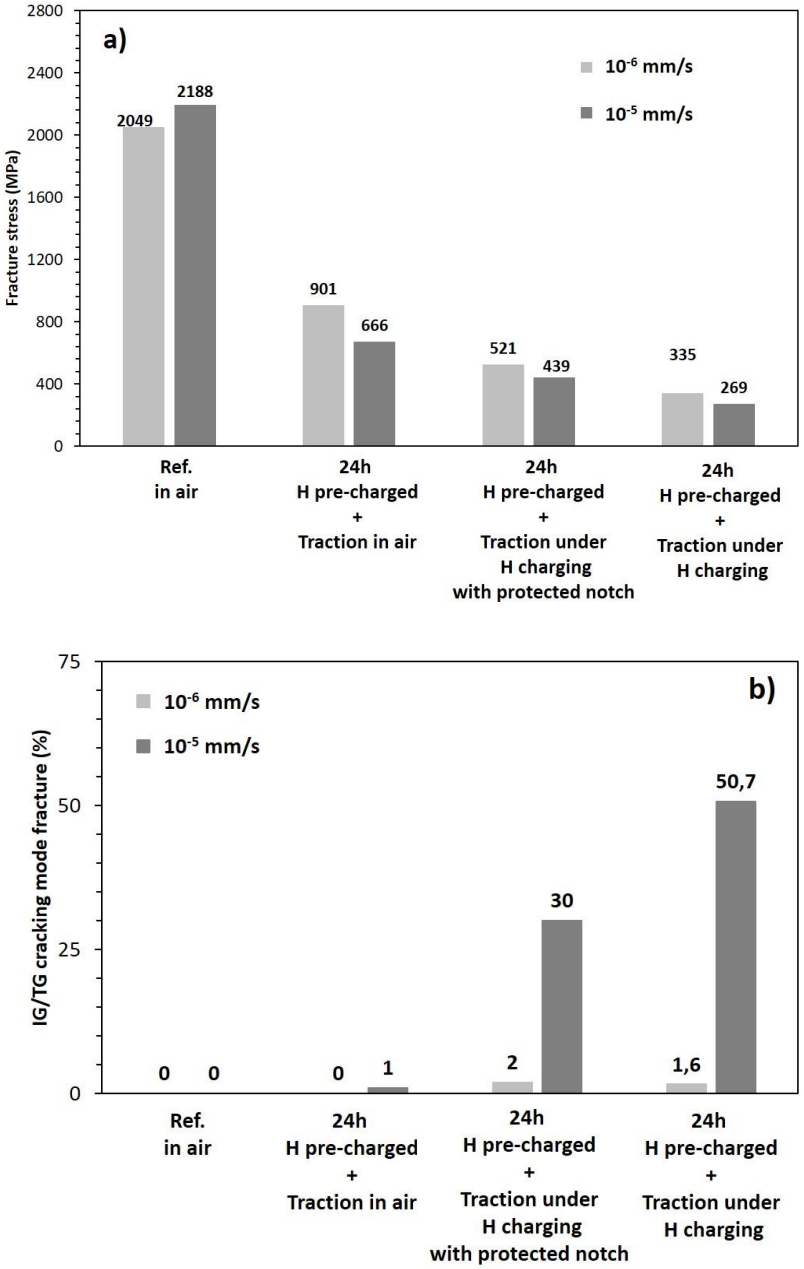

Figure 113 Histograms showing a) the fracture stresses and b) the intergranular/transgranular subcritical fracture surface for each hydrogenating condition at two different displacement rates.

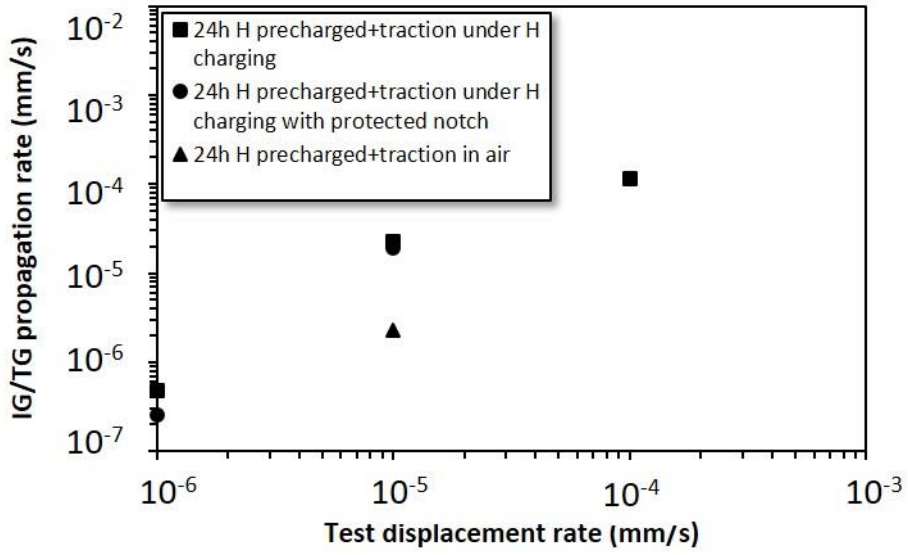

Figure 114 IG/TG crack growth rates as a function of displacement rates under different condistions.

6.6.2. Constant load tests under internal hydrogen

The results of the constant load test are summarised in Figure 115. Two loadings were explored, the one at 1500 MPa and the other at 1000 MPa. While compared to the tests without silicone notch protection, these two ones showed an increase of the time to fracture. It should be noted that the test done on 1000 MPa has been reloaded of 30 MPa after 145 hours, while no cracking seemed to occur. After this last loading, the specimen finally broke 20 minutes later.

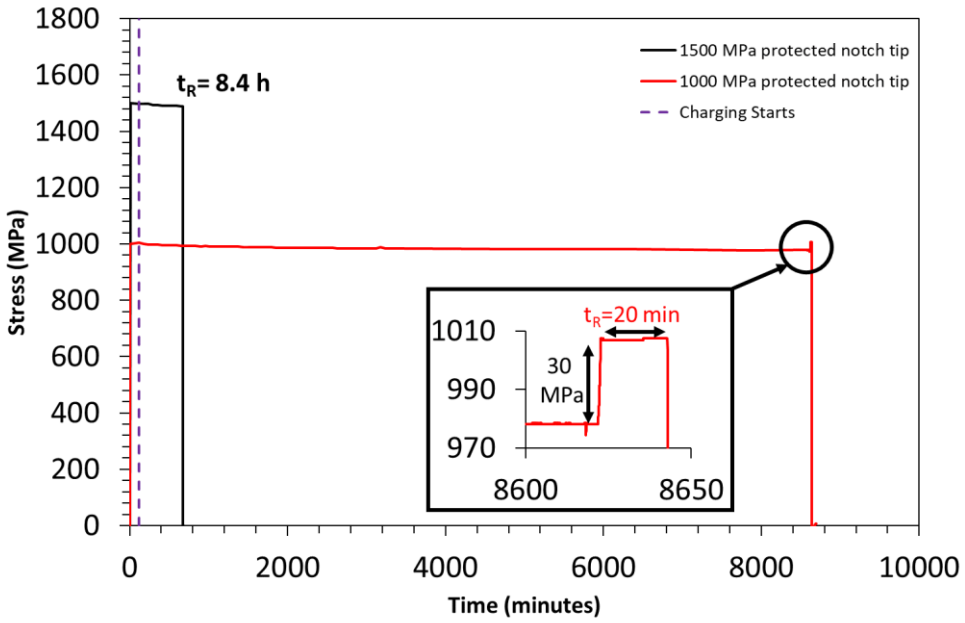

Figure 115 Constant load tests under H-charging on specimen with notch silicone protection.

Fractographic analysis showed that substantial IG/TG sub-critical crack propagation occurred on the sample loaded at 1500 MPa. The crack extended over 285 µm depth, and the mean crack growth rate, based on the time to rupture, is equal to da/dt = 9.4×10^{-6} mm/s (see Figure 116).

Finally, the 1000 MPa load specimen presented no mixed intergranular/transgranular cracking mode. On the contrary it was purely transgranular and contained brittle transgranular facets and ductile features as seen previously for this mode of fracture (Figure 117).

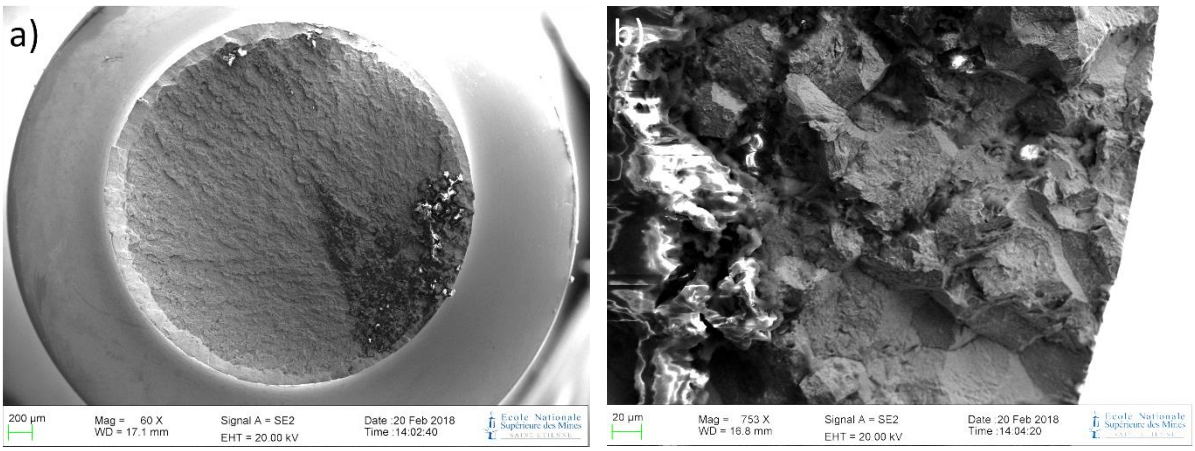

Figure 116 Fracture surfaces of 1500 MPa protected notch tip specimen.

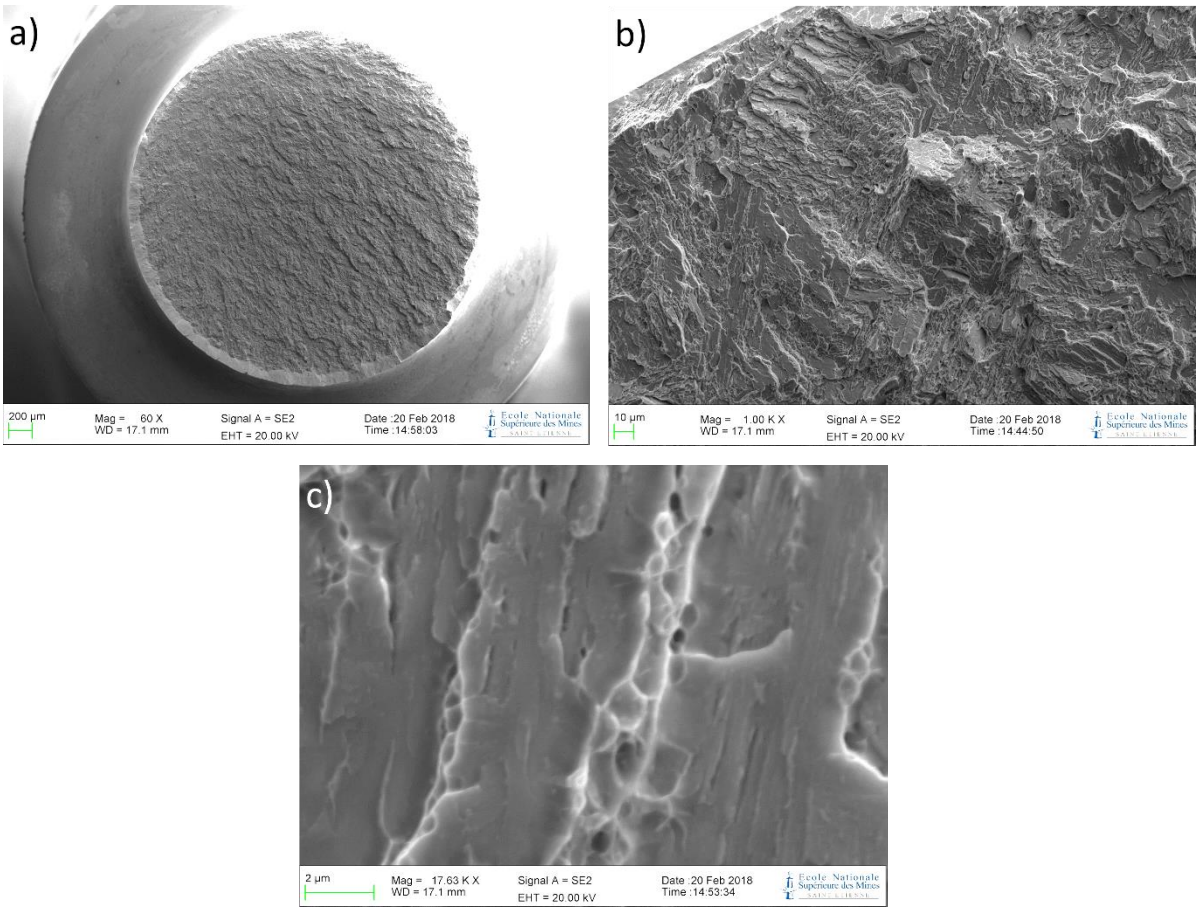

Figure 117 Fracture surfaces of 1000 MPa loaded protected notch tip specimen.

6.7. Synthesis and discussion on effects of hydrogenating conditions

6.7.1. Hydrogen intake during pre-charging

The 24h hydrogen pre-charging contributes to increase the hydrogen content in the steel from an initial concentration of 0.62 ppm up to 1.9 ppm, according to measurements presented in part § 4.2.3. We have seen that this content is not sufficient to induce a large IG crack propagation during Charpy tests, where no hydrogen diffusion during the test is possible. Just one very little intergranular facet was observed. It is due to hydrogen trapping in the near crack tip zone, the diffusion distance during the 24h being around 150 µm with a decreasing hydrogen content from the surface to the bulk.

6.7.2. Relation between hydrogen intake during slow strain rate tests and hydrogen embrittlement

The slow strain rate test at 10^{-6} mm/s did not show any IG mode of cracking on the "24h hydrogen pre-charged" specimen. This result can be due to the desorption of hydrogen during the test which lasted about 27 hours. Obviously, at the beginning of the test, the stress was too low to initiate any IG/TG subcritical cracking in the process zone, and stress triaxiality was not well developed to promote diffusion to this zone.

The test at 10^{-5} mm/s lasted about 2 hours. For this duration, desorption of hydrogen is less pronounced and IG/TG crack initiation could develop in the "24h hydrogen pre-charged" specimen. The crack growth rate in this case can be underestimated insofar the duration of crack propagation is certainly lower than the total duration of the test.

Tests under continuous hydrogen charging with protected notch showed systematically higher fracture stress while their crack growth rates are roughly similar, and their IG/TG crack depths in the same order of magnitude than those without silicone protection. These results suggest that their respective stress intensity factors are in the time-dependent plateau where crack growth rates are slightly increasing. It means that the process of crack propagation is fuelled with hydrogen while the source is delocalised outside the notch tip, on the specimen surface. Considering the geometry of the notch, the distance d between the notch root and the surface unprotected with silicone can be approximate by the following relation:

$$\mathrm{d} = 1.785 \times \mathrm{e} \qquad \textbf{(27)}$$

where e is the depth of the notch, and 1.785 the multiplicative factor taking into account the curvilinear distance from the notch root to the unprotected surface of the specimen. The calculation gives a d-value equal to 1.785 mm. Using equation (24) to calculate the diffusion time for this distance, we obtain:

$$\mathrm{t} = \frac{d^2}{4D_{eff}} \qquad \textbf{(28)}$$

where D_{eff} is the effective diffusion coefficient (D_{eff} = 6.38 10^{-14} $m^2.s^{-1}$), and d is the diffusion distance hydrogen needs to reach the process zone at the notch root. The calculation gives a time equal to about 3 470 hours, which is far too big considering the duration of slow strain

rate tests. An alternative hydrogen transport must occur to provide sufficiently the process zone at the notch tip and allow a hydrogen diffusion-assisted mechanism of cracking.

The IG/TG mode of the sub-critical cracking lets us think naturally about the intergranular diffusion of hydrogen. We have seen in part 2.2.3 the specific properties of grain boundaries in a bcc material. They have an important role in trapping but can also be at the origin of an increase in the apparent diffusion coefficient by effects of diffusion short-circuits. Brass *et al.* determined the hydrogen diffusion coefficient in grain boundaries and calculate that the ratio between $D_{Grain\ Boundary}$ and $D_{Lattice}$ can vary between 3 to 100 in pur Nickel [80]. In bcc structure the phenomenon of short-circuit by grain boundaries does not seem to be observed due to the higher interstitial diffusion coefficient [85], [86]. These results were obtained in a α-iron which has a much higher diffusion coefficient that the martensite microstructure of maraging steels. The recent works of Hoch *et al.* and Oudriss *et al.* have shown that grain boundary properties depend strongly on their nature and their connectivity in the microstructure [5], [145].

In this study, to evaluate approximatively an intergranular diffusion coefficient value that could explain the continuous hydrogen supply to the process zone, the relation (28) is used again with a 2 hours t-value and a 1.785 d-value. We rely for this on the test at 10^{-5} mm.s^{-1} with protection of the notch that lasted 2 hours. The calculation gives an apparent diffusion coefficient equal to $D_{app} = 1.1\ 10^{-10}$ m^2.s^{-1}, which must be considered as a low limit value. This value has to be compared with the diffusivity of hydrogen in iron grain boundaries, calculated by Rimoli *et al*. [112] from the results of first-principles calculations of various types of grain boundaries. For simplicity, they assumed that the grain-boundary diffusivity is isotropic and obey an Arrhenius law, giving a temperature-dependent scalar of the form:

$$D_{GB}(T) = \ D_0 \exp\left(-\frac{T_0}{T}\right) \qquad \textbf{(29)}$$

where $D_0 = 2.44\ 10^{-7}$ m^2.s^{-1} and $T_0 = 1334.42$ K. For ambient temperature, the calculation gives a grain-boundary diffusion coefficient equal to $D_{GB} = 2.77\ 10^{-9}$ m^2.s^{-1}, which is twenty times larger than the estimated D_{app}-value. Inversely, using the intergranular diffusion coefficient of iron, the diffusion distance of hydrogen from the unprotected surface of the specimen by the silicone to the process zone would take around 5 minutes. These values actually present a

certain coherency with the experimental facts, which supports the hypothesis of embrittlement assisted by hydrogen diffusion in the process zone. The diffusion rate of hydrogen could be increased by the higher diffusivity of hydrogen at the grain boundaries in the microstructure.

6.7.3. Cracking mechanism scenarios

The hydrogen effects on the 350 grade maraging steel are invariably localized at the notch tip of the specimens, whatever the hydrogen charging conditions. For hydrogen pre-charged specimens with silicone protection of the notch, the subcritical crack growth occurs when the steel is subsequently stressed at sufficiently low strain rates. Loading causes both a redistribution of dissolved hydrogen from the surrounding microstructure to the notch tip process zone to promote crack initiation and then crack growth. In the case of just pre-charged specimens, the amount of hydrogen is not sufficient to supply the process zone with hydrogen and initiate an extended subcritical cracking. On the contrary, by maintaining the hydrogen source with cathodic charging, the process zone seems to be supplied permanently with hydrogen by grain-boundary diffusion transport from the surface outside the notch to the process zone. Furthermore, direct hydrogen charging of specimens produces atomic hydrogen on notch tip surfaces, followed by hydrogen uptake and diffusion ahead of the notch tip into the process zone and subsequent embrittlement.

The stage II subcritical crack growth rates strongly suggests a hydrogen diffusion (time dependent) assisted cracking mechanism in the fracture process zone. Similarly, the effects of the strain rate on the fracture stress, in a limited range of strain rates, could be explained by the additional mechanism of hydrogen transport by dislocations. This mechanism in cubic centered structure materials is effective under specific conditions. Actually, the hydrogen dragging by dislocations in Cotrell atmospheres form is possible only when dislocations do not exceed a critical speed, which is function of trapping energy, temperature and diffusion coefficient of hydrogen [70]. At the strain rates considered in our study, the transport of hydrogen by dislocations must be effective for tests corresponding to displacement rates lower than $V_T=10^{-3}$ mm.s^{-1} (strain rate ≈ 10^{-4} s^{-1}) and can thus lead to increase the flow of hydrogen in the material. Thus, hydrogen overconcentrations can be achieved at specific interfaces, such as prior γ-grains boundaries, inter-packets or inter-blocks boundaries. These

boundaries are high-angle grain boundaries and can hinder the dislocation movement, leading to the formation of dislocation pile-ups at the boundaries. Those interfaces are also sites of high dislocation density and hydrogen trapping. Localization of plasticity and local hydrogen overconcentration can lead to reduction of cohesion forces and induce brittle cracking at critical hydrogen concentration. With lower hydrogen content, localization of plasticity can accelerate formation, growth and coalescence of cavities at these interfaces, without triggering brittle cracking (typically called “pure transgranular” mode of cracking). Actually, in pure transgranular fracture surfaces, evidence of ductile process with ductile fine tear ridges and little dimples were observed. Besides in the mixed IG/TG mode of cracking, intergranular facets of prior γ-grains do not show flat surfaces in agreement with a pure decohesion mode of fracture (HEDE model). On the contrary, they reveal a very disturbed aspect that may suggest the expression of the underlying localized plasticity, resulting in the activation of different slip systems in individual martensite lath. This activity can itself be enhanced by the hydrogen-enhanced localized plasticity (HELP model). Intergranular failure can thus occur when slip systems intersect the prior γ-grain boundaries whereas transgranular cracking in this mixed mode occurs when they intersect packets, blocks or sub-blocks boundaries. The mode of cracking activated first in the mixed IG/TG mode is dictated by where the local stress accumulation along with the required hydrogen content is reached first.

To illustrate the different situations encountered in this study, the following figures present the scenarios concerning the Charpy tests and slow strain rate tests (Figure 118), the constant load tests (Figure 119) and the tests with or without silicone protection (Figure 120).

Figure 118a shows the state of a specimen after 24 hours of cathodic charging, where hydrogen is introduced into the metal and trapped on the different defects (pre-existing dislocations (blue), precipitates (green), γ-grains or packets, blocks, and sub-blocks boundaries (yellow). Diffusible interstitial hydrogen is presented in (red)). Figure 118b, represents the situation in the process zone during the fast tensile tests (10^{-3} mm/s) and Charpy tests. In this case, plastic strain rate is high; the displacement of dislocations does not allow transport of hydrogen. The pile-up of dislocations against the high misorientation angles boundaries occurs without weakening these interfaces by supplementary additional hydrogen. The development of a stress triaxiality zone ahead of the notch tip contributes to the diffusion of hydrogen from the bulk to this process zone. Nevertheless, the diffusion kinetics of hydrogen either in the

bulk or in the grain boundaries is too slow to enrich the process zone. The crack initiation is thus mainly transgranular. The quantity of hydrogen introduced during the pre-charging still remains sufficient to induce weakening effects; the fracture energy or the fracture stress being lowered compared to the tests in air.

At lower displacement rates, the successive steps of damaging in the process zone differ from the precedent situation. Figure 118c and Figure 118d represent these steps and concern the tensile tests at $V_T = 10^{-4}$ and 10^{-5} mm/s. At these strain rates, the moving of dislocations drags the clusters of hydrogen with them and contributes to increase the hydrogen content along the various boundaries or interfaces on which they stack. These mechanisms of hydrogen diffusion contribute to increase the hydrogen content in these traps, decreasing their bonding. The additional contribution of diffusible hydrogen to the enrichment of the same traps, either by intergranular short-circuit of diffusion or transgranular diffusion, leads to intergranular and inter-packets, blocks or sub-blocks cracking at lower stresses. These conditions allow a sub-critical regime of cracking driven by a local stress intensity factor lower than the tenacity of the steel. The crack propagates following the boundary weakened by hydrogen presence.

Finally, for the slowest test (at $V_T = 10^{-6}$ mm.s^{-1}) presented in Figure 118e and Figure 118f, the same mechanisms of hydrogen transported by dislocations and lattice diffusion operate. However, the mechanical loading is slow enough to allow a more homogeneous hydrogen redistribution from the grain boundaries, and other high misorientation angle interfaces, towards the bulk. It decreases the hydrogen content in these specific sites, and contributes to increase the transgranular brittle mode of cracking. This explains why the material is less hydrogen-embrittled at 10^{-6} mm.s^{-1} than at 10^{-6} mm.s^{-1}. Unlike to the transgranular cracking at high displacement rate, there are few features of ductility. The more homogeneous hydrogen distribution in the microstructure shifts the critical cracking stress to higher values in the steel. These conditions multiply the sites of stress concentration at pile ups of dislocations in all the microstructure multiplying thereby crack initiation sites. Figure 118f shows for instance several pile-ups against precipitates/matrix boundary.

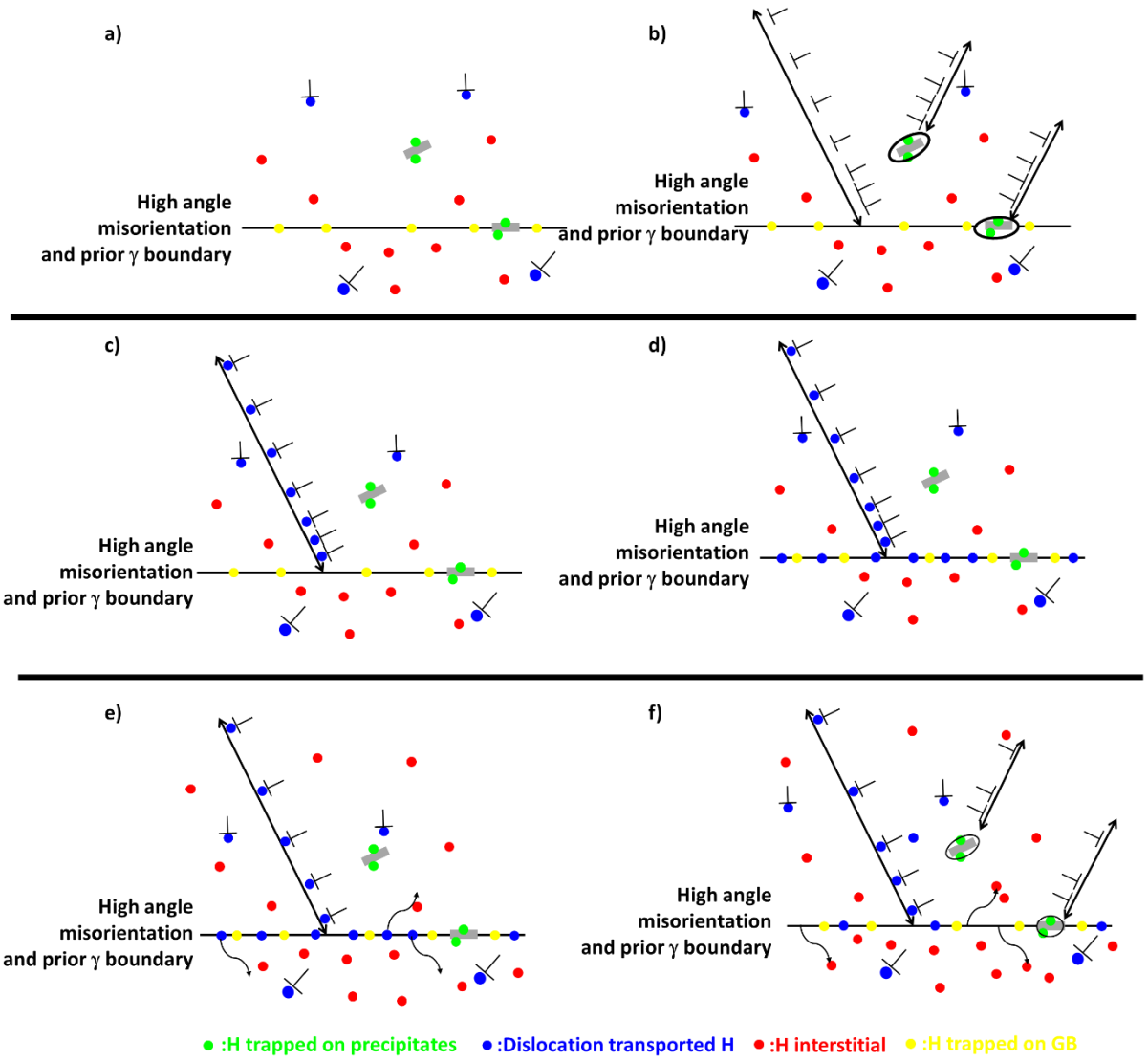

Figure 118 Schematic representation of interactions between hydrogen and metallurgical defects (dislocations, precipitates, GB…) for different displacement rates. a) corresponds to the initial state after 24 hours hydrogen charging, b) corresponds to the fast loading (Charpy test), c) and d) correspond to the critical loading rates (10^{-4} and 10^{-5} mm/s), e) and f) correspond to the slowest loading (10^{-6} mm/s). At 10^{-6} mm.s^{-1}, the grain boundaries hydrogen concentration at steady state is less than at 10^{-5} mm.s^{-1}.

The particular slow strain rate test at V_T = 10^{-5} mm s^{-1} on the pre-strained specimen have shown an even more pronounced effect of hydrogen embrittlement. The pre-deformation having been made at V_T = 10^{-3} mm.s^{-1}, it is unlikely to invoke the transport of hydrogen by dislocations to grain boundaries or interfaces with high misorientations that could have weakened them in this case. The pre-straining was done at a stress value corresponding to the plateau of homogeneous deformation. At nanoscale precipitates, the plastic pre-deformation corresponds to the shearing of precipitates by both cutting mode and by-passing mode. This stage could have relaxed the stress elastic field around precipitates and release hydrogen

trapped at these sites. Pre-strained step can have thereby provided supplementary source of hydrogen and weakened the material.

For the tensile tests at constant loading, the damaging scenario differs from the slow strain rate tests. In their case, no hydrogen pre-charging was done, so plastic strain hardening occurred in the microstructure free from hydrogen, mechanisms of dislocations multiplication and stacking against obstacles such as GB and more generally high misorientation angle interfaces operated without being affected by hydrogen. The development of high stress triaxiality ahead of the notch-tip contributes to decrease the chemical potential in this zone and generates a flux of hydrogen. The high density of dislocations decreases the apparent hydrogen diffusion coefficient due to strong and irreversible hydrogen trapping in the dislocation sub-structures. Diffusible hydrogen content is decreased in grains as much as in grain boundaries constituting the short circuit of diffusion. Figure 119a represents the initial state with residual hydrogen content in the bulk. After mechanical loading, the density of dislocations has increased and stress concentration sites were formed ahead of the pile-ups of dislocations as shown in the Figure 119b. This state corresponds also to the formation of a zone of high stress triaxiality. Figure 119c represents the trapping of hydrogen, which has diffused from the surface towards the process zone on the dislocations. The progressive increase of hydrogen content on the sites of stress concentration is at the origin of the delayed fracture for these tests. The conditions here do not favour intergranular cracking, but on the contrary, contributes to mainly transgranular fracture.

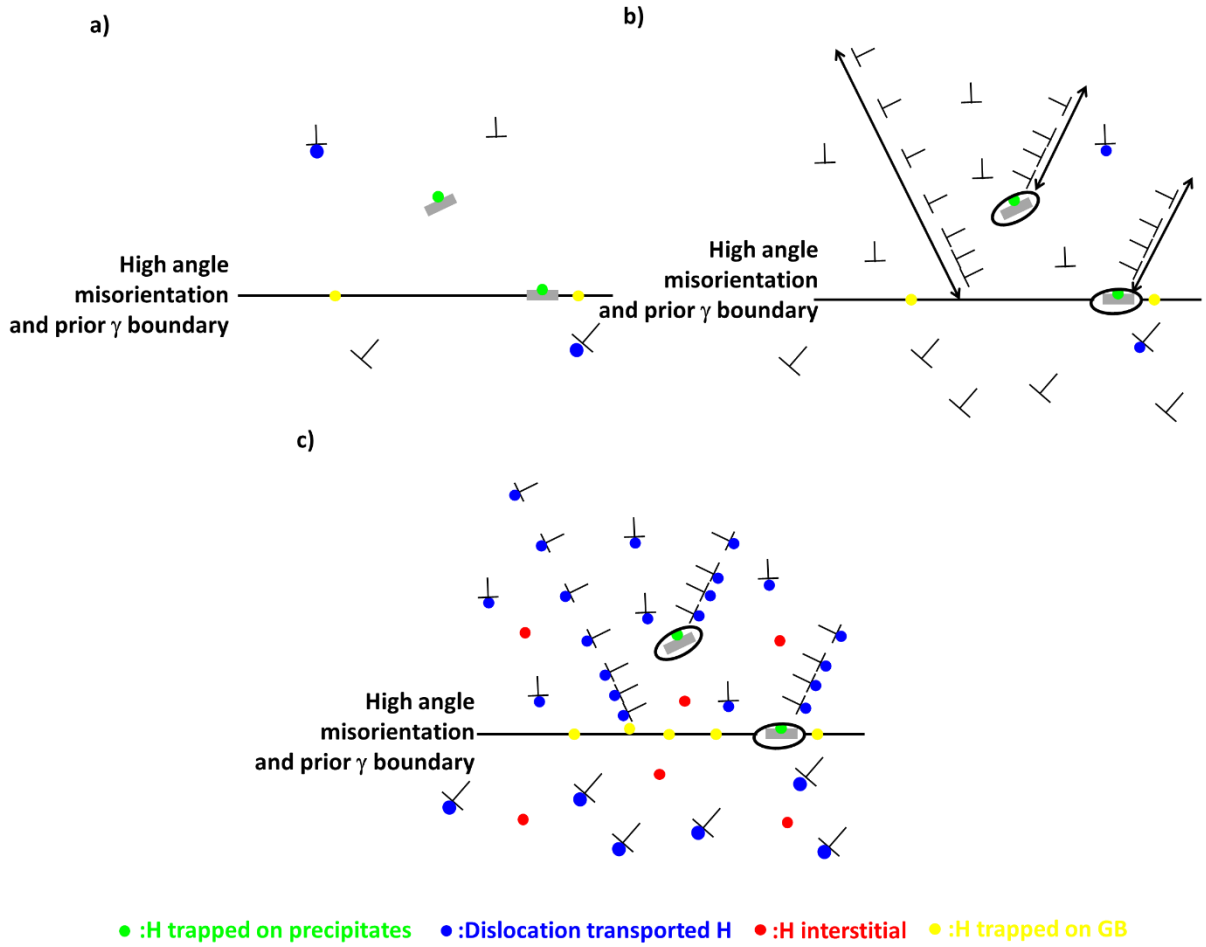

Figure 119 Schematic representation of tensile tests at constant load followed by hydrogen cathodic charging. a) corresponds to the initial state with low residual hydrogen content, b) corresponds to the state just after mechanical loading and c) corresponds to the state when diffusible hydrogen reaches the process zone and is trapped on the metallurgical defects (dislocations, precipitates, grain boundaries and high misorientations interfaces). The dislocations are considered immobile here.

For the specimens with a notch protected by silicon, the entry of hydrogen is more distant from the process zone. The Figure 120 illustrates the boundary conditions for hydrogen entry in two configurations with or without silicon protection on the notch. On the protected notch, the distance from the mouth of the notch to the process zone is increased by 1.785 mm taking into account the whole geometry of the notch. The calculation of the diffusion duration using the apparent diffusion coefficient determined by permeation gives 3468 hours, which is obviously longer than the duration of the test itself. On the contrary, by considering the diffusion of hydrogen along the grain boundaries, typically in the range of 10^{-9} m²/s [112], [145], [146], one calculates diffusion duration around 5 minutes for a hydrogen atom to reach the process zone ahead of the notch tip from the surface around the mouth of the notch. The

delayed fracture of the sample is linked to the time necessary for the hydrogen to both reach the process zone and accumulate up to a critical content in the process zone.

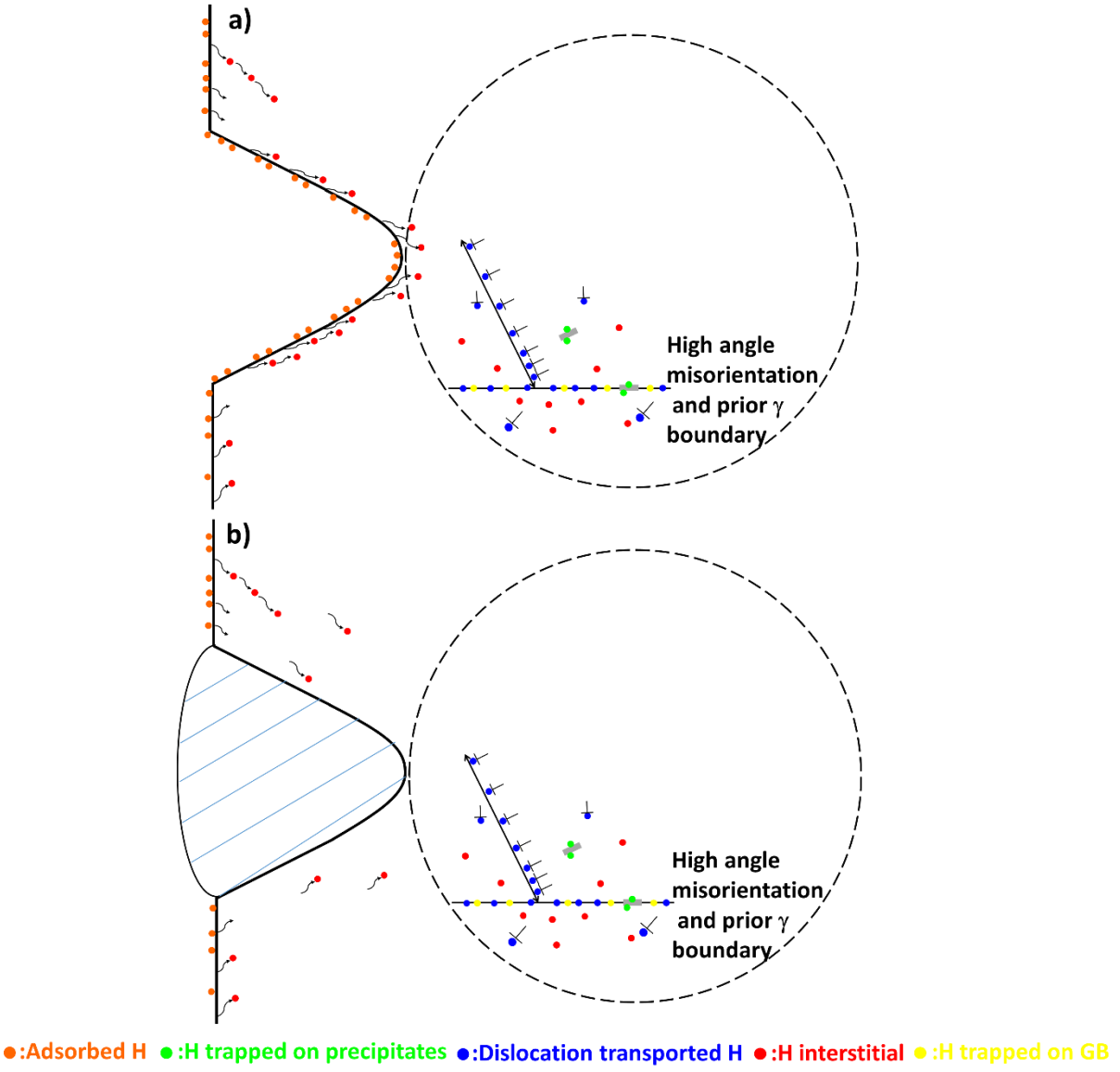

Figure 120 Schematic representation of the boundary conditions for hydrogen entry with and without silicon protection on the notch surface.

7. Conclusions

The objective of this part of the study was to better understand the phenomenon of hydrogen embrittlement on an ultra-high strength steel with regard to hydrogen diffusion and trapping/de-trapping properties. In this study, we were interested in the 350-grade maraging steel peak-aged at temperature and duration where no austenite reversion is expected. Hydrogenating conditions consisted in a cathodic hydrogen charging in a 30 g/l NaCl solution and at cathodic potential E_c = -1200 mV/SCE. Various conditions of hydrogen ingress were explored in order to study "external" and "internal" hydrogen embrittlement. These conditions refer respectively to a direct hydrogen charging at the notch-tip surface of the specimens, or via a diffusion path in the material by protecting the notch tip from the environment while cathodic charging, or just via a pre-charging of the specimen before mechanical testing. Mechanical testing consisted in slow strain rate tests on notched specimen, at strain rates ranging from 10^{-7} s^{-1} to 10^{-4} s^{-1}. Charpy tests and constant load tests were also performed. In parallel, finite element calculations were done to evaluate mechanical quantities related to test specimens. Finally, permeation tests were carried out to estimate the effective hydrogen diffusion coefficient and to approach the lattice diffusion coefficient in this 18% Ni maraging steel.

The main conclusions of the study are as follow:

Finite element modelling:

1) The model took in consideration the geometry of the specimen used in the experiments, and helped to localize the zone of maximum stress triaxiality, localizing the process zone of damage.
2) The model allowed determining the local strain rate at notch tip, before crack initiation. It also allowed determining the threshold displacement before which no plastic deformation occurred at the notch tip.

Permeation tests:

1) Permeation tests allowed determining the effective hydrogen diffusion coefficient, and approaching the lattice diffusion coefficient using method of successive hydrogen charging by increasing cathodic potential.

Mechanical tests:

1) The slow strain rate tensile tests on notched specimens have shown an effect of the strain rate on the fracture stress in the range of 10^{-7} to 10^{-4} s^{-1}. The fastest tensile test have shown a drop in the fracture stress with respect to the test in air. Moreover, the slowest tensile tests have shown a fracture stress close to the one seen for the fastest. However for intermediate strain rates, the drop was more important, and these tests have shown the lowest fracture stress. Charpy tests have shown a decrease of fracture energy with hydrogen content.
2) Two cracking modes were identified. One corresponding to a mixed intergranular/transgranular brittle mode, the other corresponding to a transgranular mode with features of ductility, such as fine tear ridges and dimples, the latter increasing with increasing strain rate. The transgranular mode in the mixed mode is related to high angle misorientation interfaces in the microstructure, such as packets, blocks and sub-blocks boundaries ; they correspond both to trapping sites and to short-circuit diffusion paths.
3) In terms of crack growth rates, we have identified three stages of propagation. The first one corresponds to the mechanical-dependent crack growth rates with stress intensity factor. This stage is limited to a threshold value of a resolved stress intensity factor estimated to about 8 MPa√m. The second stage corresponds to the time-dependent plateau of crack growth rates, which increases very slightly with stress intensity factors. The mechanisms dictating this behaviour seems to be related to hydrogen diffusion in the process zone. Preferential intergranular diffusion path can be at the origin of an accelerated diffusion. These two stages correspond to a sub-critical regime of crack growth corresponding to the mixed intergranular/transgranular mode of cracking. These results are in agreement with scientific literature on high strength steels. The third stage corresponds to the critical final crack propagation near the toughness of the material. The mode of cracking is transgranular with ductile

features in this case. The ductile character of this cracking is more or less pronounced depending on the hydrogen concentration in the material.

4) Transgranular cracking mode at very low strain rate (or at constant load) is interpreted as a de-trapping effect of hydrogen form the grain boundaries. The transport of hydrogen by moving dislocations to the GBs is counterbalanced by the lateral diffusion of hydrogen toward the bulk decreasing the intergranular hydrogen content.
5) These materials showed a high sensitivity on hydrogen since they present a surface defect. Nevertheless, below a threshold stress intensity factor around 5-6 MPa√m, no propagation is expected in the environmental conditions explored in this study. In the subcritical regime, crack growth rate is around 10^{-7} m.s^{-1}.

This study opens several perspectives. It was performed on the grade 350 maraging steel heat-treated at a single temperature and duration of treatment. The demonstration of a crack propagation regime that depends on preferential hydrogen diffusion path along the prior γ-grain boundaries and high-angle misorientation interfaces, suggests exploring different microstructures, particularly those in the presence of reverted austenite in variable amounts. Part of this austenite will be at the prior γ-grain boundaries. The higher solubility of hydrogen in the austenite would therefore certainly alter the diffusivity at the grain boundaries with consequences on crack growth rates, threshold and critical stress intensity factors.

The effect of a pre-deformation with regards to hydrogen trapping and diffusivity in the material is also an interesting topic to pursue further. Hydrogen permeation tests on strained samples at different values would more clearly demonstrate the shear effect of precipitates on hydrogen trapping, and/or detrapping, according to the mode of shearing, by cutting or by-passing the precipitates.

Table of figures

Figure 86 shows the tensile curve of this test in the stress-displacement graph with all the other curves. The pre-strain effect is detrimental, the maximum stress reached in these

Tables List

Bibliography

[1] Y. Chung, Validity of Caltrans' environmental hydrogen embrittlement tests on Grade BD anchor rods in the SAS span. 2014.

[2] L. Mair, "Third bolt breaks on Cheesegrater," Construction News. [Online]. Available: https://www.constructionnews.co.uk/companies/third-bolt-breaks-on-cheesegrater/8675045.article. [Accessed: 14-Jun-2018].

[3] F. von Zeppelin, M. Haluška, and M. Hirscher, "Thermal desorption spectroscopy as a quantitative tool to determine the hydrogen content in solids," Thermochim. Acta, vol. 404, no. 1, pp. 251–258, Sep. 2003.

[4] N. Boes and H. Züchner, "Electrochemical methods for studying diffusion, permeation and solubility of hydrogen in metals," J. Common Met., vol. 49, pp. 223–240, Sep. 1976.

[5] A. Oudriss et al., "Meso-scale anisotropic hydrogen segregation near grain-boundaries in polycrystalline nickel characterized by EBSD/SIMS," Mater. Lett., vol. 165, pp. 217–222, Feb. 2016.

[6] Y.-S. Chen et al., "Direct observation of individual hydrogen atoms at trapping sites in a ferritic steel," Science, vol. 355, no. 6330, pp. 1196–1199, Mar. 2017.

[7] C. Senöz, S. Evers, M. Stratmann, and M. Rohwerder, "Scanning Kelvin Probe as a highly sensitive tool for detecting hydrogen permeation with high local resolution," Electrochem. Commun., vol. 13, no. 12, pp. 1542–1545, Dec. 2011.

[8] S. Evers, C. Senöz, and M. Rohwerder, "Spatially resolved high sensitive measurement of hydrogen permeation by scanning Kelvin probe microscopy," Electrochimica Acta, vol. 110, pp. 534–538, Nov. 2013.

[9] S. Evers and M. Rohwerder, "The hydrogen electrode in the 'dry': A Kelvin probe approach to measuring hydrogen in metals," Electrochem. Commun., vol. 24, pp. 85–88, Oct. 2012.

[10] W. Melitz, J. Shen, A. C. Kummel, and S. Lee, "Kelvin probe force microscopy and its application," Surf. Sci. Rep., vol. 66, no. 1, pp. 1–27, Jan. 2011.

[11] M. Nonnenmacher, M. P. O'Boyle, and H. K. Wickramasinghe, "Kelvin probe force microscopy," Appl. Phys. Lett., vol. 58, no. 25, pp. 2921–2923, Jun. 1991.

[12] M. Xue, S. Peng, F. Wang, J. Ou, C. Li, and W. Li, "Linear relation between surface roughness and work function of light alloys," J. Alloys Compd., vol. 692, pp. 903–907, Jan. 2017.

[13] D. T. Glatzel, P. D. M. C. Lux-Steiner, E. Strassburg, A. Boag, and P. Y. Rosenwaks, "Principles of Kelvin Probe Force Microscopy," in Scanning Probe Microscopy, S. Kalinin and A. Gruverman, Eds. Springer New York, 2007, pp. 113–131.

[14] S. Trasatti and R. Parsons, "Interphases in systems of conducting phases (Provisional)," Pure Appl. Chem., vol. 55, no. 8, pp. 1251–1268, 1983.

[15] "CRC Handbook of Chemistry and Physics, 84th Edition Edited by David R. Lide (National Institute of Standards and Technology). CRC Press LLC: Boca Raton. 2003. 2616 pp. $139.95. ISBN 0-8493-0484-9.," J. Am. Chem. Soc., vol. 126, no. 5, pp. 1586–1586, Feb. 2004.

[16] R. F. Schaller and J. R. Scully, "Measurement of effective hydrogen diffusivity using the Scanning Kelvin Probe," Electrochem. Commun., vol. 40, no. Supplement C, pp. 42–44, Mar. 2014.

[17] D. Kohl, P. Mesquida, and G. Schitter, “Quantitative AC - Kelvin Probe Force Microscopy,” Microelectron. Eng., vol. 176, pp. 28–32, May 2017.
[18] Q. Liu, A. D. Atrens, Z. Shi, K. Verbeken, and A. Atrens, “Determination of the hydrogen fugacity during electrolytic charging of steel,” Corros. Sci., vol. 87, pp. 239–258, Oct. 2014.
[19] L. J. Gillespie and L. S. Galstaun, “The Palladium-Hydrogen Equilibrium and New Palladium Hydrides1,” J. Am. Chem. Soc., vol. 58, no. 12, pp. 2565–2573, Dec. 1936.
[20] M. Skjellerudsveen, O. M. Akselsen, V. Olden, R. Johnsen, and A. Smirnova, “Effect of Microstructure and Temperature on Hydrogen Diffusion and Trapping in X70 grade Pipeline Steel and its Weldments,” p. 13.
[21] V. Olden, A. Saai, L. Jemblie, and R. Johnsen, “FE simulation of hydrogen diffusion in duplex stainless steel,” Int. J. Hydrog. Energy, vol. 39, no. 2, pp. 1156–1163, Jan. 2014.
[22] E. Owczarek and T. Zakroczymski, “Hydrogen transport in a duplex stainless steel,” Acta Mater., vol. 48, no. 12, pp. 3059–3070, Jul. 2000.
[23] K. Kiuchi and R. B. McLellan, “The solubility and diffusivity of hydrogen in well-annealed and deformed iron,” Acta Metall., vol. 31, no. 7, pp. 961–984, Jul. 1983.
[24] A. Turnbull and R. B. Hutchings, “Analysis of hydrogen atom transport in a two-phase alloy,” Mater. Sci. Eng. A, vol. 177, no. 1, pp. 161–171, Apr. 1994.
[25] P. Tsong-Pyng and C. J. Altstetter, “Effects of deformation on hydrogen permeation in austenitic stainless steels,” Acta Metall., vol. 34, no. 9, pp. 1771–1781, Sep. 1986.
[26] P. Novak, R. Yuan, B. P. Somerday, P. Sofronis, and R. O. Ritchie, “A statistical, physical-based, micro-mechanical model of hydrogen-induced intergranular fracture in steel,” J. Mech. Phys. Solids, vol. 58, no. 2, pp. 206–226, Feb. 2010.
[27] A. Nagao, M. Dadfarnia, B. P. Somerday, P. Sofronis, and R. O. Ritchie, “Hydrogen-enhanced-plasticity mediated decohesion for hydrogen-induced intergranular and ‘quasi-cleavage’ fracture of lath martensitic steels,” J. Mech. Phys. Solids, vol. 112, pp. 403–430, Mar. 2018.
[28] H. K. Birnbaum and P. Sofronis, “Hydrogen-enhanced localized plasticity—a mechanism for hydrogen-related fracture,” Mater. Sci. Eng. A, vol. 176, no. 1, pp. 191–202, Mar. 1994.
[29] I. M. Robertson, H. K. Birnbaum, and P. Sofronis, “Chapter 91 Hydrogen Effects on Plasticity,” in Dislocations in Solids, vol. 15, J. P. Hirth and L. Kubin, Eds. Elsevier, 2009, pp. 249–293.
[30] W. W. Gerberich, P. G. Marsh, and J. W. Hoehn, “Hydrogen induced cracking mechanisms - are there critical experiments?,” presented at the Hydrogen Effects in Materials, 1996, pp. 539–551.
[31] R. A. Oriani, “Hydrogen The Versatile Embrittler,” CORROSION, vol. 43, no. 7, pp. 390–397, Jul. 1987.
[32] S. P. Lynch, “Progress Towards Understanding Mechanisms Of Hydrogen Embrittlement And Stress Corrosion Cracking,” in NACE-07493, NACE, 2007, p. 55.
[33] M. Nagumo, “Hydrogen related failure of steels – a new aspect,” Mater. Sci. Technol., vol. 20, no. 8, pp. 940–950, Aug. 2004.
[34] J.-S. Wang, “The thermodynamics aspects of hydrogen induced embrittlement,” Eng. Fract. Mech., vol. 68, no. 6, pp. 647–669, Apr. 2001.
[35] D. Guedes et al., “The Influence of Hydrogen Flux on Crack Initiation in Martensitic Steels,” Procedia Mater. Sci., vol. 3, pp. 2024–2029, Jan. 2014.

[36] I. Benedetti, V. Gulizzi, and A. Milazzo, “Grain-boundary modelling of hydrogen assisted intergranular stress corrosion cracking,” Mech. Mater., vol. 117, pp. 137–151, Feb. 2018.
[37] F.W. Jones and W.I. Pumphrey, “Free Energy and Metastable States in the Iron-Nickel and Iron-Manganese Systems,” J. Iron Steel Inst., vol. 163, p. 121, 1949.
[38] B. -Z, Weiss, “Maraging Steels—Structure, Properties and Applications,” 1989. .
[39] N. Atsmon and A. Rosen, “Reverted austenite in maraging steel,” Metallography, vol. 14, no. 2, pp. 163–167, May 1981.
[40] K. Hosomi, Y. Ashida, H. Hato, and K. Ishihara, “Embrittlement Due to the High Temperature Solution Annealing in 18% Ni Maraging Steels,” Tetsu--Hagane, vol. 61, no. 7, pp. 1012–1027, May 1975.
[41] Y. Kawabe, M. Kanao, K. Nakazawa, and S. Muneki, “Effects of the Aged Structure and the Prior Austenite Grain Size on Fracture Toughness of 18Ni Maraging Steels,” Tetsu--Hagane, vol. 60, no. 2, pp. 269–283, Feb. 1974.
[42] S. Morito, X. Huang, T. Furuhara, T. Maki, and N. Hansen, “The morphology and crystallography of lath martensite in alloy steels,” Acta Mater., vol. 54, no. 19, pp. 5323–5331, Nov. 2006.
[43] S. Morito, I. Kishida, and T. Maki, “Microstructure of ausformed lath martensite in 18%Ni maraging steel,” J. Phys. IV Proc., vol. 112, pp. 453–456, Oct. 2003.
[44] T. Schuler, “Synthesis done Thomas Schuler.” Internal document, 2018.
[45] I. Tamura, K. Tsuzaki, and T. Maki, “MORPHOLOGY OF LATH MARTENSITE FORMED FROM DEFORMED AUSTENITE IN 18% Ni MARAGING STEEL,” J. Phys. Colloq., vol. 43, no. C4, pp. C4-551-C4-556, 1982.
[46] G.P. Miller and W.I. Mitchell, “Structure of Nickel-Cobalt-Molybdenum Maraging Steels in the Air-Cooled Condition,” J. Iron Steel Inst., pp. 895–898, 1969.
[47] A. Goldberg, “Morphology of Martensite Formation in a 300 Grade Maraging Steel,” Trans. ASM, vol. 62, pp. 219–229, 1969.
[48] R. L. Patterson and G. M. Wayman, “The crystallography and growth of partially-twinned martensite plates in Fe-Ni alloys,” Acta Metall., vol. 14, no. 3, pp. 347–369, Mar. 1966.
[49] S. Floreen, “The physical metallurgy of maraging steels,” Metall. Rev., vol. 13, no. 1, pp. 115–128, Jan. 1968.
[50] W. Sha, A. Cerezo, and G. D. W. Smith, “Phase chemistry and precipitation reactions in maraging steels: Part IV. Discussion and conclusions,” Metall. Mater. Trans. A, vol. 24, no. 6, pp. 1251–1256, Jun. 1993.
[51] K. Nakazawa, Y. Kawabe, and S. Muneki, “Effect of Alloying Elements on Strengthening and Toughening of Maraging Steels through α′_??_γ Cyclic Heat Treatment,” Tetsu--Hagane, vol. 65, no. 5, pp. 542–550, 1979.
[52] M. D. Perkas, “Structure and properties of high-strength maraging steels,” Met. Sci. Heat Treat., vol. 12, no. 7, pp. 558–571, Jul. 1970.
[53] R. Tewari, S. Mazumder, I. S. Batra, G. K. Dey, and S. Banerjee, “Precipitation in 18 wt% Ni maraging steel of grade 350,” Acta Mater., vol. 48, no. 5, pp. 1187–1200, Mar. 2000.
[54] U. K. Viswanathan, G. K. Dey, and M. K. Asundi, “Precipitation hardening in 350 grade maraging steel,” Metall. Trans. A, vol. 24, no. 11, pp. 2429–2442, Nov. 1993.
[55] H. J. Rack and D. Kalish, “The strength and fracture toughness of 18 Ni (350) maraging steel,” Metall. Mater. Trans. B, vol. 2, no. 11, pp. 3011–3020, Nov. 1971.

[56] X. Li and Z. Yin, “Reverted austenite during aging in 18Ni(350) maraging steel,” Mater. Lett., vol. 24, no. 4, pp. 239–242, Jul. 1995.
[57] K. Detert, “Investigation of Transformation and Precipitation in 15the ASM,” vol. 59, pp. 262–276, 1966.
[58] C. Kato, H. J. Grabke, B. Egert, and G. Panzner, “Electrochemical and surface analytical studies on hydrogen permeation with Fe-Cu alloys in sulfuric acid with and without H2S,” Corros. Sci., vol. 24, no. 7, pp. 591–611, Jan. 1984.
[59] E. G. Dafft, K. Bohnenkamp, and H. J. Engell, “Investigations of the hydrogen evolution kinetics and hydrogen absorption by iron electrodes during cathodic polarization,” Corros. Sci., vol. 19, no. 9, pp. 591–612, Jan. 1979.
[60] H. Kaesche, Die Korrosion der Metalle: Physikalisch-chemische Prinzipien und aktuelle Probleme, 3rd ed. Berlin Heidelberg: Springer-Verlag, 2011.
[61] S. Frappart, “Des éléments de compréhension sur les mécanismes de transport et de ségrégation de l’hydrogène dans les aciers martensitiques trempés et revenus à haute limite d’élasticité,” thesis, La Rochelle, 2011.
[62] F. Vucko, Etude expérimentale et modélisation des effets de l’hydrogène sur les propriétés mécaniques et le comportement en fatigue d’un acier à haute limite d’élasticité. Saint-Etienne, EMSE, 2014.
[63] R. A. Oriani, “The diffusion and trapping of hydrogen in steel,” Acta Metall., vol. 18, no. 1, pp. 147–157, Jan. 1970.
[64] A. McNabb and P. K. Foster, “A new analysis of the diffusion of hydrogen in iron and ferritic steels.,” Trans Met. Soc AIME, vol. 227, p. 618, 1963.
[65] A. R. Troiano, “The Role of Hydrogen and Other Interstitials in the Mechanical Behavior of Metals,” Metallogr. Microstruct. Anal., vol. 5, no. 6, pp. 557–569, Dec. 2016.
[66] P. Sofronis, “The influence of mobility of dissolved hydrogen on the elastic response of a metal,” J. Mech. Phys. Solids, vol. 43, no. 9, pp. 1385–1407, Sep. 1995.
[67] “Hydrogen Embrittlement | Hydrogen | Fracture,” Scribd. [Online]. Available: https://www.scribd.com/doc/283508713/Hydrogen-Embrittlement. [Accessed: 15-Jun-2018].
[68] P. Bastien and P. Azou, “Influence de l’écrouissage sur le frottement intérieur du fer et de l’acier, chargés ou non en hydrogène,” Comptes Rendus Séances Académie Sci., vol. 232, pp. 1845–1848, 1951.
[69] A.J. Kumnick and H.H. Johnson, “Deep trapping states for hydrogen in deformed iron,” Acta Metall., vol. 28, no. 1, pp. 33–39, Jan. 1980.
[70] J. Tien, A. W. Thompson, I. M. Bernstein, and R. J. Richards, “Hydrogen transport by dislocations,” Metall. Trans. A, vol. 7, no. 6, pp. 821–829, Jun. 1976.
[71] J. Chêne and A. M. Brass, “Hydrogen transport by mobile dislocations in nickel base superalloy single crystals,” Scr. Mater., vol. 40, no. 5, pp. 537–542, Feb. 1999.
[72] H. J. Maier and H. Kaesche, “Plastic deformation: a major factor in hydrogen embrittlement of low alloy steel,” Mater. Sci. Eng. A, vol. 117, pp. L11–L15, Sep. 1989.
[73] G. M. Pressouyre, “A classification of hydrogen traps in steel,” Metall. Trans. A, vol. 10, no. 10, pp. 1571–1573, Oct. 1979.
[74] J. P. Hirth, “Effects of hydrogen on the properties of iron and steel,” Metall. Trans. A, vol. 11, no. 6, pp. 861–890, Jun. 1980.
[75] Y. Huang, A. Nakajima, A. Nishikata, and T. Tsuru, “Effect of Mechanical Deformation on Permeation of Hydrogen in Iron,” ISIJ Int., vol. 43, no. 4, pp. 548–554, Apr. 2003.

[76] W. Y. Choo and J. Y. Lee, “Thermal analysis of trapped hydrogen in pure iron,” Metall. Trans. A, vol. 13, no. 1, pp. 135–140, Jan. 1982.
[77] M. Nagumo, K. Takai, and N. Okuda, “Nature of hydrogen trapping sites in steels induced by plastic deformation,” J. Alloys Compd., vol. 293–295, pp. 310–316, Dec. 1999.
[78] B. G. Pound, “Hydrogen trapping in precipitation-hardened alloys,” Acta Metall. Mater., vol. 38, no. 12, pp. 2373–2381, Dec. 1990.
[79] V. I. Sarrak, G. A. Filippov, and G. G. Kush, Trapping and solubility of hydrogen in maraging steel., vol. 55. 1983.
[80] A. M. Brass and A. Chanfreau, “Accelerated diffusion of hydrogen along grain boundaries in nickel,” Acta Mater., vol. 44, no. 9, pp. 3823–3831, Sep. 1996.
[81] J. Yao and J. R. Cahoon, “Theoretical modeling of gain boundary diffusion of hydrogen and its effect on permeation curves,” Acta Metall. Mater., vol. 39, no. 1, pp. 111–118, Jan. 1991.
[82] A. Pedersen and H. Jónsson, “Simulations of hydrogen diffusion at grain boundaries in aluminum,” Acta Mater., vol. 57, no. 14, pp. 4036–4045, Aug. 2009.
[83] M. Ichimura, Y. Sasajima, and M. Imabayashi, “Grain Boundary Effect on Diffusion of Hydrogen in Pure Aluminum,” Mater. Trans. JIM, vol. 32, no. 12, pp. 1109–1114, 1991.
[84] A. Oudriss, J. Creus, J. Bouhattate, and X. Feaugas, “EDEM Int. Conf. 2011,” Gdansk Poland, 2011.
[85] M. Aucouturier, “Grain boundary segregations and hydrogen embrittlement,” J. Phys. Colloq., vol. 43, no. C6, pp. C6-175-C6-186, Dec. 1982.
[86] J. Chêne, “Strain-assisted transport of hydrogen and related effects on the intergranular stress corrosion cracking of alloy 600,” in Environment-Induced Cracking of Materials, S. A. Shipilov, R. H. Jones, J.-M. Olive, and R. B. Rebak, Eds. Amsterdam: Elsevier, 2008, pp. 261–272.
[87] Jai-Young Lee and S.M. Lee, “Hydrogen trapping phenomena in metals with B.C.C. and F.C.C. crystals structures by the desorption thermal analysis technique - ScienceDirect,” Surf. Coat. Technol., vol. 28, no. 3–4, pp. 301–314, Aug. 1986.
[88] I.-W. Kang, S.-I. Pyun, and K.-T. Kim, “The effects of dislocations on the trapping and transport of hydrogen in 3.3 Ni - 1.6 Cr steel during plastic deformation,” Scr. Metall., vol. 23, no. 2, pp. 223–226, Feb. 1989.
[89] M. Kurkela and R. M. Latanision, “The effect of plastic deformation on the transport of hydrogen in nickel,” Scr. Metall., vol. 13, no. 10, pp. 927–932, Oct. 1979.
[90] H. B. Aaron and G. F. Bolling, “Free volume as a criterion for grain boundary models,” Surf. Sci., vol. 31, pp. 27–49, Jun. 1972.
[91] G. M. Pressouyre and F. M. Faure, Quantitative Analysis of Critical Concentrations for Hydrogen-Induced Cracking. West Conshohocken, PA: ASTM International, 1988.
[92] L. Coudreuse, “Fragilisation par l’hydrogène et corrosion sous contrainte,” Corros. Sous Contrainte – Phénoménologie Mécanisme Ed. Phys., pp. 397–424, 1990.
[93] J. W. (Josiah W. Gibbs, On the equilibrium of heterogeneous substances / by J. Willard Gibbs ; abstract by the author. 1878.
[94] S. P. Lynch, “Environmentally assisted cracking: Overview of evidence for an adsorption-induced localised-slip process,” Acta Metall., vol. 36, no. 10, pp. 2639–2661, Oct. 1988.
[95] C. D. Beachem, “A new model for hydrogen-assisted cracking (hydrogen ‘embrittlement’),” Metall. Mater. Trans. B, vol. 3, no. 2, pp. 441–455, Feb. 1972.

[96] H. K. Birnbaum et al., “Hydrogen in aluminum,” J. Alloys Compd., vol. 253–254, pp. 260–264, May 1997.
[97] I. M. Robertson, “The effect of hydrogen on dislocation dynamics,” Eng. Fract. Mech., vol. 68, no. 6, pp. 671–692, Apr. 2001.
[98] E. Sirois and H. K. Birnbaum, “Effects of hydrogen and carbon on thermally activated deformation in nickel,” Acta Metall. Mater., vol. 40, no. 6, pp. 1377–1385, Jun. 1992.
[99] Y. Fukai, “Formation of superabundant vacancies in metal hydrides at high temperatures,” J. Alloys Compd., vol. 231, no. 1, pp. 35–40, Dec. 1995.
[100] Y. Fukai, The Metal-Hydrogen System: Basic Bulk Properties. Berlin Heidelberg: Springer-Verlag, 1993.
[101] Y. Fukai, T. Haraguchi, E. Hayashi, Y. Ishii, Y. Kurokawa, and J. Yanagawa, “Hydrogen-Induced Superabundant Vacancies and Diffusion Enhancement in Some FCC Metals,” Defect Diffus. Forum, vol. 194–199, pp. 1063–1068, 2001.
[102] Y. Fukai, M. Mizutani, S. Yokota, M. Kanazawa, Y. Miura, and T. Watanabe, “Superabundant vacancy–hydrogen clusters in electrodeposited Ni and Cu,” J. Alloys Compd., vol. 356–357, pp. 270–273, Aug. 2003.
[103] C. Zapffe and G. Moore, “A Micrographic Study of the Cleavage of Hydrogenized Ferrite,” p. 19.
[104] N. J. Petch and P. Stables, “Delayed Fracture of Metals under Static Load,” Nature, vol. 169, no. 4307, pp. 842–843, May 1952.
[105] H. H. Johnson and A. R. Troiano, “Crack Initiation in Hydrogenated Steel,” Nature, vol. 179, no. 4563, p. 777, Apr. 1957.
[106] G. Wang, Y. Yan, J. Li, J. Huang, L. Qiao, and A. A. Volinsky, “Microstructure effect on hydrogen-induced cracking in TM210 maraging steel,” Mater. Sci. Eng. A, vol. 586, pp. 142–148, Dec. 2013.
[107] L. W. Tsay, H. L. Lu, and C. Chen, “The effect of grain size and aging on hydrogen embrittlement of a maraging steel,” Corros. Sci., vol. 50, no. 9, pp. 2506–2511, Sep. 2008.
[108] R. P. Gangloff, “Hydrogen Assisted Cracking of High Strength Alloys,” Aluminium co of america alcoa center pa alcoa technical center, Aug. 2003.
[109] R. P. Gangloff and R. P. Wei, “Gaseous hydrogen embrittlement of high strength steels,” Metall. Trans. A, vol. 8, no. 7, pp. 1043–1053, Jul. 1977.
[110] R. P. Gangloff and R. P. Wei, “Fractographic Analysis of Gaseous Hydrogen Induced Cracking in 18Ni Maraging Steel,” Fractography Fail. Anal., Jan. 1978.
[111] G.E. Kerns, M.T. Wang, and R.W. Staehle, “Stress Corrosion Cracking and Hydrogen Embrittlement of Iron Base Alloys,” NACE Houst. TX, pp. 700–735, 1977.
[112] J. J. Rimoli and M. Ortiz, “A three-dimensional multiscale model of intergranular hydrogen-assisted cracking,” Philos. Mag., vol. 90, no. 21, pp. 2939–2963, Jul. 2010.
[113] Y. Hirose and T. Mura, “Growth mechanism of stress corrosion cracking in high strength steel,” Eng. Fract. Mech., vol. 19, no. 6, pp. 1057–1067, Jan. 1984.
[114] P. J. Raboin, “The mechanical behavior of maraging steel under extreme electromechanical and thermal conditions,” Thesis, Massachusetts Institute of Technology, 1989.
[115] L. F. Van Swam, R. M. Pelloux, and N. J. Grant, “Fatigue behavior of maraging steel 300,” Metall. Trans. A, vol. 6, no. 1, pp. 45–54, Jan. 1975.
[116] A. Keh and S. Weissmann, Deformation substructure in body-centered cubic metals, Electron microscopy and strength of crystals. NY-London: Interscience publishers, 1963.

[117] Y. Lan, H. J. Klaar, and W. Dahl, “Evolution of dislocation structures and deformation behavior of iron at different temperatures: Part I. strain hardening curves and cellular structure,” Metall. Trans. A, vol. 23, no. 2, pp. 537–544, Feb. 1992.
[118] M. F. Ashby, “Results and consequences of a recalculation of the frank-read and the orowan stress,” Acta Metall., vol. 14, no. 5, pp. 679–681, May 1966.
[119] T. Gladman, “Precipitation hardening in metals,” Mater. Sci. Technol., vol. 15, no. 1, pp. 30–36, Jan. 1999.
[120] R. M. Brito and H.-J. Kestenbach, “On the dispersion hardening potential of interphase precipitation in micro-alloyed niobium steel,” J. Mater. Sci., vol. 16, no. 5, pp. 1257–1263, May 1981.
[121] K. Li, B. Yu, R. D. K. Misra, G. Han, S. Liu, and C. J. Shang, “Strengthening of cobalt-free 19Ni3Mo1.5Ti maraging steel through high-density and low lattice misfit nanoscale precipitates,” Mater. Sci. Eng. A, vol. 715, pp. 174–185, Feb. 2018.
[122] “Do Izod and Charpy make the appropriate impact? By Dr.Charlie Geddes,” Hardie Polymers. .
[123] W. D. Pilkey and D. F. Pilkey, Peterson’s Stress Concentration Factors. John Wiley & Sons, 2008.
[124] Murakami Y. and Nisitani H., “Stress intensity factor for circumferentially cracked round bar in tension.,” Trans Jpn Soc Mech Engng, vol. 41, no. 342, pp. 360–369, Feb. 1975.
[125] V. Favier et al., “Slow crack propagation in polyethylene under fatigue at controlled stress intensity,” Polymer, vol. 43, no. 4, pp. 1375–1382, Feb. 2002.
[126] C. S. Carter, “The effect of heat treatment on the fracture toughness and subcritical crack growth characteristics of a 350-grade maraging steel,” Metall. Trans., vol. 1, no. 6, pp. 1551–1559, Jun. 1970.
[127] C. S. Carter, “Fracture toughness and stress corrosion characteristics of a high strength maraging steel,” Metall. Trans., vol. 2, no. 6, pp. 1621–1626, Jun. 1971.
[128] Y. He, K. Yang, W. Qu, F. Kong, and G. Su, “Strengthening and toughening of a 2800-MPa grade maraging steel,” Mater. Lett., vol. 56, no. 5, pp. 763–769, Nov. 2002.
[129] “ISO 17081:2004 - Method of measurement of hydrogen permeation and determination of hydrogen uptake and transport in metals by an electrochemical technique.” [Online]. Available: https://www.iso.org/standard/40480.html. [Accessed: 05-Sep-2018].
[130] L. Fournier, “Interactions corrosion - deformation dans l’alliage 718 : application a la corrosion sous contrainte en milieu aqueux supercritique et recherche d’une solution materiau pour le procede d’oxydation hydrothermale,” thesis, Grenoble INPG, 2000.
[131] M. J. Gomes da Silva et al., “The effect of prior austenite grain size on hydrogen embrittlement of Co-containing 18Ni 300 maraging steel,” Int. J. Hydrog. Energy, Jun. 2019.
[132] L. P. M. Santos, M. Béreš, I. N. Bastos, S. S. M. Tavares, H. F. G. Abreu, and M. J. Gomes da Silva, “Hydrogen embrittlement of ultra high strength 300 grade maraging steel,” Corros. Sci., vol. 101, pp. 12–18, Dec. 2015.
[133] M. Nageswara Rao, M. K. Mohan, and P. Uma Maheswara Reddy, “Environmentally assisted cracking of 18%Ni maraging steel,” Corros. Sci., vol. 51, no. 8, pp. 1645–1650, Aug. 2009.
[134] D. H. Bradhurst and P. M. Heuer, “Environmental Cracking of High Strength Maraging Steels: Part I — Aqueous NaCl Solution,” CORROSION, vol. 37, no. 1, pp. 50–55, Jan. 1981.

[135] K. G. Reddy, S. Arumugam, and T. S. Lakshmanan, “Hydrogen embrittlement of maraging steel,” J. Mater. Sci., vol. 27, no. 19, pp. 5159–5162, Oct. 1992.
[136] “E. Orowan: Proc. Phys. Soc. (London), 1940, vol. 52, p. 8.” .
[137] S. Frappart et al., “Hydrogen trapping in martensitic steel investigated using electrochemical permeation and thermal desorption spectroscopy,” Scr. Mater., vol. 65, no. 10, pp. 859–862, Nov. 2011.
[138] A. M. Brass and J. Chene, “Influence of deformation on the hydrogen behavior in iron and nickel base alloys: a review of experimental data,” Mater. Sci. Eng. A, vol. 242, no. 1–2, pp. 210–221, Feb. 1998.
[139] Z. Cui, Z. Liu, L. Wang, X. Li, C. Du, and X. Wang, “Effect of plastic deformation on the electrochemical and stress corrosion cracking behavior of X70 steel in near-neutral pH environment,” Mater. Sci. Eng. A, vol. 677, pp. 259–273, Nov. 2016.
[140] T. Depover, D. Pérez Escobar, E. Wallaert, Z. Zermout, and K. Verbeken, “Effect of hydrogen charging on the mechanical properties of advanced high strength steels,” Int. J. Hydrog. Energy, vol. 39, no. 9, pp. 4647–4656, Mar. 2014.
[141] T. Depover and K. Verbeken, “The detrimental effect of hydrogen at dislocations on the hydrogen embrittlement susceptibility of Fe-C-X alloys: An experimental proof of the HELP mechanism,” Int. J. Hydrog. Energy, vol. 43, no. 5, pp. 3050–3061, Feb. 2018.
[142] T. Depover, E. Wallaert, and K. Verbeken, “Fractographic analysis of the role of hydrogen diffusion on the hydrogen embrittlement susceptibility of DP steel,” Mater. Sci. Eng. A, vol. 649, no. Supplement C, pp. 201–208, Jan. 2016.
[143] H. J. Rack and D. Kalish, “The strength and fracture toughness of 18 Ni (350) maraging steel,” Metall. Mater. Trans. B, vol. 2, no. 11, pp. 3011–3020, Nov. 1971.
[144] Y. He, K. Yang, W. Qu, F. Kong, and G. Su, “Strengthening and toughening of a 2800-MPa grade maraging steel,” Mater. Lett., vol. 56, no. 5, pp. 763–769, Nov. 2002.
[145] B. O. Hoch, “Modelling of hydrogen diffusion in heterogeneous materials : implications of the grain boundary connectivity,” phdthesis, Université de La Rochelle, 2015.
[146] K. Hirayama, Y. Yoshii, Y. Morizono, S. Tsurekawa, and Y. Hidaka, “Grain boundary engineering of 10% Cr ferritic-martensitic steel SUH3,” ISIJ Int., vol. 55, no. 9, pp. 1973–1979, 2015.

École Nationale Supérieure des Mines
de Saint-Étienne

NNT : *Communiqué le jour de la soutenance*

Elia TOHMÉ

A contribution to the understanding of hydrogen diffusion and embrittlement based on SKPFM measurements and mechanical testing.

Speciality : Materials Science and Engineering
Keywords : Duplex stainless steel, Maraging, Hydrogen embrittlement, SKPFM analysis.

Abstract :

This study contributes to a better understanding of the hydrogen embrittlement phenomenon of steels.

The first part of this manuscript is devoted to the assessment of a recently developed method to study hydrogen diffusion based on the detection of the variation of the work function of the surface by Scanning Kelvin Probe Microscopy (SKPFM). A Duplex stainless steel was used in this study, due to its two different phases having different hydrogen-related characteristics (diffusivity, solubility). A palladium layer was deposited on the observation surface and behaved as a hydrogen collector. A finite element simulation of hydrogen diffusion in a multiphase system was developed to explain the experimental observations. It is shown that SKPFM should be considered as a way to monitor locally the release of hydrogen into the palladium layer, rather than a way to map the hydrogen concentration in the material microstructure.

The second part of the manuscript deals with the hydrogen embrittlement of a maraging steel under cathodic charging with regard to hydrogen diffusion and trapping properties. Dynamic and static mechanical testing were used, while various conditions of hydrogen ingress were explored corresponding to a direct cathodic hydrogen charging, or via a diffusion path in the material by protecting the notch tip from the environment. Crack initiation stage is dependent on the hydrogen transport, and accumulation, by accelerated diffusion along preferential paths. A sub-critical regime of crack propagation is identified. It corresponds to a mixed intergranular/transgranular mode of cracking, the IG mode referring to prior γ-grain boundaries and TG mode to high-angle misorientation interfaces of the martensite. This stage is hydrogen diffusion-dependent; it corresponds to a steady state crack growth rate vs stress intensity factor. The final fracture at a critical K_{IH} value is dependent on hydrogen content in the material and refers to TG mode of cracking.

École Nationale Supérieure des Mines
de Saint-Étienne

NNT : *Communiqué le jour de la soutenance*

Elia TOHMÉ

Une contribution à la compréhension de la diffusion et de la fragilisation de l'hydrogène basée sur des mesures par SKPFM et des tests mécaniques.

Spécialité: Sciences et Génie des Matériaux
Mots clefs : Acier inoxydable Duplex, acier Maraging, FPH, SKPFM.

Résumé :

Cette étude contribue à une meilleure compréhension du phénomène de fragilisation par l'hydrogène des aciers.

La première partie du manuscrit est consacrée à l'évaluation d'une méthode récemment développée pour étudier la diffusion de l'hydrogène, basée sur la détection de la variation du travail de sortie en surface par microscopie à force atomique et sonde de Kelvin (SKPFM). Un acier inoxydable Duplex a été utilisé, les deux phases ayant chacune des caractéristiques liées à l'hydrogène (diffusivité, solubilité) différentes. Une couche de palladium a été déposée sur la surface d'observation qui se comporte comme un collecteur d'hydrogène. Une simulation par éléments finis de la diffusion d'hydrogène dans un système multiphasé a été développée afin d'interpréter les observations expérimentales. Il est démontré que la technique de SKPFM doit être considérée comme un moyen de suivre localement la désorption de l'hydrogène dans la couche de Pd, plutôt qu'un moyen de cartographier la concentration en hydrogène dans la microstructure du matériau.

La deuxième partie traite de la FPH d'un acier maraging sous chargement cathodique au regard des propriétés de diffusion et de piégeage de l'hydrogène. Des essais mécaniques dynamiques et statiques ont été utilisés, tandis que différentes conditions d'entrée d'hydrogène ont été explorées : chargement cathodique direct de l'hydrogène ou, via un trajet de diffusion dans le matériau en protégeant la pointe de l'entaille de l'environnement. L'amorçage de la fissure dépend du transport de l'hydrogène par diffusion accélérée selon des chemins préférentiels. Un régime sous-critique de propagation de fissure est identifié. Il correspond à un mode de fissuration mixte inter/transgranulaire, le mode IG faisant référence aux anciens joints de grain γ et le mode TG à des interfaces de fortes désorientations. Cette étape est dépendante de la diffusion de l'hydrogène; elle correspond à des vitesses de propagation de fissure relativement stable en fonction du facteur d'intensité des contraintes.